THE EFFECTS OF THE KELVIN-HELMHOLTZ INSTABILITY OF THE MAGNETOSPHERE

Katharine J. Mills

A Thesis Submitted for the Degree of PhD
at the
University of St Andrews

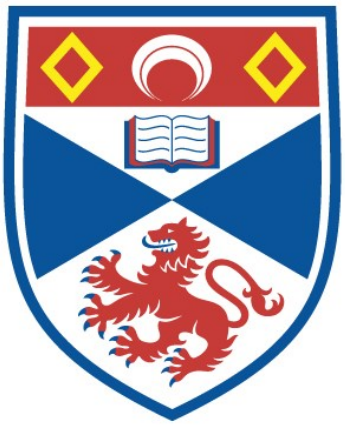

1999

The Effects of the Kelvin-Helmholtz Instability on the Magnetosphere

Katharine J. Mills

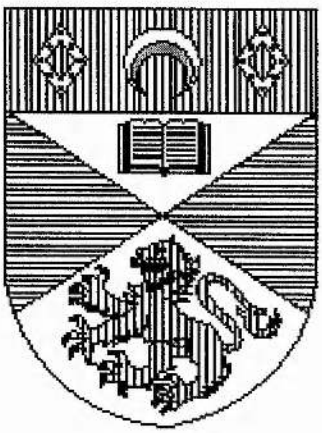

Thesis submitted for the degree of Doctor of Philosophy

of the University of St Andrews

November 21, 1999

with love to Mum, Dad and Jason

Declaration

1. I, Katharine Jane Mills, hereby certify that this thesis, which is approximately 60 000 words in length, has been written by me, that it is the record of work carried out by me and that it has not been submitted in any previous application for a higher degree.

   date ...13th..July..1999.....signature of candidate .....

2. I was admitted as a research student in September 1996 and as a candidate for the degree of PhD in September 1997; the higher study for which this is a record was carried out in the University of St Andrews between 1996 and 1999.

   date ..13th..July...1999.....signature of candidate .

3. I hereby certify that the candidate has fulfilled the conditions of the Resolution and Regulations appropriate to the degree of PhD in the University of St Andrews and that the candidate is qualified to submit this thesis in application for that degree.

   date .....12 July 1999..... signature of supervisor .

4. In submitting this thesis to the University of St Andrews I understand that I am giving permission for it to be made available for use in accordance with the regulations of the University Library for the time being in force, subject to any copyright vested in the work not being affected thereby. I also understand that the title and abstract will be published, and that a copy of the work may be made and supplied to any bona fide library or research worker.

   date ...13th..July...1999.....signature of candidate ...

Abstract

In this thesis, the behaviour of Kelvin-Helmholtz unstable modes on the magnetospheric flanks and in the magnetotail are investigated. A model of a straight bounded magnetosphere connected to a semi-infinite field-free magnetosheath which is flowing with a uniform speed is used.

First the magnetosphere is taken to be uniform with the magnetic field perpendicular to the flow in the magnetosheath and it is shown that the increase in Pc5 wave power observed for high solar wind flow speeds correlates well with the onset of instability of the fast body modes. A condition for the exact onset of instability of these modes is derived and the behaviour of fast surface and slow body and surface modes is also investigated.

Using a non-uniform magnetosphere, it is shown that these unstable body modes may couple to field line resonances. The fastest growing modes are found to have a common azimuthal phase speed which depends only on the local conditions at the magnetopause and may be predicted using the theory of over-reflection.

A finite width boundary layer is then added to the uniform magnetosphere model to investigate the space-time evolution of wave-packets on the magnetopause. Fast surface mode wave-packets are found to grow rapidly as they convect around the flanks so that non-linear effects will be important. Fast cavity mode wave-packets will remain relatively small on the flanks, explaining the robustness of the body of the magnetosphere here. Slow modes are found to grow very little in this region.

Finally, a uniform magnetosphere with the magnetic field parallel to the flow in the magnetosheath is considered. Here, the fast modes are unlikely to be Kelvin-Helmholtz unstable for realistic flow speeds, and the magnetopause boundary may be reasonably assumed to be perfectly reflecting. The low value of the plasma pressure is this region suggests that slow modes will be unimportant.

Publications

The contents of Chapters 2 and 3 have been published in *Physics of Plasmas* (Mills, Wright and Mann, 1999) and that of Chapter 4 has been published in *Journal of Geophysical Research* (Mills and Wright, 1999a). Some of the work detailed in Chapter 5 has been accepted by *Journal of Geophysical Research* (Wright, Mills, Rudermann and Brevdo, 1999), and the remaining parts have been submitted to the same journal (Mills, Longbottom, Wright and Rudermann, 1999). The work in Chapter 6 has been submitted to *Physics of Plasmas* (Mills and Wright, 1999b).

Acknowledgements

I would like to thank:

Dr Andy Wright for his excellent supervision and inspiration during my PhD.

Dr Michael Rudermann for many useful discussions, hints and ideas.

Dr Aaron Longbottom for the computer simulations in Chapter 5 and for not laughing at me when I asked him to quadruple the number of points in all directions.

Prof. Alan Hood for his excellent teaching of the Solar MHD course when I was an under-grad that sparked my interest in the subject in the first place.

Friends both within and without the research group for laughs, fun and help in too many ways to mention. In no particular order thanks to Kirsty, David W., Neil, Anna, Daniel, David B., ineke, Cheryl, Darren, Clare M., Clare P., Catriona and Margaret.

Mum and Dad for supporting and encouraging me always. Also, thanks Dad for heroically checking this thesis through.

My fiancé Jason for all your love and support over the last two years - for making me laugh when I was feeling down and for helping me keep it all in perspective - and of course for reading all this through and many helpful suggestions.

Contents

Then out of the storm the Lord spoke to Job.
"Do you know the laws that govern the skies,
and can you make them apply to the Earth?"

Job 38:1,33; GNB

Chapter 1

Introduction

1.1 The Magnetosphere

1.1.1 History of the Magnetosphere

The magnetosphere is a cavity in the solar wind formed by the Earth's magnetic field. The fact that this cavity exists has only been discovered fairly recently. In fact, the term magnetosphere was only coined by Thomas Gold in 1959. However, it has been known for a thousand years that compass needles point north-south. In 1600 William Gilbert suggested that this property may be explained by the fact that the Earth itself is a magnet. He used a small spherical magnet to demonstrate that a compass needle would always point to the magnetic poles. It took over 200 years before observations of the Earth's magnetic field were made consistently, and a global network of observation sites were set up in 1830. The result of observations from this network was the realisation that the disturbances, seen occasionally in the magnetic field causing the fluctuation of compass needles was a global phenomenon and it was proposed that the source of these disturbances came from a non-terrestrial source. Alexander von Humboldt christened these disturbances magnetic storms. Over the next century attempts to explain these storms met with little success, although it was realised that some of this activity could be linked with solar activity by the end of the nineteenth century.

In 1930, Chapman and Ferraro suggested that magnetic storms were caused by clouds of plasma from the sun hitting the Earth. They were the first to suggest that the magnetic field of the Earth would offer resistance to the force of this magnetic cloud and so form a cavity around the Earth. Chapman and Ferraro's theories could only be compared to observations once satellite observations of the space environment around

the Earth began. These showed that there is a continuous flow of plasma from the sun, the solar wind, in which the Earth's magnetic field creates a cavity. The actual onset of magnetic storms was found to be linked with coronal mass ejections which are indeed dense clouds of plasma from the sun.

It was only when observations from the Explorer spacecraft were analysed in 1958 that it was realised what a complicated magnetic environment surrounds our planet. Indeed, the boundary between the magnetopause and the solar wind, the magnetopause, was only discovered in 1961 by the Explorer 12 spacecraft.

1.1.2 The Morphology of the Magnetosphere

In the last forty years, the structure of the magnetosphere has been explored by many satellites and is now well understood. The solar wind travels at speeds of between 300 and 800km/s as it reaches the Earth. This speed is fast enough to cause the formation of a shock upstream from the Earth. As the plasma crosses the shock it is becomes denser, is slowed down and is heated. This plasma cannot, in general, cross into the magnetosphere, but flows around it to form the magnetosheath. As it moves around the magnetosphere it is accelerated and reaches the speed of the ambient solar wind downstream on the flanks of the magnetosphere (see e.g., Spreiter and Stahara, 1980). The bow shock and magnetosphere are illustrated schematically in Figure 1.1. The bow shock is the line around the magnetosphere, with the bright region at its nose indicating the heating of particles here. The main regions in the magnetosphere are illustrated in Figure 1.2. The region of plasma between the bow shock and the magnetopause is known as the magnetosheath.

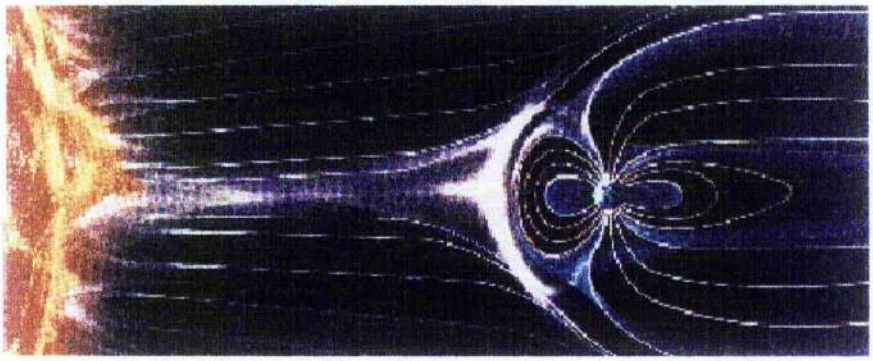

Figure 1.1: An illustration showing the interaction between the solar wind and the Earth's magnetic field (not to scale). Taken from http://www-spof.gsfc.nasa.gov/Education/Intro.html.

Figure 1.2: An illustration of the main features of the magnetosphere. Open with care!

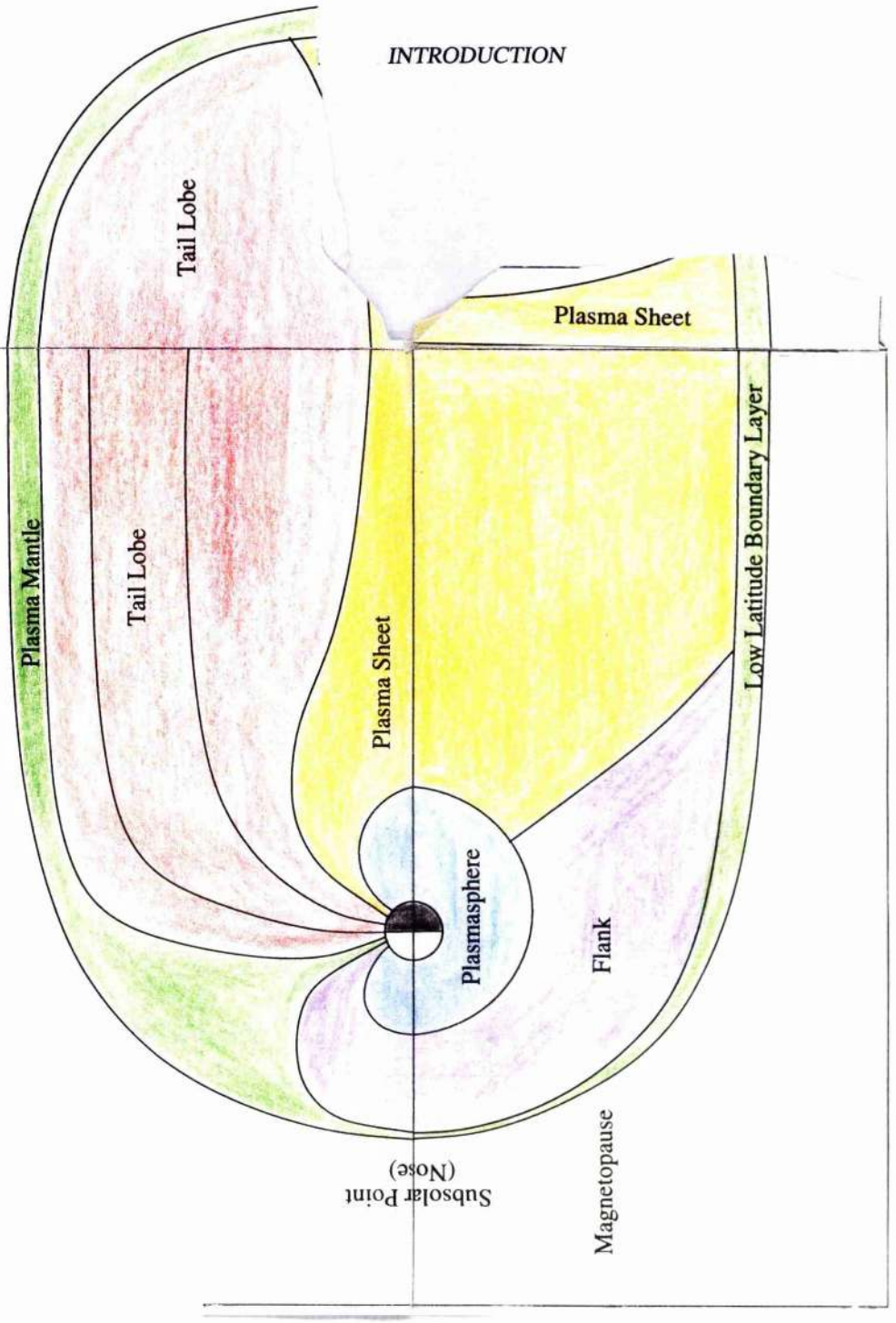
Tail Lobe
Plasma Sheet
Plasma Mantle
Tail Lobe
Plasma Sheet
Low Latitude Boundary Layer
Plasmasphere
Flank
Subsolar Point
(Nose)
Magnetopause

The nose of the magnetosphere is the part closest to the sun. Its distance from the Earth is governed by the dynamic pressure of the solar wind and varies from about 6 R_E ($1R_E$ = 1 Earth Radius = 6400 km) when large coronal mass ejections hit the magnetosphere, to about 13 R_E at times of very slow solar wind. The average distance to the nose of the magnetosphere is $10 - 11$ R_E.

When the inter-planetary magnetic field (IMF) has a southward component, reconnection may occur efficiently at the nose of the magnetosphere. This process connects closed magnetospheric field lines to those in the IMF and allows the flow of plasma from the magnetosheath into the magnetosphere. These opened field lines have foot-points in the polar regions of the ionosphere, and solar wind particles may stream along these field lines to the polar caps. The particles are mirrored by the increasing magnetic field closer to the Earth and form a plasma mantle covering the open field lines in the tail, and which is formed from a mixture of solar wind and terrestrial plasmas.

The field lines which are opened by the reconnection process are carried away from the sun by the solar wind, to form the tail of the magnetosphere. The length of the tail was calculated by Dungey (1965) to be of the order of 1000 R_E. The tail is comprised of two main parts. The plasma sheet is a hot layer of plasma stretching across the equatorial plane of the magnetotail. It is about $3 - 7$ R_E wide, with a number density of the order of 1 cm^{-3}, although these parameters can vary significantly. Magnetic substorms, disturbances seen on Earth, are believed to originate in this tail plasma sheet. The magnetic field is low in the plasma sheet and oppositely directed in the tail lobes on either side of it. Thus reconnection may occur in the plasma sheet. This results in flows of plasma both earthwards and away from the Earth. The flow towards the Earth results in precipitation of particles into the ionosphere, creating the aurorae. The flow away from the Earth is in the form of plasmoids, which flow into inter-planetary space and are lost from the magnetosphere system. The tail lobes have relatively strong smooth magnetic fields stretched parallel to the plasma sheet. The particle number density in the tail is very small, only about 0.01 cm^{-3}. The strong magnetic field stores magnetic energy which is believed to be released during substorm activity. The magnetic field is directed towards the Earth in the north tail lobe and away from the Earth in the south lobe. A steady electric current is observed in the magnetotail, flowing from east to west across the plasma sheet and then closing around both tail lobes.

The process of reconnection at the nose of the magnetosphere and in the magnetotail sets up a circulation of the magnetic field lines in the magnetosphere. The field lines are opened at the nose of the magnetosphere and closed in the magnetotail. The only field lines which do not form part of this circulation pattern are those in the plasmasphere. The plasmasphere is the region of the magnetosphere in which the field lines are permanently closed. It extends to about 5 R_E from the Earth in the equatorial planes, but does

not extend over the poles, and co-rotates with the Earth. The plasma in this region is in equilibrium with the ionosphere and the density falls off rapidly with distance form the Earth. A useful quantity in magnetospheric measurements is the L-shell value. This co-ordinate defines particular field lines and correspond to the distance from the Earth to the field lines in the equatorial plane measured in R_E. Thus observations of foot-point motions in the ionosphere can be correlated with events on the same field line by considering the L-shell value. The plasmasphere extends to an L-shell of about 5.

The boundary between the magnetosphere and the magnetosheath is known as the magnetopause. Observations of magnetopause crossings are characterised by abrupt changes in the magnetic field strength and direction as well as the plasma density and flow speed, the latter being strongly anti-sunward in the magnetosheath. Just inside the magnetopause there is boundary layer with properties intermediate between the magnetosphere and magnetosheath. This region has widths of up to 1.5 R_E on the magnetospheric flanks and is composed of both magnetospheric and solar wind ions. The magnetic field in this region is thought to be connected mostly to the Earth, but sometimes to the IMF.

1.2 Magnetohydrodynamic Waves

A central theme of this thesis is the propagation of magnetohydrodynamic (MHD) waves in the Earth's magnetosphere. The study of these oscillations enables us to examine the stability of the magnetopause as well as the evolution in space and time of any disturbances. To do this, we use the ideal MHD equations to define a dispersion relation for the system corresponding to a relationship between the frequency of a mode and its wavenumber. The solutions of this dispersion relation correspond to 'normal modes' of the disturbances in the system. In this section we will present the MHD equations and discuss the assumptions we have made in our analysis. We will then discuss the properties of the three types of MHD waves for uniform media. We will also summarise the results from Roberts (1981a,b) which discuss the behaviour of MHD waves in a non-uniform system.

1.2.1 The Magnetohydrodynamic Equations

Throughout this thesis we will be using the magnetohydrodynamic equations to model the propagation of waves in the magnetosphere. The MHD equations are a combination of the electromagnetic equations and the fluid equations. More detail on these equations may be found in Boyd and Sanderson (1969) or Siscoe (1982). We make the assumption that any plasma motion is non-relativistic, and we may then combine

these two sets of equations to give: the equation of motion

$$\rho\left(\frac{\partial}{\partial t}+\mathbf{v}.\nabla\right)\mathbf{v}=-\nabla\left(p+\frac{\mathbf{B}.\mathbf{B}}{2\mu_o}\right)+(\mathbf{B}.\nabla)\frac{\mathbf{B}}{\mu_o}+\mathbf{F}; \tag{1.1}$$

the induction equation

$$\left(\frac{\partial}{\partial t}+\mathbf{v}.\nabla\right)\mathbf{B}=(\mathbf{B}.\nabla)\,\mathbf{v}-\mathbf{B}\,(\nabla.\mathbf{v})+\eta\nabla^2\mathbf{B}; \tag{1.2}$$

the mass continuity equation

$$\left(\frac{\partial}{\partial t}+\mathbf{v}.\nabla\right)\rho=\rho\nabla.\mathbf{v}; \tag{1.3}$$

and the solenoidal constraint

$$\nabla.\mathbf{B}=0, \tag{1.4}$$

where $\mathbf{B}$ is the magnetic field vector, $\mathbf{v}$ is the fluid velocity, ρ is the density, p is the pressure, t is time, $\mathbf{F}$ is any forces acting on the plasma other than those from the magnetic field and the pressure (e.g., gravity), μ_o is the magnetic permeability of free space (taken to be $4\pi\times10^{-7}$ H/m) and η is the magnetic diffusivity which is inversely proportional to the electrical conductivity (taken as uniform here). We also take an energy equation of the form

$$\frac{\rho^\Gamma}{\rho-1}\left(\frac{\partial}{\partial t}+\mathbf{v}.\nabla\right)\left(\frac{p}{\rho^\Gamma}\right)=L, \tag{1.5}$$

where Γ is the ratio of specific heats and L represents the energy gains and losses of the system, which may, in general, be a function of space and time. In the equation of motion (1.1) we have written the force exerted by the magnetic field on the plasma in two parts. These parts can be thought of as the force exerted by the magnetic pressure,

$$-\nabla\left(\frac{\mathbf{B}.\mathbf{B}}{2\mu_o}\right) \tag{1.6}$$

and the magnetic tension force

$$(\mathbf{B}.\nabla)\frac{\mathbf{B}}{\mu_o}. \tag{1.7}$$

We also define the total pressure as the sum of the plasma and magnetic pressures, so that

$$p_T=p+\frac{B^2}{2\mu_o}. \tag{1.8}$$

In our analysis we will make several assumptions about the plasma parameters. First we assume that the plasma is perfectly conducting, so that η is taken to be zero. The magnetic Reynolds number is defined as

$$R_m=\frac{l_oV_o}{\eta}, \tag{1.9}$$

where l_o and V_o are the typical length scale and plasma velocity of the system, respectively. In the limit as η becomes small, the magnetic Reynolds number becomes large. In this limit, the induction equation reduces to

$$\left(\frac{\partial}{\partial t} + \mathbf{v}.\nabla\right)\mathbf{B} = (\mathbf{B}.\nabla)\,\mathbf{v} - \mathbf{B}\,(\nabla.\mathbf{v})\,. \tag{1.10}$$

A consequence of this limit is that the plasma becomes 'frozen in' to the magnetic field (see e.g., Boyd and Sanderson, 1969). This means that any plasma element may be associated with a particular magnetic field line at all times, and plasma motion will only occur along the field lines, not across them. We assume that the effects of other forces such as gravity and viscosity will be negligible (so $\mathbf{F} = 0$) in Equation (1.1) and that the plasma is adiabatic (so $L = 0$). Then the energy equation becomes

$$\left(\frac{\partial}{\partial t} + \mathbf{v}.\nabla\right)p = \frac{\Gamma p}{\rho}\left(\frac{\partial}{\partial t} + \mathbf{v}.\nabla\right)\rho. \tag{1.11}$$

The speed of sound in the plasma is

$$c_s = \sqrt{\frac{\Gamma p}{\rho}}, \tag{1.12}$$

and the Alfvén speed is

$$v_A = \frac{B}{\sqrt{\mu_o \rho}}. \tag{1.13}$$

An useful quantity in defining the relative importance of the magnetic and pressure forces is the plasma beta, β, defined by

$$\beta = \frac{p}{B^2/2\mu_o}, \tag{1.14}$$

which is the ratio of the plasma pressure to the magnetic pressure. In a low beta plasma, the magnetic forces dominate, whereas the plasma pressure forces dominate in a high beta plasma.

The Validity of MHD

MHD is, of course, only an approximation to the immensely complex systems of plasmas that we are attempting to examine, so it is important to consider the validity of this approximation and also the situations in which it breaks down. The approximations made in MHD are valid if the scale length of the change in magnetic field is large compared to the particle gyroradius, and the time scales are long compared to the gyroperiod. This gives the two conditions

$$\frac{r_l}{B}\frac{\partial B}{\partial l} \ll 1 \tag{1.15}$$

$$\frac{\tau_c}{B}\frac{\partial B}{\partial t} \ll 1, \tag{1.16}$$

where l and t are the distance and time over which the field varies, and r_l and τ_c are the typical gyroradius and gyroperiod, respectively. In the inner magnetosphere, $r_l \approx 10$m and $\tau_c \approx 10^{-2}$s, and in the outer magnetosphere, $r_l \approx 100$km with $\tau_c \approx 1$s. Also variations must be on length scales greater than the electron inertia length ($l_e = c/\omega_{pe}$, where c is the speed of light and ω_{pe} is the electron freqency), which is of the order of 10^3m in the equatorial flanks. Therefore we may use the MHD approximation to study structures with variation on length scales greater than 100km and on time scales greater than 1s. ULF waves typically have periods of hundreds of seconds and wavelengths larger than an Earth radius, so we may assume that the MHD approximation holds in the study of these phenomenon. The MHD assumptions will break down in regions of very weak magnetic fields (e.g., the tail current sheet or the magnetopause current sheet) or where the plasma is very hot (e.g., above the auroral zones). Although this would suggest that using MHD to model the KHI at the flanks of the magnetopause would be inappropriate, it has been used with much success in previous models.

1.2.2 MHD Waves in a Uniform Medium

In order to study the propagation of MHD waves, we first consider a uniform medium which is in static equilibrium (see Roberts,1986 for a full review of this theory). The magnetic field is taken to be purely in the z-direction. We then add a small perturbation to each of the equilibrium quantities and linearise the equations (so keeping only terms up to first order in the perturbed quantity). We then assume that any perturbations are proportional to $e^{i(k_x x + k_y y + k_z z - \omega t)}$ and obtain the dispersion relation for MHD modes

$$\left(\omega^2 - k_z^2 v_A^2\right)\left(\omega^4 - \omega^2\left(c_s^2 + v_A^2\right)k^2 + k^2 k_z^2 c_s^2 v_A^2\right) = 0, \tag{1.17}$$

where $k = \sqrt{k_x^2 + k_y^2 + k_z^2}$. There are three solutions for ω^2 to this dispersion relation and they may be divided into two main types. The first is the Alfvén wave for which

$$\omega^2 = k_z^2 v_A^2 = k^2 v_A^2 \cos^2\theta, \tag{1.18}$$

where $\theta = \cos^{-1}(k_z/k)$ and is the angle between the magnetic field, $\mathbf{B}$ and the propagation vector, $\mathbf{k}$. The phase speed of the Alfvén mode is $v_A \cos\theta$, and the group velocity is $v_A\hat{\mathbf{z}}$. This mode is driven by magnetic tension forces and does not perturb the density or pressure of the system. The group velocity of this mode is given by

$$\begin{aligned} \mathbf{v_g} &= \left(\frac{\partial\omega}{\partial k_x}, \frac{\partial\omega}{\partial k_y}, \frac{\partial\omega}{\partial k_z}\right) \\ &= (0, 0, \pm v_A), \end{aligned} \tag{1.19}$$

i.e., the group velocity of the Alfvén wave is parallel to the magnetic field, and so it carries energy along the magnetic field, but the motions it induces are perpendicular to the field. It is unable to propagate across the magnetic field.

The other main type of mode is the magnetoacoustic mode for which

$$\omega^4 - \omega^2 \left(c_s^2 + v_A^2\right) k^2 + k^4 c_s^2 v_A^2 \cos^2\theta = 0. \tag{1.20}$$

The solutions of this equation give a phase speed of

$$\frac{\omega^2}{k^2} = \frac{1}{2}\left\{\left(c_s^2 + v_A^2\right) \pm \left[\left(c_s^2 + v_A^2\right)^2 - 4c_s^2 v_A^2 \cos^2\theta\right]^{1/2}\right\}, \tag{1.21}$$

and the two solutions are classified as fast and slow magnetoacoustic modes (corresponding to the plus and minus signs respectively). These modes are driven by the magnetic tension and pressure forces and perturb the density and pressure of the system. The plasma pressure and magnetic pressure perturbations are out of phase for the slow mode, but are in phase for the fast mode. The slow mode carries energy in directions close to the magnetic field direction only and is effectively unable to propagate across the field. The fast mode is almost isotropic and propagates fastest across the magnetic field.

When $\theta = 0$ (so that $\mathbf{k}$ is parallel to $\mathbf{B}$), the fast speed is equal to the Alfvén speed and the slow speed is equal to the sound speed (assuming that the plasma beta is low and the Alfvén speed is larger than the sound speed). When $\theta = \pi/2$ (i.e., propagation across the magnetic field) the slow speed is zero and the fast speed is $\sqrt{v_A^2 + c_s^2}$. If we take a plasma in which $\beta = 0$, the slow mode disappears and the fast mode propagates isotropically with a phase speed of v_A. The group velocity of the mode in this case is

$$\begin{aligned} \mathbf{v_g} &= \left(\frac{\partial\omega}{\partial k_x}, \frac{\partial\omega}{\partial k_y}, \frac{\partial\omega}{\partial k_z}\right) \\ &= v_A^2 \frac{\mathbf{k}}{\omega} \\ &= v_A \frac{\mathbf{k}}{k}, \end{aligned} \tag{1.22}$$

so that energy is carried in the direction of the propagation vector at a speed of v_A.

1.2.3 MHD Waves in Structured Media

Waves on a Single Interface

First we will consider a single interface across which the static equilibrium parameters may change discontinuously (for more details see Roberts, 1981a). We assume that the perturbations decay away from either side of the boundary. The perturbations are then found to be 'surface modes'. These are modes which are

purely evanescent on both sides of the boundary. In a plasma with a non-zero plasma beta we find that there are both fast and slow surface modes.

Much work has been carried out on the effects of a flow on one side of such an interface (e.g., Sen, 1964; Fejer, 1964; Southwood, 1968; Pu and Kivelson, 1983), considering both flows parallel and oblique to the equilibrium magnetic field. These studies found that after a lower critical flow speed, the surface modes may become unstable so that they grow in time as well as oscillating. Increasing the flow further so that it is above an upper critical speed, the nature of the modes on both sides of the boundary becomes oscillatory and the mode becomes stable again. This corresponds to the fact that these oscillatory modes may carry energy away from the interface to restabilise it. Whilst unstable, these surface modes have growth rates which increase in proportion to the wavenumber k.

Relaxing the condition of an infinitely thin boundary layer (e.g., Walker, 1981) limits the growth rate of the unstable surface modes and removes the upper critical speed, so that the modes are unstable for all flow speeds above the lower critical speed.

Waves in a Magnetic Slab

Roberts (1981b) studied the propagation of magnetoacoustic modes in a static slab configuration. This model comprises a uniform medium for $|x| < x_o$, separated by infinitely thin interfaces from an exterior uniform medium (taken to be the same on both sides of the slab). This structure may then support 'body modes' as well as surface modes. In this case surface modes decay from each interface towards the centre of the slab and are also evanescent outside the slab. Body modes are oscillatory within the slab and evanescent outside. The modes may be further sub-divided into slow and fast modes depending on their phase speeds. Roberts (1981b) also classified the modes as 'kink' and 'sausage' modes depending on their symmetry about the central axis of the slab. Kink modes are anti-symmetric about the centre and are found by setting the gradient of the x-component of the perturbed velocity to zero at this point. Sausage modes perturb both sides of the slab symmetrically and are found by requiring that the x-component of the perturbed velocity is zero at the centre of the slab. The general form of body and surface modes, as well as the symmetry of the kink and sausage modes, is illustrated in Figure 1.3.

The propagation of modes in more complex magnetic configurations have also been studied (e.g., Edwin et al., 1986; Wright, 1994; Smith et al., 1997). However, the general definitions of body and surface modes are found to be useful in describing the modes that are found in these structures.

More recently the effects of flow on these modes has also been studied. These have generally been in a magnetospheric concept and have studied what is effectively half of a slab with only one interface. In a solar

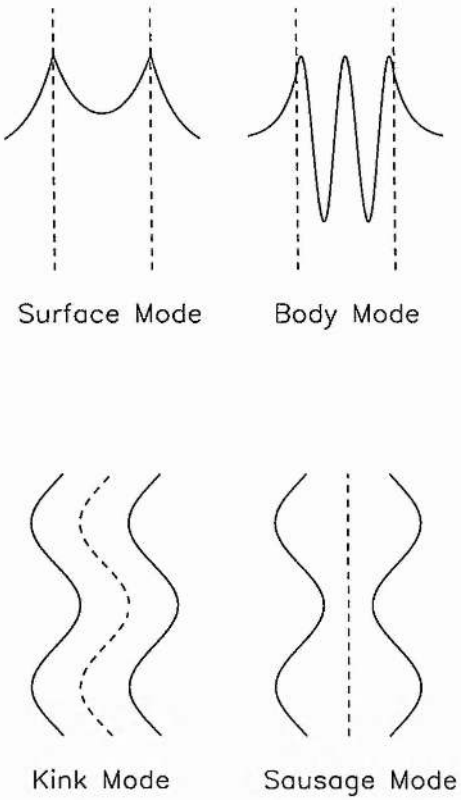

Figure 1.3: Schematic representations of surface and body modes (top) and kink and sausage modes (bottom).

context, the effects of flow on the slab geometry have been studied by Nakariakov and Roberts (1995) and Joarder et al. (1997). The inner boundary has been taken to be perfectly reflecting (which corresponds to the sausage mode condition of Roberts (1981b)). Physically, this boundary represents the reflection of modes by refraction associated with the increasing magnetic field strength near the Earth. Fujita et al. (1996) studied a non-uniform magnetosphere and Mann et al. (1999) looked in more detail at the propagation of fast modes in a uniform magnetosphere. These models and the details from them are discussed in Section 2.1. A central theme of this thesis is to extend the results from these models.

1.3 Ultra-Low Frequency Waves in the Magnetosphere

Ultra-low frequency (ULF) waves are those having periods in the range 1 mHz to 1 Hz. In the magnetosphere waves with these periods are continuously present and have amplitudes such that they may be observed using ground-based magnetometers. The first observations of magnetospheric ULF waves were made by Balfour Stewart (1861), long before the magnetosphere itself was discovered. Stewart measured oscillations in the geomagnetic field that were quasi-sinusoidal and had amplitudes of hundreds of nanotesla. These observations led Stewart to suggest that there must be an outer layer of the Earth's atmosphere that could carry electric currents. This was the first suggestion of what we now know as the ionosphere.

Since then many observations of ULF waves have been made, using both ground-based magnetometers and *in-situ* satellites. In 1964 a classification system for these observations was drawn up (Jacobs et al., 1964) which divides ULF pulsations into two main classes. The first class is the continuous pulsations (denoted Pc) which are defined to be signals that are quasi-sinusoidal in nature and exist for several cycles. The other class contains irregular pulsations (denoted Pi) which contains those signals which are short lived or broad band in frequency. These two main classes are then split into subclasses, each defining a range of wave period. The classes of waves are defined in Table 1.1. These classes of pulsation were originally intended to be identified with specific forms of waves, however increasing numbers of observations have found that there are many more types of waves than were known at the time. In this thesis we are most interested in the generation and propagation of Pc5 waves.

Continuous Pulsations (Pc)		Irregular Pulsations (Pi)	
Type	Period (sec)	Type	Period (sec)
Pc1	0.2-5	Pi1	1-40
Pc2	5-10	Pi2	40-150
Pc3	10-45		
Pc4	45-150		
Pc5	150-600		

Table 1.1: A summary of the classification of ULF waves in the magnetosphere (reproduced from Hughes, 1994).

1.3.1 Observations of Pc5 Pulsations

We may further divide observed Pc5 pulsations in the magnetosphere into three types, compressional, poloidal and toroidal Pc5 waves. We are primarily interested in the class of Pc5 pulsations known as the toroidal mode. These pulsations fit the proposal by Dungey (1954) that pulsations observed in the magnetosphere may be standing Alfvén waves on the geomagnetic field lines, and are often described as field line resonances (FLRs). Discrete FLRs with a single frequency are usually observed to be widely extended in the azimuthal direction, but narrowly confined radially, having typical widths of 0.3 to 0.6 R_E in the equatorial plane (see Samson and Rankin, 1994).

Many observations of discrete FLRs have been made (e.g., Ruohoniemi et al., 1991; Samson et al., 1991; Walker et al., 1992) showing that these oscillations tend to have quantised frequencies rather than a continuous spectrum. The frequencies observed are around 0.8, 1.3, 1.9, 2.7 and 3.3 mHz, and these frequencies are remarkably stable, with variations of only $5-10\%$ over periods of several hours (Walker et al., 1992). Ziesolleck and McDiarmid (1994) also observed multiple FLRs and found that simultaneously observed events can have a common azimuthal phase speed. Wright and Rickard (1995) noted that this is consistent with a running rather than a stationary driving pulse at the magnetopause.

FLRs are observed as regular variations in the magnetic field by ground magnetometers, and ionospheric F region flows by HF radar at the ionospheric footpoint of the FLR. They are observed almost constantly in the magnetosphere, with occurrence rates of 80% at values of L-shell greater than 8, and for magnetic latitudes greater than 10^o (see Hughes, 1994 and references therein). The high values of occurrence at larger L-shells is suggestive of an energy source for these modes at the magnetopause. Anderson et al. (1990) showed that there is little correlation between the intensity of Pc5 wave power and the direction of the inter-planetary magnetic field (IMF) or the geomagnetic indices. However, they did find that the occurrence rates increased during periods of high solar wind flow. A further study by Engebretson et al. (1998) showed a strong correlation between the solar wind flow speed and the power of Pc5 oscillations in the magnetosphere, with significantly increased power when the solar wind flow exceeds 500km/s. This correlation is a strong indication that the energy source for these modes could be the Kelvin-Helmholtz instability (KHI) at the magnetopause. Also, the flow in the magnetosheath has a stagnation point at the nose and accelerates around the magnetosphere, reaching the speed of the solar wind at the flanks (e.g., Spreiter and Stahara, 1980) where Pc5 occurrence rates are largest (e.g., Anderson et al., 1990). This is another indication that the flow in the magnetosheath may be supplying the energy for FLRs in the magnetosphere.

Observations of toroidal Pc5 oscillations have generally shown a clear dawn/dusk asymmetry, with many more events being observed on the dawn flank than at dusk (e.g., Kokubun, 1985). This may be explained by the fact that the spiral form of the IMF would tend to stabilise the KHI on the dusk flank of the magnetopause compared to the dawn flank (Lee and Olson, 1980). Also, the dawn flank is downstream from the quasi-parallel bow shock and is much more turbulent than the dusk flank which is downstream from the quasi-perpendicular shock, so there could be many more seed perturbations for the KHI at dawn (Muira, 1992).

1.3.2 The Theory of Field Line Resonances

The Southwood Box Model

Much attention has been given to the coupling of magnetopause Kelvin-Helmholtz surface modes to FLRs in the magnetosphere. In this section we summarise the results of Southwood (1974). This paper presented a simplified model for the magnetosphere, but was able to examine the coupling between fast magnetoacoustic modes and Alfvén resonances. In this model, the magnetosphere is taken to be cartesian (with the x-co-ordinate representing the radial distance, the y-co-ordinate representing the azimuthal co-ordinate, and the z-co-ordinate the North-South distance) and bounded in all directions (although the boundaries in the azimuthal (y) direction play little role in the calculation). The plasma in the magnetosphere is taken to be cold (the magnetic pressure is taken to be much larger than the plasma thermal pressure), and the equilibrium magnetic field is straight and uniform in the z-direction. The boundaries in z are formed by the ionosphere which is taken to be perfectly reflecting. The x-direction is therefore the radial direction, and there are assumed to be boundaries in the x-direction, which may also be taken to be perfectly reflecting. In order to vary the Alfvén speed in the radial direction, the number density is taken to be a function of x which is assumed to be monotonic so that the Alfvén speed increases monotonically from the outer boundary towards the Earth.

Assuming a real frequency, ω_s, there are found to be two important points in the governing equations which relate to the spatial behaviour of the normal modes supported by the box model magnetosphere. The closest to the Earth of these is the resonant point and this is the point where the frequency of the fast mode oscillation matches the Alfvén frequency of the local field line. When the frequency is real, this forms a singular point in the wave equations. The other point is a turning point which occurs where the nature of the fast mode changes from being oscillatory (near the magnetopause) to evanescent (closer to Earth). Thus, the FLRs in the box model are always coupled with the fast modes in a region where the mode is

evanescent. Taking ω to have a small imaginary part (so that there is either a source or sink of energy at the magnetopause) removes the singularity in the equations. However, the solution retains a structure indicating a resonant field line.

While this model illustrates the coupling of the fast waves in the magnetosphere to the FLRs observed, it does not fully describe mechanisms which can the drive the fast modes in the first place, and does not give any indication as to the mechanism which selects the preferred discrete frequency FLR described above. In fact, the magnetosheath flow speeds needed to drive FLRs with the observed phase velocites through KH unstable surface waves are found to be very high (Hughes, 1994).

Cavity and Waveguide Models

In order to try to explain the quantised frequencies of FLRs observed, the magnetospheric cavity wave models were developed (e.g., Kivelson and Southwood, 1986) which looked at the coupling of oscillatory cavity (body) modes to FLRs. In this case the outer boundary in x is taken to be perfectly reflecting, but the y-component of the wavenumber is still taken to be quantised as would be expected in an axisymmetric magnetosphere (the wavelength in the y-direction must then be fit an integer number of times into the length of the magnetospere). The eigenfrequencies of global cavity modes may then be used to predict the frequencies of FLRs that would be observed. The cavity modes are radially standing modes in the magnetosphere and the frequencies of these modes will be quantised to those frequencies for which the wave-lengths fit into the width of the cavity.

Later, the waveguide model was developed (Harrold and Samson, 1992; Walker et al., 1992; Wright, 1994; Rickard and Wright, 1994, 1995). Harrold and Samson (1992) modelled waves trapped between the bowshock and an inner turning point in the magnetosphere. In other models, the outer boundary is taken to be the magnetopause. In the waveguide model the magnetosphere is also taken to extend infinitely in the azimuthal direction so that any value of the wavenumber in that direction may be considered. This model allows for the fact that the magnetosphere is not axisymmetric, and the FLRs have phase speeds which are generally anti-sunward. Wright (1994) studied the propagation of modes along both radially uniform and non-uniform waveguides. In uniform waveguides, Wright found that modes with small azimuthal wavenumbers propagated slowly along the waveguide, reflecting backwards and forwards many times between the inner and outer boundary. When the waveguide is taken to be non-uniform (with an Alfvén speed increasing towards the Earth), modes starting from the magnetopause will be refracted as they propagate towards the Earth. Modes with small values of the azimuthal wavenumber (k_y) will penetrate deeply into the magnetosphere before turning around and will move slowly along the waveguide, whereas those with

large k_y will only penetrate a small distance into the magnetosphere and will travel more quickly along the magnetosphere. Thus, the modes which will drive the FLRs in the magnetosphere for the longest times will be those with small values of k_y, and the frequencies of the FLRs observed will be close to the eigenfrequency of the cavity for $k_y = 0$. These results were verified numerically by Rickard and Wright (1994, 1995).

A weakness of both the cavity and waveguide models is that they consider the magnetopause to be a perfectly reflecting boundary. This is justified in these papers by the fact that there is a large jump in density from within the magnetosphere to the magnetosheath (corresponding to a large decrease in Alfvén speed). However, Mann et al. (1999) have shown that the magnetopause may only be a perfect reflector under certain conditions, and in cases of low flow speed, the magnetopause may be a leaky boundary. In this thesis we will extend the model of Mann et al. (1999) and investigate the trapping of modes in the magnetosphere (Chapters 2 and 3), as well as the driving of resonances by cavity modes (Chapter 4) taking into account a free magnetopause boundary.

1.4 Overview of Thesis

In this thesis we extend the previous models which have considered the Kelvin-Helmholtz instability at the magnetopause, as appled to both the flanks of the magnetosphere and to the magnetotail. We also consider the driving of field line resonances by this process. More specifically:

In Chapter 2 we consider a model of a bounded uniform magnetosphere connected via a vortex sheet to a flowing field-free magnetosheath. We allow the magnetic field in the magnetosphere to be at an arbitrary angle to the flow in the magnetosheath, and also allow propagation of modes in any direction. Using linear ideal MHD we derive the dispersion relation for this system and consider the conditions for which the trapping and excitation of both slow and fast body and surface modes.

In Chapter 3 we consider the specific case of the magnetospheric flanks, where the magnetic field in the magnetosphere is perpendicular to the flow in the magnetosheath. We consider the conditions under which the magnetopause may be leaky, perfectly reflecting or over-reflecting. We use the theories of negative energy waves (Cairns, 1979) and over-reflection (McKenzie, 1970a) to explain the onset of instability of the modes and the behaviour of the growth rates.

In Chapter 4 we consider a bounded non-uniform magnetosphere and show that KH unstable fast waveguide modes couple to and drive field line resonances. In particular, we consider the azimuthal phase speeds of these modes. We again use the theory of over-reflection to explain these results.

In Chapter 5 we consider the space-time evolution of wave-packets on the flanks. In this Chapter we again study a uniform magnetosphere, but now add a boundary layer over which the flow speed changes continuously. Instead of normal modes we consider the evolution of finite wave-packets. We use the theory of absolute and convective instabilities to predict the time asymptotic response of the plasma in different reference frames. We also predict the spatial growth rates seen in the magnetospheric rest frame and assess the effect of these wave-packets on the magnetosphere. In order to verify our results we compare them to those from a numerical simulation.

In Chapter 6 we consider the trapping and excitation of modes in the magnetotail lobes. Previous models of the propagation of modes in the magnetotail have assumed the magnetopause boundary to be perfectly reflecting and we consider the validity of this assumption.

Finally, in Chapter 7 we summarise our results and suggest directions for future research.

Chapter 2

Trapping and Excitation of Magnetospheric Modes I - Background and Theory

2.1 Introduction

In this chapter we present a model for the trapping and excitation of oscillations in the magnetosphere by the shear flow discontinuity across the magnetopause.

Ultra-Low Frequency (ULF) oscillations with periods of $150 - 600$s (Pc5 pulsations) are almost continuously observed in the magnetosphere, most predominantly on the flanks and more so on the dawn flank than on the dusk flank. The discrepancy between the dawn and dusk flanks may be explained by the fact that the dawn-side magnetosheath is generally more turbulent than the dusk side, so that the necessary seeds for the KHI might be absent there (Miura, 1992). Pc5 wave power has also been shown to be well correlated to the speed of the upstream solar wind (Engebretson et al., 1998), with a significant increase in amplitude for solar wind speeds above 500km/s.

The source of energy for these modes has been suggested to be the Kelvin-Helmholtz instability (KHI) at the magnetopause driving field line resonances (FLRs) within the magnetosphere (Southwood, 1974; Chen and Hasegawa, 1974a, 1974b). Later, it was suggested that the FLRs could be driven by global standing waves rather than Kelvin-Helmholtz (KH) surface waves. Cavity mode theory (Kivelson et al.,

1984; Kivelson and Southwood, 1985, 1986) produces a structured frequency spectrum determined by the natural frequencies of the cavity. Almost all models of cavity modes in the magnetosphere have assumed the magnetopause boundary to be rigid so that the effect of flow in the magnetosheath is neglected, and the mechanism for the excitation of the modes is not normally addressed. Indeed, the question of whether or not cavity modes may even be trapped in the magnetosphere has also been little studied.

On the dawn-side the Pc5 oscillations are predominantly fundamental mode toroidal oscillations (e.g., Anderson et al., 1990) with a tendency to oscillate at a preferred set of discrete frequencies (about 0.8, 1.3, 1.9, 2.7, 3.3mHz) (e.g. Walker et al., 1992). These frequencies are believed to be the frequencies of a discrete set of waveguide modes which subsequently excite field line resonances.

That the KHI may occur at the magnetopause has been known for over 40 years (e.g., Dungey, 1955). The first work on the KHI in a magnetised plasma considered the stability of a system of unbounded incompressible plasmas either side of a shear flow discontinuity (e.g., Chandrasekhar, 1961). The addition of compressibility to the unbounded KHI model (e.g., Sen, 1964; Fejer, 1964; Southwood, 1968; Pu and Kivelson, 1983) has a significant effect on the KHI. These papers showed that there is both a lower cut-off speed and an upper cut-off speed, with the modes being stable below and above these speeds respectively. The lower cut-off speed is due to the stabilising effect of the magnetic tension and, when the propagation of the wave is along the flow, is determined by the Alfvén speed calculated using the component of the magnetic field along the flow (Miura, 1992). The upper cut-off speed corresponds to the change of wave form in either (or both) of the media from evanescent ('surface' modes) to oscillatory ('cavity', 'waveguide' or 'body' modes). The oscillatory modes carry energy away from the boundary stabilising the KHI. An incompressible plasma cannot support these propagating modes and so has no upper cut-off speed.

MHD models of unstable surface modes in an unbounded medium containing a vortex sheet show an unbounded increase of the growth rate with wavenumber, and the MHD model breaks down as the wavelengths approach kinetic scales. Studies of unstable surface modes with a boundary layer of finite thickness (Walker, 1981; Miura and Pritchett, 1982) show that the surface wave has a maximum growth rate for a finite wavenumber, with the growth rate approaching zero as the wavenumber $\rightarrow \infty$, and the upper cut-off speed is removed so that the modes are unstable for all flow speeds above the lower cut-off (e.g., Miura, 1992).

Fujita et al. (1996) considered a bounded non-uniform magnetosphere adjoining a flowing magnetosheath with a free sheet magnetopause boundary. They used the boundary condition in the magnetosheath that the amplitude of any perturbations must decay in space away from the magnetopause. They found that for large flow speeds the growth rate has a maximum with respect to the wavenumber indicating a preferred

wavelength for the oscillations. The growth rate of these modes approaches zero as the wavenumber becomes larger. They also showed that, although the growth rate still has a maximum with respect to the flow speed, it now tends to zero only as the flow tends to infinity. This is in contrast to the unbounded modes containing a vortex sheet whose growth rate has a maximum and then, above the upper cut-off speed, is identically zero. In other words, a bounded non-uniform magnetosphere has no upper cut-off speed. Physically, this corresponds to the fact that the energy can no longer simply propagate away from the magnetopause on the magnetosphere side as the waves are reflected by the inner boundary. Fujita et al. (1996) attributed these new properties to the non-uniform nature of the magnetosphere. They also looked at the solution of the dispersion relation for non-zero wavenumber perpendicular to the flow. They found that this gave rise to an enhancement in the frequencies found and that there was a cut-off flow-aligned wavenumber below which the modes were stable.

Mann et al. (1999) considered a similar model to that of Fujita et al. (1996), specifically a bounded uniform magnetosphere with zero plasma pressure connected to a field-free uniform flowing magnetosheath by a free sheet magnetopause (equivalent to the model we adopt, which is shown in Figure 2.1 with $P_1 = 0$, $B_{1y} = 0$ and $\beta = 0$). They showed that the same properties found by Fujita et al. (1996) were also found in a uniform magnetosphere and thus it is the fact that the magnetosphere is bounded (rather than non-uniform) which has the most significant effect on the behaviour of unstable surface modes at the magnetopause. Because of their model geometry (i.e., that the waves propagate parallel to the magnetosheath flow and perpendicular to the magnetic field), Mann et al. (1999) found that the fast surface mode is unstable for all non-zero flow speeds (the lower cut-off speed is reduced to zero). This is because the stabilising force of the magnetic tension is absent since the wave propagation does not bend the magnetic field. Mann et al. used an outgoing boundary condition in the magnetosheath that the group velocity of the waves there should be directed away from the magnetopause in the flowing frame of the magnetosheath. This replaces the condition of Fujita et al. (1996) that the modes should decay in amplitude away from the magnetopause. Besides the Mann et al. condition being more realistic than that of Fujita et al., it also allowed them to identify more complex behaviour of the normal modes. In particular, this condition enabled Mann et al. (1999) to find cavity modes that decay in time and grow spatially in the magnetosheath for low flow speeds. These modes carry energy from the magnetosphere to the magnetosheath. They are 'leaky' cavity/waveguide modes resulting from partial reflection and transmission of the magnetospheric waves at the magnetopause. The cavity modes were shown to become trapped for moderate flow speeds which corresponds to the total internal reflection of the magnetospheric waves by a perfectly reflecting magnetopause. The modes become unstable or 'over-reflected' for high flow speeds. In the case of over-

reflected modes, energy from the magnetosheath flow is fed into the oscillations in the magnetosphere increasing their amplitude.

In this chapter we consider a model similar to that of Mann et al. (1999), however, we include finite plasma pressure in the magnetosphere, allow the magnetic field to have components in both the y- and z-directions and also consider modes propagating in an arbitrary direction. This allows us to study both fast and slow magnetoacoustic waves in the magnetosphere. We find that the onset of instability for all modes depends strongly upon the angle between the magnetic field and the wave vector (and hence the angle between the wave vector and the magnetosheath flow) and show that the wavenumber selection found by Fujita et al. (1996) occurs for modes at all angles in a uniform magnetosphere model.

In analysing the modes that exist in our model, we employ the concept of negative energy waves (see McKenzie, 1970a; Cairns, 1979; and also Joarder et al., 1997). We show that modes with a group velocity directed away from the magnetopause in the moving frame of the magnetosheath may still feed energy from the magnetosheath into the magnetosphere. We find that the onset of instability of both fast cavity/waveguide and surface modes may be understood in terms of the coalescence of a positive energy mode with a negative energy mode.

The structure of this chapter is as follows: Section 2.2 presents our model, gives the governing equations and discusses the boundary conditions, Section 2.3 presents the concepts of wave energy and over-reflection and Section 2.4 presents a discussion of the classification of modes and the existence of stable modes. In Chapter 3 we will consider specifically the case corresponding to the trapping and excitation of modes on the flanks of the magnetosphere and in Chapter 6 we will consider the trapping and excitation of modes in the magnetotail.

2.2 Model and Equations

Our model consists of a bounded, uniform magnetosphere separated from an unbounded magnetosheath by a free sheet magnetopause, which we assume to be infinitely thin. Figure 2.1 is a schematic diagram of our model. The magnetosphere is permeated by a constant magnetic field, $\mathbf{B_1} = (0, B_{1y}, B_{1z})$, which is tangential to the discontinuity, and has a finite equilibrium plasma pressure (P_1) and density (ρ_{o1}). It has an inner boundary which is taken to be perfectly reflecting, representing the refraction of MHD modes by the increasing Alfvén speed closer to the Earth. The inner boundary is taken to be at $x = 0$ and the equilibrium magnetopause is at $x = d$. The magnetosheath is taken to be field-free with constant equilibrium pressure (P_2) and density (ρ_{o2}). The magnetosheath is flowing in the y-direction with a constant speed (v_o).

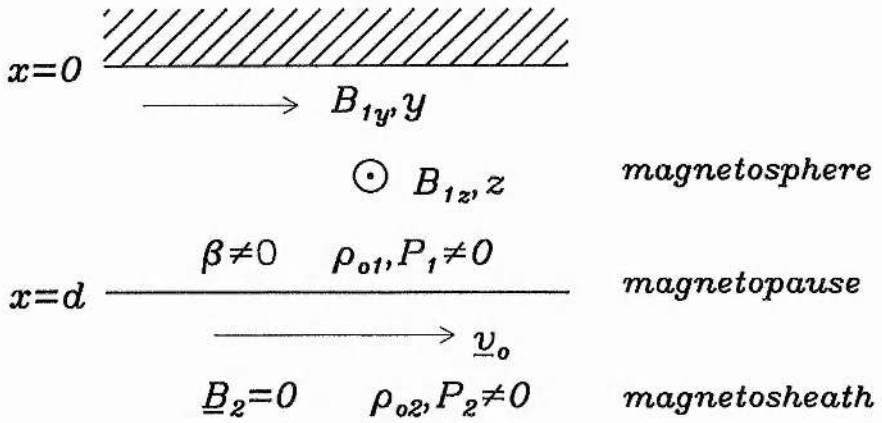

Figure 2.1: A schematic representation of our bounded magnetosphere model.

In order for this model to be in equilibrium we require total pressure balance across the magnetopause, given by

$$P_1 + \frac{B_{1y}^2 + B_{1z}^2}{2\mu_o} = P_2. \tag{2.1}$$

Here, and throughout this chapter, any quantity suffixed by a 1 defines a magnetospheric quantity, and a suffix 2 represents a quantity in the magnetosheath. By choosing the ratio of the densities in the two regions ($\epsilon = \rho_{o1}/\rho_{o2}$) and the plasma beta ($\beta$) in the magnetosphere we can now derive a formula for the equilibrium sound and Alfvén speeds (c_{s1} and v_{a1}, respectively) in the magnetosphere in terms of the sound speed in the magnetosheath, c_{s2}. The sound speed in the magnetosphere is given by

$$c_{s1}^2 = \frac{\beta}{\epsilon(1+\beta)} c_{s2}^2, \tag{2.2}$$

and the Alfvén speed by

$$v_{a1}^2 = \frac{2}{\Gamma\epsilon(1+\beta)} c_{s2}^2. \tag{2.3}$$

We have normalised the ideal MHD equations (Equations 1.1 to 1.11) with respect to the depth of the magnetosphere, d, the equilibrium sound speed, c_{s2}, and density, ρ_{o2}, in the magnetosheath. (Plasma pressure is normalised by the quantity ΓP_2, magnetic fields by $\sqrt{\Gamma P_2 \mu_o}$, where Γ is the ratio of specific heats, and time by d/c_{s2}.) Then we have added a small perturbation to each of our (constant) equilibrium quantities and linearised the ideal MHD equations for a uniform medium to give:

$$\rho_o \left(\frac{\partial}{\partial t} + \mathbf{v_o}.\nabla \right) \mathbf{u} = -\nabla (p + \mathbf{B}.\mathbf{b}) + (\mathbf{B}.\nabla)\,\mathbf{b}, \tag{2.4}$$

$$\left(\frac{\partial}{\partial t}+\mathbf{v_o}.\nabla\right)\rho=\rho_o\nabla.\mathbf{u}, \tag{2.5}$$

$$\nabla.\mathbf{b}=0, \tag{2.6}$$

$$\left(\frac{\partial}{\partial t}+\mathbf{v_o}.\nabla\right)\mathbf{b}=(\mathbf{B}.\nabla)\,\mathbf{u}-\mathbf{B}\,(\nabla.\mathbf{u}) \tag{2.7}$$

and

$$\left(\frac{\partial}{\partial t}+\mathbf{v_o}.\nabla\right)p=c_s^2\left(\frac{\partial}{\partial t}+\mathbf{v_o}.\nabla\right)\rho. \tag{2.8}$$

Here, $\mathbf{v_o}$, $\mathbf{B}$, P and ρ_o are the normalised equilibrium flow speed, magnetic field, pressure and density respectively while $\mathbf{u}$, $\mathbf{b}$, p and ρ are the perturbations to these quantities respectively. The coefficients of the perturbed quantities in these equations are now independent of t, y and z, so we may look for solutions of the form

$$\mathbf{u}\,(x,y,z,t)=\mathbf{u}\,(x)\exp i\,(k_y y+k_z z-\omega t). \tag{2.9}$$

Since the equations are normalised, the frequency, ω, and the wavenumbers, k_y and k_z, are variables of the normalised system. We define the tangential wave vector, $\mathbf{k}$, such that

$$\mathbf{k}=k_y\hat{\mathbf{e}}_\mathbf{y}+k_z\hat{\mathbf{e}}_\mathbf{z}, \tag{2.10}$$

and

$$k=\sqrt{k_y^2+k_z^2}. \tag{2.11}$$

We also define the angle between the tangential wave vector and the magnetospheric magnetic field in the $y-z$ plane as

$$\alpha=\arccos\left(\frac{\mathbf{k}.\mathbf{B}_1}{kB_1}\right), \tag{2.12}$$

and the angle between the magnetic field and the flow vector as

$$\chi=\arccos\left(\frac{\mathbf{B_1}.\mathbf{v}_o}{B_1 v_o}\right). \tag{2.13}$$

We will be studying primarily the cases where $\chi=\pi/2$ (corresponding to the flanks of the magnetosphere) in Chapter 3 and $\chi=0$ (corresponding to the magnetotail) in Chapter 6. The relative directions of $\mathbf{k}$, $\mathbf{v}_o$ and $\mathbf{B}_1$ are illustrated in Figure 2.2.

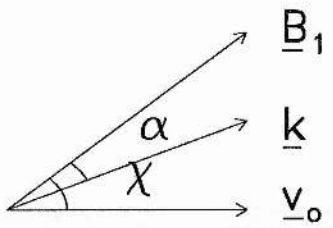

Figure 2.2: A schematic diagram showing the relative directions of $\mathbf{B_1}$, the magnetic field in the magnetosphere, $\mathbf{k}$, and $\mathbf{v_o}$, the magnetosheath velocity, in the $y-z$ plane.

We will be analysing both the stable and unstable behaviour of the system and so will assume that ω is a complex number ($\omega = \omega_r + i\omega_i$). Thus, ω_r is considered to be the frequency and ω_i is the growth (or decay) rate of the amplitude of the oscillations.

The total pressure perturbation in the magnetosphere ($p_T = p_1 + \mathbf{B_1}.\mathbf{b_1}$ in normalised units) can be shown to satisfy the second order differential equation

$$\frac{d^2 p_T}{dx^2} + m_1^2 p_T = 0, \tag{2.14}$$

where m_1 is the wavenumber in the x-direction in the magnetosphere and is given by

$$m_1^2 = \frac{\left(\omega^2 - k^2 c_f^2\right)\left(\omega^2 - k^2 c_{slow}^2\right)}{\left(c_f^2 + c_{slow}^2\right)\left(\omega^2 - k^2 c_T^2\right)}. \tag{2.15}$$

When $\alpha = 0$, Equations (2.14) and (2.15) are equivalent to the equation for the motion of waves in a magnetic slab found by Roberts (1981b), however, it should be noted that in that paper, the wave equation is written as $d^2 p_T/dx^2 - m_R^2 p_T = 0$ where the wavenumber is defined as $m_R^2 = -m_1^2$ ($\alpha = 0$). Here c_f and c_{slow} are the fast and slow magnetoacoustic speeds defined by

$$c_{f/slow}^2 = \frac{1}{2}\left(\left(v_{a1}^2 + c_{s1}^2\right) + / - \sqrt{\left(v_{a1}^2 + c_{s1}^2\right)^2 - 4 v_{a1}^2 c_{s1}^2 \cos^2\alpha}\right) \tag{2.16}$$

respectively, and c_T is given by

$$c_T^2 = \frac{c_f^2 c_{slow}^2}{c_f^2 + c_{slow}^2} = \frac{v_{a1}^2 c_{s1}^2}{v_{a1}^2 + c_{s1}^2}\cos^2\alpha. \tag{2.17}$$

When $\alpha = 0$, c_T is the tube speed for a magnetic slab defined by Roberts (1981b), and so c_T as defined here may be thought of as the component of the tube speed along the propagation vector $\mathbf{k}$. These three characteristic speeds satisfy the ordering

$$c_T^2 < c_{slow}^2 < c_f^2. \tag{2.18}$$

The perturbed pressure in the magnetosheath (p_2) satisfies the equation

$$\frac{d^2p_2}{dx^2} + m_2^2 p_2 = 0. \tag{2.19}$$

Here m_2 is the x-component of the wavenumber in the magnetosheath given by

$$m_2^2 = \frac{\omega'^2 - k^2 c_{s2}^2}{c_{s2}^2}. \tag{2.20}$$

We have defined ω' as the Doppler shifted frequency of the oscillations in the rest frame of the magnetosheath and it is related to ω by

$$\omega' = \omega - kv_o \cos(\chi - \alpha). \tag{2.21}$$

By assuming the equilibrium quantities are functions of x, rather than constants, we can obtain two first order ordinary differential equations (ODEs) which will enable us to specify the matching conditions across the magnetopause ($x = 1$ in our normalised system). We must now retain terms in our governing equations that are concerned with the gradients of our equilibrium quantities. For example, the linearised momentum equation now becomes

$$\rho_o \left[\left(\frac{\partial}{\partial t} + \mathbf{v_o}.\nabla\right)\mathbf{u} + (\mathbf{u}.\nabla)\,\mathbf{v_o}\right] = -\nabla\left(p_{To} + p_T\right) + (\mathbf{B}.\nabla)\,\mathbf{b} + (\mathbf{b}.\nabla)\,\mathbf{B}, \tag{2.22}$$

where $p_{To} = p_o + B^2/2$ is the equilibrium total pressure, and our other equations are similarly modified. The equations are:

$$\frac{dp_T}{dx} = i\rho_o(x)\left[(\omega - kv_o(x)\cos(\chi-\alpha))^2 - k^2 v_{a1}^2(x)\cos^2\alpha\right] \times \frac{u_x}{(\omega - kv_o(x)\cos(\chi-\alpha))}, \tag{2.23}$$

$$\frac{d}{dx}\left\{\frac{u_x}{(\omega - kv_o(x)\cos(\chi-\alpha))}\right\} = \frac{im^2(x)}{\rho_o(x)\left((\omega - kv_o(x)\cos(\chi-\alpha))^2 - k^2 v_{a1}^2(x)\cos^2\alpha\right)} p_T, \tag{2.24}$$

where

$$m^2(x) = \frac{\left((\omega - kv_o(x)\cos(\chi-\alpha))^2 - k^2 c_f^2(x)\right)}{\left(c_f^2(x) + c_{slow}^2(x)\right)} \times \frac{\left((\omega - kv_o(x)\cos(\chi-\alpha))^2 - k^2 c_{slow}^2(x)\right)}{\left((\omega - kv_o(x)\cos(\chi-\alpha))^2 - k^2 c_T^2(x)\right)}. \tag{2.25}$$

A fuller derivation of these equations is given in Appendix A.

We now assume that $\mathbf{v_o}(x)$ and the other equilibrium quantities are step functions at the magnetopause, and integrate Equations (2.23) and (2.24) over the region $[1-\delta, 1+\delta]$. Taking the limit as $\delta \to 0$, we find that the quantities p_T and
$u_x/(\omega - kv_o\cos(\chi-\alpha))$ must be continuous at the magnetopause. Hence, our matching conditions across the magnetopause (i.e., at $x=1$) are

$$p_T(x=1) = p_2(x=1), \tag{2.26}$$

and

$$\frac{u_{x1}(x=1)}{\omega} = \frac{u_{x2}(x=1)}{\omega'}. \tag{2.27}$$

Equation (2.26) corresponds to the continuity of total pressure across the magnetopause and Equation (2.27) implies that the displacement of the magnetopause is the same for both media (so that there is no cavitation). These are the quantities that we would expect to be conserved at a discontinuous boundary (c.f., Chandrasekhar, 1961; McKenzie, 1970). We require the boundary at $x=0$ to be totally reflecting, which may be imposed by the constraint

$$u_{x1}(x=0) = 0. \tag{2.28}$$

Equation (2.23) then implies the condition

$$\frac{dp_T}{dx}(x=0) = 0. \tag{2.29}$$

Finally, we require the x-component of the group velocity of the perturbations in the rest frame of the magnetosheath to be directed away from the magnetopause. Because ω is complex, the wave-numbers will also be complex. In this condition, therefore, we consider only the real part of the group velocity in the x-direction and require it to be positive in the rest frame of the magnetosheath. The dispersion relation for sound waves in the rest frame of the magnetosheath is

$$\omega'^2 = \left(m_2^2 + k^2\right)c_{s2}^2, \tag{2.30}$$

where in the rest frame of the magnetosheath the waves oscillate with frequency ω'. The component of the group velocity of these waves in the x-direction is given by

$$v_{gx} = \frac{\partial\omega'}{\partial m_2} = \frac{m_2}{\omega'}c_{s2}^2 = \frac{\mathrm{Re}(m_2) + i\mathrm{Im}(m_2)}{\mathrm{Re}(\omega') + i\mathrm{Im}(\omega')}c_{s2}^2. \tag{2.31}$$

The real part of this component of the group velocity is

$$\mathrm{Re}(v_{gx}) = \frac{\mathrm{Re}(\omega')\,\mathrm{Re}(m_2) + \mathrm{Im}(\omega')\,\mathrm{Im}(m_2)}{\mathrm{Re}(\omega')^2 + \mathrm{Im}(\omega')^2}c_{s2}^2. \tag{2.32}$$

The condition that the real part of the group velocity in the x-direction is positive in the rest frame of the magnetosheath then becomes

$$\mathrm{Re}\,(\omega')\,\mathrm{Re}\,(m_2) + \mathrm{Im}\,(\omega')\,\mathrm{Im}\,(m_2) > 0. \tag{2.33}$$

It can be shown that when this condition is satisfied the real part of the x-component of the phase speed, $\mathrm{Re}\,(v_{phx}) = \mathrm{Re}\,(\omega'/(m_2))$, is always positive. Therefore this condition is equivalent to requiring that the phase speed in the magnetosheath rest frame is directed away from the magnetopause. In previous models (e.g. Fujita et al., 1996) the condition that the amplitude of the observations decreases as $x \to \infty$ has been used, which in our model would involve the condition that $\mathrm{Im}\,(m_2) > 0$. The more general condition that we have used here allows us to find modes which decay in time and have a spatially growing nature in the magnetosheath (leaky modes). We find that for low flow speeds, most modes with positive phase speed in the magnetosheath are in fact leaky. In the case of stable modes ($\omega_i = 0$), however, the wavenumber in the magnetosheath is purely imaginary, and so we have the condition that the modes must be evanescent, which in this special case gives our 'outgoing' condition in the magnetosheath as

$$\mathrm{Im}\,(m_2) > 0. \tag{2.34}$$

Combining the solutions to the wave equations (2.14) and (2.19) with the various boundary conditions yields the dispersion relation

$$\epsilon\left(\frac{\omega^2 - k^2 v_{a1}^2 \cos^2\alpha}{m_1}\right)\left(\frac{\exp(im_1) + \exp(-im_1)}{\exp(im_1) - \exp(-im_1)}\right) - \frac{\omega'^2}{m_2} = 0. \tag{2.35}$$

When $\alpha = 0$, in the absence of flow, and considering ω to be real, this dispersion relation reduces to that in Roberts (1981b). The boundary condition at $x = 0$ in our model without flow is equivalent to a sausage mode boundary condition in the centre of the slab considered by Roberts and so our model will yield only half the modes found in that paper. The other class of modes (kink modes) could be generated by replacing Equations (2.28) and (2.29) with the condition $p_T\,(x = 0) = du_{x1}/dx\,(x = 0) = 0$. Depending upon the sign of m_1^2 (i.e., by considering whether m_1 is real or imaginary) this equation can describe both the body and surface modes found by Roberts. Allowing ω to be complex means that this dispersion relation describes not only purely oscillatory or evanescent modes, but also modes that have both oscillations and a background growth or decay in x.

We have used a two-dimensional Newton-Raphson code, adapted from that in Numerical Recipes (Press et al.,1992) to solve the dispersion relation numerically, yielding the complex eigenvalues ω for a given set of parameters (k, α and v_o). In order to maximise the efficiency of the code we have incorporated a back-stepping routine to check that each iteration decreases the magnitude of the complex dispersion relation.

The results of the code have been checked (by taking the appropriate limits) qualitatively against the results in Roberts (1981b) and Nakariakov and Roberts (1995), and quantitatively against the results from Mann et al. (1999). We have found that our code agreed with that of Mann et al. to at least 1 part in 10^6. The code finds the roots ($\omega = \omega_r + i\omega_i$) such that the absolute value of both the real and imaginary parts of the dispersion relation and the calculated next increment in the real and imaginary parts of the frequency are less than the value of the chosen convergence criteria, ν. In all cases the convergence criteria is chosen such that $\nu < 10^{-6}$, and in most cases, it is three or four orders of magnitude smaller.

2.3 Theory

In this section we will outline two theories that are important for the interpretation of the results from our model. The first concerns the concept of wave energy, which will help us to understand the onset of instability for the fast modes in our model. The second is the concept of wave over-reflection, which will be useful in considering the unstable behaviour of our modes.

2.3.1 Wave Energy

An important quantity in understanding the behaviour of the instability at the magnetopause is the energy of the wave. Cairns (1979) showed that the energy per unit area of a stable hydrodynamic wave is given by

$$E = \frac{1}{4}\omega_r \frac{\partial D}{\partial \omega_r} A_o^2, \tag{2.36}$$

where D is the dispersion relation of the waves and A_o is the amplitude of the displacement of the fluid.

We now show how this result can be extended to magnetohydrodynamics (see also Joarder et al., 1997). The displacement of the magnetopause is given by

$$\eta = A_o \exp i(k_y y + k_z z - \omega t), \tag{2.37}$$

where A_o is the amplitude of the oscillation. The linearised ideal MHD equations yield

$$p_T\,(x = 1) = D_1\,(\omega, k)\,\eta \tag{2.38}$$

and

$$p_2\,(x = 1) = D_2\,(\omega, k)\,\eta. \tag{2.39}$$

We have defined

$$D_1\,(\omega, k) = \frac{-\Gamma\rho_1\left(\omega^2 - k^2 v_{a1}^2 \cos^2\alpha\right)\cos m_1}{m_1}, \tag{2.40}$$

and

$$D_2(\omega, k) = \frac{-\Gamma \rho_2 \omega'^2 \sin m_1}{|m_2|}. \tag{2.41}$$

Then, the work done per unit area in setting up the wave is found to satisfy Equation (2.36) with D defined so that

$$D = \pm (D_1 - D_2). \tag{2.42}$$

The sign of D is chosen such that the energy of the wave is always positive when there is no flow in the system. In dimensional variables the dimensions of D are

$$[D] = \left[\frac{\rho\omega^2}{m}\right] = \frac{M}{L^2T^2}, \tag{2.43}$$

where the notation [ ] indicates 'dimensions of' and M, L and T correspond to dimensions of mass, length and time respectively. Thus the dimensions of the energy per unit area are

$$[E] = \left[\frac{energy}{L^2}\right] = \frac{ML^2}{T^2L^2} = \frac{M}{T^2} = [DA_o^2], \tag{2.44}$$

and so Equation (2.36) is dimensionally correct. Since we have derived our dispersion relation in dimensionless quantities, the definition of the wave energy density given in Equation (2.36) is actually the dimensionless wave energy density.

By looking at the sign of

$$C = \omega_r \frac{\partial D}{\partial \omega_r} \tag{2.45}$$

we are able to classify waves as having either positive or negative energy. The presence of a negative energy wave will reduce the energy of the system in the frame of reference being considered.

Cairns (1979) showed that this expression for the energy of a mode can be used to explain the onset of some instabilities. In particular, he showed that the Kelvin-Helmholtz instability occurs when a positive energy wave 'coalesces' with a negative energy wave, a result that we will apply later. The idea of the waves coalescing is used to describe the fact that the onset of instability occurs when the solutions for the two waves with opposite energy converge to the same value. After this point the waves are unstable and the boundary conditions will select only one of the complex roots, so the positive and negative energy modes are seen to 'merge' into the same unstable solution. This type of instability is also classed as a reactive instability.

2.3.2 The Theory of Wave Over-Reflection

Another useful concept in understanding the unstable behaviour of our modes is that of wave over-reflection. We now consider a model with an unbounded uniform magnetosphere and consider the effect of a wave impinging on the magnetopause boundary from within the magnetosphere. We assume that some part of the wave is reflected back into the magnetosphere and some part is transmitted through the magnetopause to propagate in the magnetosheath. Figure 2.3 gives a schematic view of these three waves.

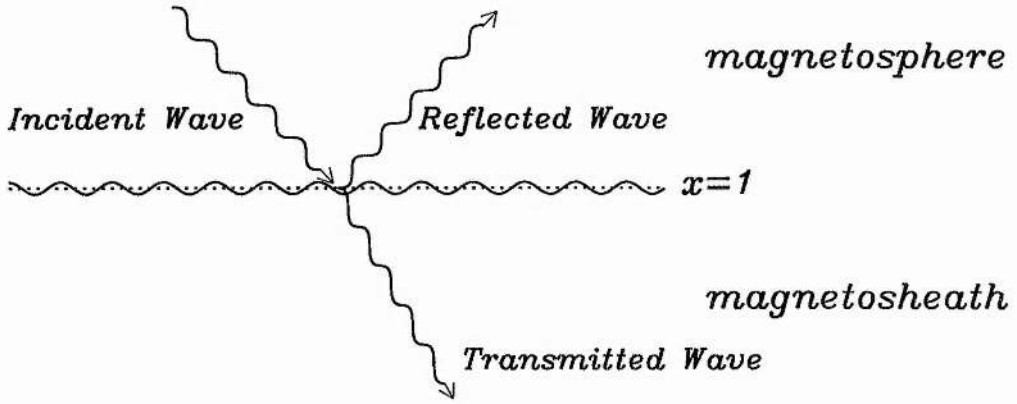

Figure 2.3: A schematic representation of the incident, reflected and transmitted waves at the magnetopause.

Sen (1964), and later Pu and Kivelson (1983), showed that for a compressible plasma, there are two important speeds in considering the development of the instability at a flow discontinuity between unbounded plasmas. Southwood (1968) also found these two speeds, and showed that they could be predicted. The first speed (v_c) is the minimum speed at which instability can occur, at a higher speed (v_u) stability is regained and the modes become purely oscillatory on both sides of the discontinuity.

McKenzie (1970a) showed that the reflection coefficient for this system (the ratio of the amplitude of the reflected wave to that of the incident wave) is given by

$$R = \frac{1 - Z}{1 + Z}, \tag{2.46}$$

where, for our system

$$Z = \frac{m_1 \left(\omega - k_y v_o\right)^2}{m_2 \epsilon \left(\omega^2 - k^2 v_{a1}^2 \cos^2 \alpha\right)}, \tag{2.47}$$

with $\epsilon = \rho_1 / \rho_2$.

In deriving Equations (2.46) and (2.47) we have assumed that ω is purely real, and that m_1 is also real (so that we do actually have a wave propagating in the magnetosphere). The sign of m_1 is taken to be positive so that the group velocities of the incident and reflected waves are in the correct sense. According to (2.20) there are two possibilities for the sign of m_2^2:

(i) $m_2^2 < 0$ and

(ii) $m_2^2 > 0$.

In case (i), m_2 is purely imaginary, and thus Z is also purely imaginary ($Z = i|Z|$). Thus

$$R = \frac{1 - i|Z|}{1 + i|Z|}, \tag{2.48}$$

and so

$$|R| = 1. \tag{2.49}$$

In this case we have total internal reflection of magnetospheric waves, and there is no transmitted wave (we have an exponential decay into the magnetosheath).

Conversely in case (ii), Z is real, and therefore R is also real. We may now subdivide this case into two further possibilities, $Z < 0$ and $Z > 0$. If $Z < 0$, then $R > 1$ and we have over-reflection. In fact, it is possible to have the $R > 1$ case where $|R| \to \infty$, which occurs when $Z = -1$, implying

$$m_1 \left(\omega - k_y v_o\right)^2 + m_2 \epsilon \left(\omega^2 - k^2 v_{a1}^2 \cos^2 \alpha\right) = 0, \tag{2.50}$$

which is the dispersion relation for stable oscillatory modes for the unbounded magnetosphere model. Note that in the case of stable oscillatory modes on both sides of the interface, the phase speed must be below $v_o \cos(\chi - \alpha) - c_s$ and therefore $\omega - k_y v_o < 0$. Thus we must choose $m_2 < 0$ in order to satisfy Equation (2.33). Hence 'a resonance is excited when the incident wave frequency matches the frequency of one of the characteristic frequencies of the vibrations of the interface' (McKenzie, 1970a). This is also the condition corresponding to waves being spontaneously radiated away from the boundary, and occurs even when the amplitude of the incident wave vanishes. When $Z > 0$, $R < 1$ and we have the normal case of partial reflection. We will derive the particular conditions for over-reflection in each case we examine.

Assuming that $m_2^2 > 0$, we may now define (following McKenzie, 1970a)

$$\mathbf{k_1} = (m_1, k_y, k_z) = k_1 \left(\cos\theta_1, \sin\theta_1 \cos(\chi - \alpha), \sin\theta_1 \sin(\chi - \alpha)\right), \tag{2.51}$$

and

$$\mathbf{k_2} = (m_2, k_y, k_z) = k_2 \left(\cos\theta_2, \sin\theta_2 \cos(\chi - \alpha), \sin\theta_2 \sin(\chi - \alpha)\right), \tag{2.52}$$

where α is the angle between the vector $(0, k_y, k_z)$ and the equilibrium magnetic field $\mathbf{B_1}$, $\theta_{1,2} = \tan^{-1}(k/m_{1,2})$ and Snell's law requires that $k_1 \sin\theta_1 = k_2 \sin\theta_2$. Substituting these values into Equation (2.47) and noting that

$$(\omega - k_y v_o)^2 = \omega'^2 = k_2^2 c_{s2}^2, \tag{2.53}$$

we obtain

$$Z = \frac{\sin 2\theta_1 c_{s2}^2}{\epsilon \sin 2\theta_2 \left(U^2 - v_{a1}^2 \sin^2\theta_1 \cos^2\alpha\right)}, \tag{2.54}$$

where U is the characteristic (fast or slow) magnetoacoustic phase speed along the vector $\mathbf{k_1}$,

$$U^2 = \frac{\omega^2}{k_1^2} = \frac{1}{2}\left\{v_{a1}^2 + c_{s1}^2 \pm \sqrt{\left(v_{a1}^2 + c_{s1}^2\right)^2 - 4v_{a1}^2 c_{s1}^2 \sin^2\theta_1 \cos^2\alpha}\right\}. \tag{2.55}$$

Noting that, using Snell's law

$$m_2^2 = k_2^2 \cos^2\theta_2 = \frac{k_1^2 \sin^2\theta_1}{\tan^2\theta_2}, \tag{2.56}$$

we may define

$$\tan\theta_2 = \pm\frac{\sin\theta_1}{\lambda}, \tag{2.57}$$

where (using Equations (2.20), (2.21), (2.51) and (2.55))

$$\lambda^2 = \frac{m_2^2}{k_1^2} = \frac{\left(U - v_o \sin\theta_1 \cos\left(\chi - \alpha\right)\right)^2 - c_{s2}^2 \sin^2\theta_1}{c_{s2}^2}. \tag{2.58}$$

Hence, we may substitute for $\sin 2\theta_2$ in Equation (2.54) using the identity

$$\sin 2\theta_2 = \pm\frac{2\lambda \sin\theta_1}{\lambda^2 + \sin^2\theta_1}. \tag{2.59}$$

Hence Z is now defined as

$$Z = \pm\frac{\cos\theta_1 \left(U - v_o \sin\theta_1 \cos\left(\chi - \alpha\right)\right)^2}{\epsilon\lambda\left(U^2 - v_{a1}^2 \sin^2\theta_1 \cos^2\alpha\right)}, \tag{2.60}$$

where the sign is again chosen to satisfy the out-going group velocity condition in the magnetosheath (Z is chosen to have the same sign as the real part of m_2).

We may now solve the equation $Z = -1$ to find the value of the angle, θ_1, at which resonance (or spontaneous radiation of modes) may occur. Then using the fact that the phase speed is

$$v_{ph} = \frac{\omega}{k} = \frac{U}{\sin\theta_1}, \tag{2.61}$$

we may also find the phase speed at which spontaneous radiation of modes from the magnetopause occurs.

2.4 Existence and Classification of Stable Modes

We first examine the results that can be obtained using a purely real frequency ($\omega = \omega_r$). With real ω, the sound waves in the magnetosheath satisfy the dispersion relation

$$(\omega_r - kv_o \cos(\chi - \alpha))^2 = (m_2^2 + k^2)\, c_{s2}^2, \tag{2.62}$$

which implies that m_2^2 is real. Thus m_2 is either purely real ($m_2^2 > 0$) implying propagating solutions in the magnetosheath, or purely imaginary ($m_2^2 < 0$) which gives evanescent solutions in the magnetosheath. Similarly, m_1^2 (as defined in Equation (2.15)), is also real when $\omega_i = 0$, and hence m_1 is either purely real or imaginary. In the case where m_1 is purely real, the dispersion relation (Equation (2.35)) becomes

$$\epsilon \left(\frac{\omega_r^2 - k^2 v_{a1}^2 \cos^2 \alpha}{i m_1} \right) \cot m_1 - \frac{\omega_r'^2}{m_2} = 0, \tag{2.63}$$

and, when m_1 is purely imaginary, Equation (2.35) becomes

$$\epsilon \left(\frac{\omega_r^2 - k^2 v_{a1}^2 \cos^2 \alpha}{i n_1} \right) \coth n_1 + \frac{\omega_r'^2}{m_2} = 0, \tag{2.64}$$

where we have defined $m_1 = i n_1$. In both cases the first term of the equation is imaginary, and if m_2 is real then the second term is real. Hence, we can see that both the first and second terms (the real and imaginary parts of the equation) must be identically zero for the equations to be satisfied. This can only be true for specific values of v_o and so, in general, there is no solution to the dispersion relation for $m_2^2 > 0$ (real m_2). If m_2 is imaginary, then the two terms may balance each other and need not be zero individually.

Thus solutions for real ω may only occur when $m_2^2 < 0$ (i.e., m_2 is imaginary), and the modes must decay exponentially away from the magnetopause in the magnetosheath. Thus, any oscillatory part of the mode is trapped or contained within the magnetosphere. With this condition, Equation (2.62) may be rearranged to give

$$\left(\frac{\omega_r}{k} - v_o \cos(\chi - \alpha) \right)^2 < c_{s2}^2. \tag{2.65}$$

This implies that either $\omega_r/k - v_o \cos(\chi - \alpha) < c_{s2}$, or $v_o \cos(\chi - \alpha) - \omega_r/k < c_{s2}$, which together give the restriction on the phase speed for a stable mode:

$$v_o \cos(\chi - \alpha) - c_{s2} < \frac{\omega_r}{k} < v_o \cos(\chi - \alpha) + c_{s2}. \tag{2.66}$$

With $\alpha = \pi/2$ and $\chi = \pi/2$ this condition reduces to that of Mann et al. (1999). It is important to note that while Equation (2.66) is a necessary condition for the existence of stable modes, it is not a sufficient one. That is, when a non-zero growth rate is included, it is still true that stable modes may only exist within the

given range of phase speed, however, there may also exist unstable modes within that range. This condition is not a sufficient condition because it takes into account only the dispersion relation for sound waves in the magnetosheath (Equation (2.62)). The total dispersion relation (Equation (2.35)) also takes into account the conditions in the magnetosphere, and this will further restrict the region in which stable modes may occur.

To include the effects of the magnetosphere, and in order to classify our stable modes, we need to examine the sign of m_1^2 when $\omega_i = 0$, (see Roberts, 1981b). We find that for $m_1^2 < 0$ we have evanescent modes in the magnetosphere (surface modes) and for $m_1^2 > 0$ we have modes that oscillate within the magnetospheric cavity (body, cavity or waveguide modes). The modes are then subdivided into fast and slow modes depending upon their nature in the magnetosphere. This distinction is also manifested in the phase speed of the modes. Modes with $v_{ph} \leq c_{slow}$ are classified as slow modes, whereas those with $v_{ph} > c_{slow}$ are fast modes. From Equations (2.15) to (2.18), we find that slow surface modes may exist for

$$0 < v_{ph} < c_T, \tag{2.67}$$

where v_{ph} is the phase speed of the mode ($v_{ph} = \omega_r/k$), and slow body modes may occur for

$$c_T < v_{ph} < c_{slow}. \tag{2.68}$$

Fast surface modes are found to exist where

$$c_{slow} < v_{ph} < c_f, \tag{2.69}$$

and fast cavity modes exist where

$$v_{ph} > c_f. \tag{2.70}$$

Taking $v_o = 0$ and letting $k \to \infty$, we find that the dispersion relation for surface modes (Equation (5.11)) becomes

$$\epsilon \frac{\omega_r^2 - k^2 v_{a1}^2 \cos^2 \alpha}{n_1} + \frac{\omega_r'^2}{n_2} = 0, \tag{2.71}$$

where $n_2 = im_2$. Assuming that as $k \to \infty$, $\omega_r/k \to const$ (as occurs in Roberts (1981b); this will also be confirmed by our numerical solutions of the dispersion relation in Chapters 3 and 6), we can solve this equation to find the asymptotic value of the phase speed for the surface modes. We find that when there is no flow in the magnetosheath, only slow surface modes may propagate for $\alpha = 0$ (when $\epsilon = 0.192$ and $\beta = 0.5$ these modes have $v_{ph} = 0.700$). We will see later that in this case fast surface modes may only propagate as a result of a non-zero flow. So now, combining the above criteria with that for the existence

of stable modes (Equation (2.66)), our full criteria for stable slow surface modes is that they may exist for phase speeds in the range

$$\max\left(0, v_o\cos\left(\chi-\alpha\right)-c_{s2}\right) < v_{ph} < \min\left(c_T, v_o\cos\left(\chi-\alpha\right)+c_{s2}\right), \tag{2.72}$$

where v_o must satisfy $v_o\cos\left(\chi-\alpha\right)-c_{s2} < c_T$ so that the above inequality may be satisfied. Similarly, stable fast surface modes may exist for phase speeds such that

$$\max\left(c_{slow}, v_o\cos\left(\chi-\alpha\right)-c_{s2}\right) < v_{ph} < \min\left(c_f, v_o\cos\left(\chi-\alpha\right)+c_{s2}\right), \tag{2.73}$$

when v_o is in the range $c_{slow}-c_{s2} < v_o\cos\left(\chi-\alpha\right) < c_f+c_{s2}$. Stable slow body modes may exist for

$$\max\left(c_T, v_o\cos\left(\chi-\alpha\right)-c_{s2}\right) < v_{ph} < \min\left(c_{slow}, v_o\cos\left(\chi-\alpha\right)+c_{s2}\right), \tag{2.74}$$

where $v_o\cos\left(\chi-\alpha\right)-c_{s2} < c_{slow}$. Finally, stable fast cavity modes may exist for

$$\max\left(c_f, v_o\cos\left(\chi-\alpha\right)-c_{s2}\right) < v_{ph} < v_o\cos\left(\chi-\alpha\right)+c_{s2}, \tag{2.75}$$

where $v_o\cos\left(\chi-\alpha\right)+c_{s2} > c_f$.

Figure 2.4 shows the dependence of the regions where modes may exist on the angle α when $\chi=\pi/2$ (the corresponding figure for the case when $\chi=0$ will be discussed in Chapter 6). For all the figures in Chapters 2 and 3 we have taken $\beta=0.5$, $\Gamma=5/3$ and $\epsilon=0.192$, and in this case we have taken $v_o=4.0$. The negative sloping shading shows regions where the magnetosphere can support a body mode ($m_1^2>0$). The unshaded regions show the values of phase speed for which the magnetosphere may support a surface mode ($m_1^2<0$). The boundaries are calculated using c_T, c_f and c_{slow} as outlined above (Equations (2.67) to (2.70)). The region with positive sloping shading is the region of phase speed within which the magnetosheath may support stable ($\omega_i=0$) modes, which are not growing or decaying in time (Equation (2.66)). All of the modes can be divided into fast and slow modes by the line $v_{ph}=c_{slow}$, above which fast modes propagate and below which slow modes may propagate. As α increases, the regions where slow modes may exist diminish, until when $\alpha=\pi/2$ only fast modes may propagate. Where the region within which stable modes may propagate (positive sloped shading between e and f) overlaps with the unshaded regions, the conditions for purely evanescent modes in both the magnetosheath and the magnetosphere are both satisfied and we may find stable surface modes. These are the regions defined by Equations (2.72) and (2.73). Similarly the overlap between the positive and negative sloping indicate the regions for which stable body modes may propagate, defined in Equations (2.74) and (2.75). The effect of changing the flow speed is to change the gradient of the outline of the positively sloping shaded region. When $\alpha=0$, the region

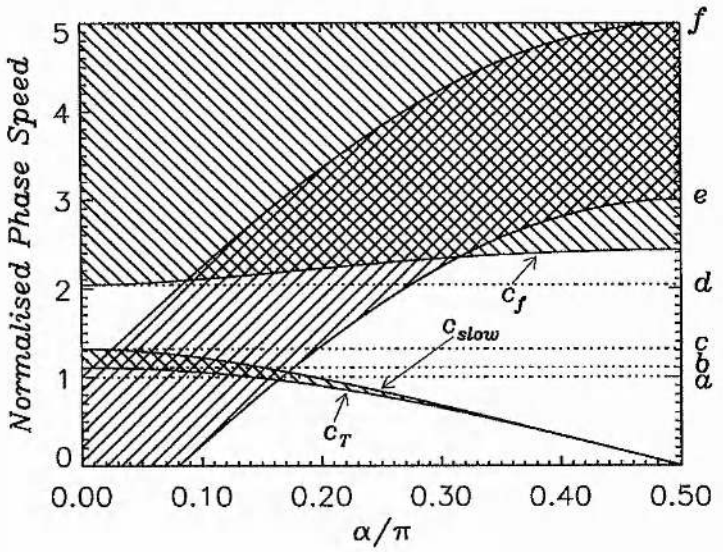

Figure 2.4: The variation of the regions of phase speed (given in units of c_{s2}) where different mode types may exist with propagation angle α. Of the dotted lines, a is the magnetosheath sound speed (c_{s2}), b is the tube speed (c_T ($\alpha = 0$)) in the magnetosphere when $\alpha = 0$, c is the sound speed in the magnetosphere (c_{s1}) and d is the Alfvén speed in the magnetosphere (v_{a1}). Of the solid curves, e is the lower cut-off for stable modes ($v_{ph} = v_o \cos(\chi - \alpha) - c_{s2}$) and f is the corresponding upper cut-off ($v_{ph} = v_o \cos(\chi - \alpha) + c_{s2}$), while the curves of the fast speed, c_f, slow speed, c_{slow} and tube speed, c_T are indicated by the arrows. Here as in all the following diagrams $\beta = 0.5$, $\Gamma = 5/3$ and $\epsilon = 0.192$. We have also taken $v_o = 4.0$ and $\chi = \pi/2$.

where stable modes may exist is independent of the value of v_o, and the region moves most rapidly with increasing v_o when $\alpha = \pi/2$. When $\alpha = \pi/2$, we effectively have the case studied by Mann et al. (1999), although they also neglected plasma pressure in the magnetosphere.

As we discussed earlier, the condition for stable modes (Equation (2.66)) is merely a necessary condition, not a sufficient one. Thus we should remember that we may have unstable modes within this region also. However, the behaviour of the slow (shown in Figure 3.14) and fast stable body modes when $v_o \cos(\chi - \alpha) - c_{s2} < c_T$ and c_f, respectively, is that the phase speed is confined between the upper and lower boundaries. For the slow body modes, the phase speed asymptotes towards the tube speed as $k \to 0$ whereas the phase speed of the fast mode asymptotes towards the fast speed as $k \to \infty$. Thus, the phase speed of the mode remains in the region where stable modes may propagate even when $v_o \cos(\chi - \alpha) - c_{s2}$ becomes arbitrarily close to c_T or c_f, and so the phase speed always remains within the bounds and the

modes may remain stable. Thus the slow body modes become unstable only when

$$v_o \cos(\chi - \alpha) - c_{s2} > c_T, \tag{2.76}$$

and similarly, the fast body modes may become unstable only when

$$v_o \cos(\chi - \alpha) - c_{s2} > c_f. \tag{2.77}$$

Chapter 3

Trapping and Excitation of Magnetospheric Modes II - On the Flanks of the Magnetosphere

In this chapter we will examine in detail the case of wave trapping and excitation on the flanks of the magnetosphere. Here we will take $\chi = \pi/2$ so that the magnetic field is perpendicular to the flow in the magnetosheath, and our dispersion relation, Equation (2.35), becomes

$$\epsilon \left(\frac{\omega^2 - k^2 v_{a1}^2 \cos^2 \alpha}{m_1} \right) \left(\frac{\exp(im_1) + \exp(-im_1)}{\exp(im_1) - \exp(-im_1)} \right) - \frac{(\omega - k v_o \sin \alpha)^2}{m_2} = 0. \tag{3.1}$$

The ranges of phase speed for which the various modes may exist are shown in Figure 2.4.

The first part of this chapter summarises the results calculated numerically for this model. In particular, Section 3.1 discusses the behaviour of the fast surface modes, while Section 3.2 discusses the slow surface modes. Section 3.3 gives the results for slow body modes and in Section 3.4 the results for fast cavity modes are shown. We then develop in Section 3.5 a technique to predict the onset of instability for fast modes, and discuss the results in the light of negative wave energy theory, and in Section 3.6 we compare the predicted values of phase speed and angle given in Section 2.3.2 to our solutions of the exact dispersion relation. Finally, in Section 3.7 we discuss our results in terms of observations of ULF waves on the flanks of the magnetosphere and summarise our results.

3.1 The Fast Surface Mode

First we will examine the behaviour of the fast surface mode with changing k. Figure 3.1 shows the phase speed ($v_{ph} = \omega_r/k$) and growth rate of this mode for various flow speeds, v_o. Here we have taken $\alpha = \pi/2$. We can see that for all non-zero flow speeds, both the phase speed and the growth rate tend to zero as $k \to 0$. With $\alpha = \pi/2$ we can see that the mode is unstable for all k. For low flow speeds, we find that the phase speed is always below the fast speed, and as $k \to \infty$, $\omega_i \to \infty$. For higher flow speeds, we find that the phase speed first exceeds the fast speed, has a maximum and tends back down to c_f as k increases. Here, the growth rate also has a maximum at a finite value of k, and then tends to zero for large k.

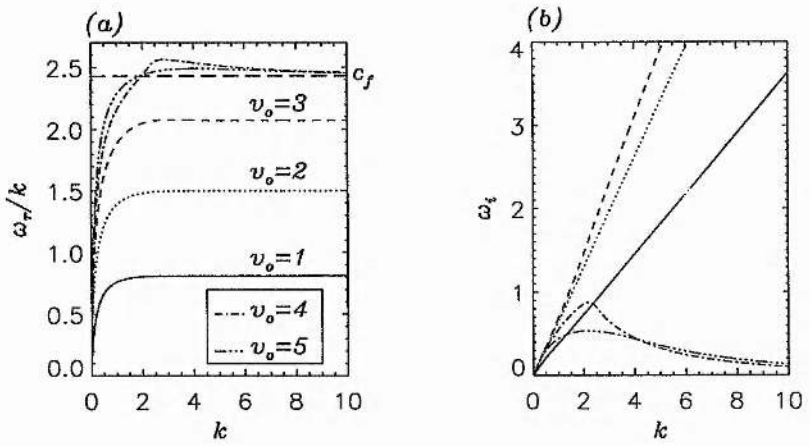

Figure 3.1: Fast surface mode (a) phase speeds and (b) growth rates as a function of k for $\alpha = \pi/2$. Here we have plots for $v_o = 1.0$ (solid line), $v_o = 2.0$ (dotted line), $v_o = 3.0$ (dashed line), $v_o = 4.0$ (dot-dashed line) and $v_o = 5.0$ (triple dot-dashed line). The magnetospheric fast speed (c_f) is shown in (a) by a horizontal dashed line.

In order to better understand these results, we now look at the x-component of the wavenumbers in the magnetosphere and magnetosheath (m_1 and m_2 respectively). Figure 3.2 shows the real and imaginary components of these two wavenumbers as functions of k. For the low flow speeds shown in Figure 3.2 (the cases with $v_o < 4$) the real and imaginary parts of both m_1 and m_2 increase in size linearly with k. In both regions, the imaginary parts of the wavenumbers increase more rapidly than the real parts, and for these flow speeds the mode is dominantly evanescent in the magnetosphere. These modes correspond to those in Figure 3.1 that have unbounded growth rate ($\omega_i \to \infty$) as $k \to \infty$. For the modes plotted in Figure 3.1 which have bounded growth rate ($v_o = 4, 5$), the imaginary parts of both m_1 and m_2 are bounded in k. The real part of m_1 approaches $\pi/2$ for large k and these modes are dominantly oscillatory in the

magnetosphere. A value of $\pi/2$ for the wavenumber in the x-direction here indicates that these modes have only a quarter of a wavelength of oscillation across the magnetosphere, whereas traditional cavity models may trap a minimum of half a wavelength. These modes display the feature that $|\mathrm{Re}\,(m_2)| \to \infty$ and $\mathrm{Im}\,(m_2) \to 0$ as $k \to \infty$. Thus for sufficiently high flow speeds, the fast surface modes also become oscillatory in the magnetosheath, although they resemble trapped modes in the magnetosphere.

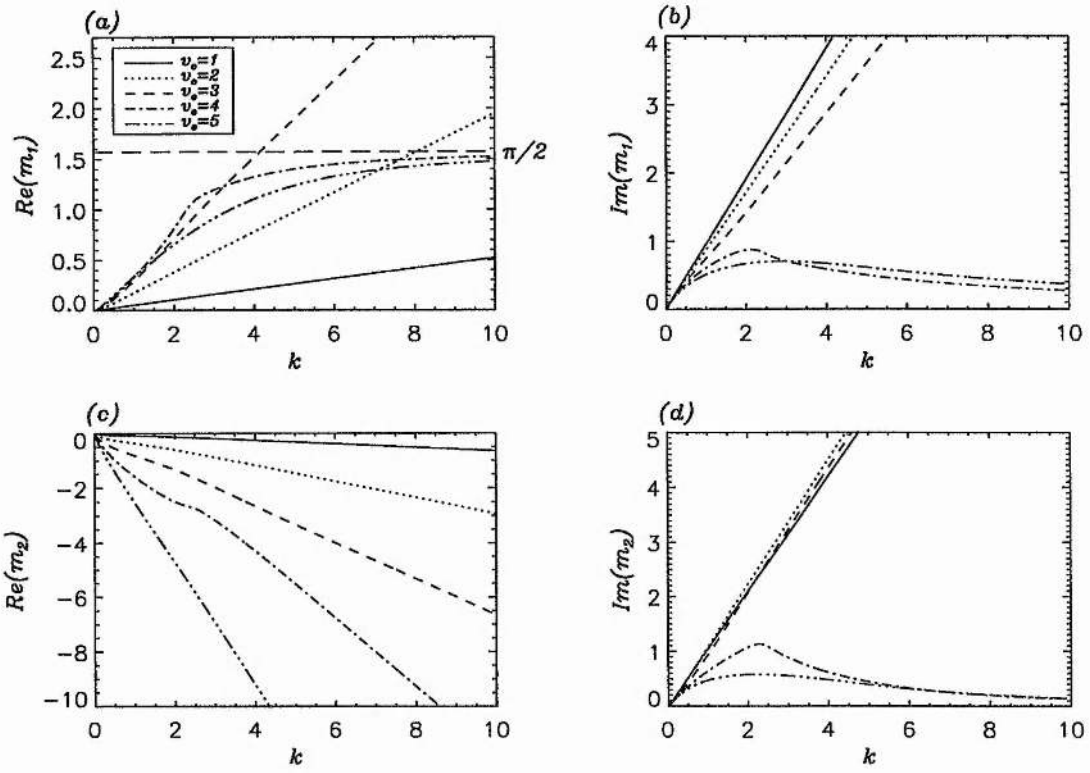

Figure 3.2: The real and imaginary parts of the x-component of the wavenumbers in the magnetosphere ((a) and (b) respectively) and the magnetosheath ((c) and (d) respectively) as functions of k for the same values of v_o as in Figure 3.1. In (a) the value $\pi/2$ is shown by a horizontal dashed line.

We now investigate the dependence of the instability on the angle α. Figure 3.3 shows how the fast surface mode depends upon α. When $\alpha = \pi/2$ this is the mode shown in Figure 3.2 for $v_o = 4.0$ and $k = 2$. The triple dot-dash lines represent the boundaries of the potentially stable region, ($v_{ph} = v_o \sin\alpha \pm c_{s2}$), and in all three plots, a solid line represents the real part of the function, whereas a dot-dashed line represents the imaginary part. As α decreases from $\pi/2$, we find that the growth rate increases slightly to a maximum

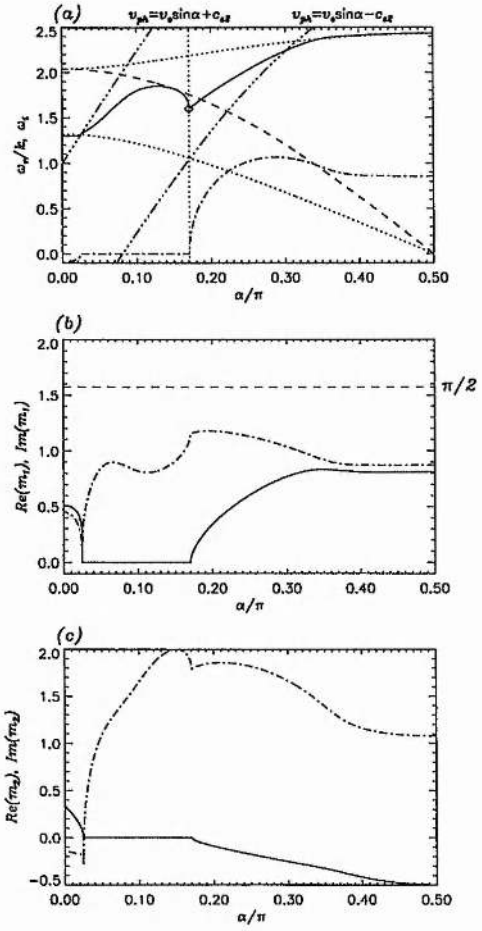

Figure 3.3: The change of the fast surface mode characteristics as α changes. (a) shows the phase speed and growth rates. (b) shows the real and imaginary parts of the x-direction wave number in the magnetosphere, with $\pi/2$ shown by a dashed line, and (c) shows the wave numbers for the magnetosheath. In all cases the real part is represented by a solid line, while the imaginary part is represented by a dot-dashed line. Here we have taken $k = 2.0$ and $v_o = 4.0$. In (a) the vertical dotted line and the diamond indicate the predicted onset of instability as explained in Section 3.5.2 and the dashed line is the maximum value of the phase speed for stable surface modes derived in Equation (3.4). The upper and lower dotted curves are the fast and slow speeds respectively.

and then decreases to zero and the system becomes stable. Decreasing α further, we find that when the phase speed crosses the line $v_{ph} = v_o \sin\alpha + c_{s2}$, the mode becomes leaky, with a negative growth rate. It is interesting to note that the mode is unstable for some values of v_{ph} within the region where modes may be (but are not necessarily) stable. Looking at the x-direction wavenumbers for the magnetosphere ((b) in Figure 3.3) and the magnetosheath ((c) in the figure), we find that when the mode is stable it is a surface mode (purely evanescent in both regions). The mode is a fast surface mode since the phase speed is always higher than the slow speed. Thus the presence of a non-zero flow in the magnetosheath allows a stable fast surface mode to exist. When the mode is unstable, the mode has both an oscillatory and an exponential part in each region. In the magnetosphere, the oscillatory and exponential parts are of the same order, whereas in the sheath the mode is still dominantly evanescent when $\omega_i > 0$, and it grows in space when $\omega_i < 0$.

By examining the dispersion relation for stable surface modes we may obtain a more accurate estimate for the onset of instability of a surface mode. The dispersion relation for a stable evanescent mode is

$$\epsilon\left(\omega_r^2 - k^2 v_{a1}^2 \cos^2\alpha\right) n_2 \coth n_1 + \left(\omega_r - k v_o \sin\alpha\right)^2 n_1 = 0, \tag{3.2}$$

where $n_1^2 = -m_1^2$ and $n_2^2 = -m_2^2$. Since $\coth n_1$ has the same sign as n_1, we may assume n_1 is positive. It can easily be seen that the second term in the equation is now positive definite, and that therefore there may only be solutions for real ω if the first term is negative. Since for stable modes our outgoing condition requires that $n_2 = \mathrm{Im}\,(m_2) > 0$ (see Equation (2.34)) this tells us that for real solutions (i.e., for stable surface modes to exist)

$$\left(\frac{\omega}{k}\right)^2 < v_{a1}^2 \cos^2\alpha, \tag{3.3}$$

and hence

$$\left|\frac{\omega}{k}\right| < v_{a1}\cos\alpha. \tag{3.4}$$

The line $\omega/k = v_{a1}\cos\alpha$ is shown as a dashed line in Figure 3.3, and we can see that the phase speed of the stable surface modes is always within this bound. However, as with our previous condition for stability (Equation (2.66)), this a necessary but not sufficient condition. Unstable modes may also exist within this range of phase speed as shown in Figure 3.3(a). An exact method of predicting the onset of the instability for surface modes will be shown in Section 3.5.2.

More generally, Figure 3.4 shows a contour plot of the growth rate against v_o and α for the fast surface mode with $k = 2.0$. The solid lines indicate positive values of ω_i, whilst the dotted lines are the negative values (in between the two sets of contours the growth rate is zero). Here it is obvious that although the

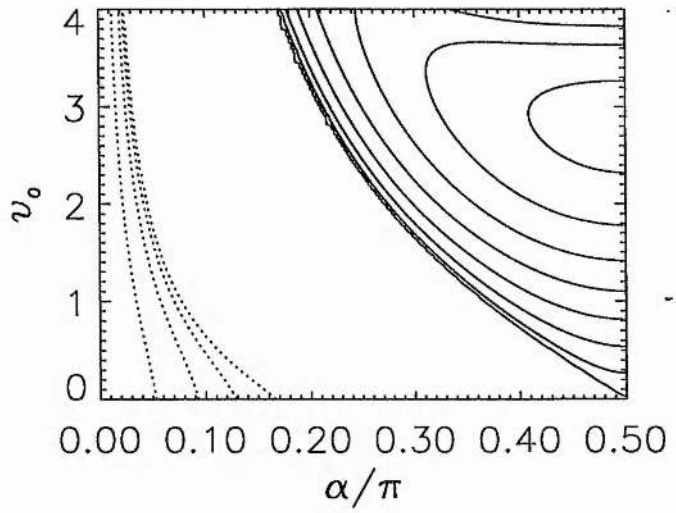

Figure 3.4: A contour plot of the growth rate, ω_i, plotted against v_o and α for the fast surface mode with $k = 2.0$. The solid contours show regions of positive growth rate indicating unstable modes, the dotted lines are in regions of negative growth rate showing leaky modes. The region containing no contour lines is the region for which stable surface modes exist.

mode is unstable for any non-zero v_o when $\alpha \neq \pi/2$, there is a non-zero lower cut-off speed for all lower values of α. As $\alpha \to 0$, the value of the cut-off tends to infinity, since propagation perpendicular to the flow does not 'feel' the flow, i.e., $(\mathbf{v_o}.\nabla) \equiv i\mathbf{v_o}.\mathbf{k} \to 0$. There is also an upper cut-off speed for the existence of leaky modes and this also tends to infinity for small α. The angle α has two effects on the properties of the modes that cause this change in stability. First, the flow speed is always multiplied by a factor of $\sin\alpha$, and so for small angles, the effect of the flow is very small. Secondly, the angle of propagation affects the magnetic forces that the background field exerts on the wave. The tension force is $(\mathbf{B_1}.\nabla)\,\mathbf{b} \equiv i\,(\mathbf{k}.\mathbf{B_1})\,\mathbf{b}$. Thus when $\alpha = \pi/2$ (i.e. when $\mathbf{k}.\mathbf{B_1} = 0$), no magnetic tension force is created. Conversely, when the propagation vector has a component along the field line (i.e., $\mathbf{k}.\mathbf{B_1} \neq 0$), the oscillations will tend to bend the field lines introducing magnetic tension forces which help to stabilise the system. Thus for a given flow, decreasing α will decrease the effect of the flow and introduce stabilising magnetic tension forces. Fujita et al. (1996) studied the effect of a non-zero k_z on the frequency and growth rate of the oscillations. However, whereas we have fixed the value of $k = \sqrt{k_y^2 + k_z^2}$ and varied the value of the angle α, Fujita et al. fixed the value of k_z and varied k_y. In this case, increasing k_y is equivalent to increasing both k and $\alpha = \tan^{-1}(k_y/k_z)$. They found that there was a lower cut-off in k_y below which the modes are stable. We

have looked at the dependence on k and α separately, and our results would indicate that the stability of the fast surface modes has very little dependence on k (see also Figure 3.6 below), but a strong dependence on α. Hence the lower cut-off in k_y found by Fujita et al. is more clearly expressed as a cut-off in α in our model.

Figure 3.5 shows the parameters of the fast surface mode as functions of k for various values of the angle α. We have again taken $v_o = 4.0$, and the different line styles represent the different angles that we have considered. In this figure we find a maximum in growth rate for finite k (indicating wavenumber selection) only for the case where $\alpha = \pi/2$, and in this case the magnetospheric x-direction wavenumber approaches $\pi/2$ as $k \to \infty$. For $\alpha = \pi/3$ and $\alpha = \pi/4$ the growth rate increases without bound as k increases and the phase speed approaches a constant (sub-fast) value for large k. The real and imaginary parts of both wavenumbers increase in magnitude without bound as $k \to \infty$. For $\alpha = \pi/6$ the mode is a stable fast surface mode, and for $\alpha = \pi/12$ the mode is leaky ($\omega_i < 0$). In this case the character of the mode is dominantly growing in the magnetosheath and in the magnetosphere, for large k, m_1 approaches $\pi/2$. Thus both the modes for $\alpha = \pi/2$ and $\alpha = \pi/12$ are quarter wavelength modes for large k. The stable, unstable or leaky nature of a particular mode appears to be independent of k. To better understand this, we may rearrange Equation (3.2) in terms of the phase speed, v_{ph}, so that

$$\epsilon \left(v_{ph}^2 - v_{a1}^2 \cos^2 \alpha\right) N_2 \coth\left(N_1 k\right) + \left(v_{ph} - v_o \sin\alpha\right)^2 N_1 = 0, \tag{3.5}$$

where $N_1 = n_1/k$ and $N_2 = n_2/k$. Now we can see that the only dependence on k in the dispersion relation is within the coth function. Since this function is very close to unity for most values of $N_1 k$, the dispersion relation for stable surface modes is almost independent of k. As we will see in Section 3.5, the onset of instability may be predicted using this form of the dispersion relation, and hence the onset of instability for fast surface modes will be almost independent of k.

Finally, Figure 3.6 shows the evolution of the fast surface mode with flow speed for various values of k and with $\alpha = \pi/4$. Here we see that the speed at the onset of instability of these modes does indeed have little dependence on k. The phase speed of the mode is almost independent of k, both for the stable and unstable regions. The growth rate of the unstable surface modes at first seems to increase linearly with k and this occurs for speeds at which the mode has unbounded growth rate as $k \to \infty$. For higher speeds, the mode has wavenumber selection and here we can see that the growth rate is small for all k. The discontinuity in ω_i occurs at the change over from unbounded to bounded growth rate. The change in behaviour of the growth rate of the fast surface mode occurs close to where the line $v_{ph} = v_o \sin\alpha - c_{s2}$

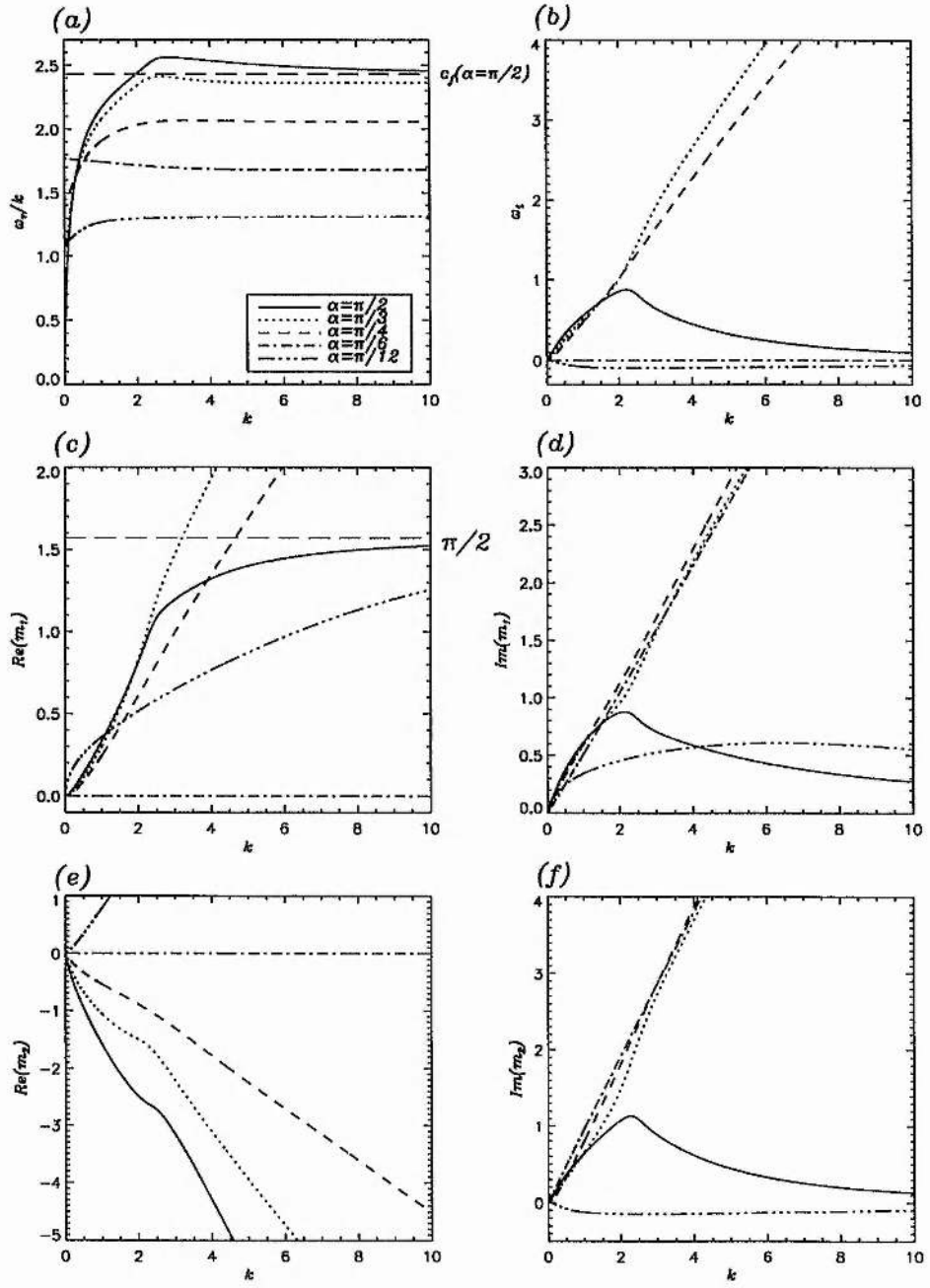

Figure 3.5: The change of: (a) the phase speed, (b) the growth rate, (c) the real part of m_1, (d) the imaginary part of m_1, (e) the real part of m_2 and (f) the imaginary part of m_2 of the fast surface mode with k for various values of α. In all plots, the values of α are: $\pi/2$ (solid line), $\pi/3$ (dotted line), $\pi/4$ (dashed line), $\pi/6$ (dot-dashed line) and $\pi/12$ (triple-dot-dashed line). Here we have taken $v_o = 4.0$.

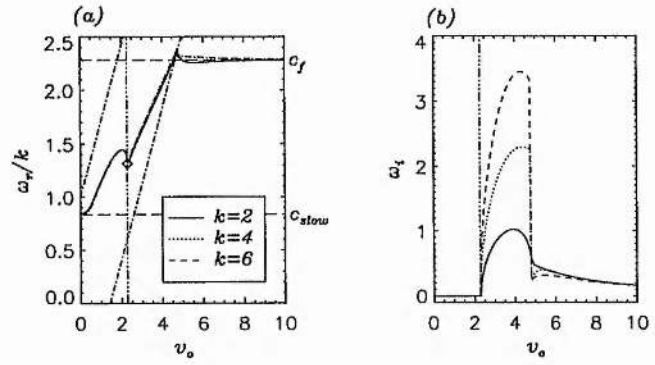

Figure 3.6: The evolution with flow speed, v_o, of (a) the phase speed, and (b) the growth rate of the fast surface mode for $k = 2$ (solid line), $k = 4$ (dotted line) and $k = 6$ (dashed line). Here we have taken $\alpha = \pi/4$. The diamond in (a) shows the predicted point of onset of instability when $k = 2$ and the triple dot-dashed line in both shows the value of v_o at this point. The region bounded by the horizontal lines and the diagonal lines is the potentially stable region (Equation (2.73)).

crosses the line $v_{ph} = c_f$. In other words the growth rate becomes bounded when

$$v_o \gtrapprox \frac{c_f + c_{s2}}{\sin\alpha}, \tag{3.6}$$

which in this case ($\alpha = \pi/4$) means that the growth rate will be bounded for $v_o \approx 4.7$.

We can also see that, unlike models of an unbounded magnetosphere with a sheet magnetopause, there is no upper cut-off speed for the instability, although the growth rates have a maximum and then decrease towards zero as v_o increases. Since the modes are purely evanescent in the magnetosphere for low v_o, they are fairly insensitive to the inner boundary. Thus there will be negligible dispersion (i.e., k dependence) of the stable fast surface modes and the phase speeds will be the same for any k.

Figure 3.7 shows the wavenumbers of these modes. The magnetospheric wavenumber is purely imaginary below the lower cut-off speed, showing that this is a surface mode, and as $v_o \to \infty$ the asymptotic value of the wavenumber depends strongly upon k. For $k = 2$, both the real and imaginary parts are tending to zero with increasing v_o, while for $k = 4$ and $k = 6$, the imaginary part tends to zero, while the real part tends to π and 2π respectively. The magnetosheath wavenumber becomes dominantly real for large v_o for all values of k. Thus for the larger values of k, the mode becomes almost stable for large v_o, but unlike the completely stable modes, the mode is oscillatory in the magnetosheath as well as in the magnetosphere.

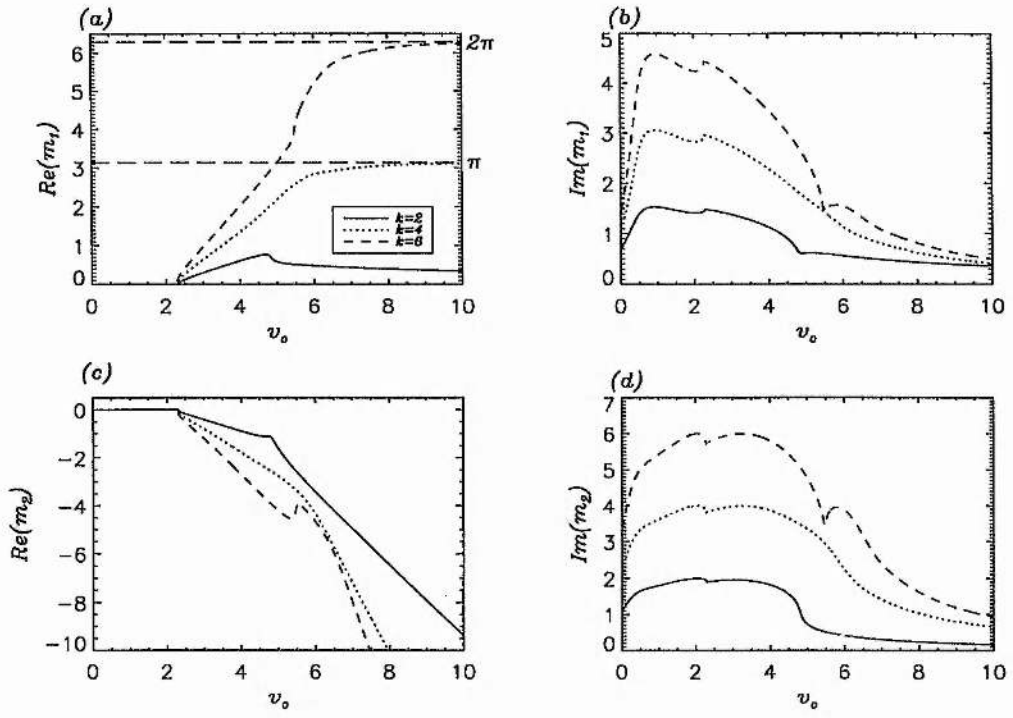

Figure 3.7: The real and imaginary parts of m_1 (plots (a) and (b)) and m_2 (plots (c) and (d)) respectively as functions of v_o for $\alpha = \pi/4$. The values of k are as in Figure 3.6.

3.2 Slow Surface Modes

Now we examine the behaviour of the slow surface mode. From Figure 2.4 we see that, for all values of α when $v_o = 0$, the region of phase speed for which slow surface modes may exist (i.e., $v_{ph} < c_T$), is almost entirely within the region for which stable modes may exist ($v_o \sin\alpha - c_{s2} < v_{ph} < v_o \sin\alpha + c_{s2}$). Figure 3.8 shows the phase speed of the slow surface mode as a function of k when $v_o = 0$ and $\alpha = 0$. For small k the phase speed approaches c_{s2}, and as k increases, the phase speed rapidly approaches its asymptotic value, which in this case is $v_{ph} = 0.700$. This mode is stable for all k, which we can explain in the same way as we did for fast surface modes: The dispersion relation for evanescent modes (Equation (2.64)) has little dependence on k, and so we expect the character of the modes to be independent of k. We have also shown the slow surface wave propagating in the opposite direction, which when $v_o = 0$ is a reflection of the mode with positive phase speed in the $v_{ph} = 0$ line.

Figure 3.9 shows the variation of phase speed with angle, α, when $v_o = 0$ and $k = 10$. This phase speed

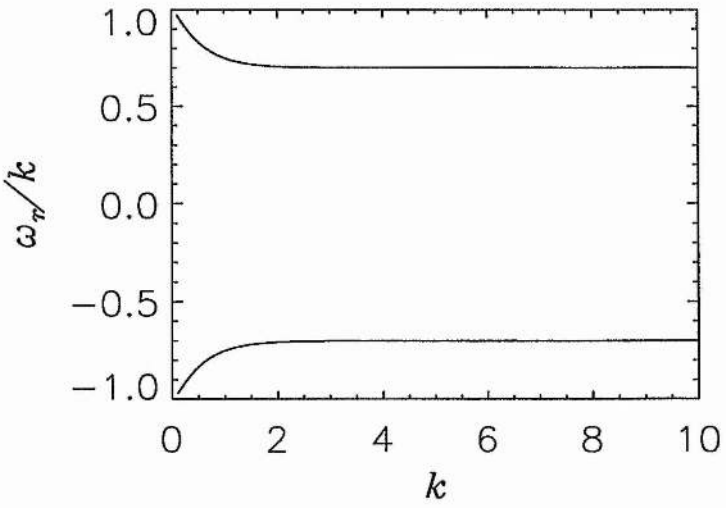

Figure 3.8: The dispersion diagram for slow surface modes when $v_o = 0$ and $\alpha = 0$. Here we have shown both the forward and backward propagating modes.

will be the phase speed of the slow surface modes for almost all k at that particular α. As α increases, the phase speed decreases, approaching zero at $\alpha = \pi/2$. The phase speed of the mode propagating backwards is simply the negative of that shown in this case. The dot-dashed line shows the value of the tube speed, c_T, as α changes. We can see that the phase speed of the slow surface mode is always below c_T when $v_o = 0$.

Now we investigate the development of the slow surface mode as v_o increases. Figure 3.10 shows both the positive and negative phase speed modes as a function of v_o when $\alpha = \pi/6$ and $k = 10$. As v_o increases from zero, the phase speeds of both modes increases. As the phase speed of the upper mode approaches the tube speed c_T, it flattens. The phase speed of the lower mode continues to increase, passing through zero, until the phase speeds of the two modes are the same. At this point the modes become unstable and our outgoing boundary condition (Equation (2.33)) selects only one of the two possible solutions. The phase speed of the unstable mode continues to increase and passes through the region where we would expect to find slow body modes ($c_T < v_{ph} < c_{slow}$). However, the modes have a significant growth rate and remain dominantly evanescent in the magnetosphere (see Figure 3.11). The growth rate reaches a maximum and decreases back to zero when the phase speed is just above c_{slow}. The modes are now stable fast surface modes, and once again we have two separate solutions. The phase speed of the lower solution decreases, tending to c_{slow} as $k \to \infty$. The mode becomes unstable when $v_o \sin\alpha - c_{s2} \approx c_{slow}$ and has a small bounded growth rate. The upper mode has an increasing phase speed and eventually coalesces with the

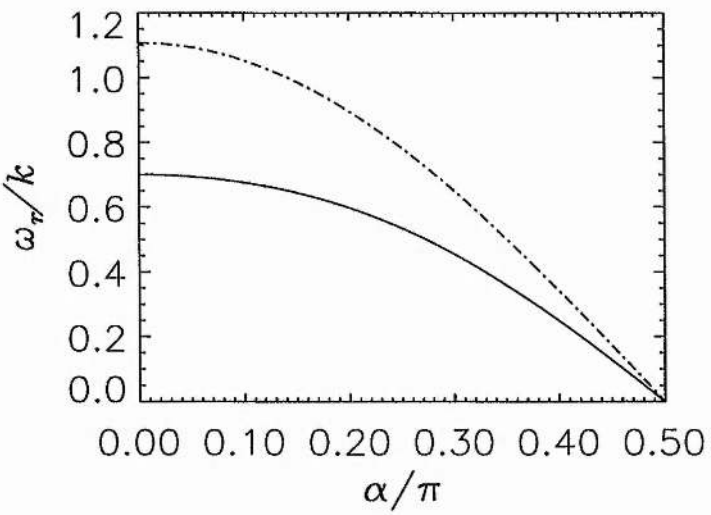

Figure 3.9: The variation of phase speed with angle for the slow surface mode when $v_o = 0$ and $k = 10$. The dot-dash lines shows the variation of the value of the tube speed, c_T, with α.

original stable fast surface mode (that has $v_{ph} > c_{slow}$ for all v_o, shown by a dashed line). These modes then become unstable, and the behaviour of the resulting unstable fast surface mode is as described in Section 3.1. The phase speed of the lower stable slow surface mode increases with the same gradient as $v_o \sin\alpha$, so that its phase speed can be approximated as

$$v_{ph} = -v_{pho} + v_o \sin\alpha, \tag{3.7}$$

where v_{pho} is the phase speed of the upper slow surface mode when $v_o = 0$. The slow surface modes become unstable when the phase speed is close to the tube speed, c_T, so we can approximate the flow speed at the onset of instability by

$$v_o \approx \frac{c_T + v_{pho}}{\sin\alpha}. \tag{3.8}$$

Similarly the modes become unstable again when the phase speed is close to the slow speed c_{slow} and so we can approximate this by

$$v_o \approx \frac{c_{slow} + v_{pho}}{\sin\alpha}. \tag{3.9}$$

The values of v_o predicted by Equations (3.8) and (3.9) are shown by the vertical dotted lines in Figure 3.10. We can see that while this is not an accurate way of predicting the onset of instability and the point at

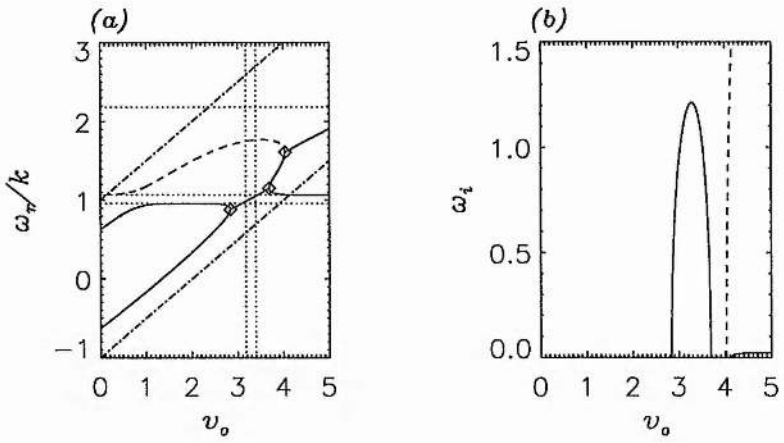

Figure 3.10: The phase speeds (a) and growth rates (b) of slow surface mode as v_o changes. In (a) the dashed line represents the stable fast surface mode, and in (b), the dashed line shows the growth rate of the unstable mode formed by the coalescence of the two stable fast surface modes. In (a) the dot-dash lines show the upper and lower boundaries of the region where stable modes may exist ($v_o \sin\alpha + c_{s2}$ and $v_o \sin\alpha - c_{s2}$ respectively), and the dotted lines in ascending order show the tube speed, c_T, the slow speed, c_{slow} and the fast speed, c_f. The diamonds mark the predicted points at which modes will coalesce. The left and right dotted lines in (a) show the values of v_o given by Equations (3.8) and (3.9), respectively. Here we have taken $k = 10$ and $\alpha = \pi/6$.

which the modes restabilise, the values are at least reasonably close. The onset of instability can be more accurately predicted, and a method for this is detailed in Section 3.5.

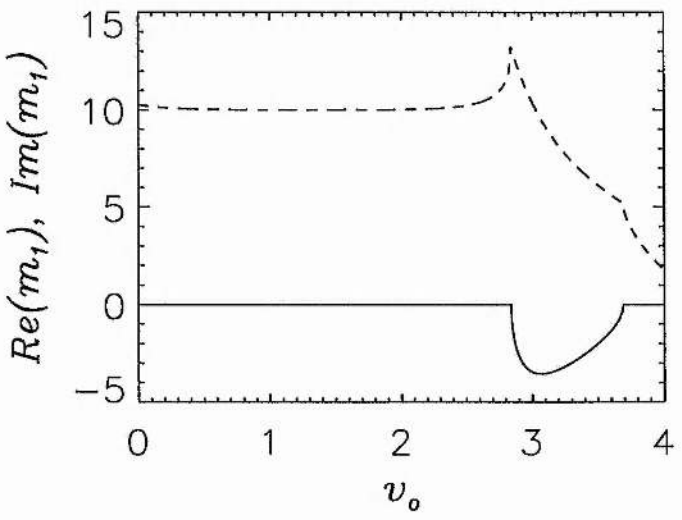

Figure 3.11: The real (solid line) and imaginary (dashed line) parts of the x-direction wavenumber in the magnetosphere, m_1, as a function of v_o for the lower slow surface mode shown in Figure 3.10.

Finally, we look at the development of the unstable slow surface mode with k. Figure 3.12 shows the phase speed and growth rate of the mode when $v_o = 3.3$ and $\alpha = \pi/6$ (close to the largest growth rate in Figure 3.10). Here we can see that the phase speed varies little with k even when the mode is unstable, however, the growth rate increases with k and $\omega_i \to \infty$ as $k \to \infty$. Thus, the unstable part of the slow surface mode has unbounded growth rate as k increases in the same way as the unstable fast surface mode. For very low k, this mode becomes stable, however the onset of instability remains independent of k for these modes.

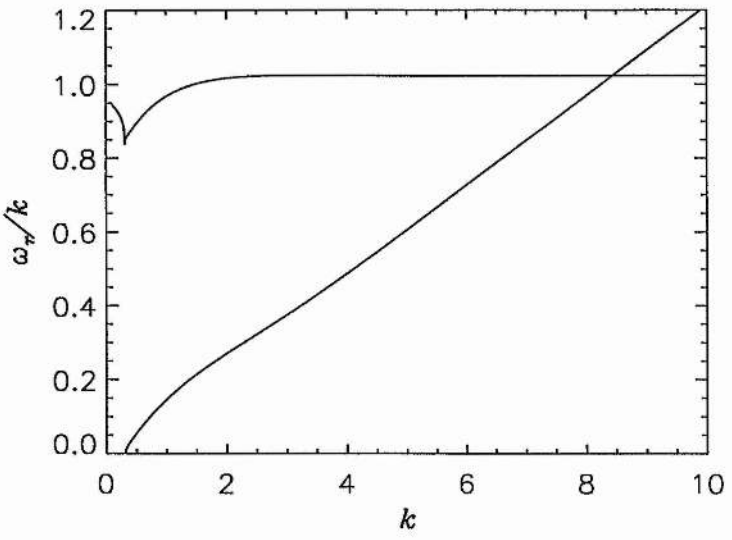

Figure 3.12: The phase speed (solid line) and growth rate (dot-dashed line) of the unstable slow surface mode when $v_o = 3.3$ and $\alpha = \pi/6$.

3.3 Slow Body Modes

As we saw in Section 2.4, the range of phase speeds for which slow cavity modes may exist depends very strongly on the value of α. Where the effect of the flow is greatest (when α is close to $\pi/2$), the slow cavity modes are confined to a very small interval of phase speed close to zero. In order to examine the modes as fully as possible we have chosen to look at modes with $\alpha = \pi/4$, where, for our given parameters, the slow cavity modes are stable when there is no flow.

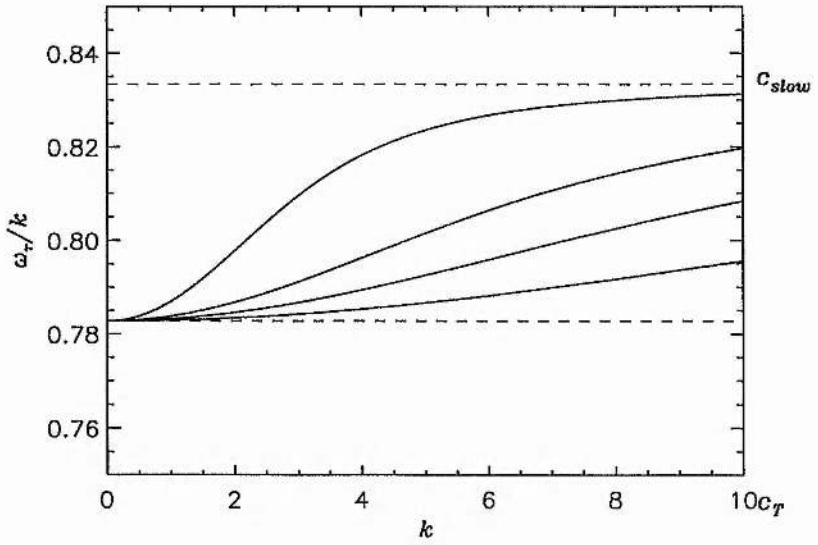

Figure 3.13: The dispersion diagram showing the stable slow cavity modes when $v_o = 2$ and $\alpha = \pi/4$.

Figure 3.13 shows the dispersion diagram for slow cavity modes $v_o = 2$ and $\alpha = \pi/4$. Here we can see that the slow cavity modes are all stable and contained within the region of the diagram between the slow speed, c_{slow}, and the tube speed, c_T. As detailed in Section 2.4, the slow cavity modes will only become unstable when the lower limit in Equation (2.74) changes from c_T to $v_o \sin\alpha - c_{s2}$ and thus the slow cavity modes can only be unstable when

$$v_o > \frac{c_T + c_{s2}}{\sin\alpha}, \tag{3.10}$$

so in this case the modes will be stable for all k when there is no flow in the magnetosheath.

Figure 3.14 (a) shows a close up of the region where the slow cavity modes exist for the same parameters as in Figure 3.13. Figures 3.14 (b) and (c) also show the x-direction wavenumbers in the magnetosphere

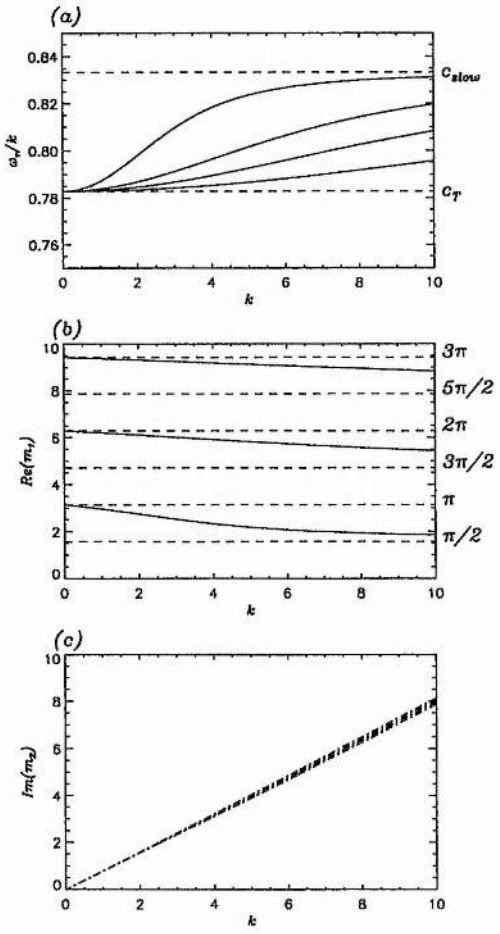

Figure 3.14: (a) An enlargement of the stable slow cavity modes on the dispersion diagram. (b) the (purely real) x-component of the wavenumbers in the magnetosphere, and (c) the (purely imaginary) x-component of the wavenumbers in the magnetosheath for the slow cavity modes.

and magnetosheath respectively (the imaginary component of the magnetosphere wavenumber and the real part of the magnetosheath wavenumber are both identically zero and are not shown here). For low k, the phase speed of all the modes is close to c_T, and as $k \to \infty$, all the modes asymptote towards c_{slow}. For purely real ω we may write the dispersion relation for slow (and fast) body modes as

$$\begin{aligned} \tan(m_1) &= \frac{n_2\left(\omega^2 - k^2 v_{a1}^2 \cos^2\alpha\right)}{m_1\left(\omega - k v_o \sin\alpha\right)^2} \\ &= \frac{n_2\left(\omega^2 - k^2 v_{a1}^2 \cos^2\alpha\right)}{\left(\omega - k v_o \sin\alpha\right)^2} \sqrt{\frac{\left(c_f^2 + c_{slow}^2\right)\left(\omega^2 - k^2 c_T^2\right)}{\left(\omega^2 - k^2 c_f^2\right)\left(\omega^2 - k^2 c_{slow}^2\right)}}, \end{aligned} \tag{3.11}$$

where $n_2 = i m_2$. In the magnetosphere these modes are purely oscillatory with $v_{ph} \to c_T$ as $k \to 0$ and $v_{ph} \to c_{slow}$ as $k \to \infty$. Thus as $k \to 0$, $\tan(m_1) \to 0$ and therefore

$$\mathrm{Re}(m_1) \to n\pi, \quad \text{as} \quad k \to 0. \tag{3.12}$$

Also, as $k \to \infty$, $\tan(m_1) \to \infty$, so that

$$\mathrm{Re}(m_1) \to \left(n - \frac{1}{2}\right)\pi, \quad \text{as} \quad k \to \infty. \tag{3.13}$$

Here n is an integer which is constant for each mode. In the magnetosheath all the modes are evanescent, with $\mathrm{Im}(m_2)$ increasing from zero with increasing k.

Next we look at the dispersion diagram for unstable slow cavity modes. Figure 3.15 shows the behaviour of ω_r/k and ω_i for $v_o = 2.55$ and $\alpha = \pi/4$ (so that $c_T < v_o \sin\alpha - c_{s2} < c_{slow}$). The upper and lower dashed lines mark the slow speed, c_{slow}, and the tube speed, c_T respectively. The triple dot-dashed line shows the position of the lower cut-off for stable slow cavity modes from Equation (2.74), which in this case is $v_{ph} = v_o \sin\alpha - c_{s2}$. Here we see that the form of the phase speed is little changed from the stable case (Figure 3.14). For low k, the phase speed is below the lower stability cut-off, and the mode is unstable. The value of the growth rate is very small and the imaginary part of the wavenumber in the magnetosphere remains small compared to the real part, hence the character of such a wave remains dominantly that of a trapped cavity mode. As k increases, ω_i also increases, reaching a maximum (which is much lower than the maximum growth rate for the globally oscillatory modes seen in Section 3.1) and then rapidly decreasing to zero. As the phase speed crosses the lower cut-off line (the triple-dot-dashed line), the modes become stable trapped slow cavity modes.

Figure 3.16 shows the phase speeds and growth rates of the fundamental slow cavity mode when $\alpha = \pi/4$ for various values of v_o. The solid curve is the case when $v_o = 2.55$ as shown in Figure 3.15. The dashed and dot-dashed lines represent the cases when $v_o = 4$ and $v_o = 5$, respectively. For both these cases,

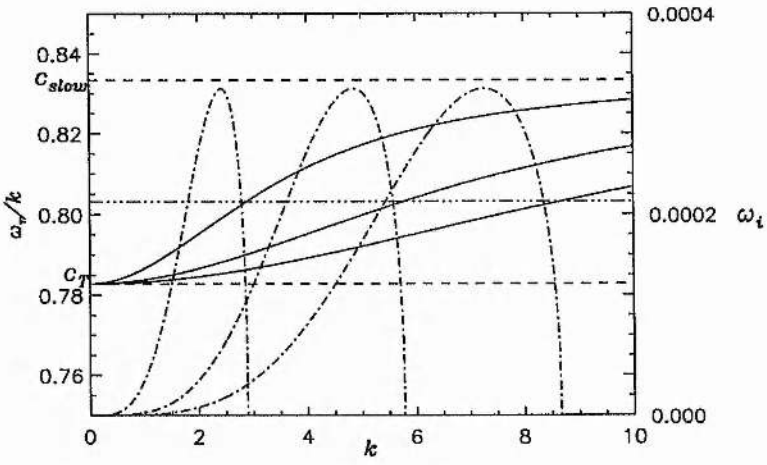

Figure 3.15: The phase speed (solid line and left hand axis) and growth rate (dot-dashed lines and right hand axis) as functions of k for slow cavity modes when $v_o > (c_T + c_{s2}) / \sin\alpha$. Here $v_o = 2.55$ and $\alpha = \pi/4$.

$v_o \sin\alpha > c_{slow} + c_{s2}$, and the maximum growth rates are about ten times larger than when $v_o = 2.55$. The maxima of the growth rates occur for much larger values of k, and in this case $\omega_i \to 0$ as $k \to \infty$.

Figure 3.17 shows the evolution of a slow cavity mode for changing v_o. Here we have taken the parameters $k = 2.0$ and $\alpha = \pi/9$ (the lower value of α is chosen here so that we can see leaky as well as stable and unstable behaviour). This shows that the phase speed remains almost constant as v_o changes. Here the mode is leaky for small v_o ($v_o < (v_{ph} - c_{s2}) / \sin\alpha$), see Equation (2.74). The mode is stable within the predicted region (see Equation (2.66)) and becomes unstable for $v_o > (v_{ph} + c_{s2}) / \sin\alpha$. The growth rate reaches a maximum, and as $v_o \to \infty$, $\omega_i \to 0$. Again, the growth rate is always several orders of magnitude smaller than the growth rates found for the fast modes. Figure 3.18 shows the wavenumbers in (a) the magnetosphere and (b) the magnetosheath for this slow mode. As long as the mode is stable, the wavenumber in the magnetosphere is purely real and as v_o increases from zero, m_1 first decreases from π to $\pi/2$ and then increases again, returning to a value of π. Using the dispersion relation defined in Equation (3.11) we can see that when $v_o \sin\alpha = v_{ph} \pm c_{s2}$, $n_2 = 0$ and thus the right hand side of the equation is zero. Hence, at the edges of the stable region the wavenumber in the magnetosphere is given by

$$m_1 = n\pi, \tag{3.14}$$

for any integer n. In the centre of the stable region, where $v_o \sin\alpha = v_{ph}$, the right hand side of Equation

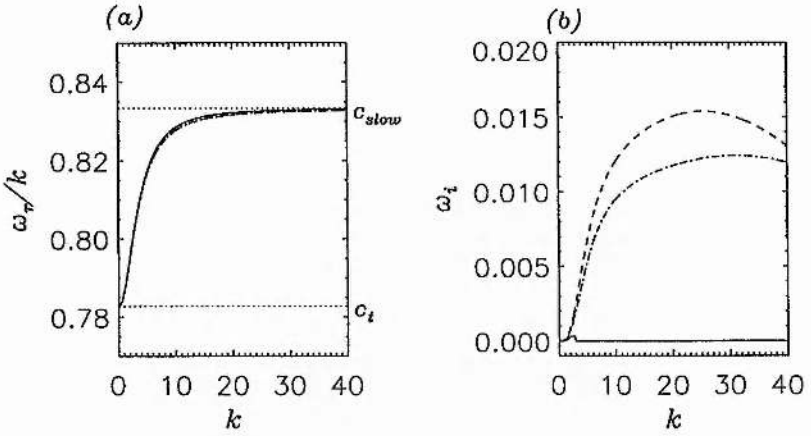

Figure 3.16: The phase speeds (a) and growth rates (b) of the fundamental slow cavity modes when $\alpha = \pi/4$ for $v_o = 2.55$ (solid line), $v_o = 4$ (dashed line) and $v_o = 5$ (dot-dashed line).

(3.11) is infinitely large, and thus the solution requires that

$$m_1 = \left(n - \frac{1}{2}\right)\pi, \tag{3.15}$$

where n is an integer that is constant for each mode. In the magnetosheath the stable mode is purely evanescent, with a maximum of m_2 corresponding to the minimum value of m_1. By differentiating n_2 with respect to the phase speed we obtain

$$\begin{aligned}\frac{dn_2}{dv_{ph}} &= \frac{1}{2n_2}\frac{d(n_2)^2}{dv_{ph}} = \frac{d}{dv_{ph}}\left(\frac{c_{s2}^2 - (v_{ph} - v_o\sin\alpha)^2}{c_{s2}^2}\right) \\ &= -\frac{(v_{ph} - v_o\sin\alpha)}{n_2 c_{s2}^2},\end{aligned} \tag{3.16}$$

from which we deduce that

$$\frac{dn_2}{dv_{ph}} = 0 \quad \text{when} \quad v_{ph} = v_o\sin\alpha. \tag{3.17}$$

In order to determine whether this is a maximum or minimum of n_2 we must look at the sign of the second derivative of n_2 with respect to v_{ph}, which is given by

$$\frac{d^2n_2}{dv_{ph}^2} = -\frac{1}{c_{s2}^2}\left(\frac{1}{n_2} - \frac{(v_{ph} - v_o\sin\alpha)}{n_2^2}\frac{dn_2}{dv_{ph}}\right). \tag{3.18}$$

At $v_{ph} = v_o\sin\alpha$ this reduces to

$$\frac{d^2n_2}{dv_{ph}^2} = -\frac{1}{n_2 c_{s2}^2}, \tag{3.19}$$

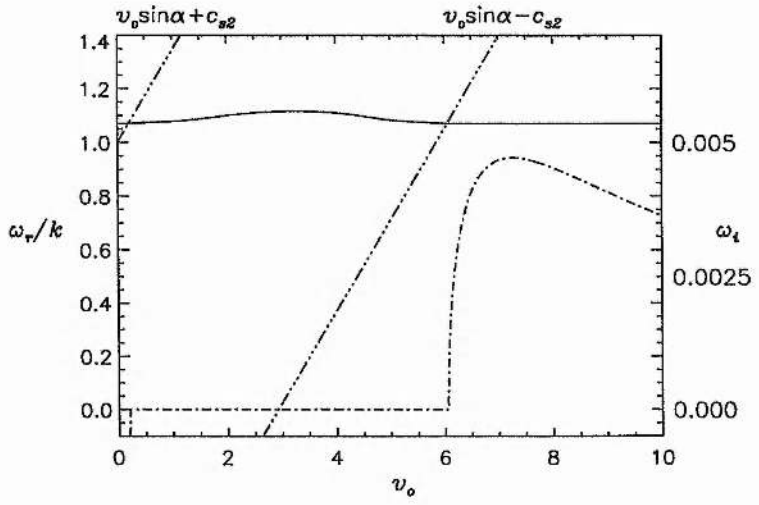

Figure 3.17: The phase speed (solid line) and growth rate (dot-dashed line) as functions of v_o for a slow cavity mode when $k = 2$ and $\alpha = \pi/9$.

which is negative since n_2 is chosen to be positive to give an exponential decay in the magnetosheath (see Equation (2.34)). Hence, this turning point in n_2 is a maximum, confirming that the minimum value of m_1 coincides with the maximum of m_2 (since k is constant in this case). When the mode is unstable, its character in the magnetosphere is still predominantly that of a half-wavelength standing wave, although there is a small exponential component. In the magnetosheath however, the mode changes to being predominantly oscillatory.

From these results we can see that the slow cavity modes are never as fast growing as either the fast modes or the slow surface mode and hence, we are much less likely to see them excited to a significant amplitude in the magnetosphere.

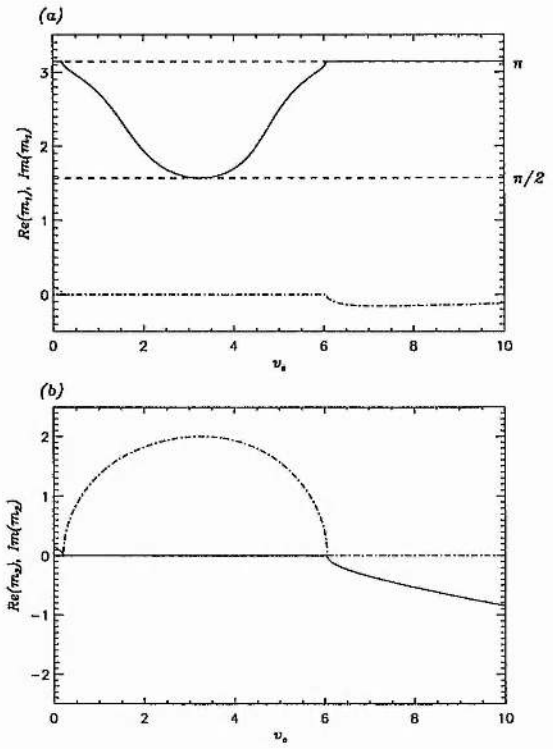

Figure 3.18: The real (solid lines) and imaginary (dot-dashed lines) parts of the x-direction wavenumbers in (a) the magnetosphere and (b) the magnetosheath as functions of v_o for the slow cavity mode shown in Figure 3.17.

3.4 Fast Cavity Modes

We saw in Section 2.4 that stable fast cavity modes may exist when $v_o \sin\alpha + c_{s2} > c_f$ and they may have phase speeds within the range

$$\max\left(c_f, v_o \sin\alpha - c_{s2}\right) < v_{ph} < v_o \sin\alpha + c_{s2}. \tag{3.20}$$

As explained in Section 2.4, the fast cavity modes will only be unstable if the lower limit of Equation (2.75) changes (in this case from c_f to $v_o \sin\alpha - c_{s2}$). Hence, the fast cavity modes will only be unstable if

$$v_o > \frac{c_f + c_{s2}}{\sin\alpha}. \tag{3.21}$$

Defining

$$A^2 = \frac{m_1^2}{k^2} = \frac{\left(v_{ph}^2 - c_f^2\right)\left(v_{ph}^2 - c_{slow}^2\right)}{\left(c_f^2 + c_{slow}^2\right)\left(v_{ph}^2 - c_T^2\right)}, \tag{3.22}$$

and using the dispersion relation as defined in Equation (3.11) we see that $n_2 = 0$ at the upper end of the range of phase speed where stable modes may exist ($v_{ph} = v_o \sin\alpha + c_{s2}$), and therefore $\tan\left(m_1\right) \equiv \tan\left(A\left(v_{ph}\right)k\right) = 0$. Thus the upper cut-off for stable fast body modes occurs when

$$k = \frac{n\pi}{A\left(v_o \sin\alpha + c_{s2}\right)}. \tag{3.23}$$

In Figure 3.19 we can see that as k increases, the phase speed of the stable fast cavity modes tends to the fast speed, c_f (see for example Roberts, 1981b). When v_o satisfies

$$\frac{c_f - c_{s2}}{\sin\alpha} < v_o < \frac{c_f + c_{s2}}{\sin\alpha}, \tag{3.24}$$

(i.e. the flow is fast enough to allow stable cavity modes (Equation (2.75)), but not fast enough for those modes to become unstable (Equation (3.21))), stable fast cavity modes may propagate for all k greater than the cut-off defined in Equation (3.23).

In Figure 3.20 we show the dispersion diagram for the fast cavity modes when the flow speed is fast enough to allow the modes to become unstable (as defined in Equation (3.21)). We have used $v_o = 6.0$ and $\alpha = \pi/4$. As well as the modes that we find when $v_o < \left(c_f + c_{s2}\right)/\sin\alpha$, we find that there are additional modes that begin at the lower cut-off (given by $v_{ph} = v_o \sin\alpha$) and have phase speed increasing as k increases. The value of k at the lower extreme of the region in which stable modes may propagate is found by placing $v_{ph} = v_o \sin\alpha - c_{s2}$ in the dispersion relation (Equation (3.11)). Noting that n_2 must be zero (for a stable mode), we find that the value of k at the cut-off is

$$k = \frac{n\pi}{A\left(v_o \sin\alpha - c_{s2}\right)}. \tag{3.25}$$

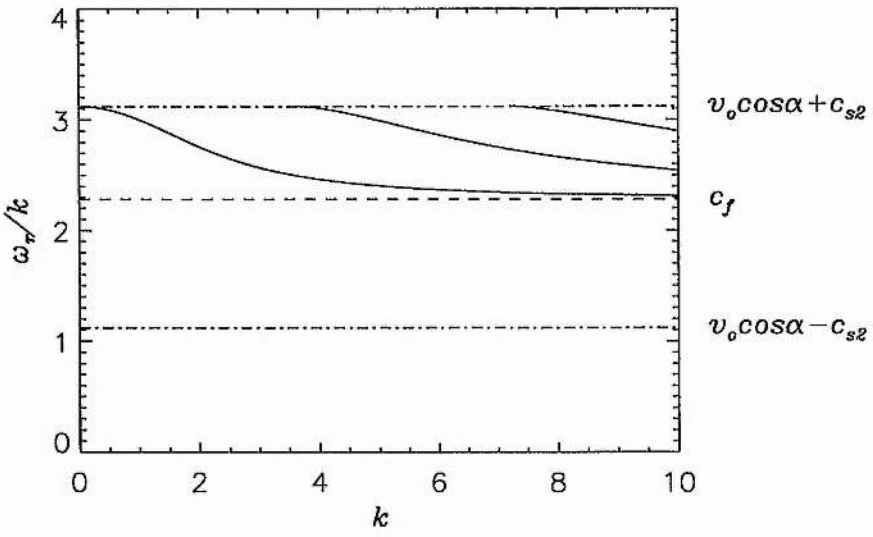

Figure 3.19: The dispersion diagram for stable fast cavity modes when $v_o = 3$ and $\alpha = \pi/2$.

Physically these waves correspond to the fast modes that exist with negative phase speed when $v_o = 0$. In the frame of the magnetosheath, these modes propagate against the flow (and at the lower extreme they have phase speed $-c_{s2}$ in the frame of the magnetosheath), but once the flow is sufficiently high, the modes become oscillatory in the magnetosphere frame. As k increases, the phase speed of the upper mode branch decreases, whilst the phase speed of the lower mode branch increases until the two modes meet and coalesce. A fuller description of this is given in Section 3.5.

For higher k beyond the point of coalescence, the modes are unstable. The phase speed decreases and asymptotically approaches c_f for large k. The growth rate of the mode is, in most cases, bounded. The growth rate is of the same order as that of the unstable fast surface mode and so these modes will also be easily observed.

However, as with the fast surface mode, the growth rate is not always bounded. The fast cavity modes have bounded growth for low v_o (above the minimum speed for instability). However, at the same speed at which the fast surface mode becomes globally oscillatory the fundamental fast cavity mode starts to have an unbounded growth rate as $k \to \infty$ and will become dominantly evanescent in the magnetosphere. Thus the 'low v_o' surface and fundamental body mode exchange character as v_o increases to being predominantly body and surface modes, respectively. Evidently the distinction between body and surface modes in a compressible plasma is not as clear as in an incompressible one. At some higher flow speed this new surface mode again becomes globally oscillatory and the second harmonic (rather than the fundamental)

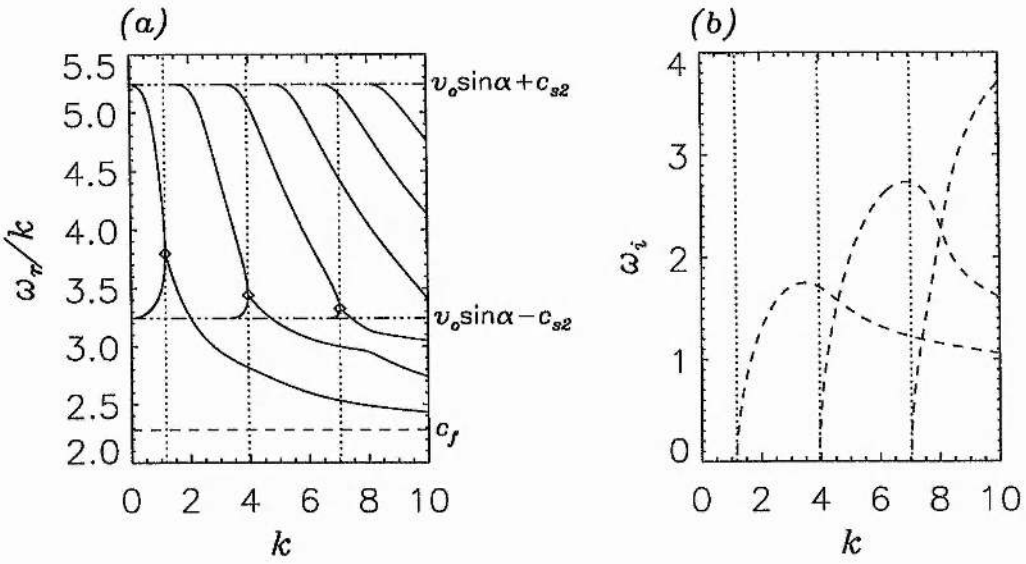

Figure 3.20: (a) The dispersion diagram for the fast cavity modes in the case $v_o > (c_f + c_{s2}) / \sin\alpha$ (in fact, here $v_o = 6.0$ and $\alpha = \pi/4$). The predicted points of onset on instability (derived in Section 3.5) are shown by diamonds, and the dotted lines mark the values of k at the onset. The upper and lower cut-offs and the fast speed are also shown. (b) The growth rates as functions of k for the modes shown in (a). The dotted lines again show the k value of the predicted onset of instability.

fast cavity mode now develops an unbounded growth rate, and assumes a surface mode structure. Indeed, it would appear that for any non-zero flow, there will always be one mode whose growth rate increases without bound as $k \to \infty$ and is predominantly a surface mode. However, these modes have large spatial decay in the magnetosphere and so are unlikely to be observed within the magnetospheric cavity far from the magnetopause.

Figure 3.21 shows the development of the magnetosheath and magnetosphere wavenumbers against k for the fundamental cavity mode. While the mode is stable it is purely oscillatory in the sphere and purely evanescent in the sheath. The wavenumber in the magnetosphere increases from zero for both fundamental modes. When $v_{ph} = v_o \sin\alpha$ for the upper mode, the right hand side of the dispersion relation (Equation

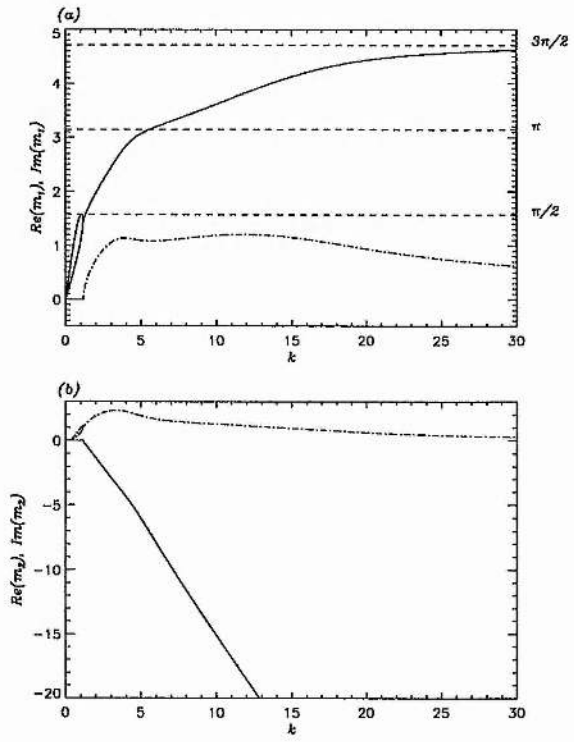

Figure 3.21: The x-direction wavenumbers in (a) the magnetosphere and (b) the magnetosheath as functions of k for the fundamental modes in Figure 3.20 with $v_o = 6.0$ and $\alpha = \pi/4$. Once again, the real parts are represented by solid lines and the imaginary parts by dot-dashed lines.

(3.11)),

$$\begin{aligned}\tan(m_1) &= \frac{n_2\left(\omega^2 - k^2 v_{a1}^2\cos^2\alpha\right)}{m_1\left(\omega - kv_o\sin\alpha\right)^2} \\ &= \frac{n_2\left(\omega^2 - k^2 v_{a1}^2\cos^2\alpha\right)}{\left(\omega - kv_o\sin\alpha\right)^2}\sqrt{\frac{\left(c_f^2 + c_{slow}^2\right)\left(\omega^2 - k^2c_T^2\right)}{\left(\omega^2 - k^2c_f^2\right)\left(\omega^2 - k^2c_{slow}^2\right)}},\end{aligned} \tag{3.26}$$

tends to ∞, and hence $m_1 \to \pi/2$. Once the modes are unstable, the mode in the magnetosphere remains dominantly oscillatory and, in this case, $m_1 \to 3\pi/2$ as $k \to \infty$. For low flow speeds (below the threshold at which the surface mode becomes globally oscillatory) the fundamental mode would have $m_1 \to \pi/2$ as $k \to \infty$. However, once the mode has been through the transition to a dominantly evanescent wave and then back to a globally oscillatory mode, the wavenumber in the magnetosphere increases by π for large k. The mode now also has an oscillatory component in the magnetosheath, and as $k \to \infty$, Im $(m_2) \to 0$,

while the real part of the wave number increases linearly with k.

The development of a fast body mode as a function of v_o is shown in Figure 3.22. The mode is leaky for small v_o with phase speed greater than that in the region where stable modes are possible. The mode remains leaky as the flow increases, even for some part of the potentially stable region. However, further into the region the mode becomes a stable fast cavity mode. Further increasing the flow, the mode becomes unstable. We again see that the mode is also unstable for some values of v_o within the range of potentially stable phase speed, and we will develop a method for predicting the onset of the instability in the next section. (The discontinuity in Im (m_2) is because of a branch cut in m_2 in the complex plane.) The ability of the magnetospheric cavity to excite, or even to trap waves is strongly dependent on the flow speed in the magnetosheath.

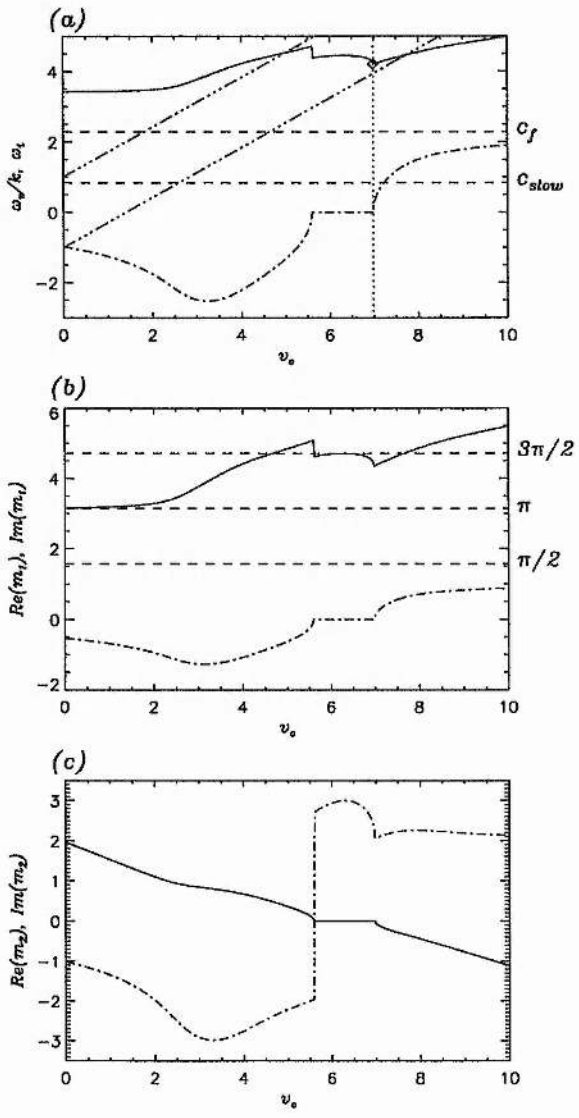

Figure 3.22: (a) The phase speed (solid line) and growth rate (dot-dashed line) as functions of v_o for the upper fundamental fast cavity mode with $k = 3$ and $\alpha = \pi/4$. The diamond represents the predicted point of the onset of the instability, and the dotted line shows the v_o value at this point. The triple-dot-dashed lines show the positions of the upper and lower cut-offs of the region where stable modes may exist. The upper and lower dashed lines indicate the fast speed, c_f, and the slow speed c_{slow}, respectively. (b) The real (solid line) and imaginary (dot-dashed line) parts of the magnetosphere wavenumber of the mode, and (c) the real (solid line) and imaginary (dot-dashed line) parts of the magnetosheath wavenumber.

3.5 Prediction of the Onset Of Instability

We have found that the onset of instability for slow cavity modes in our model is predicted exactly by the extremes of the region of phase speed for which stable modes may exist. However this is not true for either the fast cavity or surface modes, and we now show how we may predict the exact position of onset of instability for these modes.

3.5.1 Fast Cavity Modes

As we have seen from our results, the onset of instability for each fast mode occurs within the region of phase speed for which stable modes may exist. In order to examine the solutions more closely we have rewritten the dispersion relation for trapped cavity modes (having $\omega_i = 0$) as $D_R = 0$, where

$$D_R = \tan\left(A\left(v_{ph}\right)k\right) - F\left(v_{ph}\right), \tag{3.27}$$

where

$$F\left(v_{ph}\right) = \epsilon \frac{S\left(v_{ph}\right)\left(v_{ph}^2 - v_{a1}^2\cos^2\alpha\right)}{A\left(v_{ph}\right)\left(v_{ph} - v_o\sin\alpha\right)^2}, \tag{3.28}$$

$$S^2\left(v_{ph}\right) = -\frac{m_2^2}{k^2} = \frac{c_{s2}^2 - \left(v_{ph} - v_o\sin\alpha\right)^2}{c_{s2}^2}, \tag{3.29}$$

and A is as defined in Equation (3.22). As explained in Section 2.4, the fast cavity modes only become unstable as $k \to \infty$ when

$$c_f < v_o\sin\alpha - c_{s2}, \tag{3.30}$$

and, within the stable range given by Equation (2.66), both A and S are real. S is chosen to be positive to ensure spatial decay in the magnetosheath, and the sign of A is arbitrary, so we assume it to be positive (if we took A negative, the dispersion relation we are solving would simply become $-D_R = 0$).

Examining F within the region of phase speed for which stable modes may exist (Equation (2.66)) and where Equation (3.30) is satisfied, we see that it is singular at $v_{ph} = v_o\sin\alpha$, and that $F \to 0$ as $v_{ph} \to v_o\sin\alpha \pm c_{s2}$ (i.e. where $S = 0$). Although $F = 0$ when $v_{ph} = v_{a1}\cos\alpha$, this does not occur within the range of phase speed we are considering as $v_{a1}\cos\alpha \leq c_f$ for all α. Figure 3.23 shows the form of F within this region when $v_o = 5$ and $\alpha = \pi/4$. The function is shown both on a large and small scale to emphasize the behaviour at the middle and end points of the region respectively. In both plots the dotted lines represent the end points of the region where stable modes may occur, and the dot-dashed line

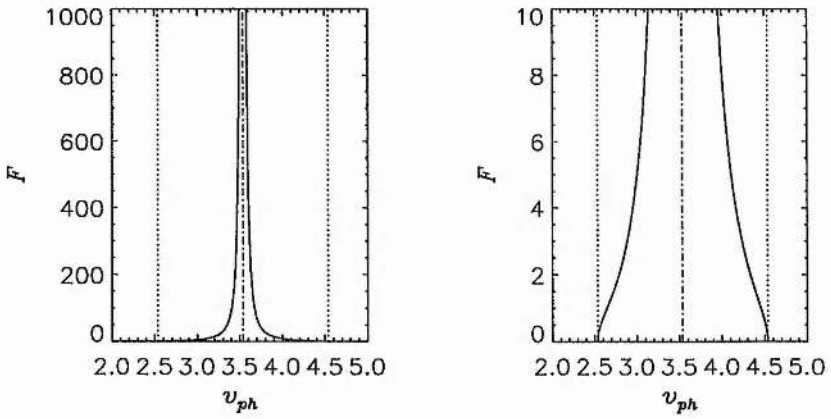

Figure 3.23: The form of F within the region of phase speed in which stable fast body modes may exist when $v_o = 5$ and $\alpha = \pi/4$.

represents the middle of the region where F is singular. Figure 3.24 shows F as a function of v_{ph} with the function $\tan(Ak)$ over-plotted as a dashed line for various values of k. We see that for low k, the dashed line is almost straight, but as k increases the period of the tan function decreases, and the number of crossing points of the two functions (corresponding to values of v_{ph} where $D_R = 0$) increases. From this we can see that there will be more stable roots of the dispersion relation as k increases, a fact which was borne out by our numerical solutions of the dispersion relation, see Figure 3.20.

Taking $v_{ph} = \psi_1 = v_o \sin\alpha - c_{s2}$ (so that $F = 0$) and a given low value of k, we know that

$$\tan(A(\psi_1)k) > 0, \tag{3.31}$$

and therefore $D_R(\psi_1) > 0$. Now we set the first value of the phase speed (above the lower cut-off for the existence of stable modes $v_{ph} = v_o \sin\alpha - c_{s2}$) at which $\tan(Ak) \to \infty$ to be phase speed $v_{ph} = \psi_2$. In the first instance we will assume that $\psi_2 < v_o \sin\alpha$. At this point, we know that $D_R(\psi_2) > 0$. The function D_R is continuous in the range (ψ_1, ψ_2) and so there are three possibilities for the solutions of the dispersion relation within this range:

(i) two real, distinct solutions of Equation (2.35),

(ii) no real solutions of the dispersion relation (there will be two complex conjugate solutions, of which we will pick the one which satisfies Equation (2.33)), or

(iii) one real, 'double' root of the equation (i.e., a root that touches but does not cross the $D_R = 0$ line).

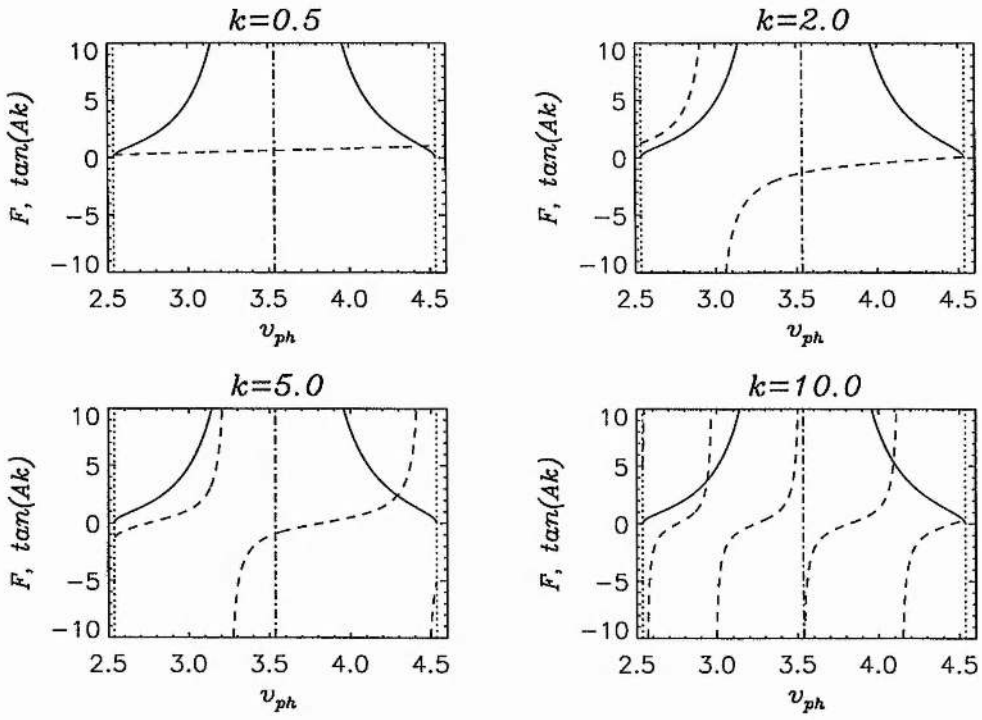

Figure 3.24: The form of F within the region of phase speed in which stable fast body modes may exist when $v_o = 5$ and $\alpha = \pi/4$ with the function $\tan(Ak)$ plotted as dashed lines for various values of k.

This must then be a turning point of the dispersion relation with respect to v_{ph} and at this point

$$D_R = 0 \quad \text{and} \quad \frac{\partial D_R}{\partial v_{ph}} = 0. \tag{3.32}$$

In fact, although F is not strictly continuous at $v_{ph} = v_o \sin\alpha$, the above analysis holds even if we relax the assumption that $\psi_2 < v_o \sin\alpha$ since F is always positive. Now, since we know from our numerical results (see Figure 3.20) that there are two real roots of the dispersion relation for low k, and at larger k these roots have become a single complex root (chosen from the two possible complex roots by our outgoing condition in the magnetosheath), it follows that the transition must occur at a 'double' real root. Thus, by solving the simultaneous equations given in Equation (3.32) for the variables k and v_{ph}, we can numerically predict the onset of instability for these two fundamental modes. As k increases, new branches of the tan function encounter the curve of F for values of v_{ph} at the lower end of this range. Thus successively higher harmonic modes have double roots at which they go unstable. However, this will not be the case for all higher k. The lower branch of each harmonic first appears at a value of k such that $\tan(Ak) = 0$ when

$v_{ph} = v_o \sin\alpha - c_{s2}$. However, if at that value of k

$$\frac{d}{dv_{ph}}\left(\tan\left(Ak\right)\right) > \frac{dF}{dv_{ph}}, \tag{3.33}$$

the tan function will only encounter the curve of F at that one point and so there will be no double root. Differentiating the left hand side of Equation (3.33), we obtain

$$\frac{d}{dv_{ph}}\left(\tan\left(Ak\right)\right) = \frac{dA}{dv_{ph}} k \sec^2\left(Ak\right), \tag{3.34}$$

and, since $\tan\left(Ak\right) = 0$ implies that $Ak = n\pi$, and A and F are independent of k, we can use this to simplify Equation (3.23) so that our upper limit on the value of k at which a double root can occur is

$$k > \frac{dF}{dv_{ph}} / \frac{dA}{dv_{ph}} \tag{3.35}$$

evaluated at $v_{ph} = v_o \sin\alpha - c_{s2}$. Once k is above this limit the fast cavity modes will become unstable at exactly $v_{ph} = v_o \sin\alpha - c_{s2}$, and the lower branch of each harmonic will not be apparent.

Figure 3.20 includes the points (marked by diamonds) that we have predicted for the onset of instability using a 2-D Newton method to solve the two equations. Here we have used a 2nd order Taylor series approximation to find the value of the derivative, but the code still converges quickly to the double root.

Similarly, if we fix k, we can solve the simultaneous Equations (3.32) for v_{ph} and v_o (or α) to predict the onset of the instability in terms of those variables. We show the predicted onset of instability in Figure 3.22 by a diamond and the dotted line marks the v_o value of this point. The predicted v_o value agrees exactly with the value at which the instability occurs for our numerical results.

3.5.2 Surface Modes

The dispersion relation for stable surface modes (Equation (3.2)) may be written as

$$D_S = N_1 \left(v_{ph} - v_o \sin\alpha\right)^2 \tanh\left(N_1 k\right) + \epsilon N_2 \left(v_{ph}^2 - v_{a1}^2 \cos^2\alpha\right) = 0, \tag{3.36}$$

where $N_1^2 = -m_1^2/k^2$ and $N_2^2 = -m_2^2/k^2$. By analysing the two terms of the equation in a similar way to that used for the dispersion relation for fast cavity modes we may again show that the onset of instability may be predicted by simultaneously solving the equations

$$D_S = 0, \quad \text{and} \quad \frac{\partial D_S}{\partial v_{ph}} = 0 \tag{3.37}$$

for v_{ph} and either of v_o and α. Figure 3.3 includes the point, shown by a diamond, at which instability is predicted by this method shown by a diamond. The vertical dotted line shows the predicted value of α and

is in excellent agreement with the onset of instability given by our numerical solution. Similarly, Figure 3.6 includes the point (shown by a diamond) at which instability is predicted by this method when $k = 2$. The vertical three dot-dash line shows the predicted value of v_o and is in excellent agreement with the onset of instability given by our numerical solution. In Figure 3.10 we have plotted the points that satisfy Equations (3.37) as diamonds. The points predict excellently the points where the stable surface modes coalesce and become unstable, as well as the point where the unstable mode becomes stable and splits into two modes.

In Section 3.1 we saw that the onset on instability of the fast surface modes is almost independent of k (see Figure 3.6). Examining Equation (3.36) we can see that the only explicit dependence on k when the dispersion relation is written in terms of the phase speed is within the function $\coth(N_1 k)$. This function only varies significantly when $N_1 k$ is small and is close to unity for $N_1 k \gtrsim 1$. Thus the double roots of the dispersion relation will vary little as k varies.

3.5.3 The Onset of Instability and the Energy of the Waves

Referring back to our definition of the wave energy of the stable modes (Equations (2.36) and (2.45)), we can show that, for given values of k, v_o and α, C can be rewritten as

$$C = v_{ph} \frac{dD_R}{dv_{ph}}. \tag{3.38}$$

Figure 3.25 shows the coalescence of the fundamental fast cavity modes in the top diagram (panel (a)), again with the predicted onset of instability shown by a diamond. The lower diagrams (panels (b) and (c)) show the value of C for the two modes while they are both stable. We can see that the upper mode has positive energy, whilst the lower mode has negative energy. As k increases towards the value at which instability occurs (represented here by a vertical dotted line), the magnitude of the energy of both modes tends towards zero. Thus this instability occurs when a positive and negative energy wave coalesce, and the mathematical analysis above identifies the point at which $C = 0$ and the two waves with energies of opposite sign meet.

In Figure 3.10 the slow surface mode that had negative phase speed when $v_o = 0$ becomes a negative energy wave when the phase speed becomes positive and so the onset of instability of the slow surface mode also corresponds to the coalescence of a negative energy wave with a positive energy wave.

Southwood (1968) showed that the points of marginal stability for the shear flow discontinuity of an unbounded magnetosphere (with both magnetic field and plasma pressure on both sides of the boundary) are given where both

$$R_1(x_1) = -R_2(x_2) \tag{3.39}$$

and

$$\xi_1 \frac{dR_1}{dx_1} = \xi_2 \frac{dR_2}{dx_2} \tag{3.40}$$

are satisfied. Here x_1 and x_2 are the phase speeds in the rest frames of the two fluids (each normalised to the Alfvén speed of that fluid) and R_1 and R_2 are the dispersion relations for each side of the boundary. ξ_1 is defined such that

$$\xi_j = \frac{\omega_i}{k v_{aj}}, \tag{3.41}$$

where $j = 1, 2$. We can show, by replacing Southwood's normalisations with ours, that these conditions are equivalent to our conditions for the onset of instability, given in Equation (3.32).

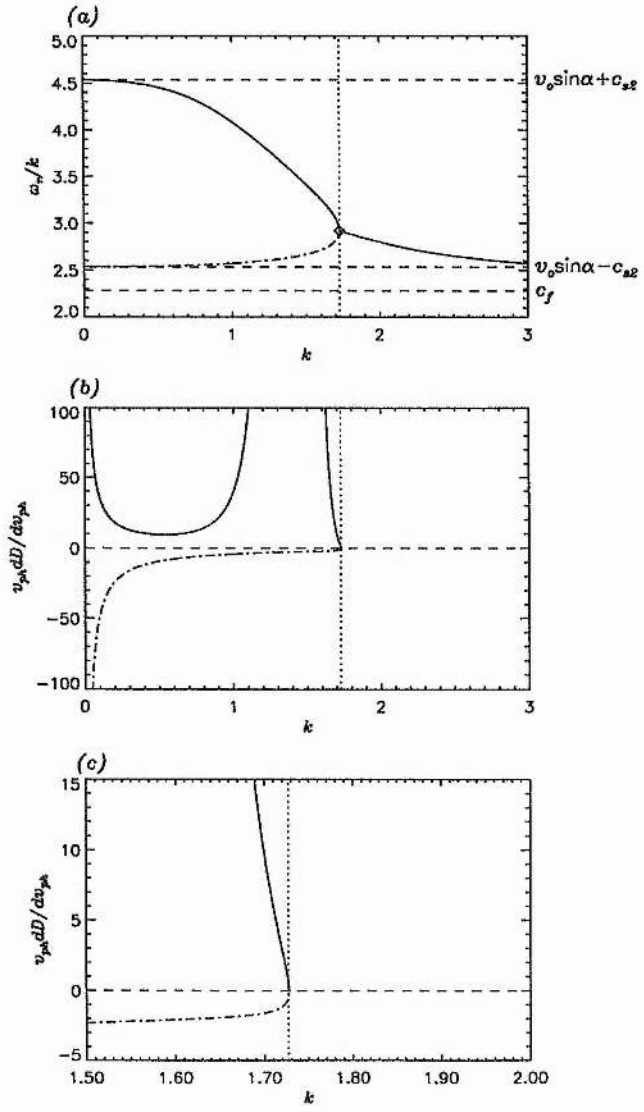

Figure 3.25: (a) The dispersion diagram showing the upper (solid line) and lower (dot-dashed line) fundamental fast cavity modes when $v_o = 5.0$ and $\alpha = \pi/2$. The diamond shows the predicted point of coalescence and onset of instability and the dotted line shows the k value of this point. (b) A plot showing C (which is proportional to the energy of the wave) as a function of k for the stable part of the two modes, and (c) an enlargement of the area around the point of coalescence. The dotted line shows the predicted k value of the coalescence.

3.6 Over-Reflection and the Maxima in the Growth Rate

As we saw in Section 2.3.2, we may use the concept of the reflection coefficient for purely oscillatory modes to predict an angle and phase speed at which spontaneous radiation (or resonance) of modes from an interface may occur for the unbounded case. In this section we compare these results to the maxima of the growth rate in our bounded case.

We saw in section 3.4 that the fast cavity modes have a maximum in growth rate for finite k and that their behaviour remains predominantly oscillatory within the magnetosphere, and becomes predominantly oscillatory in the magnetosheath for large k (note that the fast surface modes that had a bounded growth rate when unstable took on a dominantly oscillatory nature in the magnetosphere, while those cavity modes whose growth rate became unbounded were dominantly evanescent in the magnetosphere). Thus we may take the expression for the reflection coefficient (Equation (2.46), see McKenzie, 1970a) as an approximation to our system, and to find the resonant angle where $|R| \to \infty$ we must solve

$$Z = \pm \frac{\cos\theta_1 \left(U - v_o \sin\theta_1 \sin\alpha\right)^2}{\epsilon\lambda \left(U^2 - v_{a1}^2 \sin^2\theta_1 \cos^2\alpha\right)} = -1, \tag{3.42}$$

where, in the case of fast body modes we choose $U = c_f$. The sign of Z is chosen as the sign of λ ($\lambda^2 = m_2^2/k_1^2$ so that the group velocity in the magnetosheath is positive. Thus, for $v_{ph} > v_o \sin\alpha$, $\lambda > 0$, and we choose $Z > 0$, and $|R| < 1$. Our numerical results showed that for phase speeds above the range in which stable modes may occur, $v_{ph} > v_o \sin\alpha + c_{s2}$, the modes have negative growth rate. Thus we find that for leaky modes, the reflection coefficient is less than unity, and that transmission (or leaking) of modes through the magnetopause boundary occurs. Conversely, when $v_{ph} < v_o \sin\alpha$, $\lambda < 0$ and here $Z < 0$, so over-reflection occurs. We found that modes with phase speeds in this range may have a positive growth rate, so unstable modes correspond to modes which are over-reflected by the magnetopause boundary.

Using a Newton-Raphson algorithm, we have solved Equation (3.42) to find the resonant angle, θ_1, at which we may expect to find the maximum growth rate of our modes, and then used the relation

$$v_{ph} = \frac{U}{\sin\theta_1} \tag{3.43}$$

to predict the phase speed at which this occurs.

Figure 3.26 shows the predicted value of θ_1 for spontaneous radiation of modes, with the diamonds showing the value of θ_1 calculated from the results from our model at the maxima of the growth rate for the third harmonic for various speeds (the values of $theta_1$ from our model are very similar for all harmonics and converge towards the predicted line for the higher harmonics). We can see that the agreement between the predicted value (solid line) and that found by our model is excellent. The dashed line is the lowest value

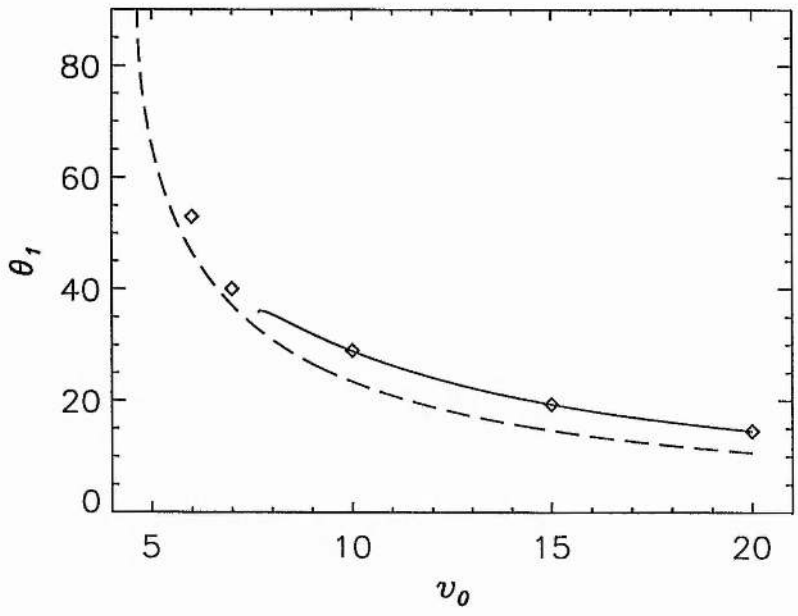

Figure 3.26: The angle θ_1 at which spontaneous radiation of modes is predicted by the equations of McKenzie (1970a) as a function of v_o (solid line). The value of θ_1 at which over-reflection may first occur is shown by the dotted line and we have shown the values of the angle at the maximum growth rate in our model with diamonds. Here we have taken $\alpha = \pi/4$.

of θ_1 at which we may have over-reflection (and is also the upper limit of θ_1 for which stable modes may exist) and is calculated by taking $\lambda = 0$. Thus the equation of this line is given by solving

$$U = v_o \sin\theta_1 \sin\alpha + c_{s2} \sin\theta_1, \tag{3.44}$$

(i.e., $v_{ph} = v_o \sin\alpha + c_{s2}$ where it should be remembered that U is also a function of θ_1. The solid line, showing the predicted values of θ_1, does not extend over the whole range of v_o. In fact the root no longer exists below $v_o \approx 7.5$. This value of v_o corresponds to the upper cut-off found by Sen (1964) and Pu and Kivelson (1983), which can be predicted using the same method as that for predicting the onset on instability given in Section 3.5, i.e., by solving the simultaneous equations

$$D_{MK} = 0 \quad \text{and} \quad \frac{\partial D_{MK}}{\partial v_{ph}} = 0, \tag{3.45}$$

where D_{MK} is the dispersion relation for oscillatory modes in the unbounded case, Equation (2.50). Thus, below this flow speed, the unbounded case is unable to support stable oscillatory modes on both sides of the interface and the solutions in this region must have complex ω. Thus, Z (as defined in Equation (2.47)) is complex, and there can be no value of θ_1 for which $|R| \to \infty$.

We can show that solving the simultaneous Equations (3.45) is equivalent to finding the point at which $|R| \to \infty$ and $\partial R/\partial\theta_1 = 0$. Firstly,

$$\frac{\partial R}{\partial \theta_1} = -\frac{2}{(1+Z)^2}\frac{\partial Z}{\partial \theta_1}, \tag{3.46}$$

so that the turning points in R must correspond to turning points in Z. Now, to simplify the algebra we may define $Z = A/B$ where $A = -\cos\theta_1 \left(U - v_o \sin\theta_1 \sin\alpha\right)^2$ and $B = \epsilon\lambda\left(U^2 - v_{a1}^2 \sin^2\theta_1 \cos^2\alpha\right)$.

Thus the dispersion relation is defined as $D_{MK} = A + B = 0$, and the two equations we must solve to find the upper cut-off speed become

$$A + B = 0 \quad \text{and} \quad \frac{\partial A}{\partial v_{ph}} + \frac{\partial B}{\partial v_{ph}} = 0, \tag{3.47}$$

the first of which is equivalent to solving $Z = -1$. Now,

$$\frac{\partial Z}{\partial \theta_1} = \frac{1}{B^2}\left(B\frac{\partial A}{\partial \theta_1} - A\frac{\partial B}{\partial \theta_1}\right), \tag{3.48}$$

and using the fact that $A = -B$ when $Z = -1$, we obtain

$$\frac{\partial Z}{\partial \theta_1} = \frac{1}{B}\left(\frac{\partial A}{\partial \theta_1} + \frac{\partial B}{\partial \theta_1}\right). \tag{3.49}$$

Using the chain rule for differentiation this becomes

$$\frac{\partial Z}{\partial \theta_1} = \frac{1}{B}\frac{\partial v_{ph}}{\partial \theta_1}\left(\frac{\partial A}{\partial v_{ph}} + \frac{\partial B}{\partial v_{ph}}\right), \tag{3.50}$$

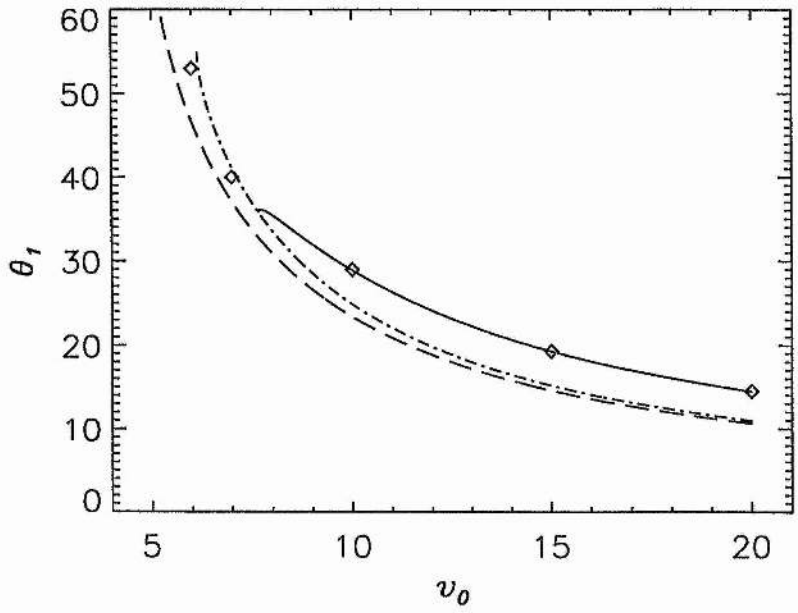

Figure 3.27: As Figure 3.26, with the triple dot-dashed line representing the maximum of the reflection coefficient for real ω in the unbounded case.

so that when Equations (3.45) are satisfied, $Z = -1$ and $\partial R/\partial\theta_1 = 0$ are also satisfied.

For values of v_o between the lower cut-off (which is shown as the point where the dashed line meets $\theta_1 = 90°$) and the upper cut-off as calculated above, there are no real roots of the dispersion relation (Equation (2.50)) and hence we cannot have resonance of the modes. In this region we calculate the position of the maximum of $|R|$, which is also a turning point in Z. Figure 3.27 shows the same diagram as Figure 3.26, however we have now over-plotted the line $\partial Z/\partial\theta_1 = 0$. We can see that this line is a reasonable prediction for the values of θ_1 at the points of maximum growth rate in our model for flow speeds below the upper cut-off for the unbounded case. Once again we find that this line does not extend across all our unstable range, however, from our results we find that there is a much less consistent value of the angle at which the highest growth rate occurs for low flow speeds.

Figure 3.28 shows the values of the phase speed at the maximum growth rate predicted by this method. Once again the agreement is excellent.

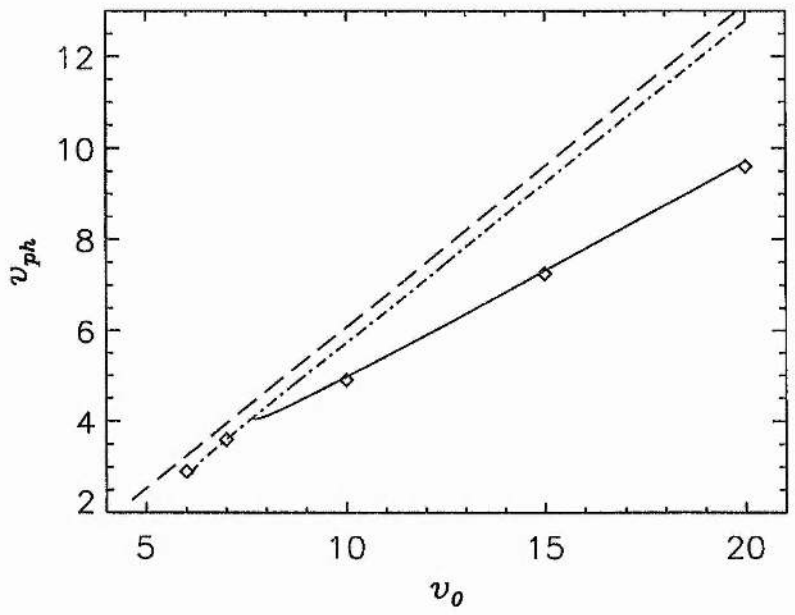

Figure 3.28: The values of the phase speed at which the maximum growth rate will occur predicted by the above methods. The solid line corresponds to $Z = -1$, the dashed line is the lower limit of v_{ph} for which stable modes may occur and the triple-dot-dashed line indicates where $\partial R/\partial\theta_1 = 0$. The diamonds again represent the values calculated for our numerical model.

3.7 Discussion and Conclusions

In comparison with waveguide mode models (e.g., Wright, 1994), which assume a perfectly reflecting magnetopause, we have looked at the trapping and excitation of cavity modes when the magnetopause is taken to be a free boundary. We have found that whether the magnetospheric cavity traps or excites modes is highly dependent upon the value of v_o (the speed of the flow in the magnetosheath). The flow around the magnetopause has a stagnation point at the nose of the magnetosphere and then accelerates approaching the speed of the upstream solar wind flow along the flanks (see Spreiter and Stahara, 1980). Our model has shown that for low flow speeds the cavity modes are leaky, for moderate flows they become trapped and for high flow speeds they become unstable and energy from the magnetosheath flow is fed into the magnetosphere increasing the amplitude of the body modes. More specifically, the trapping of fast cavity modes occurs for values of the flow speed such that $v_o \sin\alpha > c_f - c_{s2}$, while slow cavity modes are trapped when $v_o \sin\alpha > c_{slow} - c_{s2}$. Excitation of fast and slow cavity modes occurs when $v_o \sin\alpha > c_f + c_{s2}$ and $v_o \sin\alpha > c_T + c_{s2}$, respectively. The form of the flow around the magnetosphere is such that modes are most likely to be trapped or excited on the flanks and it is in this region that Pc5 oscillations are observed to be present almost continuously. On the flanks it has also been observed that there is a strong correlation between Pc5 wave power and the speed of the solar wind flow (and hence the speed of the flow along the flanks).

Although slow cavity modes may be trapped even in conditions of zero flow (e.g. when $\alpha = \pi/4$) and excited for small values of v_o, the growth rates of these modes are three orders of magnitude smaller than the growth rates of both the fast body and surface modes (when they display wavenumber selection). Also, the maximum growth rates of the slow cavity modes occur for values of v_o close to the onset of instability. Hence we can conclude that slow cavity modes are unlikely to be excited to a sufficient amplitude to be easily observed.

Since the trapping of fast cavity modes occurs for $v_o > (c_f - c_{s2}) / \sin\alpha$ and these modes are excited for $v_o > (c_f + c_{s2}) / \sin\alpha$ we can see that fast cavity modes will be most easily trapped or excited for values of α close to $\pi/2$ (i.e. those modes propagating parallel or close to parallel to the flow in the magnetosheath). Using some typical values for the various plasma parameters we obtain $v_{a1} \approx 400 - 500$km/s and $c_{s2} \approx 120$km/s (see Fujita et al., 1996 and also Mann et al., 1999). Consequently, we find that quasi-parallel propagating fast cavity modes will be trapped for solar wind speeds of $v_{sw} > 300 - 400$km/s, and excited when $v_{sw} > 500 - 600$km/s. This is in excellent agreement with Engebretson et al. (1998) who observed that Pc5 waves on the dawn flank have a much increased power index for $v_{sw} > 500$km/s. Fast

cavity modes propagating obliquely to the magnetosheath flow will need significantly higher flow speeds to be excited or even trapped. Thus, observable Pc5 waves on the magnetospheric flanks may be expected to propagate quasi-parallel to the flow in the magnetosheath.

On the dawn-side flank, observations show that Pc5 field line resonances (FLRs) are almost continuously present (Anderson et al., 1990). This agrees very well with our results. For normal values of the solar wind flow speed the magnetopause will act as a leaky boundary at the nose and, as the flow increases around the magnetosphere, the magnetopause on the flanks will be perfectly reflecting and trap the fast cavity modes. These fast cavity modes may then couple to and drive the FLRs (Kivelson and Southwood, 1986). For high solar wind flow speeds, the magnetopause will be perfectly reflecting nearer the nose of the magnetosphere, and on the flanks fast modes will be unstable taking energy from the magnetosheath flow and increasing their amplitude in the magnetosphere. This should lead to enhanced FLR driving.

Above the threshold speed for instability of fast cavity modes we have found negative energy waves. These solutions represent modes that propagate in the negative y-direction (i.e. sunward) when there is no flow. The onset of instability of the fast modes is found to occur when the dispersion curves of positive and negative energy waves meet and at this point the wave energy is zero.

The behaviour of the slow cavity modes is summarised in flow chart form in Figure 3.29. The slow cavity modes are first unstable for low k as that is where they have lower phase speed, whereas the phase speed of the fast cavity modes (the properties of which are summarised in Figure 3.30) decreases with increasing k and so these modes are first unstable for high k. The criteria for the onset of instability for fast cavity modes changes for high k (defined by Equation (3.35)) to occurring where $v_{ph} = v_o \sin\alpha - c_{s2}$. For any given value of α all the fast cavity modes will be unstable for higher values of k once $v_o \sin\alpha > c_f + c_{s2}$.

Fujita et al. (1996) found that the fast surface mode displays azimuthal wavenumber selection (a maximum value of ω_i for a finite value of k) for flow speeds above a threshold. We have shown that this is also true for the case of a uniform magnetosphere, and that both the fast and slow cavity modes also display wavenumber selection. This occurs at the frequency (and angle θ_1) at which spontaneous radiation of modes may occur for the unbounded case. This compares well to observations which show that FLRs tend to show a dominant wavenumber which increases with frequency. In comparing dawn-side FLRs Ziesolleck and McDiarmid (1994) showed that the FLR phase speed was independent of frequency and was the same for every frequency FLR observed simultaneously. Figure 3.20 shows the first three unstble fast cavity mode harmonics. Each mode of increasing frequency has a maximum in ω_i for increasing k and the maximum occurs at an approximately constant phase speed. The fast surface mode has no wavenumber selection for $v_o \sin\alpha \lessapprox 4$ and for normal solar wind conditions this mode will be closely confined to the magnetopause.

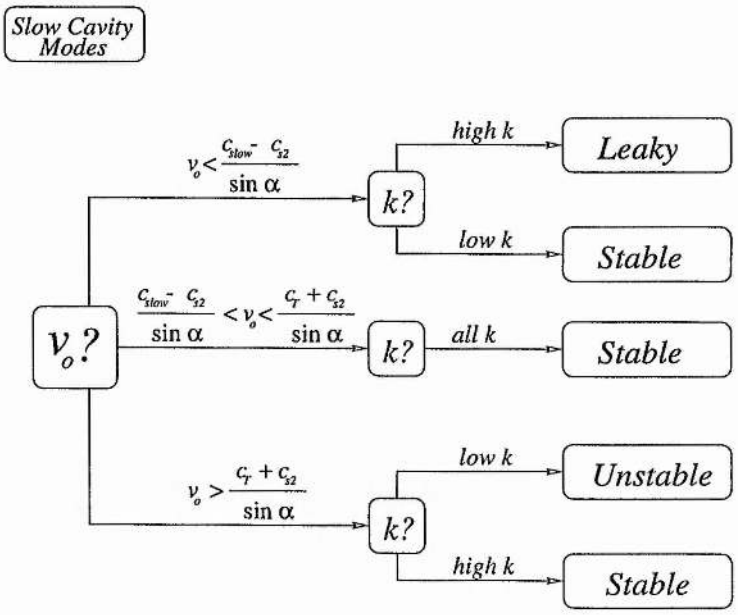

Criteria for onset of Instability: $v_o = \frac{v_{ph} + c_{s2}}{\sin\alpha}$

Criteria for change from Leaky to Stable: $v_o = \frac{v_{ph} - c_{s2}}{\sin\alpha}$

Maximum Growth Rate: $\omega_i \sim O(10^{-2})$

Figure 3.29: A summary of the properties of the slow cavity modes.

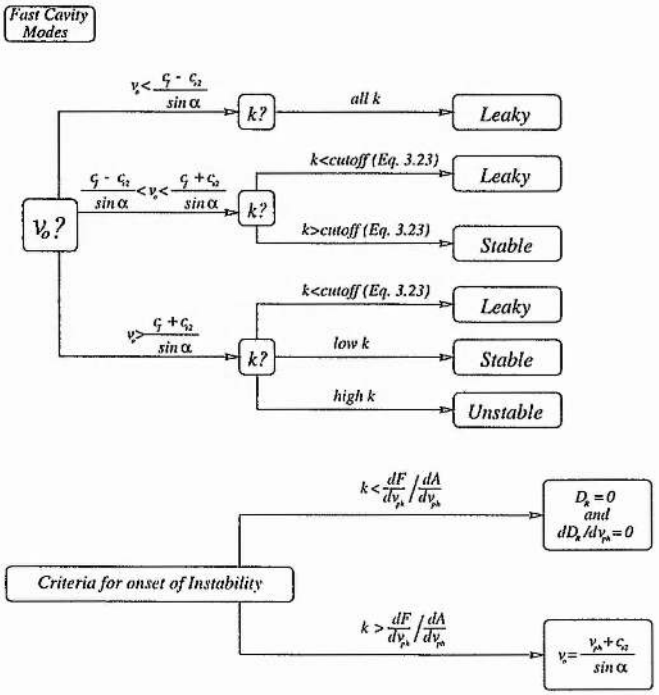

Figure 3.30: A summary of the properties of the fast cavity modes.

For $v_o \sin\alpha \gtrapprox 4$ the fast surface mode becomes a globally oscillatory mode and, as v_o increases, each successive fast mode harmonic takes on the properties of a dominantly evanescent wave with no wavenumber selection. Consequently, we find that the distinction between body and surface modes is not as clear in the compressible case as it is in the incompressible limit.

Table 3.1 shows the value of the phase speed and angle, θ_1 at which the maximum growth rate occurs for fast body modes when $v_o = 10$ and $\alpha = \pi/4$. The value of the phase speed for spontaneous radiation in McKenzie's (1970a) model is 4.967 and the value of the angle at which this occurs is 28.88^o. We can see that the value of the phase speed and angle at maximum growth rate is very similar for all the modes, becoming increasingly close to those for McKenzie's unbounded case for higher harmonics. This angle is the angle at which the modes will interfere constructively within the magnetospheric cavity and so create an amplification of the mode.

Harmonic	k	v_{ph}	θ_1 (^{o})
1st	1.60	4.55	31.53
2nd	3.21	4.83	29.71
3rd	4.89	4.90	29.28
4th	6.59	4.93	29.10
5th	8.30	4.94	29.02
6th	10.02	4.95	28.98
7th	11.75	4.95	28.95
8th	13.47	4.96	28.94
9th	15.20	4.96	28.93

Table 3.1: The values of the wavenumber, k, phase speed, v_{ph} and angle, θ_1, at which the fast body mode harmonics have the maximum growth rate when $v_o = 10$ and $\alpha = \pi/4$.

Fast and slow surface modes also exist in the magnetosphere. The behaviour of the slow surface modes is summarised in Figure 3.31. The slow surface modes become unstable for relatively low flow speeds, however, they restabilise and become fast surface modes for higher flow speeds. The upper of these surface modes coalesces with the original fast surface mode and becomes unstable. The growth rate of these modes is unbounded as k increases. The onset of instability of the fast surface modes occurs for decreasing v_o as α increases and is almost independent of k; when stable these are fast surface modes decaying away from both sides of the magnetospheric boundary. For low flow speeds the unstable modes are predominantly

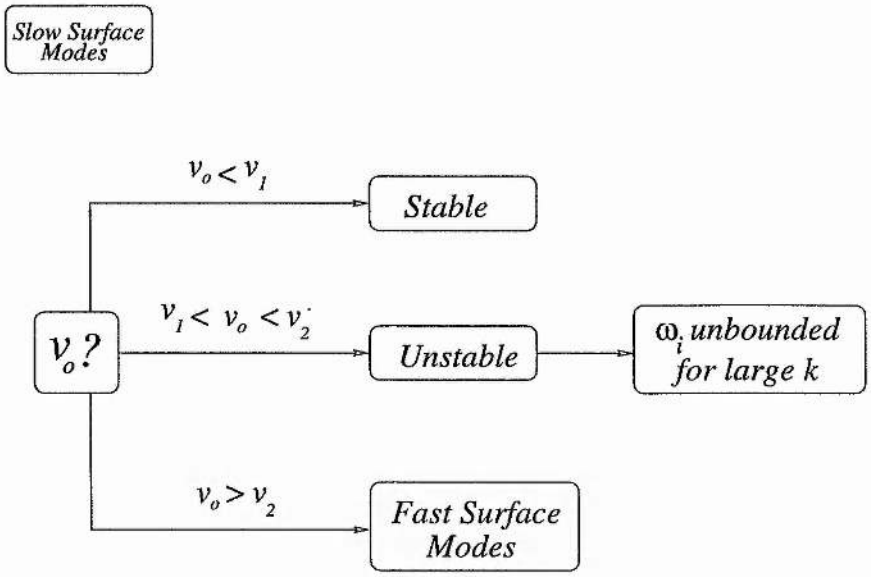

$$v_1 \approx \frac{c_T + v_{pho}}{\sin\alpha} \quad , \quad v_2 \approx \frac{c_{slow} + v_{pho}}{\sin\alpha}$$

v_1 , v_2 *given exactly by* $D_S = 0$ *and* $\frac{dD_S}{dv_{ph}} = 0$

Onset Instability independent of k.

Figure 3.31: A summary of the properties of the slow surface modes.

evanescent in the magnetosphere, but for speeds above $v_o \sin\alpha \gtrapprox c_f + c_{s2}$ the modes become globally oscillatory in the magnetosphere and display wavenumber selection. The behaviour of the fast surface modes is summarised in Figure 3.32.

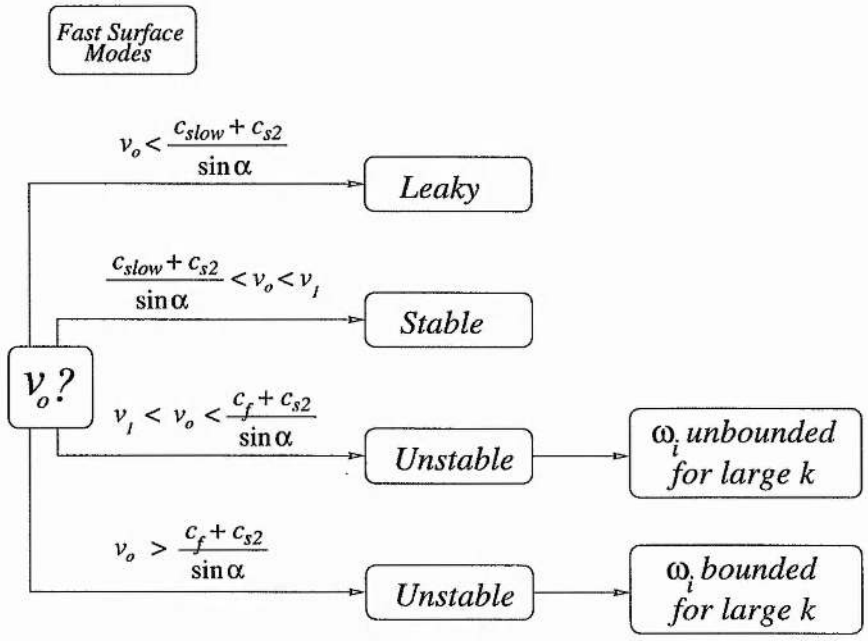

Figure 3.32: A summary of the properties of the fast surface modes.

Most of the discrete Pc5 frequencies observed have been obtained using a one-dimensional WKB box model by Samson et al. (1991, 1992). However, they were unable to find the lowest observed frequency (0.8mHz). Our model generates quarter wavelength modes within the magnetosphere (a reflecting magnetopause with $u_x\,(x = 1) = 0$ generates waves with half a wavelength or more in the cavity) and this may help explain the existence of the very low frequency.

Chapter 4

Azimuthal Phase Speeds of FLRs Driven by Kelvin-Helmholtz Unstable Waveguide Modes

4.1 Introduction

Ultra-low frequency (ULF) waves are observed almost continuously on the flanks of the magnetosphere (e.g., Engebretson et al., 1998). It was first suggested by Dungey (1955) that these pulsations were standing toroidal Alfvén modes on the dipolar field lines of the Earth. Southwood (1974) suggested that surface modes driven by the Kelvin-Helmholtz instability at the magnetopause could couple to the Alfvén waves, feeding energy into these field line resonances (FLRs). However, the magnetosheath velocities required to drive the FLRs by this mechanism were found to be much higher than those observed (Hughes, 1994) and the frequencies of the FLRs driven in this way do not explain the low frequencies observed (Walker et al., 1992).

Kivelson and Southwood (1985) showed that in a non-uniform magnetosphere, a turning point exists within the magnetosphere beyond which the cavity modes are evanescent. The Alfvén resonance is then thought to be driven by this evanescent tail. The frequencies of these cavity mode oscillations have been predicted through various models (for example Kivelson and Southwood, 1986) using the eigenfrequencies of the magnetospheric cavity to predict the frequencies of the FLRs. Wright (1994) and Rickard and

Wright (1994, 1995) showed how the waveguide cut-off frequencies (found by using an infinitely long magnetosphere, rather than a finite one) could also match FLR frequencies. However, recent observations by Ziesolleck and McDiarmid (1994) showed that FLRs observed simultaneously at different lattitudes on the flanks of the magnetosphere can, at times, have the same azimuthal speed and it is this phenomenon that we aim to explain. Wright and Rickard (1995) have already noted that such observations are consistent with resonances driven by a running pulse on the magnetopause rather than by a stationary pulse. In this chapter we identify a new mechanism associated with Kelvin-Helmholtz excited waveguide modes. We show that the azimuthal phase speeds of the waveguide mode and the FLR it can excite are the same.

We employ the theory of over-reflection of waves (McKenzie, 1970a). McKenzie modelled an infinite, uniform magnetosphere and showed that for certain parameters a wave incident on the magnetopause from the magnetosphere will be amplified when reflected. Indeed, for certain phase speeds the transmission and reflection coefficients become infinite. This solution is better described in terms of the spontaneous radiation of modes from the magnetopause into the magnetosphere and magnetosheath. Mann et al. (1999) modelled a bounded uniform magnetosphere, showed that oscillatory modes may also become unstable for realistic flow speeds, and analysed the reflection coefficient of these unstable modes. They showed that the maximum growth rate for each mode corresponded to a peak in the reflection coefficient. Mann et al. (1999) considered a uniform magnetosphere with perturbations only in the direction perpendicular to the magnetospheric magnetic field and so found no Alfvén resonances. In Chapter 3 we considered a model similar to that of Mann et al., however, we included a non-zero plasma beta and propagation of disturbances in all directions in the magnetopause plane. Once again, the uniform nature of the magnetosphere in that model prevented any Alfvén resonances. Walker (1998) gives a review of the theory of the excitation of the magnetospheric cavity, including a discussion showing that waves incident on the magnetopause from the magnetosheath may only be transmitted efficiently when their frequency matches that of one of the normal modes of the cavity.

We extend the models of Mann et al. (1999) and that in Chapter 3 by using a generalised waveguide version of the box model of Southwood (1974). It has a bounded non-uniform magnetosphere, with a free magnetopause boundary (i.e., the boundary may be disturbed and we do not require the total reflection of modes back into the magnetosphere), and is similar to that studied by Fujita et al. (1996). We find the fastest growing normal modes of this system subject to suitable boundary conditions. These modes may be interpreted as a negative energy wave in the magnetosheath which feeds energy into a magnetospheric cavity waveguide mode, which can in turn couple energy into Alfvén resonances within the magnetosphere. We show that the phase speed at maximum growth rate of the different harmonics is the same, and show

that this can be explained by the theory of over-reflection developed by McKenzie (1970a) (see also Miles, 1957; and Ribner, 1957) and used in Mann et al. (1999). We compare the phase speeds of the fastest growing Alfvén resonances (Field Line Resonances or FLRs) with those predicted by the over-reflection theory.

The structure of this chapter is as follows: Section 4.2 outlines our model and the governing equations and Section 4.3 describes our numerical results. Section 4.4 compares the numerical results to those obtained by the over-reflection theory, and finally, Section 4.5 summarises our results.

4.2 Model And Equations

In this chapter the flank equilibrium is modelled as a bounded non-uniform magnetosphere adjoining a field-free, semi-infinite magnetosheath flowing with a constant velocity. The magnetosheath is taken to be infinitely thin. This model is essentially that studied by Fujita et al. (1996). Figure 4.1 shows a schematic view of our model. Throughout this chapter we use variables normalised to the equilibrium sound speed, c_{s2}, and density, ρ_{o2}, in the magnetosheath and the width of the magnetospheric cavity, d. (Time is normalised by the quantity d/c_{s2}, pressure by ΓP_2 and magnetic fields by $\sqrt{\Gamma P_2 \mu_o}$, where Γ is the ratio of specific heats.) Thus, the magnetopause is placed at $x = 1$. The field lines are taken to be finite in extent, which we have modelled by placing perfectly reflecting boundaries at $z = \pm 1$. The perfectly reflecting boundaries in z in the magnetosphere represent the fact that the field lines in this region have a finite length and are terminated in the ionosphere, which is an efficient reflector of Alfvén waves. The finite extent of the field lines in the magnetosphere will mean that the wavenumbers in the z-direction will be quantised. The fact that the wavenumbers tangential to the magnetopause must be the same in both media will mean that the wavenumbers in z-direction in the magnetosheath will also be quantised.

In order to study only the fast modes and their coupling to the Alfvén waves, we have assumed that $\beta = 0$ in the magnetosphere so that there is no plasma pressure. Thus, in order to vary the Alfvén speed, v_a, across the cavity we must vary the equilibrium density, ρ_{o1}. We have chosen a quadratic profile for the Alfvén speed, and the coefficients are fixed by choosing the ratio between the Alfvén speeds at the inner boundary and the magnetopause ($v_R = v_a(x = 0)/v_a(x = 1)$), and by taking the gradient of the profile to be zero at the magnetopause (so that close to the boundary the profile may be reasonable approximated as constant). Therefore, our Alfvén speed profile is

$$v_a(x) = v_a(1)\left\{(v_R - 1)x^2 - 2(v_R - 1)x + v_R\right\}. \tag{4.1}$$

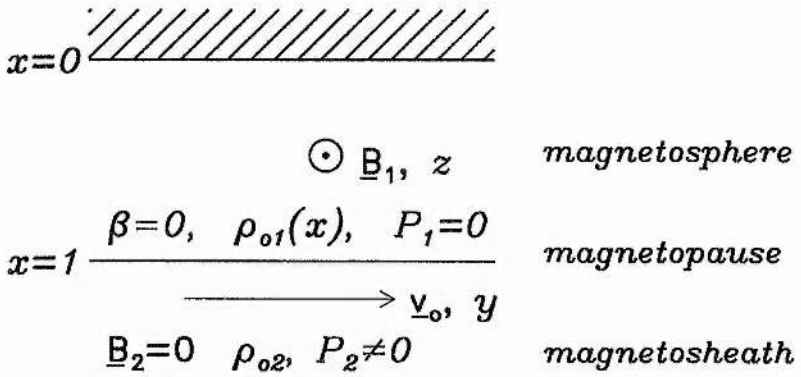

Figure 4.1: A schematic representation of our bounded non-uniform magnetosphere model.

We find the value of $v_a(1)$ using total pressure balance at the magnetopause and the ratio of densities either side of the boundary so that

$$v_a^2(1) = \frac{2}{\Gamma}\frac{\rho_{o2}}{\rho_{o1}(1)}c_{s2}^2. \tag{4.2}$$

In the magnetosheath, the linearised ideal MHD equations may be combined to give a second order ODE for the pressure perturbation,

$$\frac{d^2p_2}{dx^2} + m_2^2 p_2 = 0. \tag{4.3}$$

Here m_2 is the x-component of the wavenumber in the magnetosheath given by

$$m_2^2 = \frac{\omega'^2 - k^2c_{s2}^2}{c_{s2}^2}. \tag{4.4}$$

k is the total wavenumber tangential to the magnetopause given by $k = \sqrt{k_y^2 + k_z^2}$ where k_y and k_z are the wavenumbers in the y- and z-directions respectively, and ω' is defined to be the Doppler shifted frequency of the oscillations in the rest frame of the magnetosheath and is related to ω by

$$\omega' = \omega - k_y v_o. \tag{4.5}$$

In this chapter we will generally fix the value of k_z and then consider the dispersion of the modes with respect to k_y. However, if we define, $\alpha = \tan^{-1}(k_z/k_y)$, then the definition of ω' becomes $\omega' = \omega - kv_o \sin\alpha$ in agreement with Equation (2.21) (with $\chi = \pi/2$ as we are on the flanks). Using the outgoing boundary condition to choose the sign of the root of m_2, we can find a solution in the magnetosheath to within a

complex constant. The outgoing boundary condition is taken to be that the group velocity of the waves in the magnetosheath is positive in the rest frame of the flowing plasma, which can be shown to be equivalent to requiring that

$$\mathrm{Re}\left(\omega'\right)\mathrm{Re}\left(m_2\right)+\mathrm{Im}\left(\omega'\right)\mathrm{Im}\left(m_2\right)>0, \tag{4.6}$$

(see Mann et al., 1999 and Chapter 3). The boundary condition, Equation (4.6), cannot be applied to real frequency modes as these are trapped in the magnetosphere and decay in the magnetosheath (i.e., they have no propagating character or group velocity in the magnetosheath). Such modes require m_2 to be imaginary, and so can only occur when $\omega'^2 < k^2 c_{s2}^2$. The boundary condition we impose on these modes is that the perturbation vanishes at large x, i.e.,

$$\mathrm{Im}\left(m_2\right)>0. \tag{4.7}$$

In the magnetosphere, we have combined the linearised ideal MHD equations to obtain two first order differential equations for the perturbed total pressure p_T (which, since $\beta = 0$ is the magnetic pressure in the magnetosphere) and the x-component of the perturbed velocity, u_x. The two ODEs are

$$\frac{dp_T}{dx}=i\rho_{o1}\left(x\right)\left(\omega^2-k_z^2v_{a1}^2\left(x\right)\right)\frac{u_{x1}}{\omega}, \tag{4.8}$$

and

$$\frac{du_{x1}}{dx}=\frac{i\omega m_1^2\left(x\right)}{\rho_{o1}\left(x\right)\left(\omega^2-k_z^2v_{a1}^2\left(x\right)\right)}p_T, \tag{4.9}$$

where m_1 is given by

$$m_1^2\left(x\right)=\frac{\omega^2-k^2v_a^2\left(x\right)}{v_a^2\left(x\right)}, \tag{4.10}$$

and may be interpreted as the magnetosphere fast mode wavenumber in the x-direction. The derivation of these equations is given in Appendix A. Allowing for a complex frequency, we actually have four equations for the real and imaginary parts of the velocity and pressure.

The inner boundary of the magnetosphere ($x = 0$) is assumed to be perfectly reflecting, and thus we take

$$u_x\left(x=0\right)=0, \tag{4.11}$$

which is equivalent to requiring that

$$\frac{dp_T}{dx}\left(x=0\right)=0. \tag{4.12}$$

Starting from this point, we integrate the four ODEs using a fourth order Runge-Kutta method and match the solutions to those in the magnetosheath through the boundary conditions at the magnetopause, which are taken to be continuity of total pressure and displacement in the x-direction, ξ_x

$$p_T\left(x=1\right)=p_2\left(x=1\right) \tag{4.13}$$

and

$$\xi_{x1}\left(x=1\right)=\frac{u_{x1}}{\omega}\left(x=1\right)=\frac{u_{x2}}{\omega-k_y v_o}\left(x=1\right)=\xi_{x2}\left(x=1\right). \tag{4.14}$$

Our dispersion relation is expressed as the following two equations, which are evaluated at $x=1$,

$$\mathrm{Re}\left(\frac{p_T}{\xi_{x1}}\right) = \mathrm{Re}\left(\frac{p_2}{\xi_{x2}}\right) \tag{4.15}$$

$$\mathrm{Im}\left(\frac{p_T}{\xi_{x1}}\right) = \mathrm{Im}\left(\frac{p_2}{\xi_{x2}}\right). \tag{4.16}$$

These equations are then solved using a two dimensional Newton-Raphson method.

There is a singularity in the ODES, Equations (4.8) and (4.9) at

$$\omega^2-k_z^2 v_a^2\left(x\right)=0, \tag{4.17}$$

which, for real ω occurs when

$$\omega=\pm k_z v_a\left(x\right). \tag{4.18}$$

The singularity is associated with an Alfvén resonance at the position x defined via Equation (4.18) (see Southwood, 1974). For real ω it is not possible to integrate along the real x-axis as this contains a singularity, and so we cannot solve our dispersion relation numerically in this case. For complex $\omega=\omega_r+i\omega_i$, Equation (4.17) becomes

$$\omega_r^2-\omega_i^2-k_z^2 v_a^2\left(x\right)+2i\omega_r\omega_i=0, \tag{4.19}$$

and the singularity is removed from the real x-axis and moves into the complex x-plane. Thus, for unstable modes, we may integrate across the magnetospheric cavity (i.e. along the real x-axis), and solve our dispersion relation. As we are interested in studying the fastest growing modes in our system, the singular behaviour for real ω poses no problems in our study. Note that the singularity (even at complex x) is actually a branch pole. Integration along the real x-axis for modes that decay in time is not straightforward since the branch cut will be encountered. With some care this case can be treated too (Zhu and Kivelson, 1988).

We define the resonant point, x_R, such that

$$v_a(x_R) = \frac{\omega_r}{k_z}, \tag{4.20}$$

i.e., at the point at which a singularity would occur for real ω. We also define the turning point, x_t, to be the point at which the nature of the mode in the magnetosphere changes from oscillatory to evanescent. For real ω this point is defined by

$$m_1(x_t) = 0, \tag{4.21}$$

which gives that

$$v_a(x_t) = \frac{\omega_r}{k}. \tag{4.22}$$

This will remain a reasonable approximation to the point where the nature of the mode becomes dominantly evanescent for complex ω if $\omega_r/\omega_i \gg 1$, which will be the case for the waveguide modes that we will examine.

Since $k = \sqrt{k_y^2 + k_z^2} \geq k_z$ the turning point occurs for a lower value of the Alfvén speed than the resonant point, which in our model means that

$$x_t > x_R. \tag{4.23}$$

In other words, the resonant point is deeper in the magnetosphere than the turning point.

The strength of the resonant coupling depends upon the distance between the turning point and the resonant point, and on the strength of the fast mode driving. The points may only coincide when $k = k_z$ (i.e. $k_y = 0$). However, the resonance occurs in the y-component of the perturbed velocity, and since this is defined from the linearised ideal MHD equations as

$$u_{y1} = \frac{k_y \omega}{\rho_{o1}(\omega^2 - k_z^2 v_a^2)} p_T, \tag{4.24}$$

there will be no coupling when $k_y = 0$. As k_y increases from zero, the decay length in x of the fast mode ($\approx 1/m_1$) decreases, and the separation of x_t and x_R increases. Thus the amplitude of the fast mode becomes very small as k_y becomes large, and very little energy may penetrate to drive a resonance in this limit. Thus, the strength of the resonant coupling first increases and then decreases with k_y as the resonant point moves away from the the turning point (Kivelson and Southwood, 1986).

4.3 Results

We will examine the behaviour of the first three body mode harmonics when $k_z = \pi$, taking also the flow speed $v_o = 10$ and $\rho_{o1}\ (x = 1) = 0.192$ (which we will use for all our results).

We have used a flow speed slightly higher than those commonly observed on the flanks of the magnetosphere in order to examine various unstable harmonics in both x and z. As shown in Chapter 3 the onset of instability for fast cavity modes is given by

$$v_o = \frac{v_a + c_s}{\sin\alpha}, \tag{4.25}$$

where $\alpha = \tan^{-1}(k_y/k_z)$ and is the angle between the vector $\mathbf{k}$ and the equilibrium magnetic field $\mathbf{B_1}$. Thus choosing a large value of the flow ensures that we can study several harmonics for larger values of k_z. In this section we will consider only modes having $k_z = \pi$. However we will consider the phase speeds for other k_z, v_o and ϵ in Section 4.4.

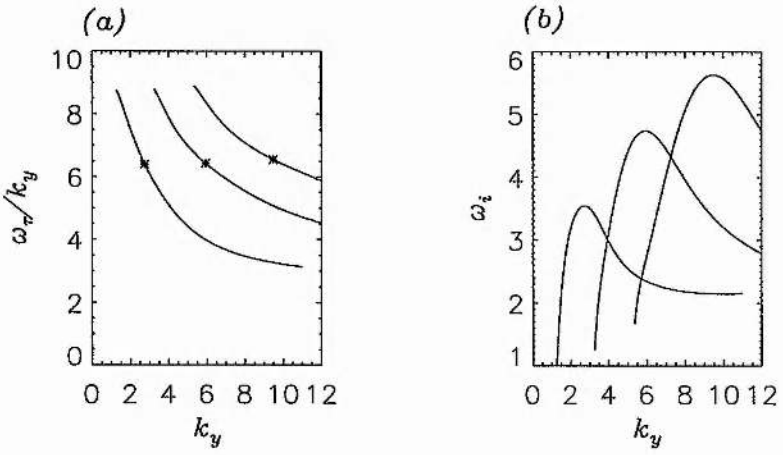

Figure 4.2: The phase speeds (a) and growth rates (b) of the first three harmonics in x when $k_z = \pi$, $v_R = 8$ and $v_o = 10$. The asterisks show the phase speed at maximum growth rate for each of the modes.

Figure 4.2 shows the phase speeds and growth rates of the first three harmonics of the body modes when $k_z = \pi$ and $v_R = 8$. The maxima in the growth rates of the modes occur for $k_y = 2.73,\ 5.93$ and 9.48. The corresponding phase speeds at maximum growth rate are $\omega_r/k_y = 6.40,\ 6.43$ and 6.55, respectively and these are shown by asterisks in Figure 4.2a. The modes most likely to be observed are those that have the largest growth rates, i.e., those for which the growth rate is a maxima. The phase speeds of these modes at the maxima are very similar and this implies that the observed modes would have similar phase speeds: a prediction in excellent agreement with the observations reported by Ziesolleck and McDiarmid (1994).

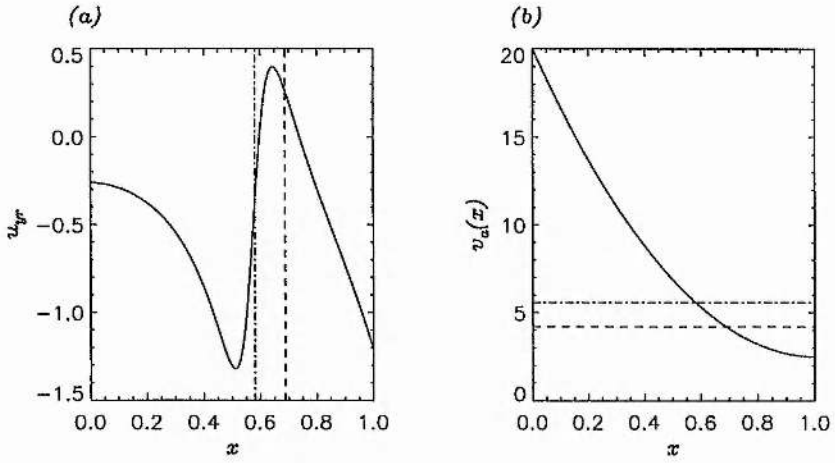

Figure 4.3: The eigenfunction u_{y1} (a) and the Alfvén speed profile (b) for the fastest growing part of the fundamental mode (corresponding to $k_y = 2.73$, $v_p = 6.40$ and $\omega_i = 3.55$) when $v_o = 10$ and $v_R = 8$. The vertical lines in the (a) show the positions of the turning point, x_t, (dashed line) and the resonant point, x_R (dot-dashed line). The horizontal lines in the (b) show the corresponding values of v_a (x) at those points.

Now we look at the fastest growing part of these three modes in more detail. Figure 4.3 shows the eigenfunction u_{yr} (the real part of the perturbed velocity in the y-direction) as a function of x in Figure 4.3a and the Alfvén speed profile in Figure 4.3b. In Figure 4.3a, the dashed and dot-dashed lines indicate the positions of the turning and resonant points (x_t and x_R) respectively and in Figure 4.3b show the corresponding values of the Alfvén speed. The wavenumber is dominantly imaginary when $x < x_t$ and it would be reasonable to expect the solution to appear evanescent in this region. However, we see a clearly defined wave form centred around the point x_R. This is an Alfvén resonance centred close to the predicted position of the singularity based upon ω_r. Figure 4.4 shows the magnitude of $u_y (= \sqrt{u_{yr}^2 + u_{yi}^2})$ as a function of x. The strong peak here corresponds to the Alfvén resonance.

Figure 4.5 shows the eigenfunction and Alfvén speed profile for the fastest growing part of the second harmonic mode. Again we see there is a clearly defined resonance near the predicted value of x_R. The resonant point is deeper inside the magnetosphere for this mode, and is further from the turning point.

Figure 4.6 shows the eigenfunction and speed profile for the fastest growing part of the third harmonic. Here, k_y is much larger than for the fundamental mode and the resonant point is much deeper in the magnetosphere. The coupling strength is also much weaker and the resonance is much smaller compared to the background oscillation. However, in this case, due to the fact that this is a higher harmonic, we can more clearly see that the mode is dominantly oscillatory between the magnetopause and the turning point, but

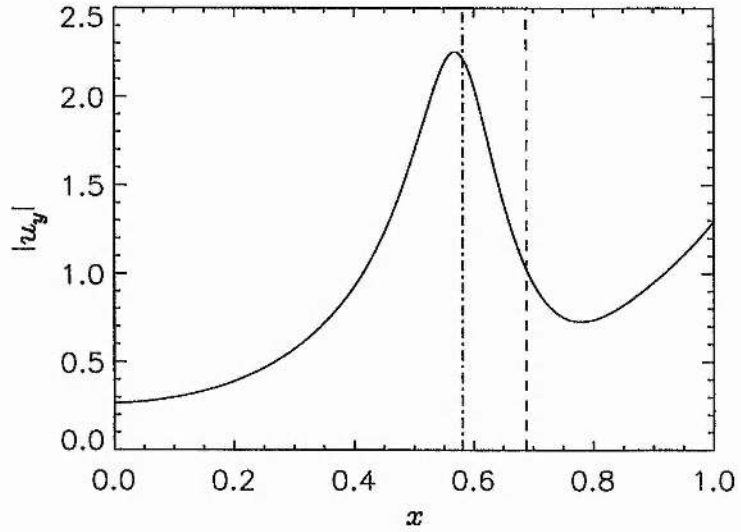

Figure 4.4: The magnitude of the complex function u_y as a function of x for the parameters shown in Figure 6. The vertical lines again show the position of the turning point, x_t, (dashed line) and the resonant point, x_R, (dot-dashed line) predicted for stable modes.

that it becomes dominantly evanescent beyond that point.

Finally, we examine the dependence of the position and strength of the resonance on k_z. Firstly we compare the value of k_y at the maximum of the growth rate of a given radial cavity mode harmonic for various values of k_z. Table 4.1 shows the values of k_y at maximum growth rate for several k_z values. We

k_z	k_y	ω_r/k_y
$\pi/2$	9.29	6.52
π	9.48	6.55
$3\pi/2$	9.79	6.60
2π	10.17	6.65
$5\pi/2$	10.58	6.71

Table 4.1: The values of k_y and ω_r/k_y at which the growth rate has its maximum for various values of k_z for the third harmonic mode when $v_R = 8$.

can see that although the value of k_y is increased when k_z is increased, a doubling of k_z (for example from $k_z = \pi$ to $k_z = 2\pi$), does not result in a doubling of k_y (in this case the increase is less than 10%). Thus

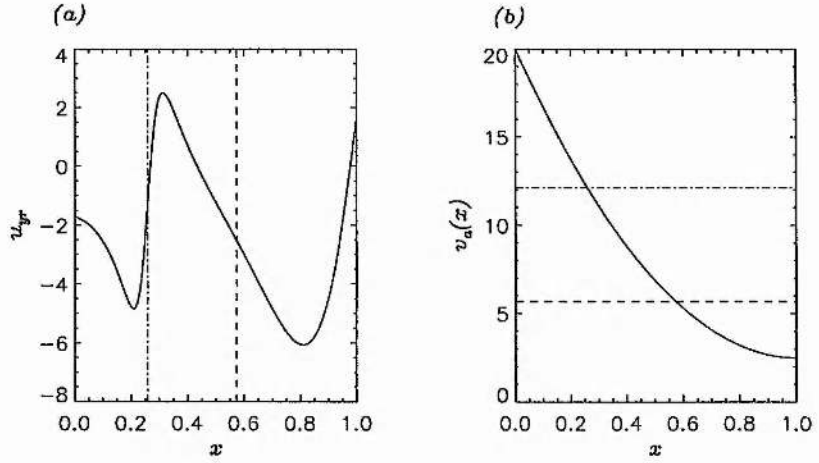

Figure 4.5: The eigenfunction u_{y1} (a) and the Alfvén speed profile (b) for the fastest growing part of the second harmonic mode (corresponding to $k_y = 5.93$, $v_p = 6.43$ and $\omega_i = 4.74$) when $v_o = 10$ and $v_R = 8$. The vertical lines in the (a) show the positions of the turning point, x_t, (dashed line) and the resonant point, x_R (dot-dashed line). The horizontal lines in the (b) show the corresponding values of $v_a\,(x)$ at those points.

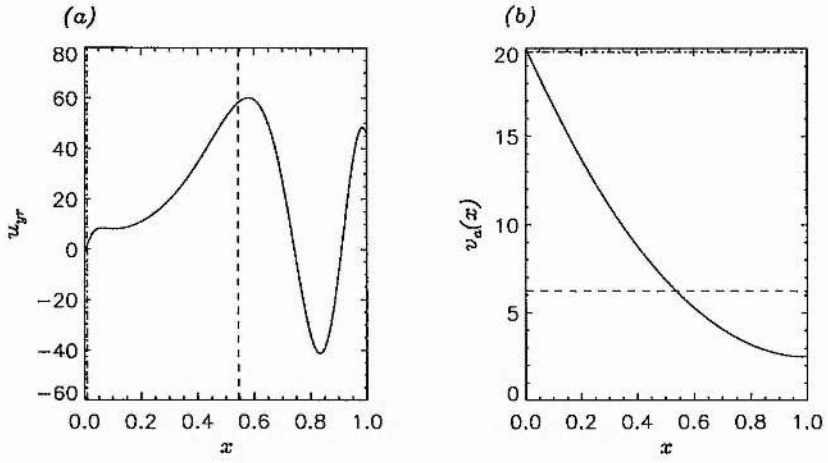

Figure 4.6: The eigenfunction u_{y1} (a) and the Alfvén speed profile (b) for the fastest growing part of the second harmonic mode (corresponding to $k_y = 9.48$, $v_p = 6.55$ and $\omega_i = 5.63$) when $v_o = 10$ and $v_R = 8$. The vertical lines in the (a) show the positions of the turning point, x_t, (dashed line) and the resonant point, x_R (dot-dashed line). The horizontal lines in the (b) show the corresponding values of $v_a\,(x)$ at those points.

the angle between the propagation vector and the magnetic field (α) decreases with increasing k_z. Now, we can write k_z as

$$k_z = k\cos\alpha, \tag{4.26}$$

where $k = \sqrt{k_y^2 + k_z^2}$. Thus, we may show that

$$v_a\left(x_{TP}\right) = \frac{\omega_r}{k} = \frac{\omega_r}{k_z}\cos\alpha = v_a\left(x_R\right)\cos\alpha. \tag{4.27}$$

Thus, as k_z is increased, the turning point and resonance point will move closer together. Note also, the similarity between the phase speeds at maximum growth rate for all these harmonics in z.

Figure 4.7 shows the eigenfunction and Alfvén speed profiles for the third harmonic for $v_R = 8$ and various values of k_z. Here we can see that increasing k_z moves the position of the resonance towards the magnetopause, and closer to the turning point. Thus, the coupling strength is greater for higher k_z. Thus, for higher harmonics in x, observed resonances are likely to be higher harmonics in z also.

For the values of flow speed, v_o, Alfvén profile, v_R, and wavenumber, k_z, chosen there are three resonances occurring within the magnetosphere all having very similar values of phase speed. Now we examine the theory of wave over-reflection at the magnetopause which enables us to understand the consistency of the phase speeds.

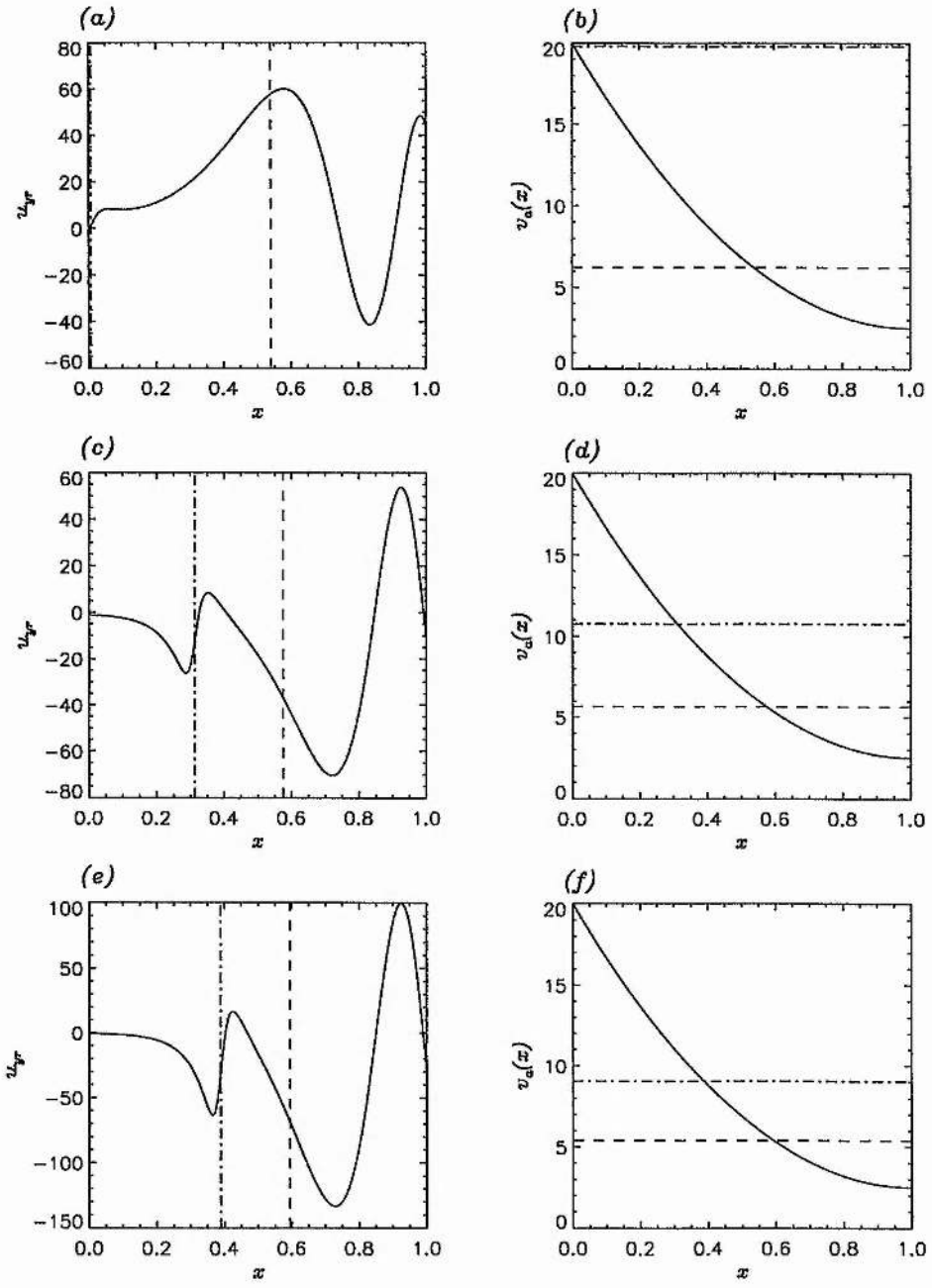

Figure 4.7: The eigenfunctions and Alfvén speed profiles of the third harmonic mode when $k_z = \pi$ ((a) and (b)), $k_z = 2\pi$ ((c) and (d)), and $k_z = 5\pi/2$ ((e) and (f)) when $v_R = 8$. The dashed and dot-dashed lines again indicate the positions of the turning and resonant points respectively.

4.4 Comparing Numerical Results to Predicted Values

Now we compare the phase speeds found at the maxima of the growth rate for the modes found in Section 4.3 with those predicted by the formula in Section 2.3.2. Although Section 2.3.2 modelled the unbounded case for purely real ω, this method of predicting an angle and phase speed for spontaneous radiation will be useful in analysing the unstable behaviour of our modes in the bounded non-uniform model. The Alfvén speed profile that we have chosen has zero gradient at the magnetopause, so that close to this boundary, a uniform approximation is reasonable. Since there is no scale length in the unbounded case the equation to predict this phase speed (Equation (2.61)) is independent of k, and depends only on the angle between the magnetic field and the propagation vector, α. Since $\alpha = \tan^{-1}(k_y/k_z)$, for a fixed k_z the angle will depend only on k_y. As k_y becomes large, $\alpha \to \pi/2$, and the phase speed will tend to a constant value. This agrees with the observations of Ziesolleck and McDiarmid (1994) that simultaneously observed field line resonances on the flanks (which are believed to be driven by the shear flow discontinuity at the magnetopause) have the same azimuthal phase speed. In this section we will use the formula to predict the azimuthal phase speed, $v_{ph} = \omega_r/k_y$, given by

$$v_{ph} = \frac{\omega_r}{k_y} = \frac{U}{\sin\theta_1 \sin\alpha}, \tag{4.28}$$

where U is the fast magnetoacoustic speed and θ_1 is found by setting $Z = -1$ in Equation (2.60) and evaluating Equation (2.61). Figure 4.8 shows the value of ω_r/k_y predicted by the over-reflection theory (solid line) as a function of k_y (using $v_o = 10$ and $k_z = \pi$). The symbols represent the values found by the numerical model with $v_R = 8$ for the fundamental mode (cross), second harmonic (asterisk) and third harmonic (diamond). We can see that the numerical values fall very close to the predicted values, with the fit getting better for higher harmonics. The larger discrepancy seen for the fundamental mode may be explained by the fact that this mode has a wavelength approximately twice the width of our cavity and so the approximation of an infinite, uniform magnetosphere does not compare well to this mode which has no real oscillations between the magnetopause and the turning point. Note that the predicted value of the phase speed is almost constant for $k_y > 3$, which agrees well with the fact that observed FLRs have constant phase speed.

Figure 4.9 shows the predicted value of the phase speed at the maximum growth rate as a function of α with the actual values for the second, third and fourth harmonics (represented by triangles, diamonds and asterisks respectively). The values of k_z for those harmonics are (from right to left) $\pi/2$, π, $3\pi/2$, 2π and $5\pi/2$. The variation of the predicted phase speed for these angles is relatively small, again corresponding well to observed modes having a consistent phase speed. The agreement between the predictions and the

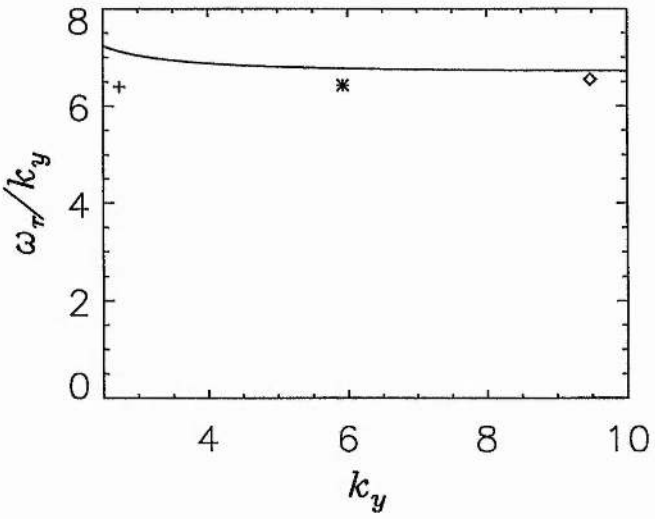

Figure 4.8: A comparison between the phase speed predicted by the over-reflection theory of McKenzie (1970a) (solid line) with the phase speeds at the maxima of the growth rate found by our model when $k_z = \pi$, $v_R = 8$ and $v_o = 10$ for the fundamental (cross), second harmonic (asterisk) and third harmonic (diamond) in x.

results found by our model is excellent, with best agreement occurring for higher harmonics in both x and z.

Finally, we compare the numerical and analytical results for the different harmonics in x and several values of v_R when $k_z = \pi/2$. Figure 4.10 shows the predicted value of the phase speed (solid line) with the values found at maximum growth rate in our model for the first, second and third harmonics (represented by crosses, stars and diamonds respectively). The values of v_R increase from left to right. Once again, the agreement is excellent, with the higher modes agreeing more closely. The agreement is best for low values of v_R (which corresponds most closely to a uniform magnetosphere), but is good for all values. Thus, the phase speeds predicted by the infinite uniform magnetosphere model may be used as a reasonable estimate of the phase speeds we expect to observe in the magnetosphere.

We saw in Figures 4.9 and 4.10 that the value of the phase speed at which we expect spontaneous radiation of modes varies little with k_y or α. The values of the phase speed at maximum growth rate found in our model are also remarkably insensitive to the variation of the Alfvén speed in the magnetosphere. In fact, if we take the limit $k_y/k_z >> 1$, then $\alpha \approx \pi/2$ and this provides a simple limit which we can use to evaluate the approximately constant phase speed. Thus, we may now calculate the phase speed for spontaneous radiation of waves from the magnetopause when $\alpha = \pi/2$ and use this to predict the values of

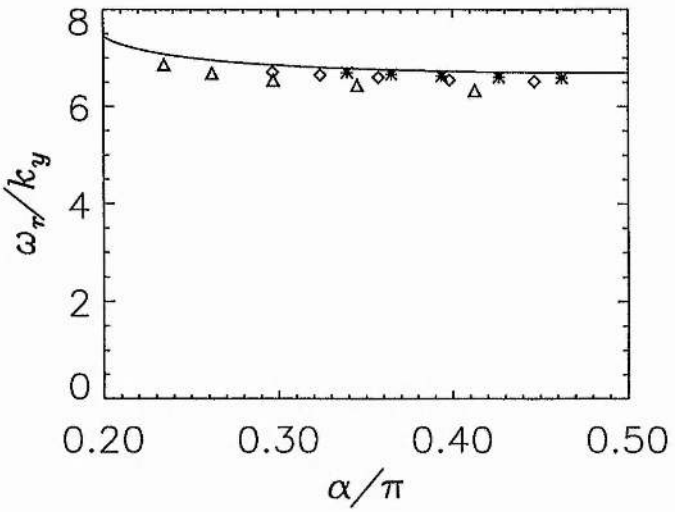

Figure 4.9: The predicted phase speed at maximum growth rate and the values found by our model for the second (triangles), third (diamonds) and fourth (asterisks) harmonics for various values of k_z (from left to right for each harmonic, the values of k_z are $5\pi/2$, 2π, $3\pi/2$, π and $\pi/2$) when $v_o = 10$. Here we have used $v_o = 10$ and $v_R = 8$.

the phase speeds of field line resonances in the magnetosphere. To simplify the algebra, we also assume that $\Gamma = 2$ for this calculation so that the fast speed, U may be simplified such that

$$U = v_{a1} = \frac{c_{s2}}{\sqrt{\epsilon}}, \tag{4.29}$$

where $\epsilon = \rho_{o1}(1)/\rho_{o2}$. Using these approximations, we find that

$$\begin{aligned} Z &= \pm\frac{\cos\theta_1 \left(c_{s2}/\sqrt{\epsilon} - v_o \sin\theta_1\right)^2}{\lambda c_{s2}^2} \\ &= \pm\frac{\cos\theta_1 \left(\epsilon^{-1/2} - v_o \sin\theta_1\right)^2}{\left[\left(\epsilon^{-1/2} - v_o \sin\theta_1\right)^2 - \sin^2\theta_1\right]}, \end{aligned} \tag{4.30}$$

where we have used the fact that $c_{s2} = 1$ since we have normalised our variables. Solving, for θ_1, we can then find the phase speed,

$$v_p = \frac{1}{\sqrt{\epsilon}\sin\theta_1}. \tag{4.31}$$

Figure 4.11 shows the values of the phase speed as a contour plot as function of v_o (the sonic Mach number of the flow in the magnetosheath) and the ratio of the density in the magnetosphere to that in the magnetosheath, ϵ. Spontaneous radiation of modes may only occur above the upper critical speed (at which the modes stabilise in the unbounded uniform case) and thus, we may only predict a phase speed for relatively

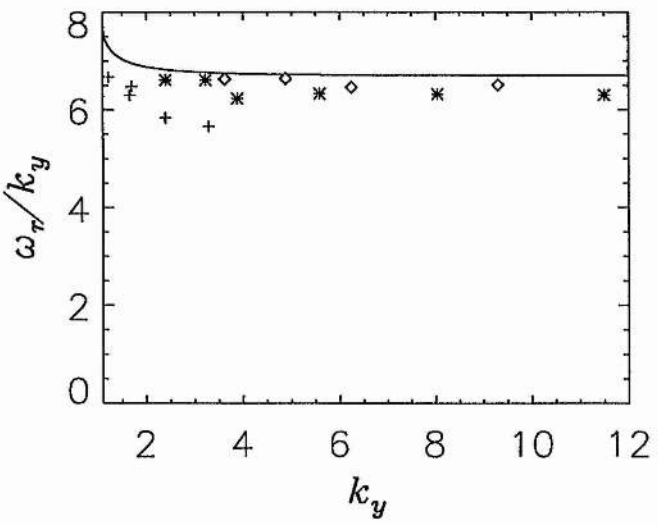

Figure 4.10: The predicted phase speed at maximum growth rate and the values found by our model for the first (crosses), second (asterisks) and third (diamonds) radial harmonics for various values of v_R (from left to right $v_R = 1$, 2, 4, 8 and 16) when $v_o = 10$ and $k_z = \pi/2$.

high flow speeds. We can see that for a given density ratio the phase speed at spontaneous radiation increases for increasing flow speed. However, increasing the ratio of densities, ϵ, decreases the predicted phase speed. Although the phase speeds in Figure 4.11 are approximate, they provide very reliable estimates. For example, the parameters used in Figure 4.10 ($\epsilon = 0.192$, $v_o = 10$) may be used in conjunction with Figure 4.11 to infer a phase speed of 6.7, which is in good agreement with the value found by solving the exact dispersion relation.

Observations show that the density ratio (and therefore the ratio of the Alfvén speed in the magnetosphere to the sound speed in the magnetosheath) across the magnetopause varies greatly for different magnetopause crossings. Eastman et al. (1985) found Alfvén speeds in the magnetosphere ranging from 200 to 1500 km/s. Typical magnetosheath sound speeds are in the range 100 to 150 km/s (see the observations discussed in McKenzie, 1970a). Thus, the ratio of the Alfvén speed at the magnetopause, v_a (1), to the sound speed in the magnetosheath, c_s, can be related to the density ratio, ϵ, using

$$\frac{v_a\,(1)}{c_s} = \sqrt{\frac{5}{6\epsilon}}. \tag{4.32}$$

Using Figure 11, our predictions may be compared to observational results if either the ratio of the densities, or of the speeds is measured. For the values quoted above, ϵ lies in the range 0.005 to 0.5.

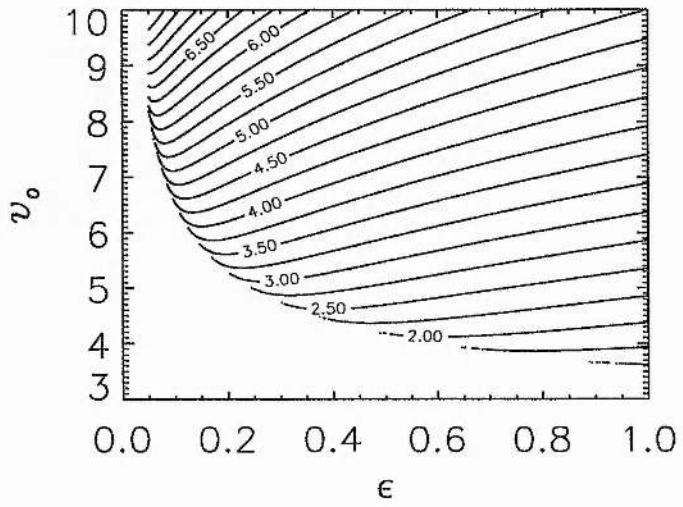

Figure 4.11: The predicted phase speed at maximum growth rate as a function of the ratio of densities ϵ and the flow speed in the magnetosheath, v_o.

4.5 Conclusions

We have presented a model for the excitation of Alfvén resonances in the magnetosphere by fast cavity modes driven by the shear flow discontinuity at the magnetopause. We calculated the expected phase speed at maximum growth rate following McKenzie (1970a) and showed that the total variation of this speed over the unstable cavity modes was of the order of 10%. We compared our results to this prediction and showed that our results agree well with the predictions, with accuracy increasing for higher harmonics in both x and z. We would expect observed phase speeds to be close to the predictions and, for any given flow speed, to be similar for all simultaneously excited resonances. This is in excellent agreement with the observations of Ziesolleck and McDiarmid (1994).

Taking the sound speed in the magnetosphere to be about 100 km/s, the depth of the magnetosphere to which modes will penetrate to be of the order of 10 R_E and the plasma density in the magnetosheath to be 5 times that in the magnetosphere, we may compare the values predicted by our model to those observed in the magnetosphere. For a flow speed of 600 km/s, the phase speed we predict is about 400 km/s. Observations using HF radar which report simultaneously observed Pc5s having phase speeds of between 50 and 250 km/s (see Table 1 of Fenrich et al., 1995). Magnetometer data show Pc5 oscillations having phase speeds of between 500 and 1000 km/s (Ziesolleck and McDiarmid, 1994), which is somewhat higher than those observed by radar. Our predicted phase speed lies between these observed values. At this flow speed, the fundamental body mode for $v_R = 1$, has $\omega_r \approx 10$, which corresponds to a period of oscillation of about 400 s or a frequency of the order of 2.5 mHz, which agree excellently with observations of Pc5 modes having periods between 150 and 600 s.

Chapter 5

Absolute and Convective Instabilities on the Flanks of the Magnetosphere

5.1 Introduction

As suggested by Dungey (1954), the Kelvin-Helmholtz instability (KHI) can operate at the magnetopause. In models comprising an unbounded, uniform magnetosphere containing compressible plasma (Sen, 1964; Fejer, 1964; Southwood, 1968; Pu and Kivelson, 1983) there exist both upper and lower cut-off values for the flow speed in the magnetosheath, corresponding to the onset of instability and the restabilising of the system, respectively. The lower cut-off speed occurs due to the stabilising effects of the magnetic tension force (Miura and Pritchett, 1982). The upper cut-off speed occurs when the the form of the disturbance in both of the media changes from evanescent ('surface' modes) to oscillatory ('body' modes) (Pu and Kivelson, 1983). These oscillatory modes enable energy to be carried away from the magnetopause, stabilising the boundary.

Recently, models of both a uniform (Mann et al., 1999; Mills et al., 1999a, see also Chapter 3) and a non-uniform (Fujita et al., 1996; Mills and Wright, 1999 and Chapter 4) bounded magnetosphere have been studied. These models show that for a flank-like configuration (i.e., when the magnetic field in the magnetosphere is perpendicular to the flow in the magnetosheath) the surface mode propagating parallel to the plasma flow is unstable for any non-zero flow speed. Waveguide modes (which are oscillatory in the magnetosphere) may also become unstable for realistic flow speeds, grow in amplitude and perhaps explain the enhancement of Pc5 wave power at high flow speeds observed by Engebretson et al. (1998). Fujita et

al. (1997) also found that the upper cut-off speed is removed in a bounded model and that the modes are unstable for all flow speeds above the lower cut-off. This occurs because the reflection/refraction of modes due to the existance of the inner boundary of the magnetosphere stops the complete removal of energy from the boundary.

A difficulty with all models that treat the magnetopause as a tangential discontinuity is that the growth rate of at least some of the modes are unbounded as the wavenumber increases. Including a finite boundary layer over which the flow speed changes continuously (Walker, 1981; Miura and Pritchett, 1982) stabilises the system when the wavelength is comparable to the width of the shear layer or less, thus resolving the inconsistency in models of a vortex sheet. A finite boundary layer also removes the upper cut-off speed.

Simulations of the non-linear KHI at the magnetopause have also been undertaken (e.g., Miura, 1984; Miura, 1987). These show that the disturbances initially grow exponentially, with the growth rate predicted by linear theory and only saturate at later times causing the formation of vortices. These vortices allow some diffusion of magnetosheath plasma into the magnetosphere, which in turn forms a velocity boundary layer just inside the magnetopause - the low latitude boundary layer (LLBL). However, these simulations of the KHI have, in general, taken the length of the numerical box to be the same as the length of the initial perturbation and considered a symmetrical profile of flow speed. Thus, there has been very little study of the spatial development of the KHI. Miura (1995) increased the box size to accommodate two wavelengths of the initial perturbation and found that two vortices formed initially but these soon merged to form one large vortex.

In order to study the spatial development of the KHI we will use the theory of absolute and convective instabilities. Detailed reviews of the theory of absolute and convective instabilities may be found in Briggs (1964) and Bers (1983). This analysis enables the examination of the way in which a linear instability modifies the original equilibrium into a non-linear state by studying its space-time evolution. Twiss (1951, 1952) and Landau and Lifschitz (1953) first suggested that a localised pulse disturbance in an unstable system may evolve in two distinct ways - it may be either an 'absolute' or a 'convective' instability. An 'absolute' instability is one in which the growing pulse expands to encompass all space, so that eventually the pulse grows at every fixed point in space. A 'convective' instability is one in which the pulse grows, but also propagates away from its starting point rapidly enough so that at any fixed point the disturbance eventually decays in time. The two types of instability are illustrated in Figure 5.1.

The concept of absolute and convective instabilities is frame dependent. A pulse which moves away as it grows (a convective instability) would be viewed to be growing for all time at fixed points in a reference frame moving with the pulse (i.e., it would be seen to be an absolute instability to the moving observer).

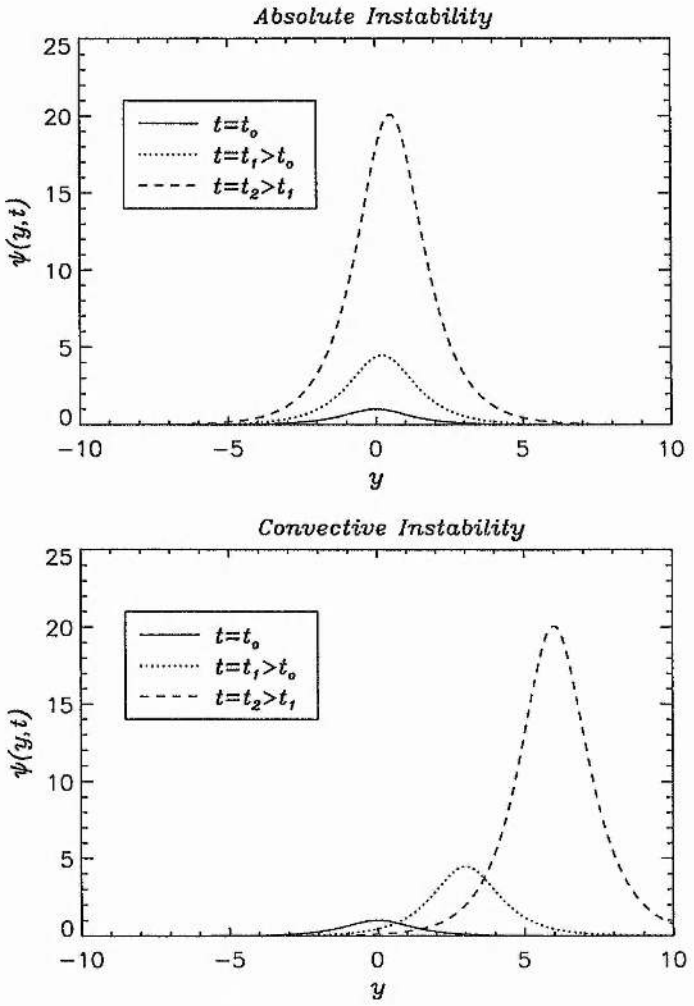

Figure 5.1: A schematic diagram of the space-time development of an absolute instability (upper plot) and a convective instability (lower plot).

Similarly, an observer moving with respect to a frame in which the pulse is an absolute instability could see the instability as convective. As we can see from Figure 5.1, the pulse will tend to widen as it grows, and therefore, an instability will certainly be viewed as absolute in all the reference frames for which the pulse extends in both directions. Thus, for any instability, there will be a set of reference frames for which the instability is absolute. We can therefore think of the classification of an instability as a measure of the speed with which the fastest growing part of the pulse convects away compared to the rate of change of the width of the pulse and the growth rate of the wave-packet.

The conditions under which the linear hydrodynamic KHI is absolutely or convectively unstable have been considered for an incompressible fluid by Triantafyllou (1994). The instability was prevented from having an unbounded growth rate by surface tension at the interface. In this simplified case, an analytical expression for the transition between the absolute and convective instability was obtained. Triantafyllou found that the instability is convectively unstable only for a small range of values of the flow speed and density ratio, and absolutely unstable for most cases.

Wu (1986) states that the KHI at the magnetopause boundary should be convective. However, the definition of convective is limited to implying that the disturbances excited by the KHI should convect tailwards with a finite velocity with no reference to the widening of the pulse and the comparative speeds of these factors. Wu uses the term 'convective instability' in a rather informal fashion compared to the body of literature this chapter draws on. Indeed, in the numerical simulation, Wu chooses a reference frame moving with the group velocity of the fastest growing normal mode (i.e., one in which the instability would be expected to be absolute). The numerical box was chosen to be much larger than the initial pulse so that the spatial development of the instability could be studied. Wu found that the pulse expanded to fill the whole domain, confirming that, in the particular reference frame chosen, the instability is absolute.

Manuel and Samson (1993) investigated the spatial development of the KHI along the magnetopause using an ideal MHD computer simulation in which seed perturbations of small disturbances were fed in at the upstream end and an outgoing boundary condition was applied at the downstream end of the waveguide. They showed that the disturbances generated increased in amplitude while convecting downstream, only exhibiting non-linear behaviour several Earth radii (R_E) from their origins. They explained how this spatial development could account for the broadening of the LLBL around the magnetosphere. A hybrid simulation of the KHI at the magnetopause studied by Thomas and Winske (1993) also showed that the amplitude of the perturbations increases along the magnetospheric boundary, and they estimated that non-linear effects would occur within about 1 R_E.

In this chapter we review the mathematical formulation used to distinguish between absolute and con-

vective instabilities and use the theory to predict the spatial behaviour of both the surface and body modes found in the magnetosphere.

In Section 5.2 we review the theory of absolute and convective instabilities discussed by Bers (1983) and Briggs (1964). Section 5.3 describes the model we have examined and the derivation of the governing equations. In Section 5.4 we outline our results and compare them with those from a numerical simulation, in Section 5.5 we show an analytic approximation for the frame dependent growth rate, and in Section 5.6 we discuss the implications of these results for the terrestrial magnetosphere.

5.2 The Mathematical Theory of Absolute and Convective Instabilities

5.2.1 Classification of Instabilities

In order to classify an instability as either absolute or convective, we examine the space-time response of the plasma, $\psi(\mathbf{r}, t)$, defined by the Laplace-Fourier integral

$$\psi(\mathbf{r}, t) = \int_L \int_F \frac{w(\omega, \mathbf{k})}{D(\omega, \mathbf{k})} e^{i(\mathbf{k}.\mathbf{r} - \omega t)} d\mathbf{k} d\omega. \tag{5.1}$$

For simplicity we will consider the case where $\mathbf{k} = (0, k_y, 0)$ in this section. The plasma response, $\psi(y, t)$ is then

$$\psi(y, t) = \int_L \int_F \frac{w(\omega, k_y)}{D(\omega, k_y)} e^{i(k_y y - \omega t)} dk_y d\omega, \tag{5.2}$$

where L is the Laplace (or Bromwich) contour in the complex ω-plane, F is the Fourier contour which in general may be placed in the complex k_y-plane, and $D(\omega, k_y) = 0$ is the dispersion relation for normal modes of the form $e^{i(k_y y - \omega t)}$, $w(\omega, k)$ is the driving function of the disturbance, and we have taken our equilibrium flow to be in the positive y-direction. The Laplace and Fourier contours must be chosen so as not to pass through any singularities of the integrand (which are the solutions of the dispersion relation) and the choice of these contours is, in general, interdependent.

By examining the asymptotic time response of the plasma we may determine the nature of the instability. For a stable system, there are no solutions of the dispersion relation that have $\omega_i > 0$, and the plasma response obeys

$$\lim_{t \to \infty} \psi(y, t) \to 0, \tag{5.3}$$

for all values of y in all reference frames. In the case where there is one or more solutions of the dispersion relation for real k_y for which $\omega_i > 0$, the system is unstable, and we must further classify the system as absolutely or convectively unstable. An absolute instability occurs in the rest frame of a system for which

$$\lim_{t\to\infty} \psi(y,t) \to \infty, \tag{5.4}$$

for all fixed values of y, whereas for a convective instability in the rest frame

$$\lim_{t\to\infty} \psi(y,t) \to 0, \tag{5.5}$$

for all fixed y. However, for some reference frame, moving with a speed v_f with respect to the rest frame of the system, we can define $y_v = y - v_f t$, and an instability which is convective in the y-frame may have the following asymptotic time response in the y_v-frame

$$\lim_{t\to\infty} \psi(y_v,t) \to \infty, \tag{5.6}$$

so the instability is absolute in the y_v-frame. Similarly we may choose a reference frame moving with a particular speed relative to the rest frame for which an absolute instability would appear to be a convective instability.

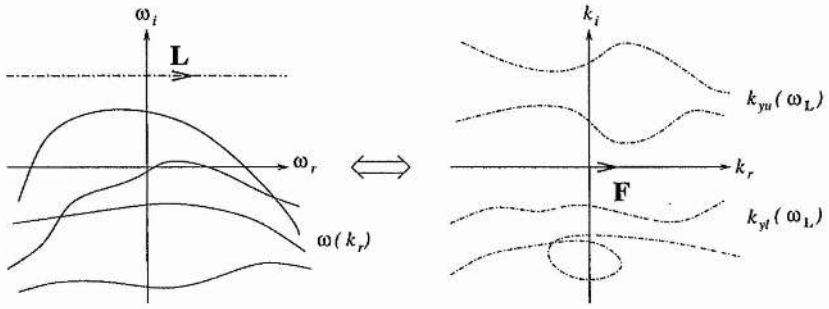

Figure 5.2: The mappings through the dispersion relation $D(\omega, k_y) = 0$ from the Laplace contour, L, onto the complex k_y-plane showing the division of roots into k_{yu} and k_{yl}. Also shown is the mapping from the Fourier contour, F, onto the complex ω-plane, showing that all the roots occur below the Laplace contour.

Initially we will choose the Fourier contour to be the real k_y-axis. Then we may map the solutions of the dispersion relation for real k_y ($k_y = k_r$) onto the complex ω-plane obtaining branches of the solution $\omega(k_r)$. Figure 5.2 shows the complex k_y- and ω-planes and the mapping of the Fourier contour onto the

complex ω-plane through the dispersion relation. Then we may choose the Laplace contour to be above the branch of $\omega(k_r)$ which has the highest value of ω_i. Thus we may integrate in ω from $-\infty + i\sigma$ to $\infty + i\sigma$ where

$$\sigma > max\{\omega_i : D(\omega, k_r) = 0\}. \tag{5.7}$$

We map the Laplace contour onto the complex k_y-plane through the dispersion relation obtaining branches of the solution $k_y(\omega_L)$. We find that none of the solutions may cross the real k_y-axis (since there are no solutions of the dispersion relation for real k_y that have $\omega_i = \sigma$), and so both the Fourier and the Laplace contours are within the domains of absolute convergence of the integrand. Since none of the solutions $k_y(\omega_L)$ may cross the real k_y-axis we may divide them into two sets, those in the upper half of the k_y-plane, with $k_i > 0$ ($k_{yu}(\omega_L)$), and those with $k_i < 0$ ($k_{yl}(\omega_L)$), which are in the lower half of the k_y-plane.

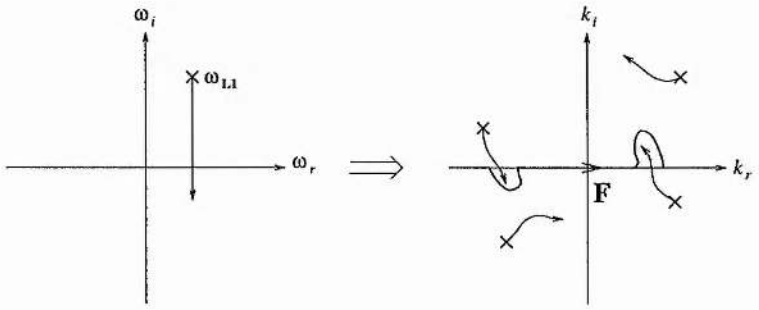

Figure 5.3: The mapping of the roots of the dispersion relation $D(\omega, k_y) = 0$ onto the complex k_y-plane as ω_i is reduced from its value on the Laplace contour. We see that although some of the roots may cross the real k_y-axis, the Fourier contour, F, may be deformed around the roots.

In order to determine the asymptotic time behaviour of the plasma we try to lower the Laplace contour. If the whole of the Laplace contour may be placed below the real ω-axis then the instability is convective as the asymptotic time response will tend to zero. If this is not possible, then the instability is absolute. The Laplace contour may only be lowered if the Fourier contour may be deformed around the singularities of the integrand. For example, we choose a point, ω_{L1} on the Laplace contour and map the roots of the dispersion relation ($D(\omega_{L1}, k_y) = 0$) onto the complex k_y-plane (see Figure 5.3). We then fix ω_r and decrease ω_i and follow the movements of the roots in the k_y-plane. In Figure 5.3 we see that two of the roots have crossed the k_r axis as we have decreased ω_i. However, in this case we can deform the Fourier contour around these

roots so that all the upper roots $k_{yu}(\omega_L)$ still lie above the contour, and all the lower roots still lie below it. Thus, in this case, we may lower the Laplace contour at this value of ω_r. In Figure 5.4 we show the converse situation. Here, as we decrease the value of ω_i, two of the roots in the k_y-plane (one k_{yu} and one k_{yl}) move to the same point. This situation can also be viewed as one of the k_{yu} contours and one of the k_{yl} contours from Figure 5.3 kissing. Now we can no longer deform the Fourier contour between these two roots, and hence the Laplace contour can be lowered no further for this value of ω_r. The point where the two roots meet is a double root of the dispersion relation satisfying the equations

$$D(\omega_o, k_{yo}) = 0, \tag{5.8}$$

and

$$\frac{\partial D}{\partial k_y}(\omega_o, k_{yo}) = 0. \tag{5.9}$$

The double root is also a saddle point of the solutions $\omega(k_y)$ on the complex ω-plane. The existence of a double root of the dispersion relation will only inhibit the lowering of the Laplace contour if the two roots merge from opposite sides of the Fourier contour. If, for example, two solutions $k_{yu}(\omega_L)$ merge, the Fourier contour may still be deformed around the double root to keep both roots above the contour. The condition that the double root must result from the merging of one k_{yu} and one k_{yl} is called the 'pinching' condition and a point satisfying that condition is described as a 'pinching double root'. The derivation of this condition is given in Appendix B.

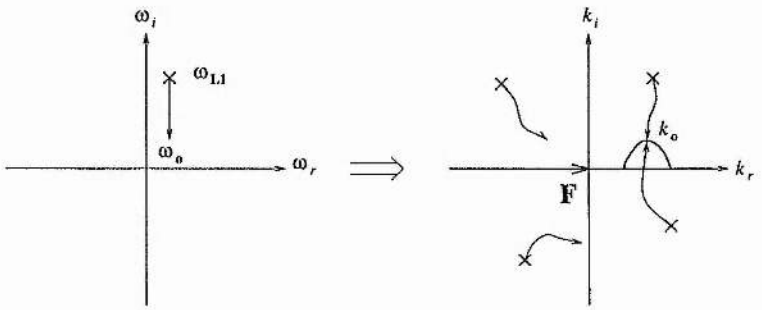

Figure 5.4: The mapping of the roots of the dispersion relation $D(\omega, k_y) = 0$ onto the complex k_y-plane as ω_i is reduced from its value on the Laplace contour. Here two roots merge forming a 'pinching' double root which inhibits the further reduction of ω_i for this value of ω_r.

By repeating the above analysis for the whole Laplace contour, we obtain a contour deformed as in

Figure 5.5. The time asymptotic response of the plasma is dominated by the pinching double root with the largest imaginary part of ω, say ω_d, and wavenumber, k_{yd} satisfying Equations (5.8) and (5.9) with

$$\lim_{t\to\infty} \psi(y,t) \sim \frac{e^{-i\omega_d t}}{\sqrt{t}} e^{ik_{yd}y}, \tag{5.10}$$

e.g., Briggs (1964).

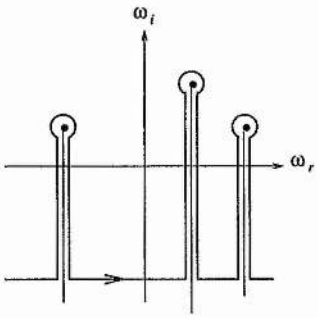

Figure 5.5: The lowered Laplace contour deformed around the double roots of the dispersion relation.

Thus, by finding all the pinching double roots of the dispersion relation, we may determine the asymptotic time response of the plasma.

5.2.2 Finding Pinching Double Roots of the Dispersion Relation

In the previous section we showed that the asymptotic response of a plasma to an instability is determined by the pinching double roots of the dispersion relation and, in principle, we can find whether an instability is absolute or convective by finding all these double roots of the dispersion relation. However, searching through all values of complex ω and k_y in order to find double roots is extremely time consuming and difficult. Fortunately, there is a short cut to finding double roots of the dispersion relation (described in Briggs, 1964): we may identify a double root with each normal mode. By solving the dispersion relation for real k_y we find the unstable normal modes of our system, and we may find the maximum of the growth rate for each mode, occurring at say (k_m, ω_m). The group velocity of the mode at the maxima of the growth rate is

$$v_g = \left(\frac{\partial \omega_r}{\partial k_y}\right)_{(\omega_m, k_m)}. \tag{5.11}$$

Now if we transform into a reference frame moving with a speed v_f with respect to the rest frame ($y' = y - v_f t$), the frequency of the modes in that frame is the Doppler shifted frequency defined by

$$\omega' = \omega - k_y v_f. \tag{5.12}$$

Then

$$\frac{\partial \omega'}{\partial k_y} = \frac{\partial \omega}{\partial k_y} - v_f = \frac{\partial \omega_r}{\partial k_y} - v_f + i\frac{\partial \omega_i}{\partial k_y}. \tag{5.13}$$

Considering a wavenumber at which there is a maxima of ω_i ($\partial\omega_i/\partial k_y = 0$) and choosing the frame velocity to equal the group velocity (i.e., $v_f = \partial\omega_r/\partial k_y = v_g$) we obtain

$$\left(\frac{\partial \omega'}{\partial k_y}\right)_{(\omega_m, k_m)} = 0, \tag{5.14}$$

i.e., ω'_m has a saddle point. Thus, in the reference frame moving with the group velocity of a normal mode with a maximum in growth rate we have identified a double root of the Doppler shifted dispersion relation. Note that a saddle point in ω (k_y) for real k_y must have $\partial\omega_i/\partial k_y = 0$ and $\partial\omega_r/\partial k_y = v_f$ and therefore this is a necessary and sufficient condition for finding double roots when k_y is real. It is now relatively easy to follow the development of the double root as we change reference frames and find the range of reference frames for which we have an absolute instability. We are most interested in the value of the growth rate at the double roots as a function of reference frame speed, v_f. We will define this asymptotic growth rate to be γ to distinguish it from the growth rate of a normal mode, ω_i. The values of v_f at which $\gamma = 0$ identify the speeds with which the front and back of a pulse will travel with respect to an observer in the rest frame of the magnetosphere. Thus, the width of the range of reference frames gives a measure of the rate at which the pulse widens with time.

In this chapter we will identify double roots of the dispersion relation corresponding to the different types of normal modes that the wave-packet is made up of. We will then examine the movement of each double root as we change reference frame to discover whether that root has a positive growth rate in the rest frame of the magnetosphere. If, for example, the double root corresponding to a fast body mode has $\gamma > 0$ when $v_f = 0$, then we would expect the whole wave-packet to be absolutely unstable. The asymptotic behaviour of the wave-packet in any reference frame is governed by the double root that has the largest positive value of γ in that reference frame. If this double root is associated with a surface mode, then we would expect the disturbance to appear to be a surface mode for large time. If it were associated with a body mode, the disturbance should have a variation in x of that body mode, asymptotically.

We are most interested in whether the instability is absolute or convective in the rest frame of the

magnetosphere, and our analysis will enable us to see if this frame is within the range of reference frames for which the instability is absolute.

5.2.3 The Spatial Growth Rate

If an instability is absolute then the initial pulse will grow infinitely large at all points in space as time becomes infinitely large. Conversely, a convective instability moves through space, disturbing the plasma as it moves, but ultimately leaving the situation undisturbed. An important aspect in considering the effects of a convective instability is the growth rate in space, or the distance over which the initial pulse grows by a factor of e (see the lower plot of Figure 5.2).

Consider a pulse growing in time as it propagates along a system. In a given reference frame moving with speed v_{f1}, and having an asymptotic growth rate γ_1, the rate of change of magnitude of any of the eigenfunctions in y in the magnetospheric rest frame (e.g., the x-component of the perturbed velocity, v_x) is given by

$$\frac{dv_x}{dy} = \frac{dv_x}{dt}\frac{dt}{dy}, \tag{5.15}$$

where the quantities on the right hand side are measured in the frame moving with speed v_f which, since in this reference frame $dy/dt = v_{f1}$, and $dv_x/dt = \gamma_1 v_x$ gives

$$\frac{dv_x}{dy} = \frac{\gamma_1}{v_{f1}} v_x, \tag{5.16}$$

(see Brevdo, 1994). Thus the spatial behaviour (in the magnetospheric rest frame) of the fastest growing disturbance in the reference frame moving at speed v_{f1} is given by

$$v_x = A e^{\gamma_1 y / v_{f1}}, \tag{5.17}$$

and the spatial growth rate is γ_1/v_{f1}. In general, the spatial growth rate is $\gamma(v_f)/v_f$, and may be viewed as a function of v_f. The maximum spatial growth rate is given by

$$\frac{d}{dv_f}\frac{\gamma}{v_f} = 0, \tag{5.18}$$

which requires that

$$\frac{1}{v_f}\frac{d\gamma}{dv_f} - \frac{\gamma}{v_f^2} = 0, \tag{5.19}$$

so that

$$\frac{\gamma}{v_f} = \frac{d\gamma}{dv_f}. \tag{5.20}$$

In other words, the maximum spatial growth rate occurs where the line γ/v_f is tangential to the curve of γ as a function of v_f. The e-folding length of the spatial growth is then given by v_f/γ at the point where Equation (5.20) is satisfied. This will provide a useful measure for the extent to which a localised perturbation will disturb the equilibrium, and where that disturbance will take place.

5.3 Model and Equations

We wish to examine the space-time evolution of unstable modes in the magnetosphere driven by the shear flow in the magnetosheath. Several models of a vortex sheet magnetopause separating two infinite media have been studied (e.g., Sen, 1964; Fejer, 1964; Southwood, 1968). In such models the modes studied are limited to those which are evanescent on both sides of the boundary. Recently the effects of a bounded magnetosphere have been considered (Fujita et al., 1996; Mann et al., 1999; Chapter 3), allowing the consideration of propagating modes in the magnetosphere. For models containing a vortex sheet magnetopause, either with a bounded and or an infinite magnetosphere, at least some of the modes propagating parallel to the flow in the magnetosheath have growth rates tending to infinity as the tangential wavenumber becomes large. In the bounded magnetosphere model, the growth rate of the surface mode is restricted for larger flow speeds, however at the same speed, the growth rate of the first harmonic fast body mode becomes unbounded and the form of the disturbance in the magnetosphere becomes dominantly evanescent, while the original surface mode has an oscillatory form. In fact each of the body mode harmonics has a surface mode-like nature for some flow speed (see Section 3.4). The unbounded nature of the growth rate poses a problem for our analysis. As we saw in Section 5.2, the Laplace contour must be placed above the largest positive growth rate when the Fourier contour is placed along the real k-axis. If the growth rate is unbounded, the Laplace contour cannot be placed and our analysis may not progress.

Walker (1981) included a finite boundary layer in a model of an unbounded magnetosphere. The flow speed changes continuously across the boundary layer and Walker found that the inclusion of this boundary layer inhibits the growth rate at large k of the unstable surface modes. Specifically he found that the growth rate was reduced for $k\delta \gtrsim 0.6$ where δ is the half-width of the boundary layer. Thus, in order to examine the space-time evolution of magnetospheric modes, we have modelled a uniform bounded magnetosphere connected to a uniform flowing magnetosheath by a boundary layer of finite width over which the flow speed changes continuously. A sketch of our model is shown in Figure 5.6. Throughout this chapter we use variables normalised to the equilibrium sound speed, c_{s2}, and density, ρ_{o2}, in the magnetosheath, and the width of the magnetospheric cavity (from the inner boundary to the middle of the boundary layer), d. (Time

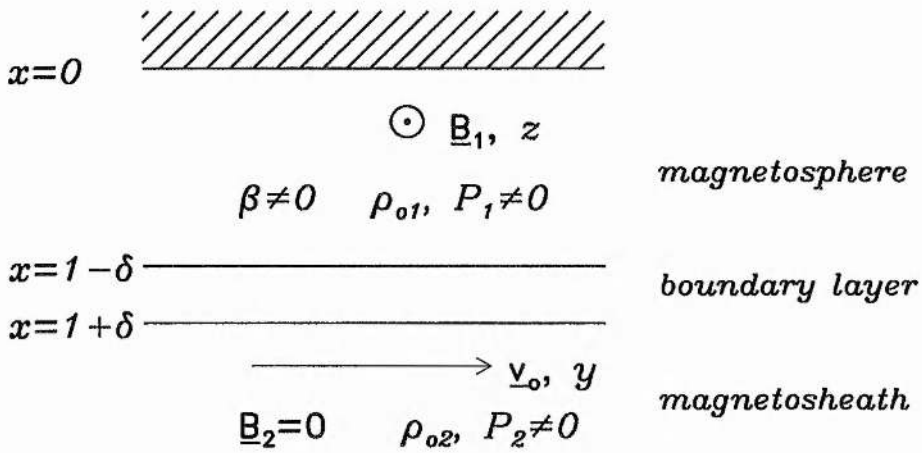

Figure 5.6: A schematic diagram of our bounded magnetosphere model containing a finite width boundary layer.

is normalised by the quantity d/c_s, pressure by ΓP_2 and magnetic fields by $\sqrt{\Gamma P_2 \mu_o}$, where Γ is the ratio of specific heats.) The boundary layer is thus centred at $x = 1$, and has width 2δ.

The magnetic field in the magnetosphere, $\mathbf{B_1}$, is perpendicular to the flow in the magnetosheath, $\mathbf{v_o}$, and both are tangential to the boundary layer. We have, in general, assumed the plasma beta, β, in the magnetosphere to be finite, so that we have a finite plasma pressure, P_1, with an equilibrium density, ρ_{o1}. The magnetosheath is assumed to be field-free. The plasma parameters in both the magnetosphere and magnetosheath are taken to be constant, with variation only occurring across the boundary layer, $1 - \delta < x < 1 + \delta$. The form of the velocity profile we have considered in this region is

$$v(x) = \frac{v_o}{2} + \frac{v_o}{4}\left\{\frac{3(x-1)}{\delta} - \frac{(x-1)^3}{\delta^3}\right\}. \tag{5.21}$$

The cubic form of the velocity profile we have chosen was introduced by Walker (1981) and is determined by matching the equilibrium velocities at $x = 1 \pm \delta$ as well as requiring that the gradient of the velocity profile is zero at the edges of the boundary layer. The other plasma parameters (e.g., magnetic field, plasma pressure, etc.) are taken to change discontinuously from magnetospheric values to those in the magnetosheath at the inner edge of the boundary layer, $x = 1 - \delta$. This corresponds to observations showing that the magnetopause is much narrower than the LLBL (Paschmann, 1979). The jump is chosen to occur on the inner edge of the boundary in order to remove any Alfvèn resonances from the system. Figure 5.7 shows the profile of the flow speed, $v(x)$, across the boundary layer (solid line) and the profile of the other plasma parameters (dot-dashed line), shown here by the variable Ψ, with magnetospheric values represented by Ψ_1 and those in the magnetosheath given by Ψ_2.

In regions of uniform plasma (i.e., the magnetosphere and the magnetosheath), the linearised ideal MHD

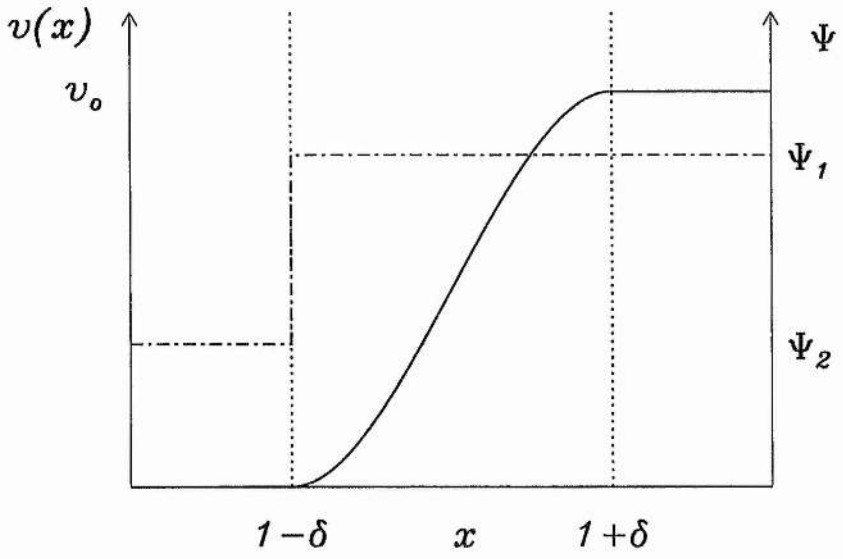

Figure 5.7: The profiles of the flow profile (solid line) and the other plasma parameters (dot-dashed line) across the boundary layer ($1-\delta < x < 1+\delta$).

equations may be combined to form a single second order ODE. In the magnetosphere the perturbed total pressure ($p_T = p_1 + \mathbf{B_1}.\mathbf{b}$) is given by

$$\frac{d^2 p_T}{dx^2} + m_1^2 p_T = 0, \tag{5.22}$$

where m_1 is the magnetospheric x wavenumber given by

$$m_1^2 = \frac{\left(\omega^2 - k^2 c_f^2\right)\left(\omega^2 - k^2 c_{slow}^2\right)}{\left(c_f^2 + c_{slow}^2\right)\left(\omega^2 - k^2 c_T^2\right)}. \tag{5.23}$$

We have defined c_f and c_{slow} as the fast and slow magnetoacoustic speeds along the tangential wave-vector ($\mathbf{k} = (0, k_y, k_z)$), respectively, and

$$c_T^2 = \frac{c_f^2 c_{slow}^2}{c_f^2 + c_{slow}^2} = \frac{v_{a1}^2 c_{s1}^2}{v_{a1}^2 + c_{s1}^2} \cos^2 \alpha, \tag{5.24}$$

where v_{a1} and c_{s1} are the Alfvén and sound speeds in the magnetosphere respectively, and α is the angle between the vector $\mathbf{k}$ and the equilibrium magnetic field, $\mathbf{B_1}$.

The perturbed plasma pressure in the magnetosheath, p_2, is given by

$$\frac{d^2 p_2}{dx^2} + m_2^2 p_2 = 0, \tag{5.25}$$

where m_2 is the wavenumber in the x-direction given by

$$m_2^2 = \frac{(\omega - kv_o \sin\alpha)^2 - k^2 c_{s2}^2}{c_{s2}^2}. \tag{5.26}$$

In the boundary layer we may combine the linearised equations to obtain two first order ODEs (the derivation for which is given in Appendix A) for the total pressure perturbation (which is in fact the plasma pressure perturbation since there is no equilibrium magnetic field in this region) and the x-component of the displacement ($\xi_x = u_x / (\omega - kv(x)\sin\alpha)$). The equations are

$$\frac{dp_T}{dx} = i\rho_{o2}\omega'^2(x)\left(\frac{u_x}{\omega'(x)}\right), \tag{5.27}$$

and

$$\frac{d}{dx}\left(\frac{u_x}{\omega'(x)}\right) = \frac{im^2(x)}{\rho_{o2}\omega'^2(x)} p_T, \tag{5.28}$$

where

$$m^2(x) = \frac{\omega'^2(x) - k^2 c_{s2}^2}{c_{s2}^2}, \tag{5.29}$$

and $\omega'(x)$ is the Doppler shifted frequency at x given by $\omega'(x) = \omega - kv(x)\sin\alpha$.

We have assumed the boundary at $x = 0$ to be perfectly reflecting, so our boundary condition there is that

$$u_{x1}(x = 0) = 0 = \frac{dp_T}{dx}(x = 0). \tag{5.30}$$

In the magnetosheath we require the real part of the x-component of the group velocity to be positive in the rest frame of the magnetosheath (so that energy is carried away from the magnetopause in that reference frame). This requires that (see also Mann et al., 1999 and Chapter 3)

$$\mathrm{Re}(\omega')\,\mathrm{Re}(m_2) + \mathrm{Im}(\omega')\,\mathrm{Im}(m_2) > 0. \tag{5.31}$$

For stable modes $\mathrm{Im}(\omega) = 0$, we require the modes to decay exponentially into the magnetosphere, i.e.,

$$\mathrm{Im}(m_2) > 0. \tag{5.32}$$

Using these boundary conditions and Equations (5.22) to (5.26), we may find the solutions in the magnetosphere and magnetosheath to within an arbitrary phase and amplitude. We then assume the phase in the magnetosphere to be zero and the amplitude to be unity and use a fourth order Runge-Kutta scheme to integrate across the boundary layer and match the solutions to those in the magnetosheath. At both edges

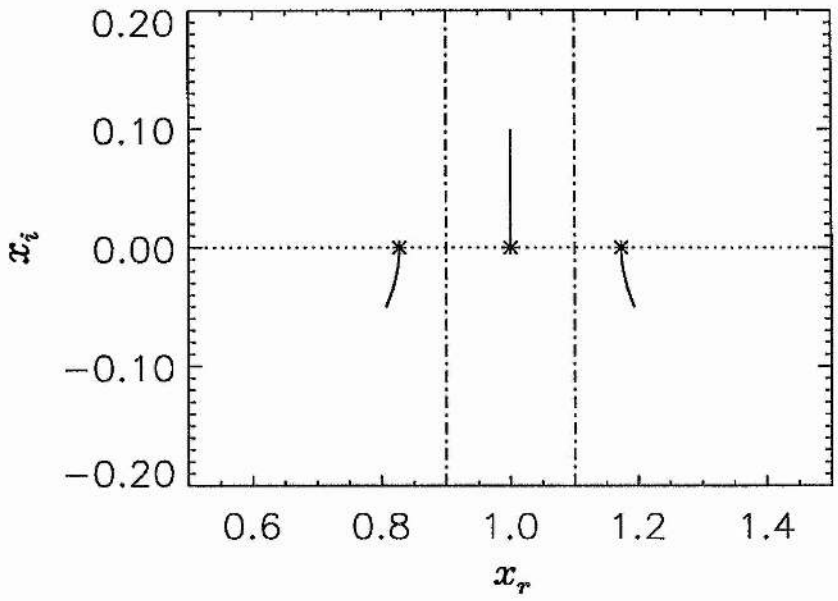

Figure 5.8: The movement of the three roots of Equation (5.34) as ω_i is increased from 0 (the values at $\omega_i = 0$ are marked by asterisks) to 5 when $v_o = 5$, $\delta = 0.1$, $k = 1$ and $\omega_r = 2.5$. The horizontal dotted line indicates the line $x_i = 0$ and the vertical dot-dashed lines show the extend in x_r of the boundary layer, $1 - \delta < x_r < 1 + \delta$.

of the boundary layer ($x = 1 \pm \delta$) we require that total pressure and the x-component of the displacement are continuous.

For purely real ω, Equations (5.27) and (5.28) contain a singularity where

$$\omega'(x) = \omega - kv(x)\sin\alpha = 0, \tag{5.33}$$

which would inhibit the integration along the real x-axis. In order to solve this problem, we perform the integration in the complex x-plane. To do this we need to ensure that we do not integrate through any branch cuts in the complex x-plane. As we are primarily interested in the unstable behaviour of the system we need to determine where the singularity that sits on the real x-axis moves to when $\omega_i > 0$ in order to choose whether to place our contour in the upper or lower half of the x-plane. To do this, we find solutions of the equation

$$\frac{v_o}{2} + \frac{v_o}{4}\left\{\frac{3(x-1)}{\delta} - \frac{(x-1)^3}{\delta^3}\right\} = \frac{\omega}{k\sin\alpha}, \tag{5.34}$$

for complex values of x where ω may, in general, be complex. For complex x, our flow profile, $v(x)$ must be considered to be complex also, so that $v(x) = v_r + iv_i$. If we extend this speed profile beyond the boundary layer $1 - \delta < x < 1 + \delta$ we find that there are three values of $x = x_r + ix_i$ that are solutions of Equation (5.34). When $\omega_i = 0$, all three roots will be real. We will look at the movement of all of these roots for $\omega_i > 0$ in order to ensure that none of the roots that are outside of the boundary layer for real ω will affect our integration when ω is complex. Figure 5.8 shows the movement of the three roots of Equation (5.34) as we increase ω_i from 0 (the positions of the roots when $\omega_i = 0$ are shown by asterisks). Here we have chosen $v_o = 5$, $k = 1$, $\omega_r = 2.5$, $\delta = 0.1$ and have increased ω_i to a value of 5. We can see that the middle root (the only one actually within the boundary layer we will be considering) has positive x_i when we increase ω_i. This root stays within the boundary layer. The outer roots move away from the boundary layer as we increase ω_i and have negative x_i. Therefore, for these parameters, only the middle root will affect our integration path.

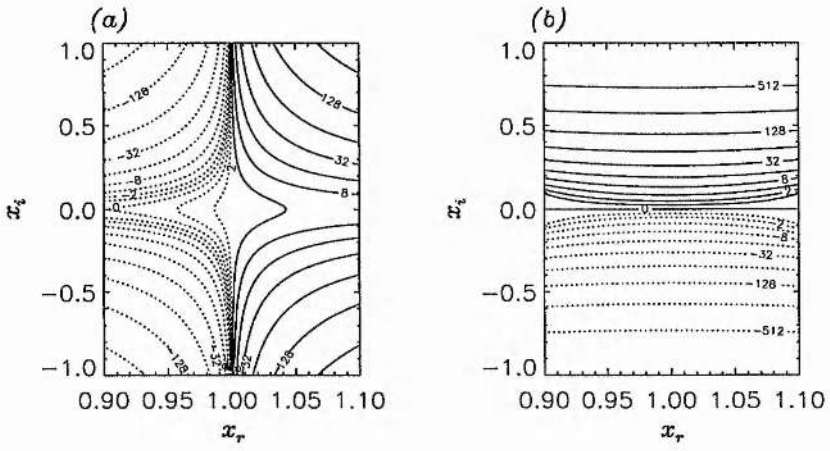

Figure 5.9: (a) A contour plot of the real part of the speed profile, v_r, across the boundary layer as a function of x_r and x_i with solid lines indicating $v_r \geq 2.5$ and dotted lines indicating $v_r < 2.5$. (b) A contour plot of the imaginary part of the speed profile, v_i across the boundary layer as a function of complex x with solid lines when $v_i \geq 0$ and dotted lines otherwise.

In order to confirm that the boundary layer may indeed include only one singularity, Figure 5.9 shows contour plots of the real and imaginary parts of the flow profile (in (a) and (b), respectively) for $|x_r - 1| < \delta$ and for $|x_i| < 1$. In (a) we have plotted all values of v_r that are less than 2.5 as dotted lines and all those that are greater than 2.5 as solid lines. In (b) the contours are solid lines when $v_i \geq 0$ and dotted lines otherwise. We can see that, in this region of complex x-space, $v_r < 2.5$ for all $x_r < 1$ and $v_r > 2.5$ for

all $x_r > 1$ and increases monotonically across the width of the boundary layer. On the other hand, v_i is negative for all negative x_i and positive for all positive x_i and increases monotonically as x_i increases. Therefore the complex function $v(x)$ in the boundary layer is a one-to-one mapping from complex x. In other words, for any complex value of ω/k (indeed we may choose either ω or k or both to be complex) there may only be one point within the boundary layer such that

$$v(x) = \frac{\omega}{k \sin \alpha}, \tag{5.35}$$

i.e., only the singularity that is within the boundary layer for real ω may be within it for complex x, and when we consider $\omega_i > 0$ we find that the singularity is in the upper half of the x-plane.

Cauchy's theorem states that if a function $f(z)$ is analytic in a region R and on its boundary C, (that is there are no singularities of the function either on or within the closed curve C) then

$$\oint_C f(z) = 0, \tag{5.36}$$

or, in other words, the integral of $f(z)$ between any two points is independent of the path taken if the paths do not cross any singularities of f. Therefore, we may integrate along any path in the complex x-plane that does not have any singularities of our functions between the path and the real x-axis and converge to the correct value.

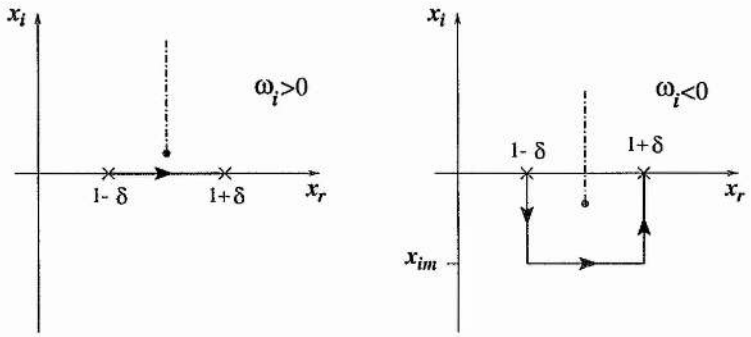

Figure 5.10: The integration contours in the complex x-plane for $\omega_i > 0$ (left plot) and $\omega_i < 0$ (right plot). The dot-dashed line indicates the position of the branch cut.

Since the singularity moves above the real x-axis when $\omega_i > 0$, then when we integrate along the real x-axis, we are integrating below the singularity. Therefore, we choose the branch cut associated with the singularity to be vertically upwards from it, and when we wish to consider either real ω or cases when $\omega_i < 0$

we choose to integrate along a path in the lower half of the x-plane. For simplicity we choose the path so that we integrate first from $x = 1 - \delta$ to $x = 1 - \delta + ix_{im}$ (where $x_{im} < 0$), then to $x = 1 + \delta + ix_{im}$ and then finally back to $x = 1 + \delta$ (see Figure 5.10). The value of x_{im} is chosen in order to ensure that the solution converges. If x_{im} is not sufficiently large, the branch cut will not be circumvented. This will result in the integration path arriving at $x = 1 + \delta$ on a different Riemann sheet to that required for a physical solution. This behaviour manifests itself as poor numerical convergence as the integration contour crosses the singularity, and a jump in the solution at $x = 1 + \delta$ thereafter, corresponding to the switching from one Riemann sheet to another.

We will primarily be considering cases when $\omega_i > 0$ and in these cases, there will, in general, be no problem integrating along the real x-axis and the solution will be the same as that given by performing the complex integration described above. However, in some cases, particularly when $\omega_i << 1$ it may need a very large number of points for the integration along the real x-axis to converge, and it will be simpler to perform the integration in the complex x-plane.

The differential equation for p_T (Equation (5.27)) may be written as

$$\frac{dp_T}{dx} = A(x)\,\xi_{x1}, \tag{5.37}$$

where ξ_{x1} is the displacement of the boundary and $\xi_{x1} = u_{x1}/\omega'$ and

$$A(x) = i\rho_{o1}\omega'^2(x). \tag{5.38}$$

When we consider unstable modes, both p_T and ξ_{x1} are complex, as is $A(x)$. Therefore

$$\frac{d}{dx}(p_{Tr} + ip_{Ti}) = (A_r\xi_{x1r} - A_i\xi_{x1i}) + i(A_r\xi_{x1i} + A_i\xi_{x1r}), \tag{5.39}$$

where a subscripted r indicates the real part of a quantity and a subscripted i indicates the imaginary part. Thus, if we integrate in real x, we can find the real part of p_T by calculating the integral

$$p_{Tr} = \int_{1-\delta}^{1+\delta} (A_r\xi_{x1r} - A_i\xi_{x1i})\,dx. \tag{5.40}$$

The imaginary part of p_T, and the real and imaginary parts of ξ_{x1}, may be calculated in a similar manner. When we consider complex x such that $x = x_r + ix_i$, then instead we must calculate p_{Tr} using the integral

$$p_{Tr} = \int_C (A_r\xi_{x1r} - A_i\xi_{x1i})\,dx_r - (A_r\xi_{x1i} + A_i\xi_{x1r})\,dx_i, \tag{5.41}$$

and p_{Ti} is calculated using the integral

$$p_{Ti} = \int_C (A_r\xi_{x1i} + A_i\xi_{x1r})\,dx_r + (A_r\xi_{x1r} - A_i\xi_{x1i})\,dx_i, \tag{5.42}$$

where C is the curve in the complex x-plane along which we integrate. The ends of C are placed at $x = 1 \pm \delta$. The real and imaginary parts of the displacement, ξ_{x1}, are calculated in a similar manner.

We have used a fourth order Runge-Kutta scheme, with a maximum step size $\approx 5 \times 10^{-4}$, giving a maximum global error $\approx 10^{-10}$. The root finder we have used finds the roots such that both the values of the equations being solved and the next increment required to improve the solution are less then ν where $\nu \leq 10^{-6}$.

5.4 Results

5.4.1 Double Roots Corresponding to Fast Modes

The Effect of a Finite Boundary Layer on the Dispersion of Fast Modes

In order to find the double roots corresponding to the fast surface and body modes we must find the maxima of the growth rates. To do this we solve the dispersion relation to find the normal modes of the system. In this section we examine the effect of introducing a finite boundary layer on the dispersion of fast normal modes.

Initially, we will examine the case where $\alpha = \pi/2$ (the wave propagation vector, k, aligned with the magnetosheath flow, but perpendicular to the magnetic field in the magnetospheres i.e., $k_z = 0$, $k_y = k$) which is the case for which the modes are unstable for the lowest values of the flow speed. In fact, in this case, the fast surface mode is unstable for all non-zero flow.

Figure 5.11 shows the phase speed (a) and growth rate (b) of the fast surface mode when $v_o = 2$ (throughout this chapter we have taken $\Gamma = 5/3$ and the ratio of equilibrium densities $\epsilon = \rho_{01}/\rho_{o2} = 0.192$) for three different values of δ. The $\delta = 0.1$ curve is only shown up to $k \approx 8$, as the convergence of the numerical integration requires many more points as the growth rate decreases. However, the main feature of interest (the maximum in the growth rate) is shown. The fast surface mode is the only unstable mode for this flow speed, since the fast body modes may only be unstable for

$$v_o > \frac{c_f + c_{s2}}{\sin \alpha}, \tag{5.43}$$

which in this case would require a flow speed, $v_o = 3.5$ (see Chapter 3). We can see that when $\delta = 0$ (solid lines) the phase speed rapidly approaches a constant value as k increases, whereas the growth rate is unbounded. For $\delta = 0.05$ (dashed lines), the growth rate is significantly reduced as k increases, and has a maximum when $k \approx 9$. The phase speed is also reduced as k increases from its value when $\delta = 0$, and does

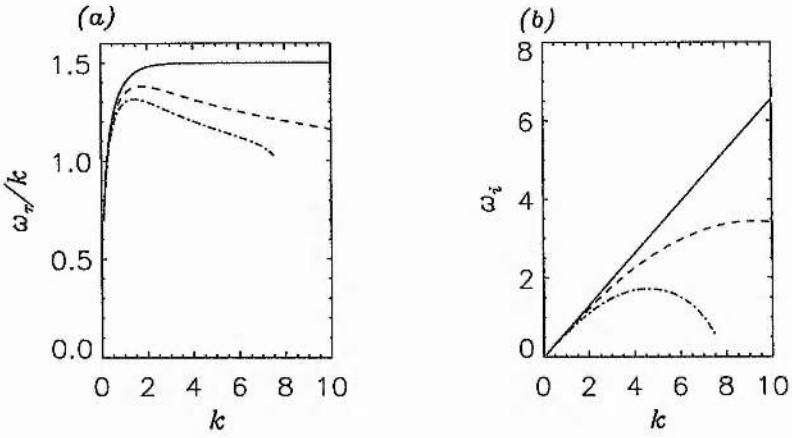

Figure 5.11: The phase speeds (a) and growth rates (b) of the fast surface mode when $v_o = 2$ and $\alpha = \pi/2$ for $\delta = 0$ (solid line), $\delta = 0.05$ (dashed line) and $\delta = 0.1$ (dot-dashed line).

not appear to be approaching a constant value. When $\delta = 0.1$ (dot-dashed line), the growth rate reaches a maximum when $k \approx 4.5$ and the growth rate becomes very small when $k \approx 8$ (after which we have no longer traced the root). The value of the phase speed is further reduced. Thus, in agreement with Walker (1981), the introduction of a boundary layer limits the growth rate of the fast surface modes for large k.

Figure 5.12 shows the effect of a finite boundary layer on the dispersion of the fast body modes when $v_o = 5$. The phase speed and growth rate of both the fundamental and second harmonic modes have been plotted for $\delta = 0$ (solid line), $\delta = 0.05$ (dashed line) and $\delta = 0.1$ (dot-dashed line). The dotted lines in 5.12(a) and (c) show the value of the Alfvén speed in the magnetosphere. Again, the range of k over which the solution has been found has been chosen to ensure convergence of the numerical integration for a reasonable number of points while still illustrating the main features of the curves. Changing the width of the boundary layer has little effect on the phase speeds of these modes. However, the growth rate is reduced for both the harmonics. In both cases, the peak of the growth rates occurs for much lower k when $\delta \neq 0$, and at lower k when the boundary layer is wider. The maximum value of the growth rate is much smaller for cases where $\delta \neq 0$ than for the model without a boundary layer. Also, the maximum value of the growth rate is smaller for the higher harmonics when $\delta \neq 0$, whereas it is approximately constant when there is no boundary layer. Thus, the first harmonic is the most unstable of the body modes when we include a finite width boundary layer.

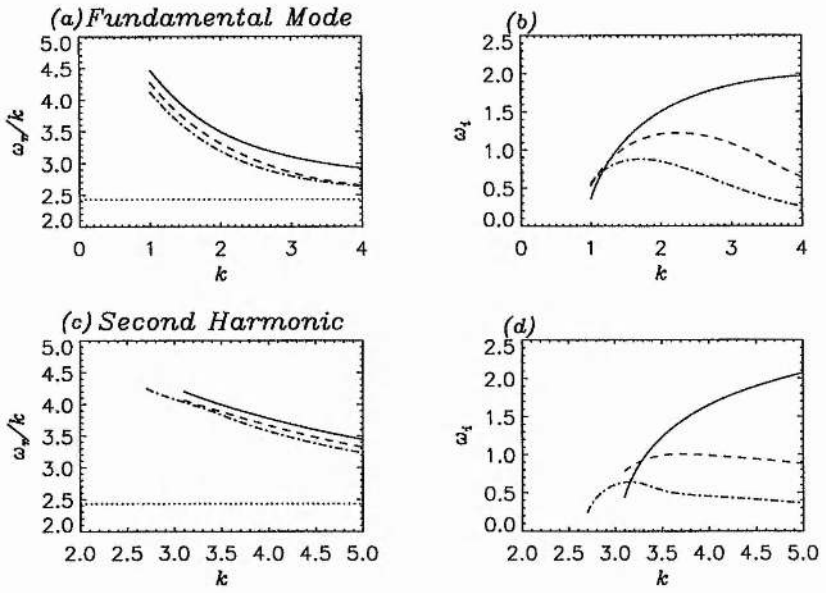

Figure 5.12: The phase speeds (a and c) and growth rates (b and d) of the fast body mode harmonics when $v_o = 5$ and $\alpha = \pi/2$ for $\delta = 0$ (solid line), $\delta = 0.05$ (dashed line) and $\delta = 0.1$ (dot-dashed line). The dotted lines in (a) and (c) show the value of the fast speed, c_f, in the magnetosphere.

The Fast Surface Mode

Now we may examine the double roots of the dispersion relation corresponding to the unstable fast surface mode, and determine the range of reference frames for which this double root has $\gamma > 0$. When $v_o = 2$ and $\delta = 0.1$ the maxima of the growth rate for the fast surface mode occurs when $k = 4.61$, with $\omega_i = 1.72$ and group velocity $v_g = 0.99$. Thus in the reference frame moving with speed $v_f = v_g$ there is a double root at this value of k and the Doppler shifted frequency in this frame ($\omega_r - kv_g$). First, we must check whether this double root does in fact satisfy the 'pinching' condition. To do this, we increase the value of γ from the value at the double root while keeping ω_r constant, and follow the movement of the two roots in the complex k-plane. Figure 5.13 shows this development. Since γ at this double root is the maximum value of the growth rate for any mode, the Laplace contour may be placed anywhere above this value when the Fourier contour is placed along the real k-axis. Thus, we need only increase γ by a small amount to check from which side of the original Fourier contour the two roots originate. As we can see in Figure 5.13, the two roots diverge as we increase γ and one is in the upper half k-plane (it is a k_u) while the other is in the lower half k-plane (k_l). Therefore, this is a pinching double root.

Now we change reference frame and follow the movement of the double root in the complex ω- and k-

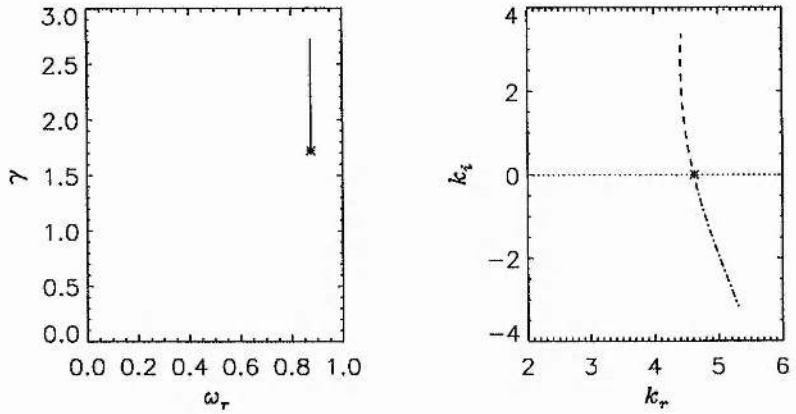

Figure 5.13: The development of the two roots in the complex k-plane as γ is increased from its value at the double root (marked in both plots by an asterisk).

planes. The singularities in the ODEs restrict the validity of our integration scheme to considering positive values of ω_i, so we are unable to track the behaviour of the double root when $\gamma < 0$, unless we deform the contour as discussed at the end of Section 5.3. Figure 5.14 shows the values of the frequency, ω_r, growth rate, γ, and the real and imaginary parts of the wavenumber (k_r and k_i) as functions of the reference frame velocity, v_f. Since we shall be considering how the solution appears in different reference frames (v_f) which will have different magnetospheric flow speeds, it is clearer to define the quantity Δv as the change in flow speed across the boundary layer. Δv is frame-independent, and equal to v_o in the magnetospheric rest frame considered previously. We can see that the instability is absolute in reference frames moving with speeds $0.15 \lesssim v_f \lesssim 1.7$ relative to the rest frame of the magnetosphere. Thus, in the rest frame of the magnetosphere, the instability is convective, and we would expect the disturbance to propagate away from its source as it grows.

Figure 5.15 shows the asymptotic growth rate, γ as a function of reference frame, v_f, for various values of the flow speed in the magnetosheath, when $\delta = 0.1$. We can see that the maximum growth rate initially increases as Δv increases, but then decreases again. The group velocity at the maximum growth rate increases with Δv so that the curve is moved further from the $v_f = 0$ line. The double root corresponding to the fast surface mode indicates that the system is convectively unstable in the rest frame of the magnetosphere for values of Δv above 1, but the double root has a positive value of γ in the rest frame of the magnetosphere when $\Delta v = 0.5$. Since this is the only unstable mode for that flow speed, we may say that the instability is absolute in the rest frame of the magnetosphere for very low flow speeds.

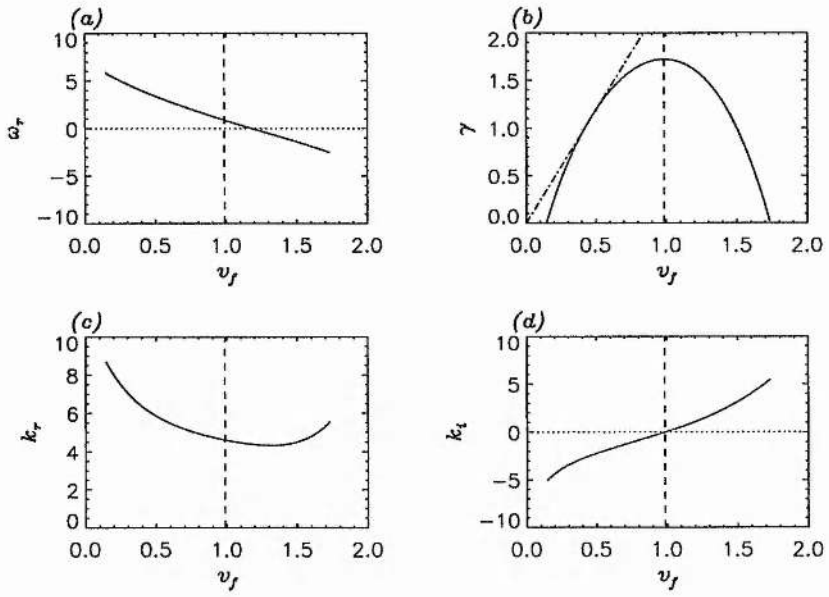

Figure 5.14: The (a) frequency, ω_r, (b) growth rate, γ, (c) real component of the wavenumber, k_r, and (d) imaginary part of the wavenumber, k_i as functions of the speed of reference frame, v_f, for the fast surface mode when $\Delta v = 2$ and $\delta = 0.1$. The vertical dashed lines indicate the reference frame with maximum growth rate and the horizontal dotted lines show where the variables are zero. The dot-dashed line in (b) indicates the maximum spatial growth rate of this mode in the frame $v_f = 0$, and has a gradient of $\gamma/v_g = 2.4$.

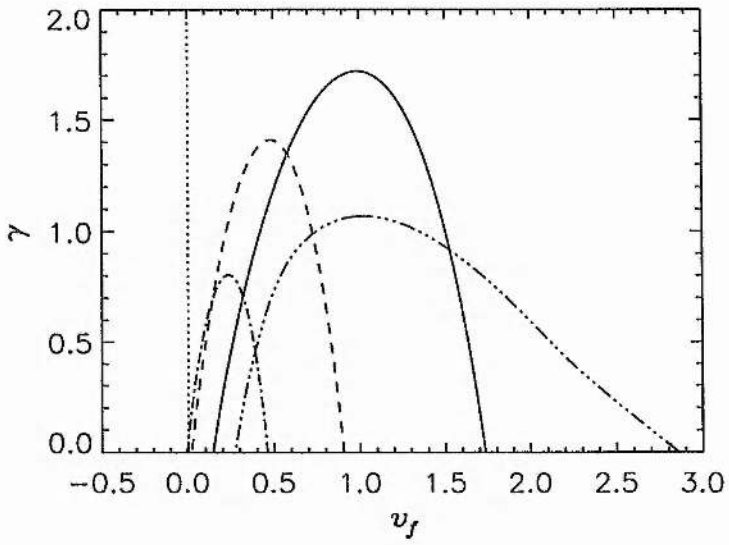

Figure 5.15: The growth rate, γ, of the fast surface mode as a function of reference frame, v_f, for $\Delta v = 0.5$ (dot-dashed line), $\Delta v = 1$ (dashed line), $\Delta v = 2$ (solid line) and $\Delta v = 5$ (triple-dot-dashed line).

Manuel and Samson (1993) modelled the surface mode numerically, using a super-sonic flow speed in the magnetosheath, and found that the pulse convected downstream as it grew, which is predicted by our model.

Figure 5.16 shows the variation of the growth rate as a function of v_f when $\Delta v = 2$ for various values of δ. We can see that the range of reference frames for which the double root has $\gamma > 0$ has little dependence on the value of δ. This indicates that the dominant length scale for these surface modes is the width of the boundary layer rather than the full depth of the magnetosphere. In order to show this more clearly, we renormalise the growth rate to the half-width of the boundary layer (δ), obtaining

$$\omega_{i\delta} = \gamma \frac{\delta}{d}. \tag{5.44}$$

The values of $\omega_{i\delta}$ at maximum growth rate are $\omega_{i\delta} = 0.172, 0.172, 0.169$ for the half-width of the boundary layer, $\delta = 0.05, 0.1, 0.2$, respectively. In other words, the maximum growth rate normalised to the depth of the magnetospheric cavity, d, scales as $1/\delta$. Thus the dimensional e-folding length over which the disturbance grows is proportional to δ. Physically, this corresponds to the surface mode being confined to the vicinity of the boundary layer, and being insensitive to the inner boundary where its amplitude is very small.

Finally, we consider the space-time evolution of fast surface modes propagating at an oblique angle to the flow, i.e., $\alpha \neq \pi/2$. The surface mode is unstable for all flow speeds when $\alpha = \pi/2$, however, for other

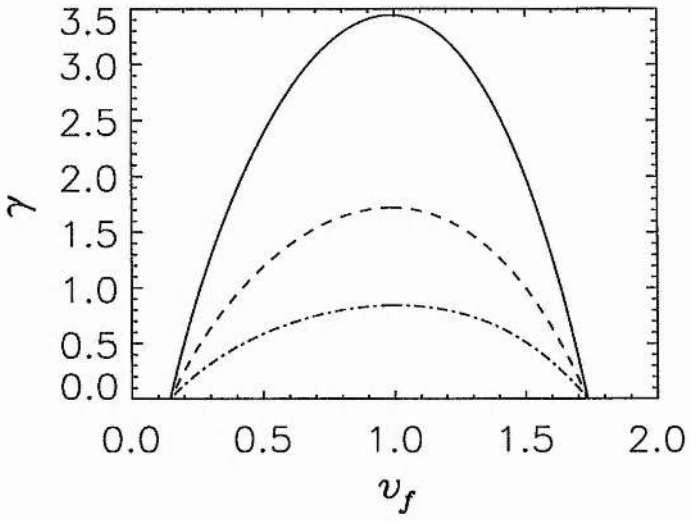

Figure 5.16: The growth rate, γ, of the fast surface mode as a function of reference frame, v_f, for $\Delta v = 2$ when $\delta = 0.05$ (solid line), $\delta = 0.1$ (dashed line) and $\delta = 0.2$ (dot-dashed line).

values of α, there is a cut-off speed below which the surface mode is stable. Conversely, if we choose a value of the flow speed, there is a value of α below which the mode is stable. For the case where $\Delta v = 2$, the surface mode is only unstable for $\alpha \gtrsim \pi/4$ (Figure 3.4). Figure 5.17 shows the growth rate as a function of reference frame when $\Delta v = 2$ for $\alpha = \pi/2$ (solid line), $\alpha = 2\pi/5$ (dashed line) and $\alpha = \pi/3$ (dot-dashed line). Here we have assumed v_f to be in the y-direction in order to consider the convection of the modes around the magnetospheric cavity flanks. Decreasing α slightly reduces the range of v_f for which the double root has $\gamma > 0$ and increases the value of v_f at which γ is first positive.

Fast Waveguide Modes

Next we examine the double roots corresponding to fast body modes. We saw in Figure 5.12 that the fast waveguide modes have bounded growth rates when $\delta > 0$. Thus, we may examine the double roots corresponding to the maximum in the growth rate for each mode.

Firstly, we examine the double root corresponding to the fundamental body mode when $\Delta v = 5$ and $\alpha = \pi/2$. Figure 5.18 shows the asymptotic growth rate of this double root as a function of reference frame. We can see that for these parameters, γ is positive in reference frames in the range $0.8 \lesssim v_f \lesssim 4.1$. Thus, this double root does not indicate that the pulse would be absolutely unstable in the rest frame of the magnetosphere. This is the case examined in Wright et al. (1999).

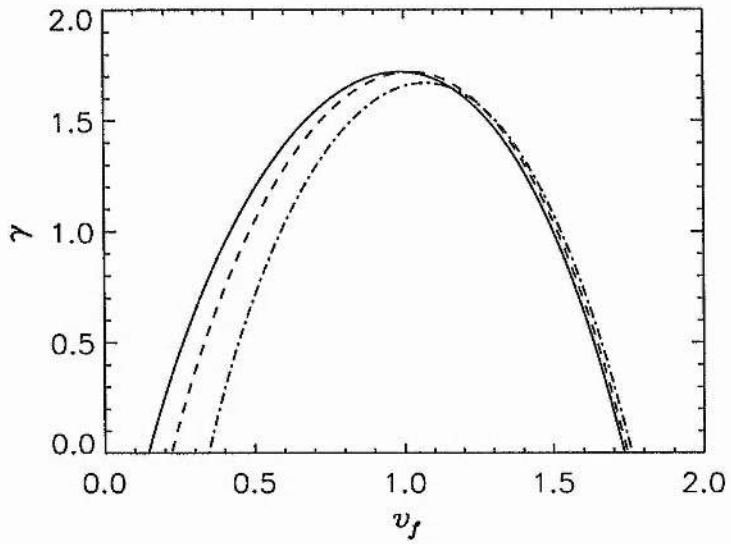

Figure 5.17: The growth rate, γ, of the fast surface mode as a function of reference frame, v_f, for $\Delta v = 2$ when $\alpha = \pi/2$ (solid line), $\alpha = 2\pi/5$ (dashed line) and $\alpha = \pi/3$ (dot-dashed line).

Now we examine the dependence of the asymptotic growth rate, γ, of the fundamental fast body mode on the reference frame speed, v_f, for different values of δ. Figure 5.19 shows the curves when $\delta = 0.05$ (solid line) and $\delta = 0.1$ (dashed line). Unlike the fast surface modes, the asymptotic growth rate does not simply scale as $1/\delta$. The peak of the growth rate occurs for a slightly lower value of v_f for the lower value of δ, and both of the points at which $\gamma = 0$ occur for lower values of v_f for lower δ.

Figure 5.20 shows the growth rate as a function of reference frame for $\Delta v = 5$ (solid line), $\Delta v = 7.5$ (dashed line) and $\Delta v = 10$ (dot-dashed line). Here, the left-most point where $\gamma = 0$ occurs for lower v_f as Δv increases. However, γ remains negative in the rest frame of the magnetosphere, even when the flow speed in the magnetosheath is ten times the equilibrium sound speed, c_{s2}, (for typical values, this corresponds to a magnetosheath flow speed of 1000 km/s) which is much larger than any observed. The range of reference frame in which $\gamma > 0$ becomes larger as the flow speed increases.

The fast body modes may only be unstable when

$$\Delta v \sin\alpha > c_f + c_{s2}, \tag{5.45}$$

(see Chapter 3). Thus decreasing α from $\pi/2$ will increase the change in flow speed (Δv) required for the modes to become unstable. Therefore, for $\Delta v = 5$, we require $\alpha \gtrsim \pi/4$ for instability. Figure 5.21 shows the range of reference frames for which the double root corresponding to the fundamental body

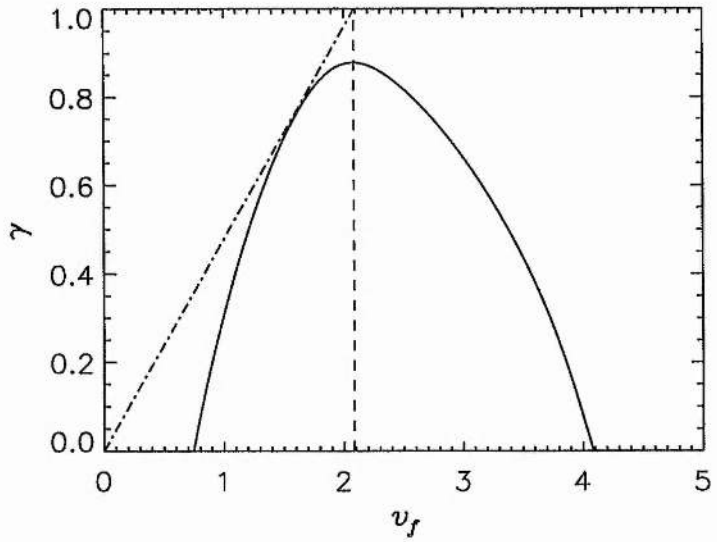

Figure 5.18: The growth rate, γ, of the fundamental fast body mode as a function of reference frame, v_f, for $\Delta v = 5$ when $\alpha = \pi/2$. The dot-dashed line shows the tangent to the curve having maximum gradient. In this case, $\gamma/v_f \approx 0.5$.

mode indicates that the system is absolutely unstable for this flow speed for $\alpha = \pi/2$ (solid line), $\alpha = \pi/3$ (dashed line) and $\alpha = \pi/4$ (dot-dashed line). Here the value of v_f at which the largest value of γ occurs is increased, while the maximum value of the growth rate is decreased, for smaller values of α. The range of reference frames for which $\gamma > 0$ is slightly decreased for $\alpha \neq \pi/2$.

Therefore, the double root corresponding to the fundamental fast body mode has $\gamma < 0$ in the rest frame of the magnetosphere for all directions of propagation and for all realistic values of the flow in the magnetosheath (or for all realistic flow speeds for which the mode is unstable).

Finally, we compare the growth rate against reference frame plots for the first two fast waveguide mode harmonics when $\Delta v = 5$ and $\alpha = \pi/2$. Figure 5.22 shows the growth rate as a function of reference frame for the first (solid line) and second (dashed line) harmonics. We can see that values of the group velocity at which the second harmonic has its maximum growth rate (corresponding to the value of v_f at which γ has its peak) is larger than that for the first harmonic, but that the maximum value of γ decreases with increasing harmonic number. Also, the speed of the reference frame for which γ first becomes positive increases with harmonic number.

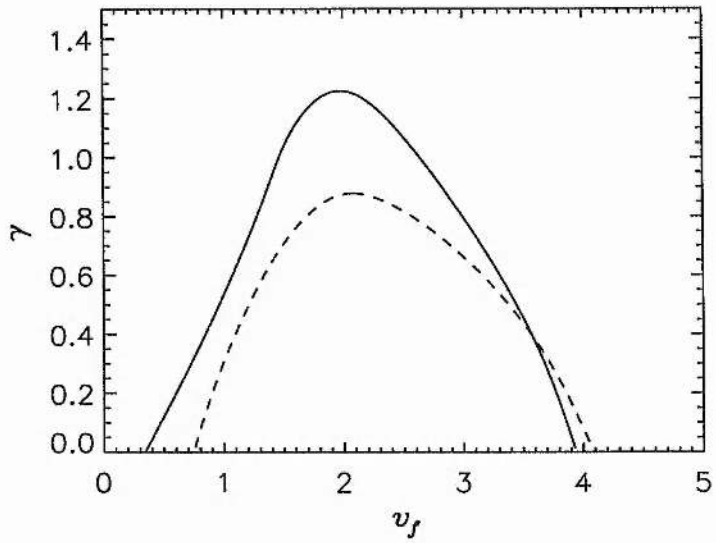

Figure 5.19: The growth rate, γ, of the fundamental fast body mode as a function of reference frame, v_f, for $\Delta v = 5$ and $\alpha = \pi/2$ and for two different values of δ. We have taken $\delta = 0.05$ (solid line) and $\delta = 0.1$ (dashed line).

Thus, the double roots corresponding to the fast waveguide modes do not indicate an absolute instability in the rest frame of the magnetosphere for all values of α and all realistic values of Δv for any mode harmonic.

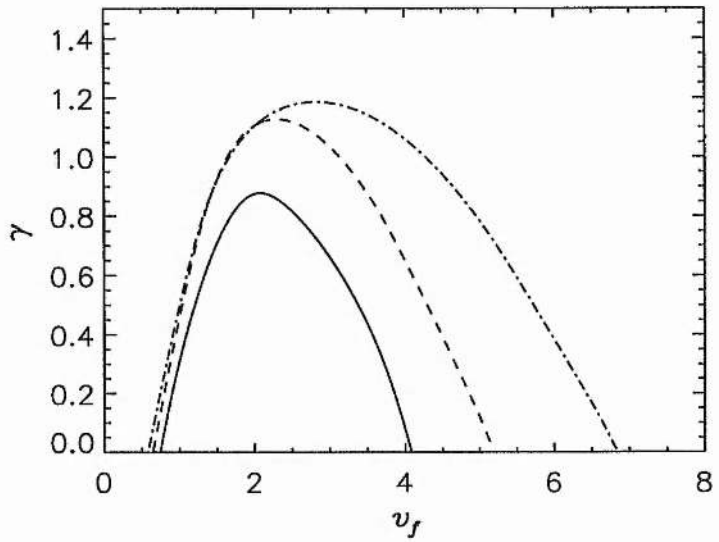

Figure 5.20: The growth rate, γ, of the fundamental fast body mode as a function of reference frame, v_f, for $\Delta v = 5$ (solid line), $\Delta v = 7.5$ (dashed line) and $\Delta v = 10$ (dot-dashed line) when $\alpha = \pi/2$.

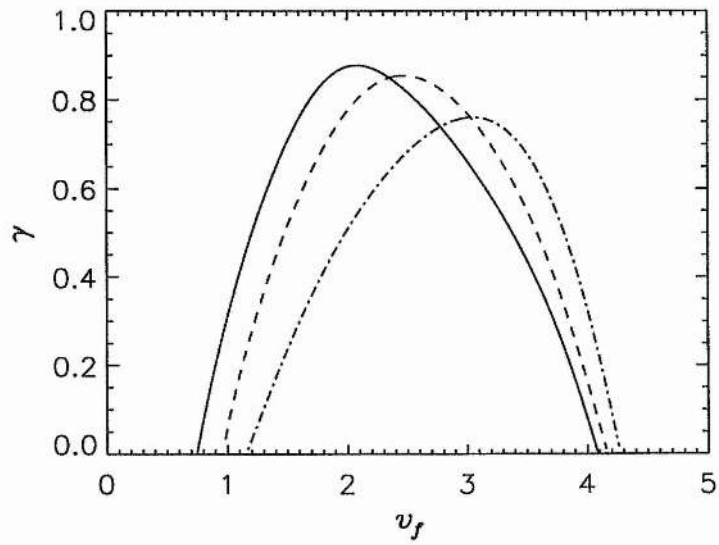

Figure 5.21: The growth rate, γ, of the fundamental fast body mode as a function of reference frame, v_f, for $\Delta v = 5$ when $\alpha = \pi/2$ (solid line), $\alpha = \pi/3$ (dashed line) and $\alpha = \pi/4$ (dot-dashed line) and $\delta = 0.1$.

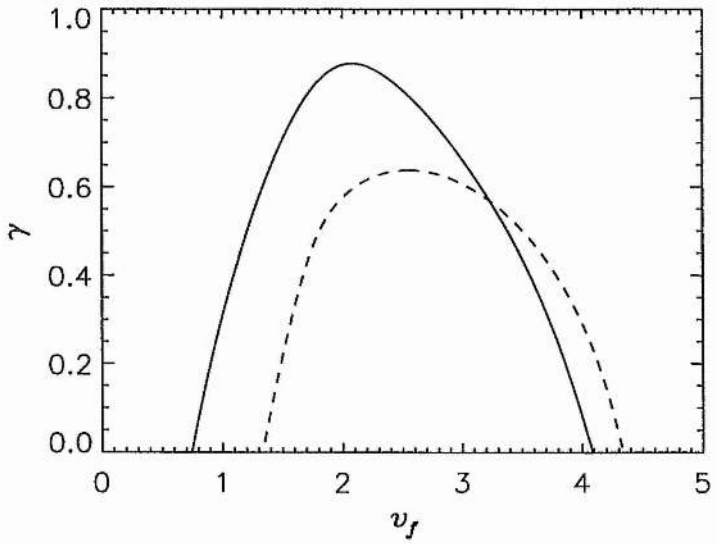

Figure 5.22: The growth rates, γ, of the fast body modes as a function of reference frame, v_f, for $\Delta v = 5$ when $\alpha = \pi/2$ and $\delta = 0.1$. The harmonics shown are the fundamental mode (solid line) and the second harmonic (dashed line).

Comparison Between Results Found by Theory and Those from a Numerical Simulation

Since we have used the fact that there is a double root of the dispersion relation at the maximum value of the growth rate for each mode rather than searching through four-dimensional (ω, k)-space, we cannot be totally sure that we have found all the double roots of the dispersion relation. However, we know that all the double roots having $k_i = 0$ must correspond to maxima of the growth rate in a reference frame moving with the group velocity of that normal mode. Thus, any double roots we have not found must have $k_i \neq 0$ for all v_f. Therefore, we compare the behaviour that we predict for two cases to that found by a two-dimensional, time-dependent, linear MHD code. For both these cases we have taken $\alpha = \pi/2$. The numerical simulations were performed by Dr A. W. Longbottom (Personal Communication, 1999) who wrote the code and supplied the raw data. These were then post-processed to produce the figures shown in this thesis.

First, we consider the case when $\Delta v = 2$. Here we have only one unstable mode to consider: the fast surface mode. Referring back to Figure 5.14, we see that we expect this mode to be absolutely unstable for references frames moving with speeds in the range $0.15 \lesssim v_f \lesssim 1.7$. In the numerical simulation, we disturb the equilibrium with an initial perturbation onto the equilibrium and solve for the system's evolution in time. The initial perturbation is chosen to have a wavelength in the y-direction similar to that of the fastest growing mode found by solving the dispersion relation (here we have used $k_y = 4$). This simply helps to minimise the time taken for the dominant modes to develop. The initial perturbation is also bounded in space. The form of the x-component of the perturbed velocity, u_{x1} of the initial perturbation along $x = 1$ is taken to be

$$u_{x1}(y) = \frac{1}{2}\left[1 + \cos\left(\frac{2\pi y}{5}\right)\right]\cos(k_y y), \quad -2.5 < y < 2.5, \tag{5.46}$$

and $u_{x1} = 0$ elsewhere. Figure 5.23 shows the initial perturbation, and the envelope enclosing it (dotted line). In the x-direction, we have assumed an exponential decay. Notice that the width of the initial perturbation is five times the depth of the magnetosphere (corresponding to a width of approximately 50 R_E); this is much wider than any 'localised' pulse we would expect to see on the magnetopause. However, the qualitative behaviour of the pulse should be the same in the (effectively) infinitely long numerical simulation as that of a small pulse on the magnetosphere. We merely choose this condition for numerical convenience and efficiency.

Now we look at the temporal evolution of the perturbation in different reference frames, v_f, and at different positions in these frames ($y' = y - v_f t$). In all cases we have plotted the value of the eigenfunction u_{x1} at $x = 0.5$. Figure 5.24 shows the perturbation as a function of time in the rest frame of the magne-

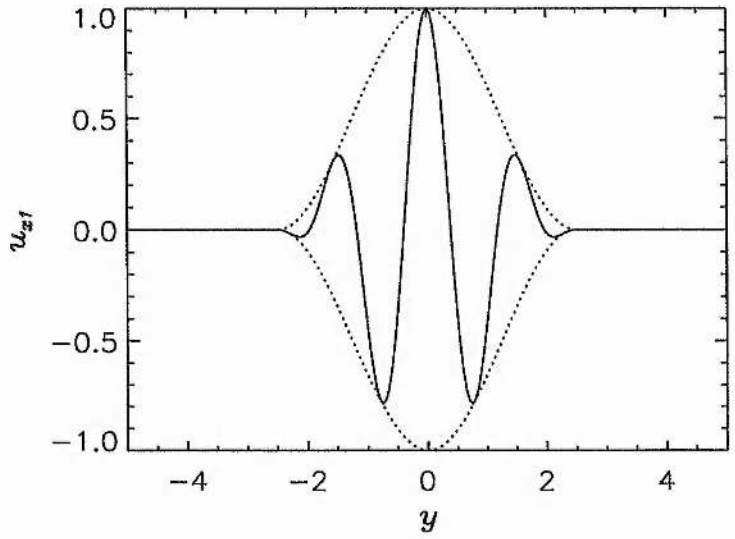

Figure 5.23: The initial pulse applied to the magnetospheric boundary (solid line), and its envelope (dotted line).

tosphere ($v_f = 0$) at the positions $y' = y = 0$ (the centre of the initial perturbation) and $y' = y = 2.5$ (on the leading edge of the perturbation). At $y' = 0$ we can see that the pulse initially grows, and then decays again so that at large time the signal is zero. This confirms that the instability is convective in this reference frame.

Figure 5.25 shows u_{x1} as a function of time for the same starting points as in Figure 5.24, this time in a reference frame moving with speed $v_f = 1$ (i.e., $y' = 0, 2.5$ or $y = t, 2.5 + t$). This reference frame is moving with a speed close to that of the fastest growing mode (which is $v_g = 0.986$), and we would expect the instability to be absolute in this frame. Indeed, we find that at both points the perturbations become very large within the time scale of our simulation. We have used log plots in this frame so that the oscillations and growth of the wave-packet can be more easily seen. Figure 5.26 shows a comparison between the function found in the numerical simulation with that predicted by our model. We can see that the two curves are very well matched at larger times. The global growth rate found by measuring the increase of the kinetic energy in the numerical simulation is 1.74, which should agree with the growth rate of our fastest growing mode. The fastest growing mode has a growth rate of 1.72, so the simulation and the prediction agree well.

Figure 5.27 shows u_{x1} as a function of time when $v_f = 2$. We see from Figure 5.14b that we expect to see a convective instability, and our simulation shows that this is indeed the case. This time we have plotted the function at $y' = -2.5$ (the trailing edge of the initial disturbance in the rest frame of the magnetosphere) and $y' = 0$ since we expect the observer's frame to convect across the pulse in the positive y-direction.

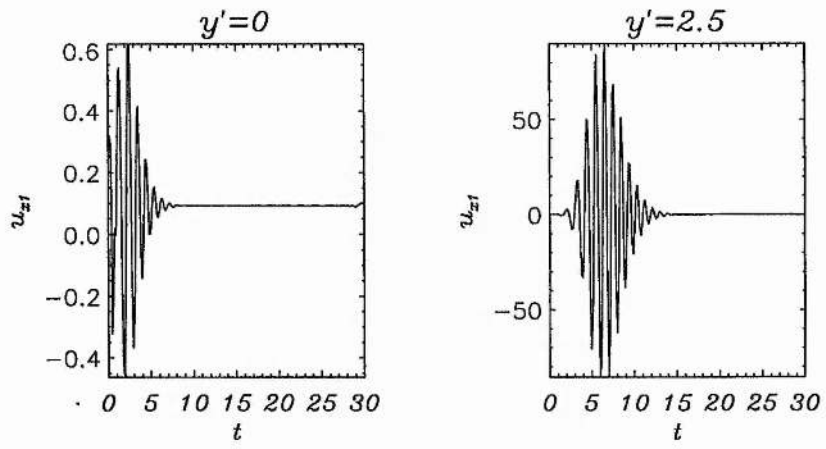

Figure 5.24: The perturbed velocity in the x-direction as a function of t for $y' = 0$ and $y' = 2.5$ in the rest frame of the magnetosphere ($v_f = 0$) at $x = 0.5$ and with $\Delta v = 2$.

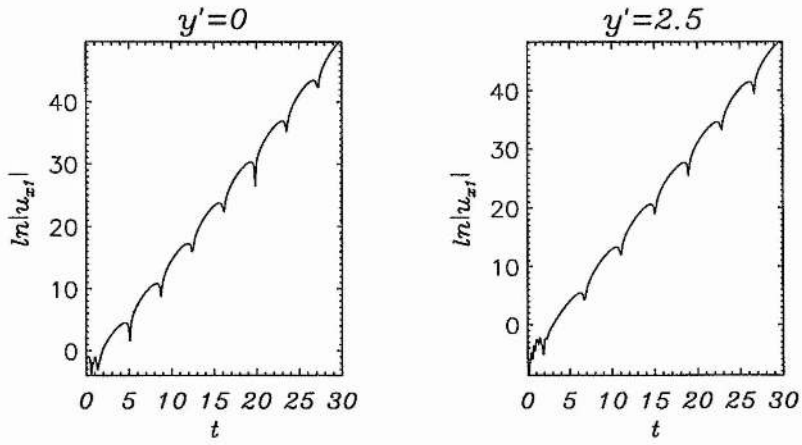

Figure 5.25: The logarithm of the magnitude of the perturbed velocity in the x-direction as a function of t for $y' = 0$ and $y' = 2.5$ in the reference frame moving with speed $v_f = 1$ at $x = 0.5$ and with $\Delta v = 2$.

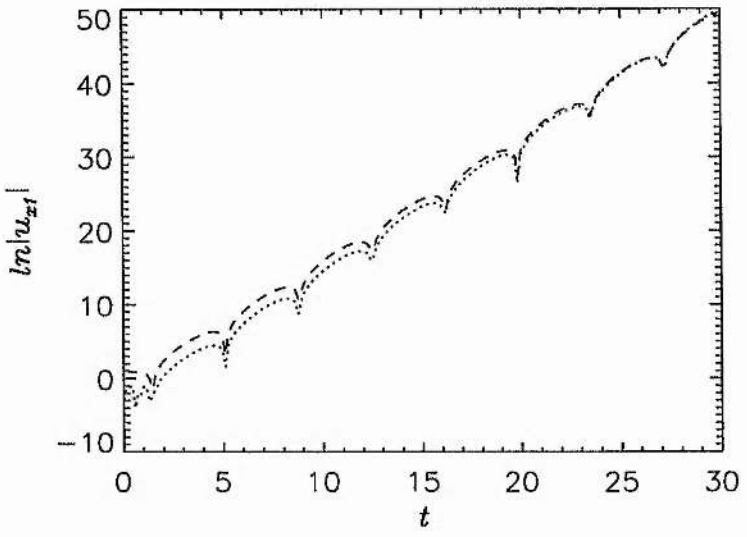

Figure 5.26: The logarithm of the absolute value of the perturbed velocity found by the numerical simulation (dotted line) and that predicted by our analysis (dashed line) at $y' = 0$, $x = 0.5$ and with $\Delta v = 2$.

In the case $\Delta v = 2$, $\alpha = \pi/2$ we have shown that the behaviour predicted by our analysis is the same as that shown in our numerical simulation. It is therefore unlikely that we have missed any double roots in our analysis of this case.

Next we compare our results to the numerical simulation when $\Delta v = 5$. Figure 5.28 shows the growth rates of the double roots corresponding to the first two body mode harmonics and the fast surface mode as functions of reference frame speed. We can see that the curve corresponding to the second harmonic (dashed line) is almost entirely beneath that of the fundamental fast body mode (solid line). Therefore we would expect the dominant plasma response to be governed by the fast surface mode when $v_f \lesssim 1.5$, and by the fundamental body mode in faster moving reference frames ($1.5 \lesssim v_f \lesssim 3.2$). Figure 5.29 shows the eigenfunction u_{x1} (the x-component of the perturbed velocity) as a function of t and y' when $v_f = 1.8$. From Figure 5.28 we can see that this reference frame moves faster than the fastest growing part of the fast surface mode, but slower than the fastest growing part of the fast waveguide mode. Therefore we would expect to see the wave-packet split into two parts, one body-like wave-packet moving in the positive direction and one surface-like wave-packet moving in the negative direction, and this is confirmed by Figure 5.29.

To confirm the spatial nature of these modes we have plotted the perturbed velocity, u_{x1}, as a function of y' and x in this reference frame when $t = 20$ in Figure 5.30. The part of the wave-packet that is centred

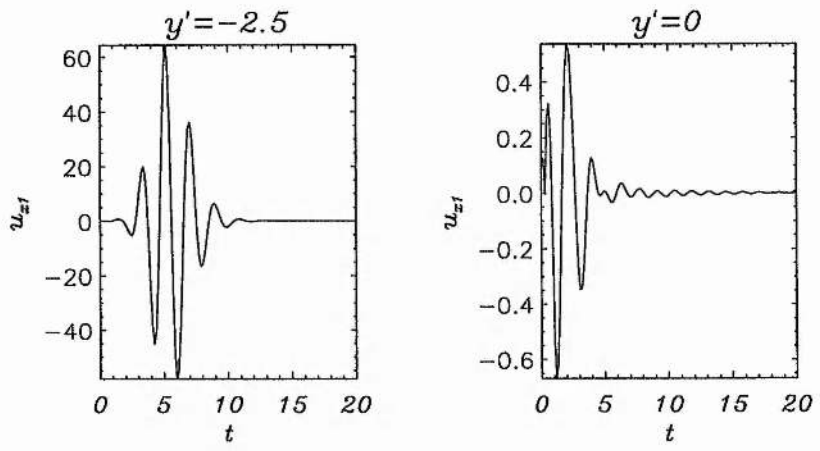

Figure 5.27: The perturbed velocity in the x-direction as a function of t for $y' = -2.5$ and $y' = 0$ in the reference frame moving with speed $v_f = 2$ at $x = 0.5$ and with $\Delta v = 2$.

with negative y' is clearly dominantly a surface mode with the perturbed velocity decaying away from the magnetopause, whereas the part with positive y' has a quarter wavelength body mode structure. We have also plotted the form of the eigenfunctions at $t = 20$ with x in Figure 5.31. The left hand plot shows the form of the disturbance at $y' = 0$ in the reference frame moving with speed $v_f = 1.05$. Here we expect the fast surface mode to dominate, and we see that the eigenfunction is indeed exponentially decaying into the magnetosphere. In the left hand plot, we show the form of the eigenfunction at $y' = 0$ in the reference frame moving with speed $v_f = 2.175$, in which we expect the body mode to dominate. Here, a half wavelength is trapped in the magnetosphere with decaying oscillations in the magnetosheath. In both plots we have normalised the eigenfunction to its maximum value.

Finally, we compare the perturbed velocity found in the numerical simulation with that predicted by our analysis in Figure 5.32. From Figure 5.28 we can see that the growth rate of the fast body mode is slightly larger than that of the fast surface mode in this reference frame and so we would expect to see the fast body mode dominant in the asymptotic limit. Therefore we have compared the results using the frequency and growth rate corresponding to the double root of the fast body mode. We can see that the two results agree for many cycles as t becomes large. The predicted value of the growth rate in this reference frame is 0.84, and that of the frequency is 2.72. The frequency found from the numerical results was 2.7, and the growth rate was 0.84, so once again the agreement is excellent.

These numerical results show good agreement with the behaviour predicted for the fast body and surface modes.

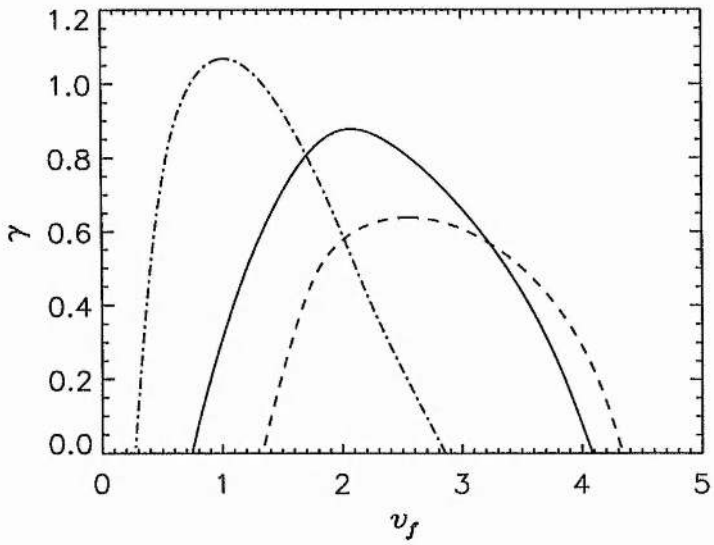

Figure 5.28: The growth rates, γ, of the fast modes as a function of reference frame, v_f, for $\Delta v = 5$ when $\alpha = \pi/2$ and $\delta = 0.1$. The modes shown are the fundamental body mode (solid line), the second harmonic (dashed line), and the fast surface mode (triple-dot-dashed line).

Spatial Growth Rates

In Figure 5.14b we included the tangent to the curve that passes through the origin and has the maximum gradient as a dot-dashed line. The gradient of this line is equal to the maximum spatial growth rate (in the magnetospheric rest frame) of the fast surface mode for this set of parameters ($\Delta v = 2$, $\alpha = \pi/2$ and $\delta = 0.1$). Here the spatial growth rate is $\gamma/v_f = 2.38$, corresponding to an e-folding length of $v_f/\gamma = 0.42$. Taking the depth to which modes may penetrate the magnetosphere to be 10 R_E, this implies that the modes will grow by a factor of e in a length along the magnetopause of 4.2 R_E.

The LLBL is very narrow at the nose of the magnetosphere, widening around the magnetopause and reaching a width of up to 1.5 R_E on the flanks. The flow speed is low near the nose, accelerating around the magnetopause to reach approximately the value of the flow speed in the up-stream solar wind at the flanks. Considering Figures 5.15 and 5.16 we can see that the spatial growth rate of the modes will generally decrease around the magnetosphere (we would expect to see an absolute instability very close the the nose of the magnetosphere). Since the growth rate is proportional to $1/\delta$, and $\gamma > 0$ for low values of v_f when the flow speed is low, we will expect to see large spatial growth rates (short e-folding lengths) near the nose of the magnetosphere. On the flanks, δ has increased and, taking $\Delta v = 5$, we can see from Figure 5.15 that the maximum growth rate has decreased. Thus, the spatial growth rate here is smaller than at the nose (the

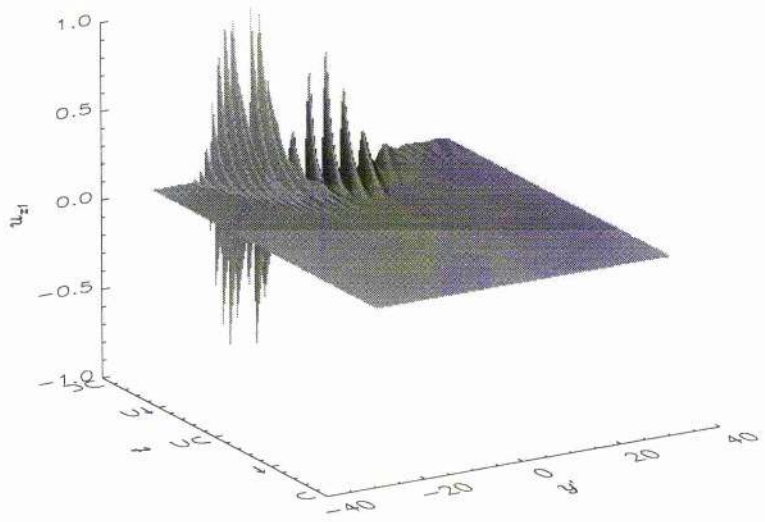

Figure 5.29: The eigenfunction u_{x1} as a function of t and y' in the reference frame moving with speed $v_f = 1.8$ at $x = 0.5$ and with $\Delta v = 5$.

e-folding length is about 7 R_E when $\delta = 0.1$).

Thus, although the fast surface mode is convectively unstable around most of the magnetosphere, we would expect it to grow to a significant amplitude as it convects around the flanks of the magnetosphere due to the short e-folding lengths near the nose. We would therefore expect non-linear effects to be responsible for the stabilisation of this mode, and to lead to vortex creation and merging. These non-linear effects have been shown to lead to the broadening of the LLBL in numerical simulations (Manuel and Samson, 1993).

Conversely, the fast waveguide modes only become unstable for relatively high magnetosheath flow speeds, at which point the width of the boundary layer is already relatively large. For the case shown in Figure 5.18 ($\Delta v = 5$, $\alpha = \pi/2$ and $\delta = 0.1$) the spatial growth rate of the fundamental fast body mode is $\gamma/v_f = 0.48$ which corresponds to an e-folding length around the magnetopause of about 20 R_E. This is of the same order as the distance from the nose of the magnetosphere to the point at which the field lines become aligned with the flow. For the same parameters, the e-folding length of the second harmonic is about 30 R_E. Therefore we would expect the amplitude of the fast waveguide modes to remain small on the flanks of the magnetosphere and would not expect non-linear effects to be significant for these modes. Decreasing the value of δ slightly decreases the e-folding length of the fast body modes, however halving the width of the boundary layer does not half the length over which the perturbation grows by a factor of e. Taking $\Delta v = 5$ and $\alpha = \pi/2$ with $\delta = 0.05$ for the fundamental fast body mode, we obtain an e-folding

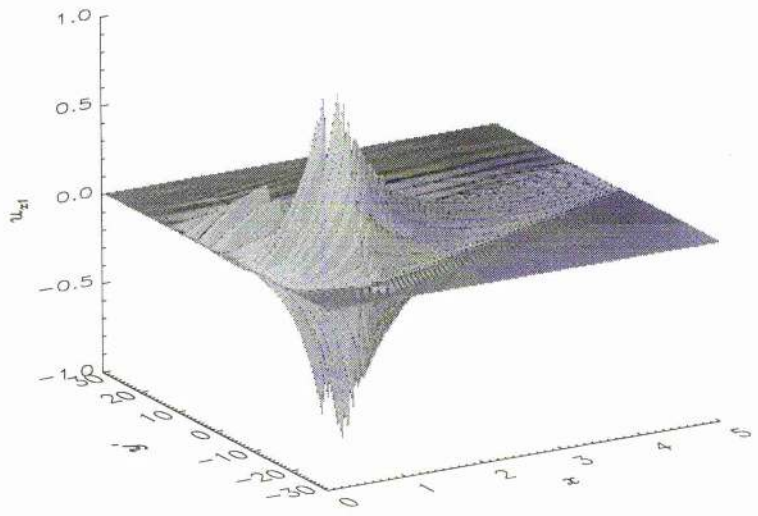

Figure 5.30: The eigenfunction u_{x1} as a function of x and y' in the reference frame moving with speed $v_f = 1.8$ when $t = 20$.

length of 15 R_E. In this case the amplitude of the mode would grow by a factor of e^2 over the distance around the flanks if the mode were excited at the nose. However, the fast body modes may only become unstable further around the flanks. Thus, even taking into account a thinner boundary layer, the fast body modes will probablu not grow to non-linear amplitudes on the flanks of the magnetosphere.

It has been suggested that field line resonances (FLRs) may be driven by Kelvin-Helmholtz unstable fast waveguide modes (Chapter 4). Here we show that the fast waveguide modes will convect along the magnetopause and will only drive the FLRs for a finite number of cycles. Mann et al. (1995) showed that the width of a continuously driven FLR decreases as $1/t$ while the amplitude grows as t. Continuously driven resonances are assumed to be damped by currents which they drive in the resistive ionosphere which limit the growth and prevent the formation of a singularity. If the fast body mode wave-packets are impulsively excited, our model suggests that the FLRs are unlikely to be driven continuously and so will never tend to a singular solution. However, it is also possible that there may be a quasi-steady source exciting unstable body modes in the magnetosphere. In this case, our model suggests that the driving source of the FLRs will remain small for all time. Either way, our model helps to explain the success of the linear theory of FLRs.

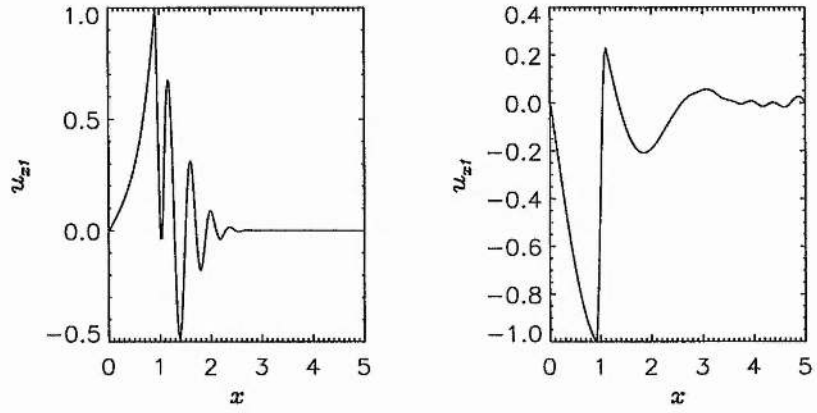

Figure 5.31: The perturbed velocity in the x-direction as a function of x when $t = 20$ at $y' = 0$ in (left) the frame moving with $v_f = 1.05$ and (right) the frame moving with $v_f = 2.175$.

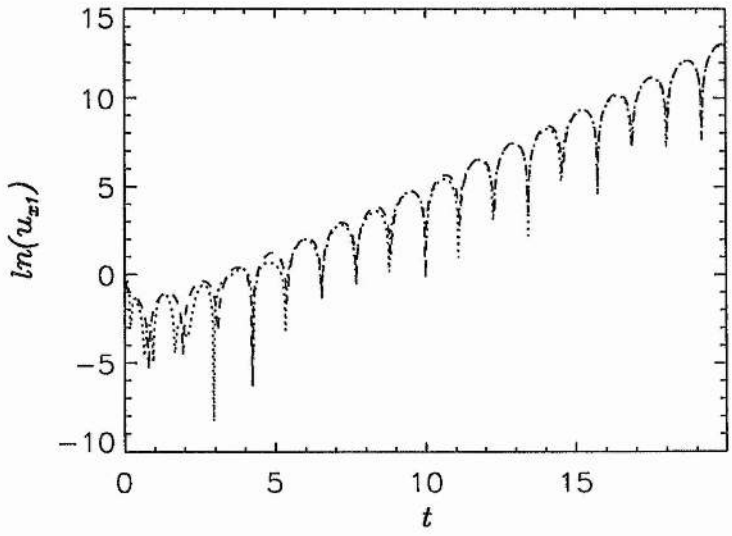

Figure 5.32: A comparison between the results found by the numerical simulation (dotted line) and the prediction from our instability analysis (dashed line).

5.4.2 Double Roots Corresponding to Slow Modes

The Slow Surface Mode

The slow surface mode is only unstable for a small range of flow speeds, which is strongly dependent on the direction in which the mode is propagating (see Section 3.2). For low flow speeds the surface mode is stable, and above the range for which it is unstable, it becomes a stable fast surface mode. Thus, for any value of the flow speed in the magnetosheath there will only be a narrow range of propagation angles for which the slow surface mode may be unstable. When unstable, this mode has a phase speed in the range for which slow body modes are expected ($c_T < v_{ph} < c_{slow}$). However, the growth rate is large enough that the mode remains dominantly evanescent in the magnetosphere.

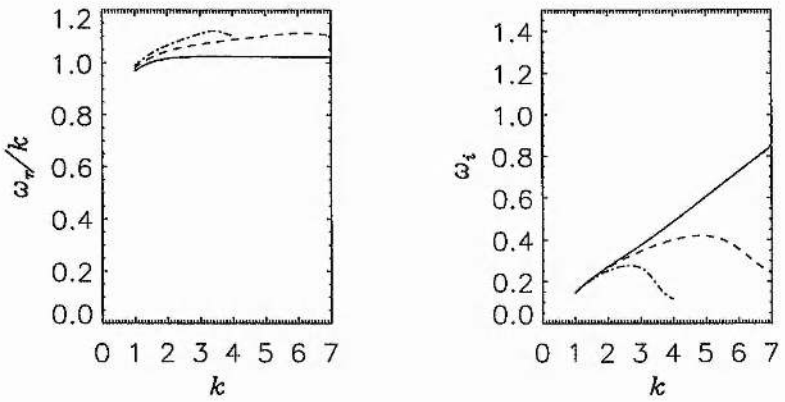

Figure 5.33: The phase speeds (a) and growth rates (b) of the slow surface mode when $v_o = 3.3$ and $\alpha = \pi/6$ for $\delta = 0$ (solid line), $\delta = 0.05$ (dashed line) and $\delta = 0.1$ (dot-dashed line).

Figure 5.33 shows the dispersion diagram for the unstable slow surface mode when $v_o = 3.3$ (i.e., $\Delta v = 3.3$) and $\alpha = \pi/6$ for different values of δ. Here again, the convergence of the numerical integration becomes difficult when the growth rate becomes low and we have selected ranges of k that preserve the main features of the curves. When $\delta = 0$ (solid line) we can see that the growth rate increases linearly with k so that $\omega_i \to \infty$ as $k \to \infty$. In a similar way to the fast surface modes, the introduction of a boundary layer with finite width dramatically changes this behaviour. For $\delta = 0.05$ (dashed line) and $\delta = 0.1$ (dot-dashed line) the growth rate has a maximum and $\omega_i \to 0$ as $k \to \infty$. Thus, we may study the double root corresponding to the slow surface mode only when $\delta \neq 0$ (otherwise it is not possible to define a suitable Laplace contour).

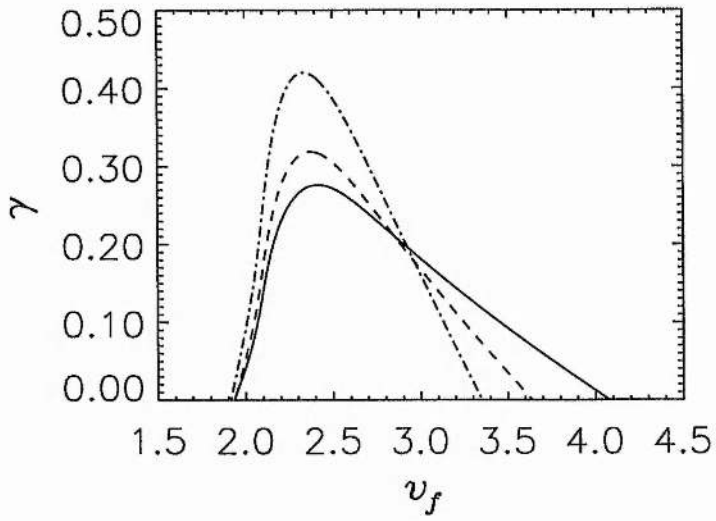

Figure 5.34: The asymptotic growth rate, γ as a function of reference frame speed, v_f, for the slow surface mode when $\Delta v = 3.3$, $\alpha = \pi/6$ and $\delta = 0.1$ (solid line), $\delta = 0.075$ (dashed line) and $\delta = 0.05$ (dot-dashed line).

Figure 5.34 shows the growth rate as a function of reference frame when $\Delta v = 3.3$, $\alpha = \pi/6$ and three different values of δ ($\delta = 0.1$ (solid line), $\delta = 0.075$ (dashed line) and $\delta = 0.05$ (dot-dashed line)). We can see that this double root clearly indicates a convective instability in the rest frame of the magnetosphere for all values of δ. As for the fast surface mode, the maximum growth rate is approximately proportional to $1/\delta$. The curves lie over each other for v_f lower than the maximum, however they diverge for higher v_f. This is due to the effect of the inner boundary in the magnetosphere which is felt due to the large value of the decay length for these modes.

Due to the narrow range of Δv for which the slow surface mode is unstable for any given α, we have compared the curves of γ as a function of v_f for various combinations of Δv and α rather than varying each independently. For each α we have selected a Δv close to the maximum in the growth rate as a function of the change in flow speed across the boundary layer, Δv. Figure 5.35 examines the dependence of the growth rate on the speed of reference frame for various combinations of Δv and α when $\delta = 0.1$. For $\Delta v = 1.9$, $\alpha = \pi/4$ (dashed line), the maximum growth rate is smaller and occurs for a lower value of v_f than for $\Delta v = 3.3$, $\alpha = \pi/6$ (solid line). The range of v_f for which $\gamma > 0$ is also reduced for the case with larger α. When $\Delta v = 1.1$ and $\alpha = \pi/3$ (dot-dashed line) the maximum growth rate is again reduced and the range of reference frame is again narrower. For all sets of parameters, the double root corresponding to the slow surface mode indicates a convective instability in the rest frame of the magnetosphere. The range

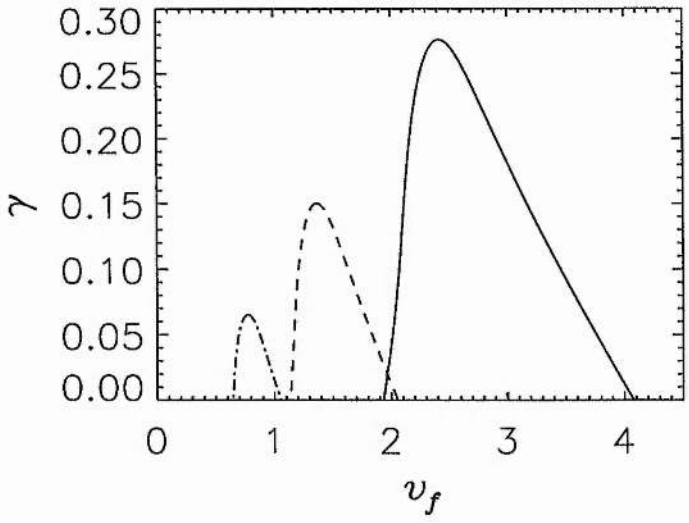

Figure 5.35: The asymptotic growth rate, γ as a function of reference frame speed, v_f, for the slow surface mode when $\delta = 0.1$ for $\Delta v = 3.3$ and $\alpha = \pi/6$ (solid line), $\Delta v = 1.9$ and $\alpha = \pi/4$ (dashed line) and $\Delta v = 1.1$ and $\alpha = \pi/3$ (dot-dashed line).

of v_f for which the mode is absolutely unstable is smaller than for either fast surface or fast body modes.

The Slow Waveguide Modes

The slow waveguide (or body) modes are the only type of modes which have bounded growth rate for all values of the flow speed, v_o, and propagation angle, α. The growth rates of these modes are small, with maximum values of the order of 10^{-2}. Figure 3.16 shows the dispersion of the slow waveguide mode when it is unstable for various values of v_o when $\delta = 0$. We recall that the mode is unstable for all k for which

$$v_{ph} < v_o \sin\alpha - c_{s2}, \tag{5.47}$$

so that for relatively low v_o the mode is unstable only for small k. For larger values of v_o, the mode is unstable for all k with the maximum of the growth rate occurring for large k. First we will examine the effect of a non-zero boundary layer on the dispersion of the slow body mode in the first instance, i.e., where $c_T < v_o \sin\alpha - c_{s2} < c_{slow}$. Figure 5.36 shows the dispersion of the fundamental slow body mode when $v_o = 2.55$ and $\alpha = \pi/4$ for different values of δ. When $\delta = 0$ (solid line) the growth rate of the mode is zero for $k \gtrsim 3$ and below that value it has a small positive value which tends to zero as $k \to 0$. Increasing the width of the boundary layer, so that $\delta = 0.05$ (dashed line), we find that the phase speed of the mode

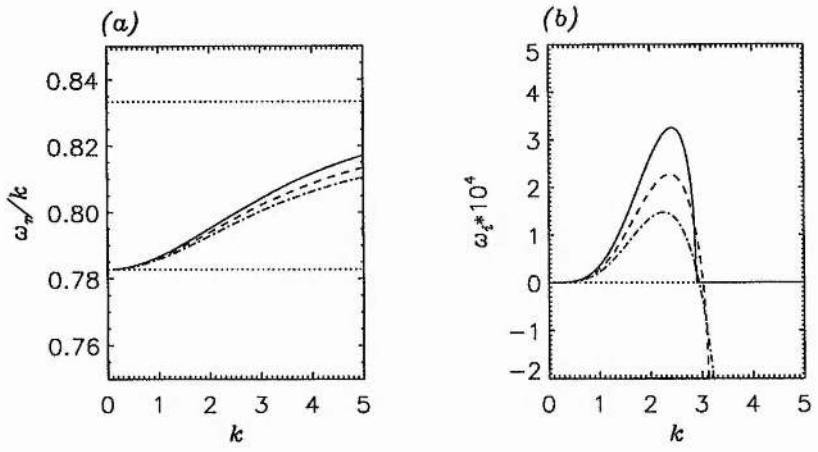

Figure 5.36: The phase speeds (a) and growth rates (b) of the fundamental slow body modes when $\alpha = \pi/4$ and $v_o = 2.55$ when $\delta = 0$ (solid line), $\delta = 0.05$ (dashed line) and $\delta = 0.1$ (dot-dashed line). The upper and lower dotted lines in (a) show the slow speed, c_{slow}, and the tube speed, c_T, respectively. The dotted line in (b) indicates the line $\omega_i = 0$.

is decreased slightly, and the growth rate is smaller than when $\delta = 0$. In this case, when $k \gtrsim 3$ the growth rate is negative. This trend is continued when we further increase the width of the boundary layer ($\delta = 0.1$, dot-dashed line).

Figure 5.37 shows the asymptotic growth rate of the fundamental slow body mode for the parameter values shown in Figure 5.36. The shapes of the curves are similar for all values of δ, and the point at which $\gamma = 0$ on the left side of the maximum is the same for all three curves and occurs at $v_f \approx 1.115$. As δ is increased, the maximum value of γ becomes smaller, and occurs for slightly lower v_f, with the right hand point where $\gamma = 0$ also occurring at lower values of v_f for higher values of δ.

Now we examine a case where the growth rate is positive for all k when $\delta = 0$. Figure 5.38 shows the phase speeds (a) and growth rates (b) of the fundamental slow body mode with $v_o = 5$ (i.e., $\Delta v = 5$) and $\alpha = 0$ for various values of δ. When $\delta = 0$ (solid line), the dispersion diagram of the mode is that shown in Figure 3.16, and the mode has a maximum when $k \approx 30$. Increasing the width of the boundary layer so that $\delta = 0.05$ (dashed line), we find that the phase speed of the mode is slightly reduced, and that the growth rate has a maximum when $k \approx 7$, and that the growth rate at the maximum is nearly an order of magnitude smaller than that of the mode when $\delta = 0$. Increasing δ further (dot-dashed line), we find that the growth rate is now negative when $k = 10$ and the maximum is smaller and occurs for lower k. Thus, as for the other modes, the introduction of a boundary layer with finite width decreases the growth rates of the modes.

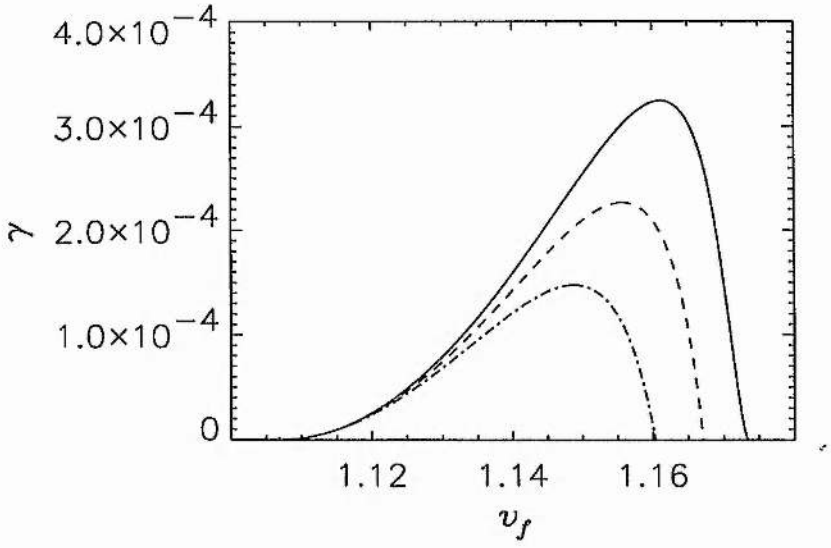

Figure 5.37: The asymptotic growth rate, γ of the fundamental slow body mode as a function of v_f when $v_o = 2.55$, $\alpha = \pi/4$ and $\delta = 0$ (solid line), $\delta = 0.05$ (dashed line) and $\delta = 0.1$ (dot-dashed line).

In Figure 5.39 we examine the asymptotic growth rate as a function of reference frame for the mode shown in Figure 5.38 (we have taken $\alpha = \pi/4$, $\Delta v = 5$ and the two non-zero values of δ). The range of reference frames for which the mode is absolutely unstable ($\gamma > 0$) is, like that of the slow surface modes, much narrower than for the fast modes. For $\delta = 0.05$, the mode is unstable for $1.18 \lesssim v_f \lesssim 1.1875$, whereas for $\delta = 0.1$ it is unstable for $1.11 \lesssim v_f \lesssim 1.18$. This mode is convectively unstable for all values of δ in the magnetospheric rest frame.

Finally, in Figure 5.40 we examine the asymptotic growth rate, γ, as a function of v_f for other combinations of Δv and α. In (a) we look at the case where $\alpha = \pi/6$ and $\Delta v = 4$. The maximum growth rate in this case is small, $\sim 10^{-3}$, and the mode is absolutely unstable for $1.9 \lesssim v_f \lesssim 2.1$, i.e., the wave-packet is convectively unstable in the rest frame of the magnetosphere. In (b) we have increased the angle at which the mode propagates so that $\alpha = \pi/3$, so that the effect of the flow is greater (here we have taken $\Delta v = 1.8$). Waveguide modes have smaller phase speeds as α increases so that the group velocity of the modes at maximum growth rate will also be smaller. In this case, $\gamma > 0$ for $0.639 \lesssim v_f \lesssim 0.640$, so the wave-packet remains convectively unstable in the rest frame of the magnetosphere. The growth rate is much smaller, with a maximum $\sim 10^{-8}$. These results imply that double roots corresponding to slow waveguide modes will not contribute to an absolute instability in the magnetospheric rest frame.

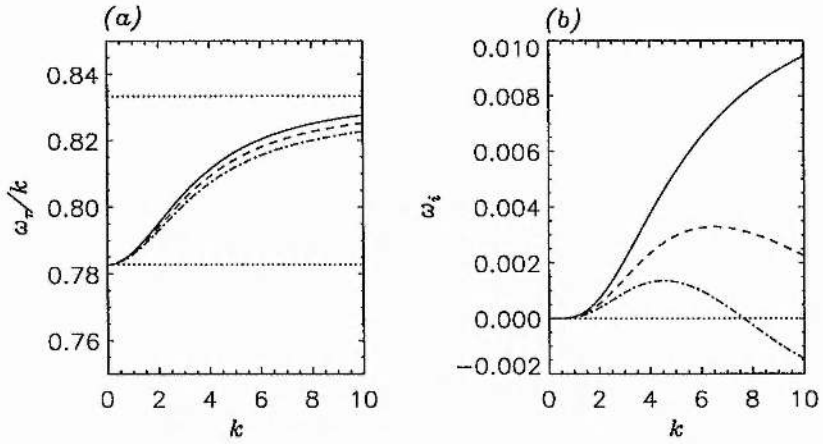

Figure 5.38: The phase speeds (a) and growth rates (b) of the fundamental slow body modes when $\alpha = \pi/4$ and $v_o = 5$ when $\delta = 0$ (solid line), $\delta = 0.05$ (dashed line) and $\delta = 0.1$ (dot-dashed line). The upper and lower dotted lines in (a) show the slow speed, c_{slow}, and the tube speed, c_T, respectively. The dotted line in (b) indicates the line $\omega_i = 0$.

Spatial Growth Rates

For all the slow surface modes shown in Figure 5.35 we find that the maximum spatial growth rate (the point that satisfies Equation (5.20)) for each mode is $\gamma/v_f \approx 0.1$, which corresponds to an e-folding length of $v_f/\gamma \approx 10$, i.e., about 100 R_E. This is much larger than the distance from the nose of the magnetosphere to the region of magnetotail geometry, so we would not expect to see this mode grow to a significant amplitude on the flanks of the magnetosphere. Like the fast surface mode, the growth rate (and therefore the spatial growth rate) varies as $1/\delta$, so we would expect to see a shorter e-folding length near the nose of the magnetopause where the LLBL is narrow. However, as the LLBL broadens the growth rate will drop and the overall increase in amplitude of the slow surface mode will remain small.

The maximum growth rates for slow waveguide modes occur when

$$\Delta v \sin\alpha - c_{s2} > c_{slow}, \tag{5.48}$$

and in the case $\Delta v = 5$, $\alpha = \pi/4$ and $\delta = 0.1$ the e-folding length of these modes is 1000 R_E. In the case where the mode is only just unstable with $\alpha = \pi/4$, $\Delta v = 2.55$, so that

$$c_T < \Delta v \sin\alpha - c_{s2} < c_{slow}, \tag{5.49}$$

the growth rates are much smaller, and in this case the e-folding length is about 10^5 R_E. Increasing the

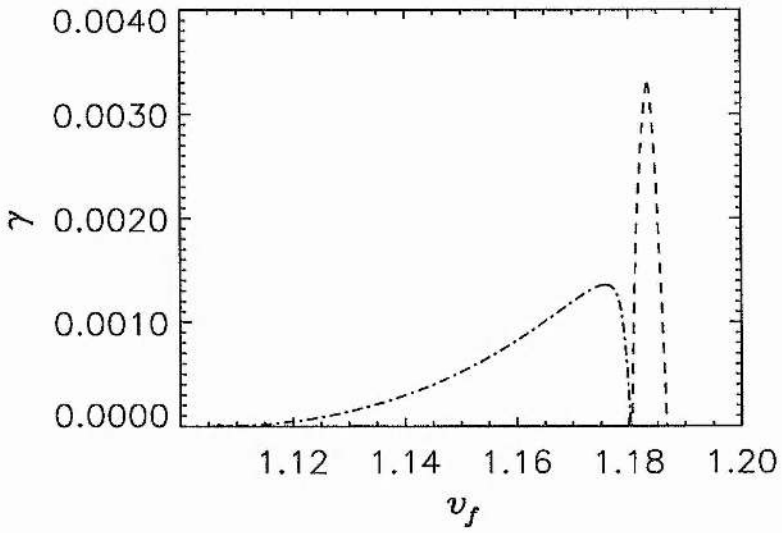

Figure 5.39: The asymptotic growth rate, γ of the fundamental slow body mode as a function of v_f when $\Delta v = 5$, $\alpha = \pi/4$ and $\delta = 0.05$ (dashed line) and $\delta = 0.1$ (dot-dashed line).

angle so that the propagation of the modes is more aligned with the flow decreases both the group velocity at maximum growth rate and the growth rate itself. In the case when $\Delta v = 1.8$ and $\alpha = \pi/3$, the e-folding length becomes $5 \times 10^7\ R_E$. Therefore, these modes will not grow significantly as they propagate around the flanks of the magnetosphere.

5.5 Obtaining an Approximate Result

The space-time response of the plasma is given by the Fourier-Laplace integral (Equation (5.2))

$$G(y,t) = \int_{-\infty}^{\infty} \int_{-\infty+i\sigma}^{\infty+i\sigma} \frac{w(\omega,k_y)}{D(\omega,k_y)} \mathrm{e}^{i(k_y y - \omega t)} d\omega dk_y, \tag{5.50}$$

where $w(\omega,k_y)$ is a driving function which is assumed to be analytic everywhere, $D(\omega,k_y)$ is the dispersion relation for the system, and σ satisfies

$$\sigma > \max\{\mathrm{Im}(\omega) : D(\omega,k_y) = 0, k_y \in \mathrm{R}\}. \tag{5.51}$$

Equation (5.50) can be expressed as

$$G(y,t) = \int_{-\infty}^{\infty} J(t,k_y)\, \mathrm{e}^{ik_y y} dk_y, \tag{5.52}$$

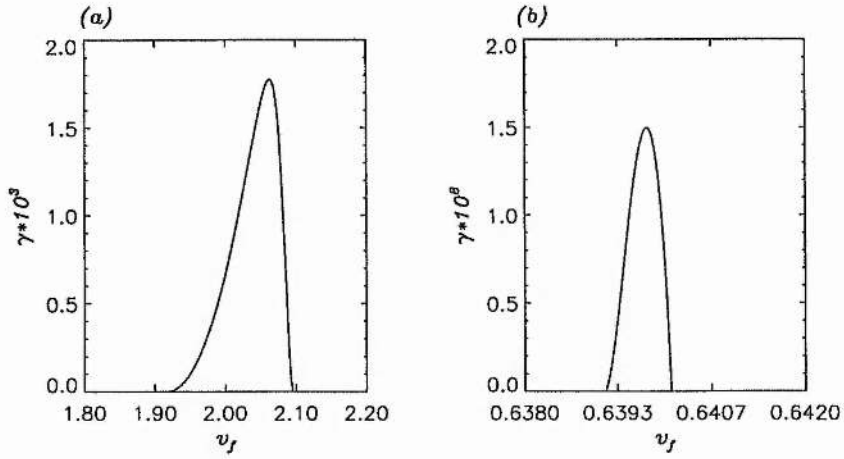

Figure 5.40: The asymptotic growth rate, γ, as a function of v_f for the fundamental slow body mode when (a) $\alpha = \pi/6$ and $\Delta v = 4$ and (b) $\alpha = \pi/3$ and $\Delta v = 1.8$. Here we have used $\delta = 0.1$ in all cases.

where

$$J(t, k_y) = \int_{-\infty+i\sigma}^{\infty+i\sigma} \frac{w(\omega, k_y)}{D(\omega, k_y)} \mathrm{e}^{-i\omega t} d\omega. \tag{5.53}$$

Now we assume that the dispersion relation $D(\omega, k_y)$ is analytic everywhere, and is defined such that for any value of k_y there is only one root $\omega(k_y)$ such that $D(\omega(k_y), k_y) = 0$. Choosing a value of k_y (e.g., $k_y = k_{y1}$), the integrand in Equation (5.53) has only one singularity (at $\omega(k_{y1})$), which will occur below the integration contour. Then by closing the integration contour in the negative half plane (so that causality is satisfied) and assuming that $\lim_{\omega\to\infty}\left(D^{-1}\right) \to 0$ at least as fast as $\omega^{-1} \to 0$, we may use the residue theorem to calculate $J(t, k_y)$. Therefore

$$J(t, k_y) = 2\pi i R, \tag{5.54}$$

where R is the residue of the integrand at $\omega = \omega(k_{y1})$, defined by

$$R = \lim_{\omega\to\omega(k_{y1})} \left\{ \frac{w(\omega, k_{y1})(\omega - \omega(k_{y1}))}{D(\omega, k_{y1})} \mathrm{e}^{-i\omega t} \right\}. \tag{5.55}$$

We use a Laurent series to approximate the dispersion relation close to $\omega(k_{y1})$, i.e.,

$$\begin{aligned} D(\omega, k_{y1}) &= D(\omega(k_{y1}), k_{y1}) + (\omega - \omega(k_{y1})) \frac{dD}{d\omega}(\omega(k_{y1}), k_{y1}) \\ &\quad + \frac{(\omega - \omega(k_{y1}))^2}{2} \frac{d^2 D}{d\omega^2}(\omega(k_{y1}), k_{y1}) + \ldots \\ &= A(\omega - \omega(k_{y1})) + B(\omega - \omega(k_{y1}))^2 + \ldots, \end{aligned} \tag{5.56}$$

(the principal part of the Laurent series is zero since D is assumed to be analytic). Therefore,

$$\begin{aligned} R &= \lim_{\omega\to\omega(k_{y1})}\left\{\frac{w\left(\omega,k_{y1}\right)\left(\omega-\omega\left(k_{y1}\right)\right)\mathrm{e}^{-i\omega t}}{A\left(\omega-\omega\left(k_{y1}\right)\right)+B\left(\omega-\omega\left(k_{y1}\right)\right)^{2}+\ldots}\right\} \\ &= \lim_{\omega\to\omega(k_{y1})}\left\{\frac{w\left(\omega,k_{y1}\right)\mathrm{e}^{-i\omega t}}{A+B\left(\omega-\omega\left(k_{y1}\right)\right)+\ldots}\right\} \\ &= \frac{w\left(\omega\left(k_{y1}\right),k_{y1}\right)}{A}\mathrm{e}^{-i\omega(k_{y1})t}, \end{aligned} \tag{5.57}$$

where A is also a function of k_{y1}. Therefore, we may write the Green's function for the plasma response as

$$G\left(y,t\right)=\int_{-\infty}^{\infty}C\left(k_{y}\right)\mathrm{e}^{-i\omega(k_{y})t}\mathrm{e}^{ik_{y}y}dk_{y}, \tag{5.58}$$

where

$$C\left(k_{y}\right)=\frac{2\pi iw\left(\omega\left(k_{y}\right),k_{y}\right)}{A\left(k_{y}\right)}, \tag{5.59}$$

and C represents the Fourier spectrum coefficient of the wave-packet. If there is more than one root of the dispersion relation for $k_y = k_{y1}$, the integral in Equation (5.53) must be expressed as the sum of the residues of the integrand at all these roots, and Equation 5.58 becomes

$$G\left(y,t\right)=\int_{-\infty}^{\infty}\sum_{n}\left\{C_{n}\left(k_{y}\right)\mathrm{e}^{-i\omega_{n}(k_{y})t}\right\}\mathrm{e}^{ik_{y}y}dk_{y}. \tag{5.60}$$

Now, if we expand $\omega\left(k_{y}\right)=\omega_{r}+i\omega_{i}$ in the region of the maxima of the growth rate of a mode (which we take to be located at $k_y = k_{ym}$, with $\omega\left(k_{ym}\right)=\omega_{rm}+i\omega_{im}$), we obtain

$$\omega_{r}\left(k_{y}\right)=\omega_{rm}+V_{gm}\left(k_{y}-k_{ym}\right)+\beta_{1}\left(k_{y}-k_{ym}\right)^{2}, \tag{5.61}$$

and

$$\omega_{i}\left(k_{y}\right)=\omega_{im}-\alpha_{1}\left(k_{y}-k_{ym}\right)^{2}, \tag{5.62}$$

where V_{gm} is the group velocity of the mode at $k_y = k_{ym}$ defined by $V_{gm}=\partial\omega_{r}/\partial k_{y}\left(k_{ym}\right)$, and

$$\alpha_{1}=-\frac{1}{2}\frac{\partial^{2}\omega_{i}}{\partial k_{y}^{2}}\left(k_{ym}\right)\quad\text{and}\quad\beta_{1}=\frac{1}{2}\frac{\partial^{2}\omega_{r}}{\partial k_{y}^{2}}\left(k_{ym}\right), \tag{5.63}$$

and we recall that $\partial\omega_{i}/\partial k_{y}\left(k_{ym}\right)=0$ since we are considering the maxima of the growth rate. Now we substitute these functions into Equation (5.58), to obtain

$$G\left(y,t\right)=\int_{-\infty}^{\infty}C\left(k_{ym}\right)\exp^{\left[\omega_{im}-\alpha_{1}\tilde{k_{y}}^{2}-i\left(\omega_{rm}+V_{gm}\tilde{k_{y}}+\beta_{1}\tilde{k_{y}}^{2}\right)\right]t+i(\tilde{k_{y}}+k_{ym})x}d\tilde{k_{y}}, \tag{5.64}$$

where $\tilde{k_{y}}=k_{y}-k_{ym}$. Since we are considering the fastest growing mode, it may be assumed that the amplitude of the Fourier spectrum will have a maximum at this value of k_{ym} after some finite time, as that

mode grows faster than modes with other values of k_y. Therefore, we have used only the leading term in the expansion of the Fourier spectrum. Then we can factorise the constant terms out of the Fourier integral so that

$$G(y,t) = C(k_{ym})\, I(y,t)\, \mathrm{e}^{-i\omega_{rm}t+\omega_{im}t+ik_{ym}y}, \tag{5.65}$$

where

$$\begin{aligned} I(y,t) &= \int_{-\infty}^{\infty} \mathrm{e}^{-(\alpha_1+i\beta_1)\tilde{k_y}^2 t+i(y-V_{gm}t)\tilde{k_y}}\, d\tilde{k_y} \\ &= \exp\left\{-\frac{(y-V_{gm}t)^2}{4\Delta t}\right\} \int_{-\infty}^{\infty} \exp\left\{-\Delta t\left(\tilde{k_y} - i\frac{y-V_{gm}t}{2\Delta t}\right)^2\right\} d\tilde{k_y}, \end{aligned} \tag{5.66}$$

where $\Delta = \alpha_1 + i\beta_1$. Now, using the substitution $h = \sqrt{\Delta t}\left(\tilde{k_y} - i\,(y - V_{gm}t)\,/2\Delta t\right)$, we obtain the integral,

$$I(y,t) = \frac{1}{\sqrt{\Delta t}} \exp\left\{-\frac{(y-V_{gm}t)^2}{4\Delta t}\right\} \int_{-\infty}^{\infty} \mathrm{e}^{-h^2}\, dh, \tag{5.67}$$

and, using the fact that

$$\int_{-\infty}^{\infty} \mathrm{e}^{-h^2}\, dh = \sqrt{\pi}, \tag{5.68}$$

we find

$$G(y,t) = C(k_{ym}) \sqrt{\frac{\pi}{\Delta t}} \exp\left\{-\frac{(y-V_{gm}t)^2}{4\Delta t}\right\} \mathrm{e}^{-i\omega_{rm}t+\omega_{im}t+ik_{ym}y}. \tag{5.69}$$

The growth in time of the wave-packet is then defined by

$$\frac{1}{\sqrt{t}} \mathrm{e}^{-i\omega_{rm}t+\omega_{im}t} \mathrm{e}^{-\frac{(y-V_{gm}t)^2}{4\Delta t}}. \tag{5.70}$$

If we change into a reference frame moving with speed V_f, so that $y' = y - V_f t$, this becomes

$$\frac{1}{\sqrt{t}} \mathrm{e}^{-i\omega'_{rm}t+\omega_{im}t} \mathrm{e}^{-\frac{\left(y'+\left(V_f-V_{gm}\right)t\right)^2}{4\Delta t}}, \tag{5.71}$$

where $\omega'_{rm} = \omega_{rm} - k_{ym}V_f$ is the Doppler shifted frequency at maximum growth rate in the frame moving with speed V_f. Expanding the quadratic and taking the limit $t \to \infty$, we find that the leading asymptotic behaviour of the exponent is

$$-i\omega'_{rm} + \omega_{im} - \frac{(V_f - V_{gm})^2}{4\Delta}, \tag{5.72}$$

so that the asymptotic growth rate in the reference frame moving with speed V_f is given by

$$\begin{aligned}\gamma &= \omega_{im} - \mathrm{Re}\left(\frac{(V_f - V_{gm})^2}{4\Delta}\right) \\ &= \omega_{im} - \frac{\alpha_1 (V_f - V_{gm})^2}{4(\alpha_1^2 + \beta_1^2)}.\end{aligned} \tag{5.73}$$

The analysis from Equation (5.58) to (5.73) is based upon a personal communication from Dr. M. S. Rudermann and Dr. A. N. Wright (1999). If there is more than one singularity of the integrand, we may expand each of the $\omega_n(k_y)$ as a quadratic in k_y, and obtain an equation of the form of 5.73 for each case. The asymptotic growth rate in any reference frame will be given by the largest growth rate given by the quadratic approximations for each singularity.

It is interesting to compare this asymptotic growth rate with that found from the pinching root condition of Briggs (1964). To arrive at the above result we assumed a second order Taylor series expansion of the dispersion relation was valid (Equations (5.61) to (5.63)). Now let us suppose that a dispersion relation exists that is exactly of the form of Equations (5.61) and (5.62), so that the above growth rate can be expected to be valid for all ω and not just in the vicinity of the maximum growth rate. We wish to confirm that the growth rate predicted using this method coincides with the growth rate of the double roots of an approximated dispersion relation defined by setting

$$D(\omega, k_y) = \omega - \omega_m - V_{gm}(k_y - k_{ym}) - (\beta_1 - i\alpha_1)(k_y - k_{ym})^2, \tag{5.74}$$

where $\omega_m = \omega_{rm} + i\omega_{im}$. In order to find double roots we wish to simultaneously solve

$$D = 0 \quad \text{and} \quad \frac{\partial D}{\partial k_y} = 0, \tag{5.75}$$

and with the approximated form of the dispersion relation, we may find the double roots analytically. In a reference frame moving with speed V_f, the dispersion relation may be rewritten as

$$\begin{aligned}D(\omega, k_y) &= D(\omega' + k_y V_f, k_y) \\ &= \omega' - \omega'_m + (k_y - k_{ym})(V_f - V_{gm}) - (\beta_1 - i\alpha_1)(k_y - k_{ym})^2 \\ &= 0,\end{aligned} \tag{5.76}$$

where $\omega' = \omega - k_y V_f$ and $\omega'_m = \omega_m - k_{ym} V_f$. Then, differentiating Equation (5.76) with respect to k_y and setting the result to zero we obtain the relationship

$$k_y - k_{ym} = \frac{V_f - V_{gm}}{2(\beta_1 - i\alpha_1)}. \tag{5.77}$$

Substituting this into Equation (5.76) we obtain

$$\omega' = \omega'_m - \frac{(V_f - V_{gm})^2}{4(\beta_1 - i\alpha_1)}. \tag{5.78}$$

Thus, the growth rate in the reference frame moving with speed V_f is given by

$$\begin{aligned} \gamma &= \omega_{im} - \mathrm{Im}\left(\frac{(V_f - V_{gm})^2}{4(\beta_1 - i\alpha_1)}\right) \\ &= \omega_{im} - \frac{\alpha_1 (V_f - V_{gm})^2}{4(\beta_1^2 + \alpha_1^2)}, \end{aligned} \tag{5.79}$$

which is identical to the result found above (Equation (5.73)).

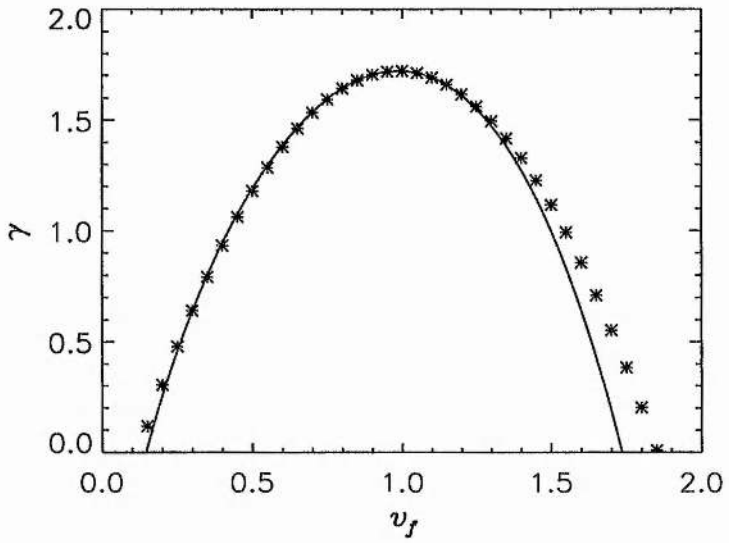

Figure 5.41: The asymptotic growth rate, γ, of the fast surface mode as a function of reference frame, v_f, for $v_o = 2$, $\alpha = \pi/2$ and $\delta = 0.1$. The solid line shows the growth rate at the double roots of the exact dispersion relation solved by our code, and the asterisks show the double roots of the quadratic approximation to the dispersion relation.

Now we compare this result with the results found using our code to find double roots of the exact dispersion relation as a function of frame. We may find the values of V_{gm}, α_1 and β_1 from the solutions of the dispersion relation found using our Runge-Kutta code, and use these to calculate the approximate growth rate. Figure 5.41 shows the comparison between the values of the asymptotic growth rate as a function of reference frame speed, v_f, found by solving for the double roots of the exact dispersion relation (solid line) and those found using the quadratic approximation for the dispersion relations (asterisks) for the fast surface mode when $v_o = 2$, $\alpha = \pi/2$ and $\delta = 0.1$ (this is the mode shown in Figure 5.14). We can see that for this mode, the quadratic approximation gives an accurate prediction for the growth rate as

a function of reference frame. The approximation is best for the lower values of v_f for which the growth rate is positive, and it is this side of the curve that we are most interested in, as the point where this curve crosses the $\gamma = 0$ line determines whether this double root may contribute to an absolute instability in the rest frame of the magnetosphere. Thus, in this case, we can estimate that the system is convectively unstable in the rest frame of the magnetosphere simply from the information contained in the dispersion of the mode for real k_y around the maximum of the growth rate, ω_i.

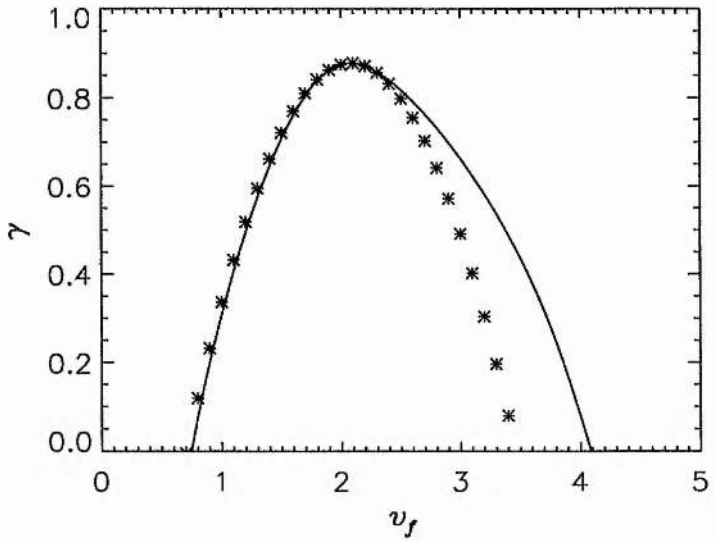

Figure 5.42: The asymptotic growth rate, γ, of the fundamental fast waveguide mode as a function of reference frame, v_f, for $v_o = 5$, $\alpha = \pi/2$ and $\delta = 0.1$. The solid line shows the growth rate at the double roots of the exact dispersion relation solved by our code, and the asterisks show the double roots of the quadratic approximation to the dispersion relation.

Figure 5.42 shows the asymptotic growth rates found by solving for double roots of the exact dispersion relation (solid line) compared with those found using our quadratic approximation to the dispersion relation (asterisks) as a function of reference frame speed, v_f, for the fundamental fast waveguide mode when $v_o = 5$, $\alpha = \pi/2$ and $\delta = 0.1$. Again the agreement is excellent for values of v_f below the maximum, however, here the agreement is not so good for higher values of v_f. The quadratic approximation will still predict correctly the fact that this double root indicates a convective instability in the rest frame of the magnetosphere. More accurate approximations could be made using higher order Taylor series approximations for the dispersion relation.

5.6 Conclusions

We have presented a method for determining whether an instability is absolute or convective and applied it to the Kelvin-Helmholtz instability on the flanks of the magnetosphere. We have discussed how the 'pinching' double roots of the dispersion relation determine the time-asymptotic behaviour of a wave packet impinging on the magnetopause and have shown that each normal mode of the system may be identified with one of these double roots. This allows us to study the space-time evolution of different types of modes to assess their effect on the magnetosphere. We have used the definition of the e-folding length of the wave-packet to determine which modes will grow to the largest amplitudes.

We have modelled a uniform, bounded magnetosphere connected to a uniform, semi-infinite magnetosheath by a finite width boundary layer over which the flow speed changes continuously. The inner boundary of the magnetosphere allows us to study a system in which both surface and body modes may propagate, so that we may study the evolution of a pulse made up of both kinds of modes.

Most numerical simulations of the KHI at the magnetopause boundary have considered an unbounded magnetosphere, leading to the generation of surface modes only (e.g., Miura, 1984, 1987; Manuel and Samson, 1993; Wu, 1986). Simulations using a long numerical domain and feeding seed perturbations in at one end (Manuel and Samson, 1993) show that the disturbances are convected downstream as they grow - in other words, these simulations have shown that we would expect the KHI at the magnetopause to be convectively unstable. Wu (1986), also showed that in a reference frame moving at half the total change in flow speed across the boundary, the disturbance eventually fills the whole domain, i.e., in that reference frame it is an absolute instability; however Wu claimed this phenomenon as proof that the instability is convective. We have shown that the surface mode is indeed convective in the rest frame of the magnetosphere for most flow speeds, and that in the reference frame in which the flow is symmetric across the boundary layer we would expect to see an absolute instability. However, seeing an absolute instability in one reference frame is not evidence for the behaviour in a different frame. A particular example we have found is for the surface mode when the flow speed is low. When $v_o = 0.5$ the fast surface mode is absolutely unstable in the magnetospheric rest frame, yet if studied in a simulation such as Wu's, we would find that the pulse would expand to fill the whole domain. Thus, Wu's claim that the KHI is convective could not be substantiated by his results.

We have presented the formalisation of the concepts of absolute and convective instabilities, and shown that (for most flow speeds) the fast surface mode is convectively unstable in the magnetospheric rest frame, and that it is absolutely unstable in a rest frame moving with half the jump in flow speed. Despite their

convective nature, the fast surface modes will grow significantly as they convect around the flanks of the magnetosphere. The e-folding length is typically about 4 R_E, so that the modes will grow to amplitudes at which non-linear effects will occur within the distance around the magnetospheric flanks. This non-linear behaviour has been shown to lead to vortex creation and merging, and in turn to the formation (or broadening) of the LLBL (Miura, 1987; Manuel and Samson, 1993).

Fast body modes may also become unstable on the flanks of the magnetosphere, although these modes require higher flow speeds than the fast surface modes. These modes may couple to, and drive, FLRs in the magnetosphere (Mills and Wright, 1999a, see also Chapter 4). However, these globally oscillatory modes have proved surprisingly elusive in data, suggesting that the body of the magnetosphere on the flanks is not significantly disrupted. We have shown that we would expect these modes to also convect around the magnetosphere as they grow, leaving zero disturbance at large time. The e-folding lengths of these modes are of the order of the distance from the nose of the magnetosphere to the start of the tail-like geometry ($\approx 20 - 30\ R_E$). Thus, we may conclude that they may not grow sufficiently large to be observable in this region. However, these modes will still drive FLRs as they convect around the flanks. Depending on the nature of the driving source for the fast body modes, the FLRs will either be continuously driven, but with the driving amplitude remaining small, or the FLRs will be driven for only a finite amount of time. Either way, this theory helps to explain why the linear theory of FLRs has been so successful in explaining the observations. The results for both fast surface and body modes are summarised in Figure 5.43. In order to calculate the flow speeds we have taken the sound speed in the magnetosheath to be 100km/s, and the lengths are calculated by assuming that waves may penetrate the magnetosphere to a depth of 10 R_E.

We have also considered unstable slow body and surface modes and found that the double roots corresponding to these modes also indicate that they represent a convective instability in the rest frame of the magnetosphere. We have found that the e-folding lengths of the slow surface modes are of the order of 100 R_E, and those of the slow body modes are of the order of at least 1000 R_E. Thus neither of these types of modes are likely to grow to an observable amplitude as they convect around the magnetosphere.

We have compared our results to those from a two-dimensional, time-dependent MHD code and found that the behaviour predicted by our method agrees well with that found in the numerical code. We have also derived an approximation for the frame dependent growth rate using a quadratic approximation for the dispersion relation. We found that this approximate result agrees well with the curves found using the exact dispersion relation, especially for the surface modes.

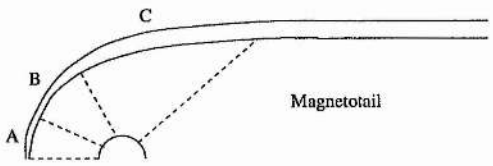

Region	Δv /kms^{-1}	LLBL Width /R_E	Fast Surface Modes	Waveguide Modes
A	$\Delta v \leq 100$	$\leq 0.5 R_E$	Absolutely Unstable	Leaky
B	$100 \leq \Delta v \leq 400$	$0.5 \rightarrow 1.5 R_E$	Convectively Unstable $L_c \sim 2 R_E$ Non-linear effects $\rightarrow$ LLBL	Trapped
C	$\Delta v \geq 400$	$\sim 1.5 R_E$	Convectively Unstable $L_c \sim 7 R_E$	Convectively Unstable $L_c \sim 20 R_E$ Driving of FLRs

Figure 5.43: A schematic of the regions of the magnetosphere we are considering, with a summary of the behaviour of the fast surface and body modes.

In summary, our results suggest that the fact that all the unstable wave-packets on the flanks of the magnetosphere represent convective instabilities can explain the robustness of the body of the magnetospheric flanks.

Chapter 6

Trapping and Excitation of Magnetospheric Modes III - In the Magnetotail

6.1 Introduction

In this chapter we examine Kelvin-Helmholtz driven waves in a magnetotail like geometry. Here the magnetic field lines are stretched out parallel to the flow in the magnetosheath (see Figure 6.1). The fact that the magnetosphere has a long tail has been known since the proposal of the open magnetosphere model by Dungey (1961). Dungey (1965) calculated the length of the magnetotail using the fact that reconnected field lines are connected to the Earth via the polar caps. Knowing the electic and magnetic field strengths at the caps, the speed at which a field line would move across the cap was calculated and thus the time taken for a field line to convect from the reconnction point at the nose of the magnetosphere to the point at which the lines reconnect in the tail could be calculated. Multiplying this time by the solar wind speed, Dungey obtained a value of about 1000 R_E for the length of the magnetotail. Magnetometer data show observations of oscillations with frequencies of the order of millihertz and lower (Herron, 1967) and eigenfrequencies of the right order have been found by McClay and Radoski (1967) using a cylindrical magnetotail (the 'theta' model). The magnetic field in the 'theta' model was taken to be uniform in the top and bottom of the waveguide, but with a reversal of direction across the middle. Models including the plasma sheet were

also developed (Siscoe, 1969; McKenzie, 1970b).

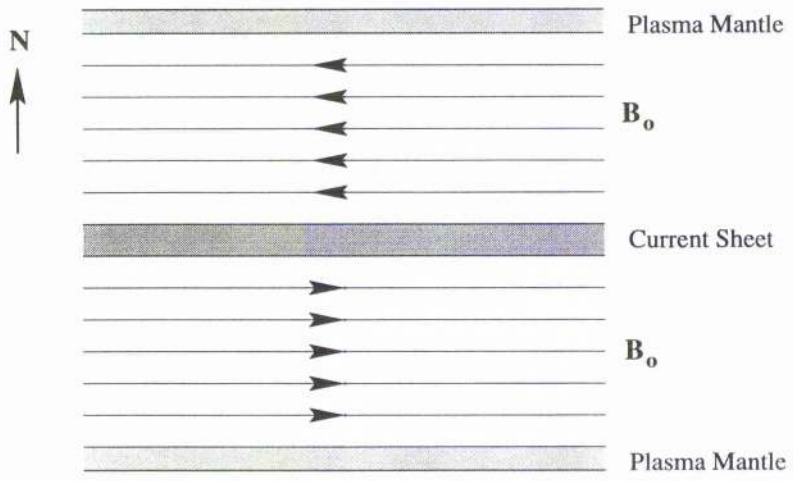

Figure 6.1: A schematic diagram of the geometry in the magnetotail. We have taken a cut from North to South and the Earth is to the left in this picture.

More recently work has included the behaviour of waves in the neutral sheet at the centre of the magnetotail (e.g., Seboldt, 1990; Liu et al., 1995). It has been shown that waves may be trapped in the low Alfvén speed region at the centre of a current sheet (Edwin et al., 1986; Smith et al., 1997).

Pu and Kivelson (1983) modelled the surface waves at the magnetopause in a magnetotail like geometry. They considered an infinite uniform region on either side of the magnetopause with both the magnetic fields in the magnetosphere and magnetosheath being parallel to the flow in the magnetosheath. They showed that the flow speed at the onset of the instability of the fast surface mode varies little with the angle of propagation and was close to the onset of the instability for an incompressible plasma.

Elphinstone et al. (1995) observed fast waves travelling towards the Earth using the IMP 8 satellite. These modes were linked with a source 30 R_E down tail and indicated that the magnetotail could act like a waveguide for these modes. Allan and Wright (1998) showed that the non-uniform nature of the magnetic field allows these fast waveguide modes to couple to Alfvén waves in the outer tail which will travel earthward faster than the fast modes that are generated in the neutral sheet.

In this Chapter we study the nature of the magnetospheric boundary in the tail. Consequently, we do not concern ourselves with a detailed model of the plasma sheet and its boundary layer, but take a uniform magnetotail, which serves as a suitable channel within which modes may be trapped, excited or

leaky. Just as in the flank case (Chapter 3), it is the local properties on either side of the magnetopause that determine the nature of the boundary, and so we model our tail as effectively an extended lobe. Our solutions correspond to fast and slow surface and body/waveguide modes. We have taken a node of the x-component of perturbed velocity at $x = 0$ (corresponding to the inner tail) so our modes are equivalent to sausage modes in the model of Roberts (1981b). The structure of this chapter is as follows: in Section 6.2 we set up our model, the results for slow modes are presented in Section 6.3 and those for fast modes are presented in Section 6.4. Finally, in Section 6.5 we summarise our results and discuss the consequences for the magnetotail.

6.2 Model

We use the model set up in Chapter 2 and place the magnetic field in the magnetosphere parallel to the flow in the magnetosheath - i.e., we have set $\chi = 0$ in Equations (2.13) to (2.35) and $B_{oz} = 0$ in Figure 2.1. Therefore, our necessary condition for the existence of stable modes becomes

$$v_o \cos\alpha - c_{s2} < v_{ph} < v_o \cos\alpha + c_{s2}. \tag{6.1}$$

Figure 6.2 shows the regions of $v_{ph} - \alpha$ space for which stable modes may exist as the region with negatively sloped shading, and the regions for which we would expect stable modes to be oscillatory in the magnetosphere (where we expect to find body modes) as regions with positively sloped shading. The unshaded regions are those where we would expect to find modes that are evanescent in the magnetosphere (surface modes) if the modes were stable. As with Figure 2.4 the overlap of the shaded regions indicates the regions of parameter space in which we would expect to see stable body modes and the overlap between the region where stable modes may exist and the unshaded regions show where we would expect to find stable surface modes. In this figure we have taken $\beta = 0.5$, $\epsilon = \rho_1/\rho_2 = 0.192$ and $v_o = 4$.

Measurements of magnetopause crossings in the tail show that the density ratio between the magnetosphere and magnetosheath can lie anywhere within the range $0.01 < \epsilon < 0.2$. We have chosen a value close to the upper end of this range as this allows us to see unstable modes for lower flow speeds. Figure 6.3 shows the dependence of the characteristic wave speeds in the magnetosphere on the density ratio ϵ. We can see that, when the density range is lowest, the fast slow and tube speeds become much larger than the sound speed in the magnetosheath and since the onset of instability for the fast body modes (for example) requires that

$$v_o > \frac{c_f + c_{s2}}{\cos\alpha}, \tag{6.2}$$

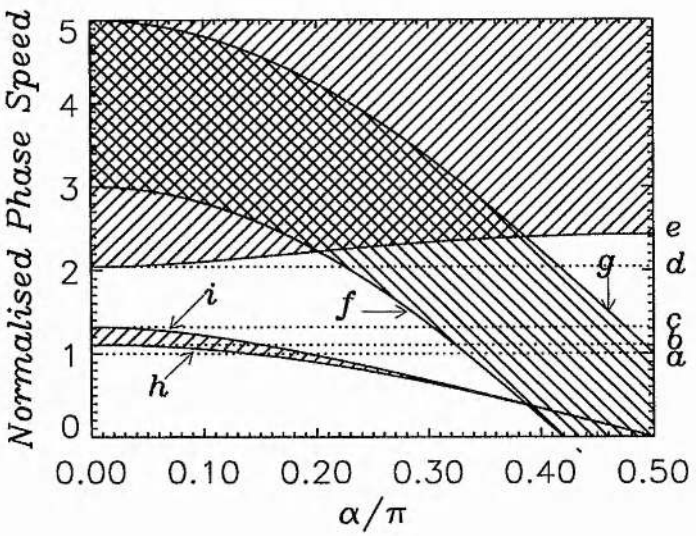

Figure 6.2: The variation of the regions of phase speed (given in units of c_{s2}) where different mode types may exist with propagation angle α. Of the dotted lines, a is the magnetosheath sound speed (c_{s2}), b is the tube speed ($(c_T\ (\alpha = 0))$ in the magnetosphere when $\alpha = 0$, c is the sound speed in the magnetosphere (c_{s1}) and d is the Alfvén speed in the magnetosphere (v_{a1}). Of the solid curves, f is the lower cut-off for stable modes ($v_{ph} = v_o \cos\alpha - c_{s2}$) and g is the corresponding upper cut-off ($v_{ph} = v_o \cos\alpha + c_{s2}$), while the curve of the fast speed, c_f, is represented by line e, the slow speed, c_{slow}, by i and tube speed, c_T by line h. Here as in most of the following diagrams $\beta = 0.5$, $\Gamma = 5/3$ and $\epsilon = 0.192$. We have also taken $v_o = 4.0$.

we can see that we would require very large values of the sonic Mach number, v_o in the magnetosheath in order for the modes to become unstable. Indeed, for the trapping of fast body modes we require

$$v_o > \frac{c_f - c_{s2}}{\cos\alpha}, \tag{6.3}$$

which would still be very high.

6.3 Slow Modes

6.3.1 Slow Surface Modes

Here we examine the behaviour of the slow surface modes in this geometry. When $v_o = 0$, there is effectively no difference between this geometry and that on the flanks (discussed in Chapter 3). Therefore, the values of the phase speed of the slow surface modes for large values of k as a function of α will be the same

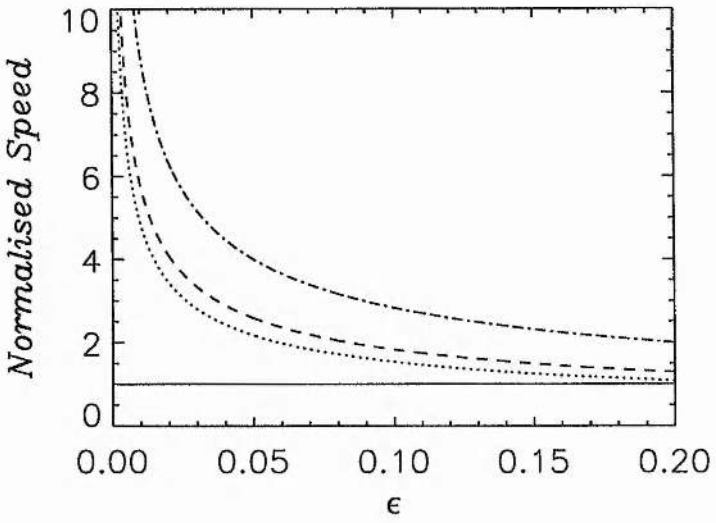

Figure 6.3: The variation of the characteristic wave speeds in the magnetosphere as a function of the density ratio, ϵ. The sound speed in the magnetosheath, c_{s2}, is shown as a solid line, the tube speed in the magnetosphere, c_T, is shown as a dotted line, with the slow speed, c_{slow} represented by a dashed line, and the fast speed, c_f, as a dot-dashed line. We have taken $\alpha = 0$ in this figure.

as those in Figure 3.9.

Figure 6.4 shows the dispersion of the slow surface mode when $v_o = 0$ and $\alpha = 0$. For these parameters the mode is stable, and we have shown both the mode with positive phase speed and that with $v_{ph} < 0$. When $v_o = 0$ the positive and negative modes are symmetrical with $v_{ph} \to \pm 0.700$ as $k \to \infty$.

In Figure 6.5 we see the evolution of the slow mode with increasing magnetosheath flow speed when $k = 3$ for various values of α. We see that the phase speeds of both the positive and negative waves increases as the flow speed increases. In all cases, the forward propagating mode levels out with $v_{ph} \approx c_T$ and then decreases slightly to the point of coalescence with the negative wave. The phase speed of the backward propagating wave increases with gradient close to $\cos\alpha$ up to the point at which the two modes coalesce and become unstable. Thus, the onset of instability for these modes is given approximately by

$$v_o \approx \frac{c_T + v_{pho}}{\cos\alpha}, \tag{6.4}$$

where v_{pho} is the phase speed of the mode with positive phase speed when $v_o = 0$. The growth rate of the unstable mode is bounded, and the phase speed increases until the mode becomes stable again, and once more separates into two distinct modes. The phase speed is now in the interval $c_{slow} < v_{ph} < c_f$ and so these modes have become stable fast surface modes. The upper of these two modes goes on to coalesce

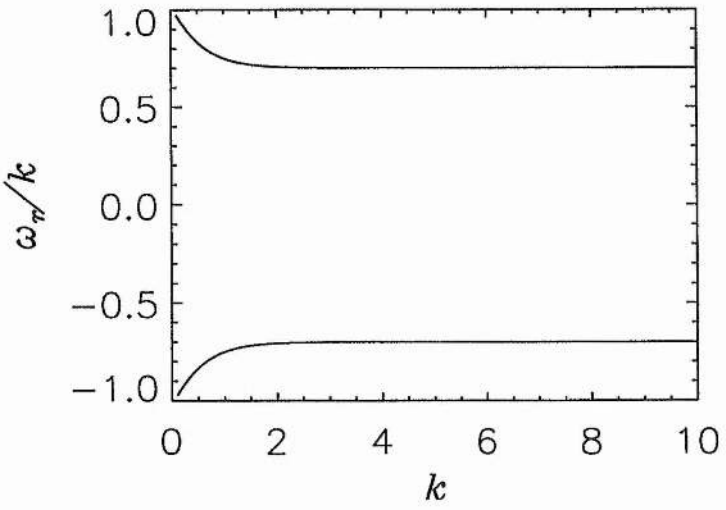

Figure 6.4: The dispersion of the slow surface modes when $v_o = 0$ and $\alpha = 0$.

with the original fast surface mode which we have also shown in this plot. The behaviour of these modes will be described in more detail in Section 6.4. The phase speed of the lower of these modes decreases and $v_{ph} \to c_{slow}$ as $v_o \to \infty$. This mode becomes unstable when $v_{ph} = v_o \cos\alpha - c_{s2}$, but the growth rate is bounded and remains small.

The energy density of a wave is defined as (see Equation (2.36) in Section 2.3.1)

$$E = \frac{1}{4}\omega_r \frac{dD}{d\omega_r} A_o^2, \tag{6.5}$$

where A_o is the amplitude of the plasma displacement. This definition requires that the energy density of both of the slow modes must be positive when $v_o = 0$. We use this definition to plot the energy of the modes when $k = 3$ and $\alpha = 0$ while they are stable in Figure 6.6. Note that this expression for the energy density is for a wave with real frequency. When ω is complex, we simply plot the energy as zero for convenience. The phase speeds of the modes are shown in the Figure 6.6a, with different line styles representing different modes (the horizontal dashed line represents the fast speed in the magnetosphere). We can see that the energy of the lower slow surface mode (dotted line) becomes negative when the phase speed of the mode becomes positive in the rest frame of the magnetosphere. The energy of the upper slow surface mode (dot-dashed line) remains positive until the onset of the instability which occurs when the positive and negative energy waves coalesce as described in Section 3.5. When these modes restabilise, we see that the upper branch (dotted line) is now a negative energy wave, whereas the lower branch (triple-dot dashed line) is a

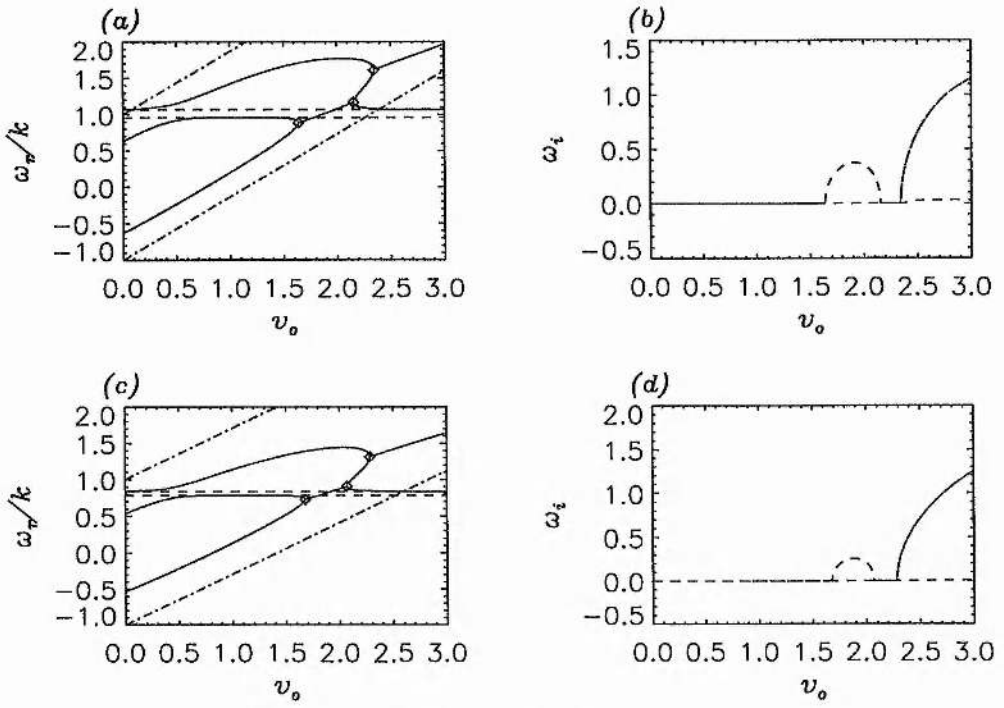

Figure 6.5: The phase speeds (a and c) and growth rates (b and d) of the fundamental slow surface modes as functions of v_o when $k = 3$ and $\alpha = \pi/6$ (a and b) and $\alpha = \pi/4$ (c and d). In each case we have shown both the modes with positive and negative phase speed when $v_o = 0$. We have also shown the fast surface mode which is leaky when $v_o = 0$ in the case $\alpha = \pi/6$. The diamonds mark the points where modes coalesce as predicted by Section 3.5. The diagonal dot-dashed lines show the upper and lower cut-off speeds, $v_{ph} = v_0 \cos\alpha \pm c_{s2}$ and the lower and upper dashed lines show the characteristic phase speeds, c_T and c_{slow}, respectively.

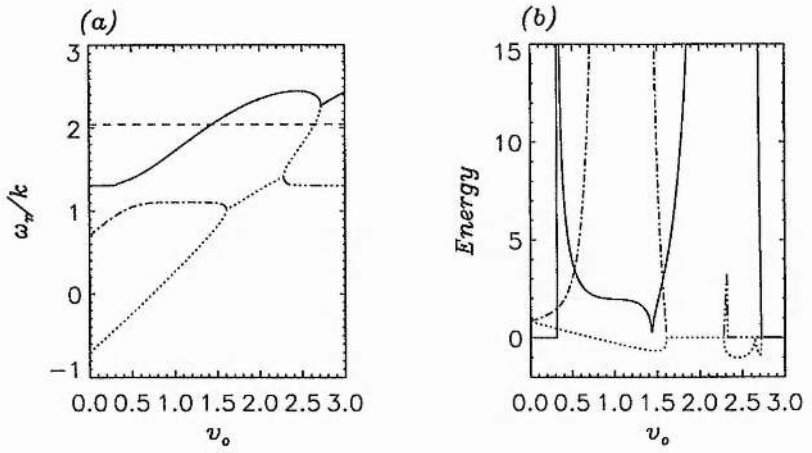

Figure 6.6: The evolution of the phase speed (a) and energy density (b) of the various surface modes with v_o when $k = 3$ and $\alpha = 0$. The different modes are shown with different line styles to show which energy plot corresponds to which mode. The horizontal dashed line in (a) indicates the position of the fast speed in the magnetosphere c_f.

positive energy wave. Therefore, the restabilising of the mode occurs due to the splitting into a positive and negative energy wave of the unstable mode. The original fast surface mode (solid line) has positive energy for low values of v_o. The energy of this mode approaches zero when $v_{ph} = c_f$ and the mode changes to a body mode, but remains positive. Similarly, the energy of the negative energy fast surface mode (dotted line) approaches zero as the mode changes from a fast surface to a fast body mode. The onset of instability once more occurs at the point at which two modes with opposite energies coalesce.

Figure 6.7 shows the dispersion diagram of an unstable slow surface mode. We have taken $\alpha = 0$ and $v_o = 2$. This mode is unstable for all values of k, and the growth rate grows nearly linearly as k increases. The phase speed is in the region where $c_T < v_{ph} < c_{slow}$ for almost all k except thos near $k = 0$, however, the wavenumber in the magnetosphere is dominantly imaginary (as shown in Figure 6.8), so that the character of the mode is that of a surface mode.

Looking at Figure 6.3 we can see that for all realistic values of ϵ, the slow surface mode is the only mode propagating parallel to the magnetic field which can be stable for $v_o = 0$, since this is the only mode which has a phase speed in the stable range ($-c_{s2} < v_{ph} < c_{s2}$). Figure 6.9 shows the value of the asymptotic (as $k \to \infty$) value of the phase speed of the slow surface mode as a function of ϵ when $v_o = 0$ and $\alpha = 0$ (we have taken $k = 10$). The value of the phase speed for large k varies very little with ϵ, so that the mode will always be stable for low flow speeds. However, for lower values of ϵ the value of the tube speed, c_T,

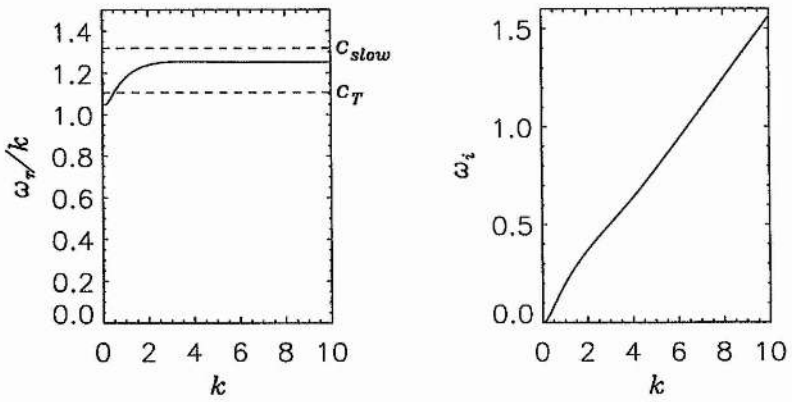

Figure 6.7: The phase speed and growth rate of the slow surface mode as functions of k when $v_o = 2$ and $\alpha = 0$.

becomes much larger, so that the modes will only become unstable for much higher values of the flow speed.

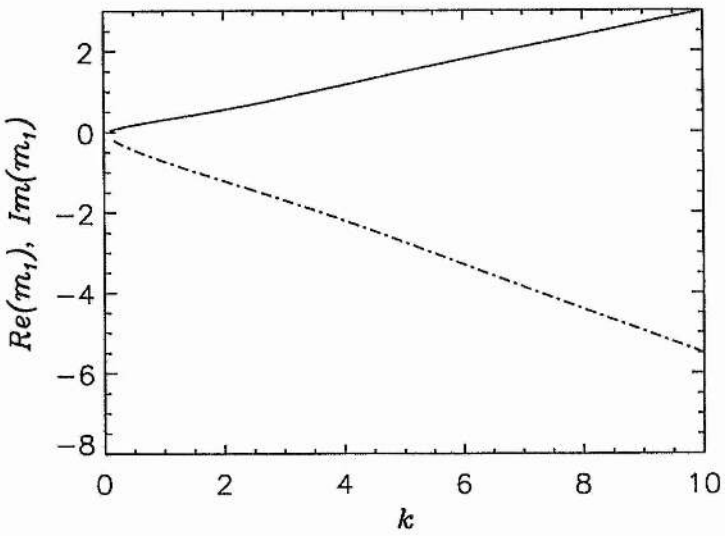

Figure 6.8: The real (solid line) and imaginary (dot-dashed line) parts of the wavenumber of the unstable slow surface wave as functions of k when $\alpha = 0$ and $v_o = 2$.

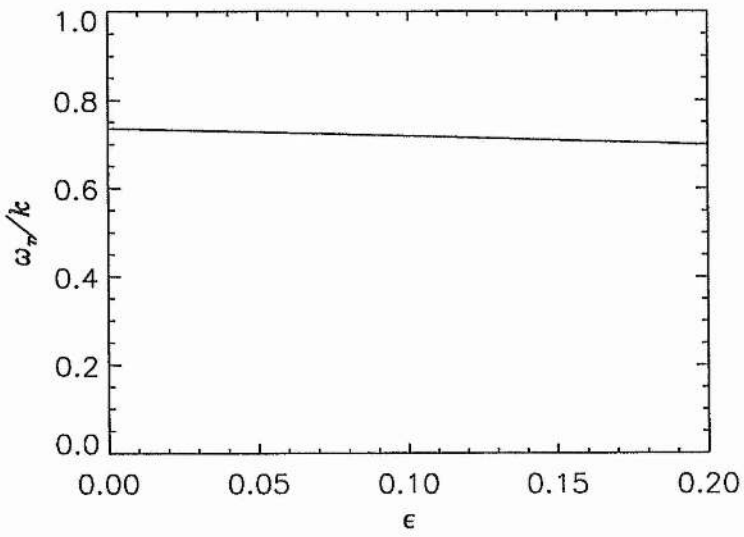

Figure 6.9: The phase speed of the slow surface mode as a function of ϵ when $v_o = 0$, $k = 10$ and $\alpha = 0$.

6.3.2 Slow Cavity Modes

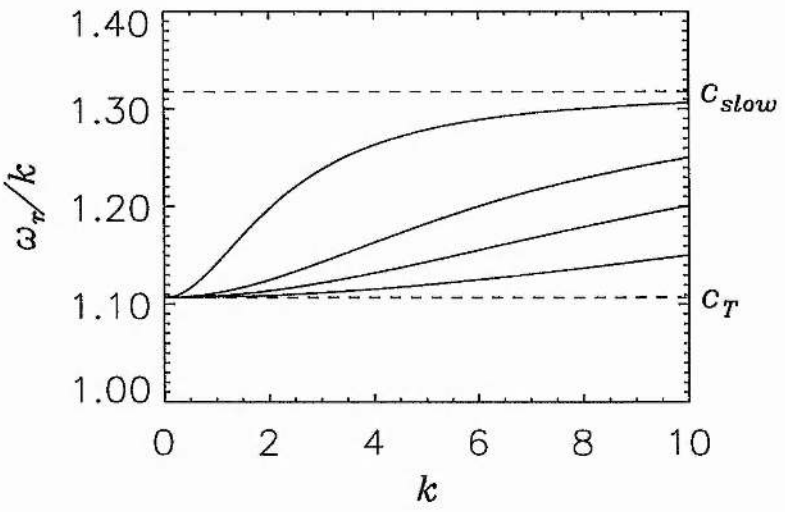

Figure 6.10: The dispersion of the slow cavity modes when $v_o = 1$ and $\alpha = 0$.

In this section we examine the behaviour of the slow cavity modes in a magnetotail like geometry. The phase speed of the slow cavity modes is always in the interval

$$c_T < v_{ph} < c_{slow}. \tag{6.6}$$

The dispersion diagram for stable slow cavity modes is shown in Figure 6.10. We have taken $v_o = 1$ and $\alpha = 0$ here so that $v_o \cos\alpha + c_{s2} > c_{slow}$ and $v_o \cos\alpha - c_{s2} < c_T$ and the modes are stable for all k. The phase speeds of the harmonics tend to the tube speed, c_T, as $k \to 0$ and to the slow speed, c_{slow} as $k \to \infty$. Since the phase speeds of the modes are at their lowest for low k, the modes will be unstable first for low k, since the approximate condition for instability is that (see Equation 2.66),

$$v_{ph} < v_o \cos\alpha - c_{s2}. \tag{6.7}$$

In Figure 6.11 we see the behaviour of the fundamental slow cavity mode once the condition for the onset of the instability of slow cavity modes,

$$v_o > \frac{c_T + c_{s2}}{\cos\alpha}, \tag{6.8}$$

has been met. In all cases we have taken $\alpha = 0$ and in (a) and (b) we have used $v_o = 2.15$ so that $v_o \cos\alpha - c_{s2} < c_T$. In this case the mode is unstable only when the phase speed is below the lower

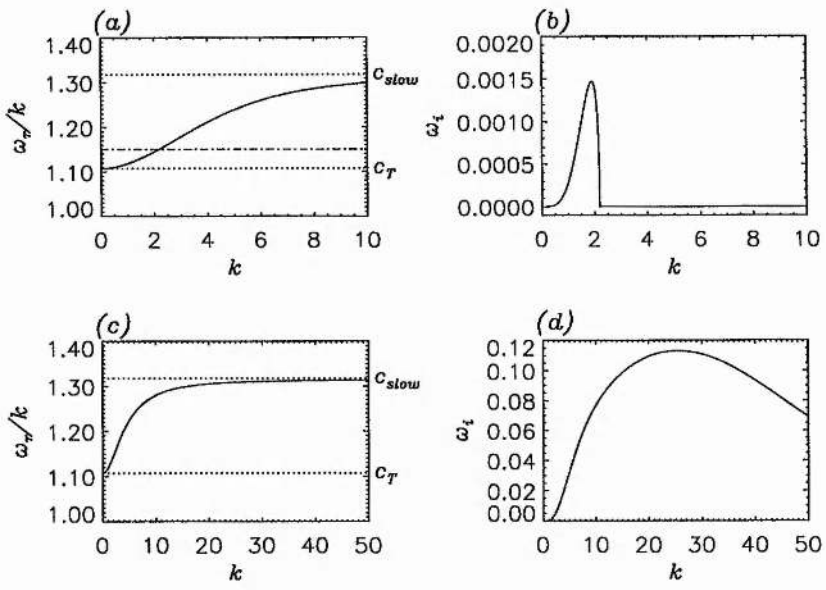

Figure 6.11: The phase speed (a and c) and growth rate (b and d) of the fundamental slow cavity mode as functions of k when $\alpha = 0$ and (a and b) $v_o = 2.15$ and (c and d) $v_o = 5$.

cut-off speed (Equation (6.7)) and has a small bounded growth rate of the order of 10^{-3}. The onset of instability for these modes occurs exactly at the point when $v_{ph} = v_o \cos\alpha - c_{s2}$, shown as a dot-dashed line in Figure 6.11(a). In (c) and (d) we have taken $v_o = 5$ so that $v_o \cos\alpha - c_{s2} > c_T$ and here we find that the mode is unstable for all values of k, The growth rate is again bounded, with a maximum of the order of 10^{-1}. The maximum growth rate in this case occurs for a much higher value of k than for the case when the mode is only just unstable ($k \approx 25$ compared to $k \approx 2$) and $\omega_i \to 0$ as $k \to \infty$.

The evolution of the phase speed and growth rate of the first four slow cavity modes as a function of v_o is shown in Figure 6.12. We have taken $\alpha = 0$ and $k = 10$ for this figure. The phase speed of each mode changes very little with v_o. While the mode is stable, the phase speed increases slightly to a maximum and then decreases before becoming unstable, and this effect is more pronounced for the lower harmonics of the modes than for the higher harmonics. The onset of the instability occurs exactly at the lower cut-off (shown by the second triple dot-dashed line in the left hand plot) and the transition between the mode being leaky and stable occurs exactly at the predicted upper cut-off (shown by the first triple dot-dashed line). The growth rates of all the modes are bounded with a maximum close to the onset of the instability. The maximum growth rate of the fundamental mode is larger than that of the higher harmonics.

Figure 6.13 shows the dispersion of the unstable fundamental slow cavity modes when $v_o = 5$ for vari-

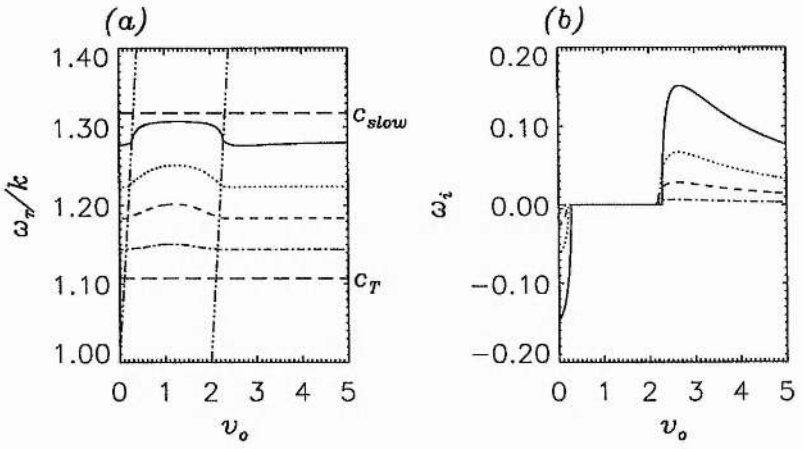

Figure 6.12: The dependence of the phase speeds (a) and growth rates (b) of the slow cavity mode harmonics v_o when $\alpha = 0$ and $k = 10$. We have shown the fundamental (solid line), second harmonic (dotted line), third harmonic (dashed line) and fourth harmonic (dot-dashed line) modes. The triple dot-dashed lines indicate the positions of the upper and lower cut-off speeds, $v_{ph} = v_o \cos\alpha \pm c_{s2}$.

ous values of α. In (a) and (b) we have taken $\alpha = 0$ and this is the mode shown in Figure 6.11. In (c) and (d) we have taken $\alpha = \pi/6$, and here the phase speed of the mode is lower due to the lower values of c_T and c_{slow}. The maximum of the growth rate is much smaller than when $\alpha = 0$, and is broader, although it still occurs at $k \approx 25$. In (e) and (f) we consider the case when $\alpha = \pi/4$, and here the growth rate is smaller again than the $\alpha = \pi/6$ case. The maxima of the growth rate occurs for slightly higher k and the peak is again broader.

Therefore, the slow body modes that are aligned with the flow are those most likely to be excited to significant amplitudes, although the growth rates of these are still small compared to those found for the slow surface modes and the fast modes (see Section 6.4). Also, the maximum growth rates for slow body modes occur for large values of k, and so we would be most likely to observe these modes as short wavelength perturbations. For $\alpha = 0$ and $v_o = 5$ we find that the frequency at the maximum of the growth rate is $\omega_r \approx 30$.

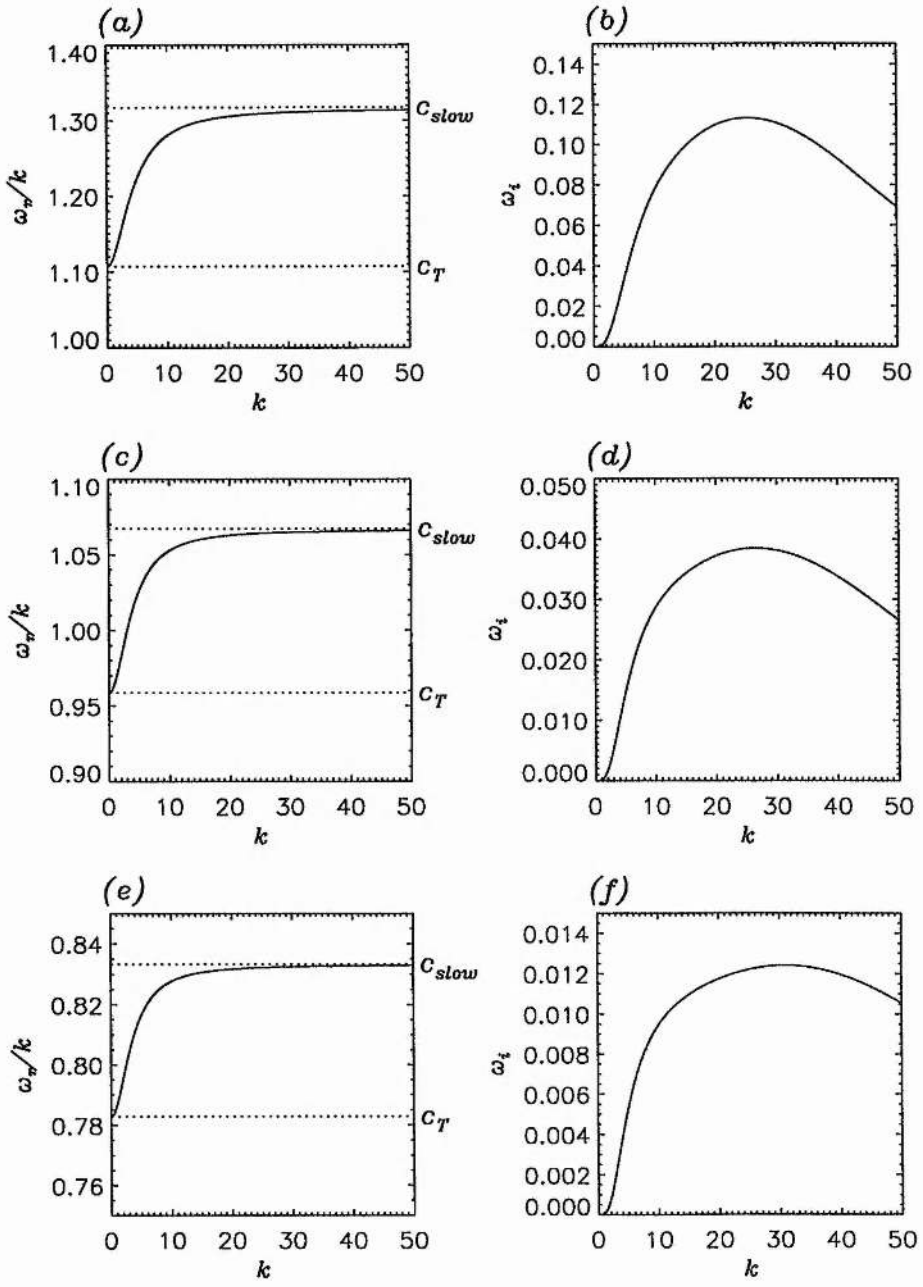

Figure 6.13: The phase speeds (a, c and e) and growth rates (b, d and f) of the fundamental slow cavity mode as functions of k when $v_o = 5$ and $\alpha = 0$ (a and b), $\alpha = \pi/6$ (c and d) and $\alpha = \pi/4$ (e and f).

6.4 Fast Modes

6.4.1 $\alpha \neq 0$

First we investigate the properties of the fast surface and body modes when $\alpha \neq 0$.

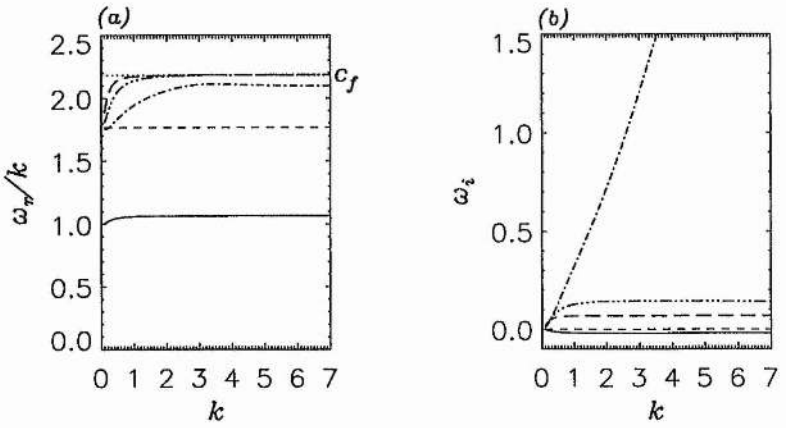

Figure 6.14: The dependence of the phase speed (a) and growth rate (b) of the fast surface mode on k when $\alpha = \pi/6$ and $v_o = 0$ (solid line), $v_o = 2$ (dashed line), $v_o = 3.25$ (dot-dashed line), $v_o = 6$ (triple dot-dashed line) and $v_o = 10$ (long dashed line). The dotted line indicates the position of the fast speed, c_f in the magnetosphere.

Figure 6.14 shows the dependence of the phase speed and growth rate of the fast surface mode on k when $\alpha = \pi/6$ for various values of v_o. When $v_o = 0$ (solid line) the mode is leaky with a small bounded negative growth rate. The mode is stable in the case when $v_o = 2$ and the phase speed is almost constant for all k. As v_o continues to increase, having first an unbounded growth rate ($v_o = 3.25$ - dot-dashed line) and then a bounded one ($v_o = 6, 10$, triple dot-dashed line and long dashed line respectively). When the growth rate becomes bounded, we find that the phase speed tends to c_f as $k \to \infty$.

Figure 6.15 shows the evolution of the fast surface modes with v_o for various values of the tangential wavenumber k. The phase speed is almost independent of k for all values of v_o, however when the mode is first unstable, the growth rate increases linearly with k (so that the growth rate is unbounded), and is then discontinuous at the point at which it becomes bounded in k in Figure 6.14, i.e., when $v_o \approx 3.75$.

Now we investigate the onset of instability of these modes for different values of α. Figure 6.16 is a contour plot of the growth rate of the fast surface mode against v_o and α for $k = 10$. We can see that, unlike the flank case, the flow speed at the onset of instability varies very little with angle. In fact, the onset of instability occurs when v_o is close to the Alfvén speed, a result which is in good agreement with

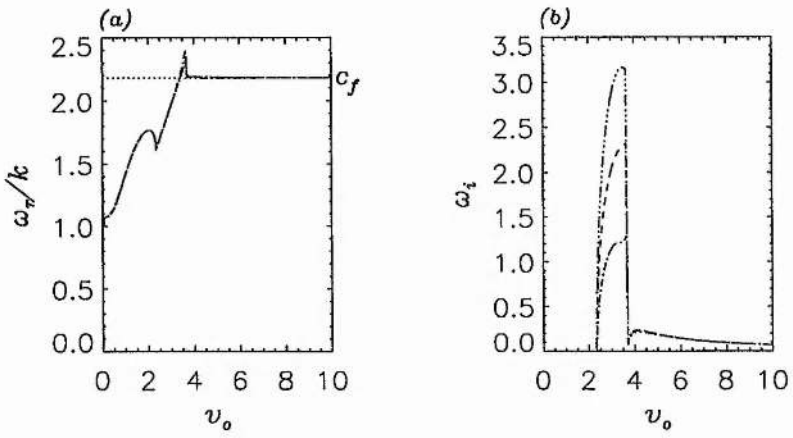

Figure 6.15: The dependence of the phase speed (a) and growth rate (b) of the fast surface mode on v_o when $\alpha = \pi/6$ and $k = 3$ (dot-dashed line), $k = 5$ (dashed line) and $k = 7$ (triple dot-dashed line). The dotted line indicates the position of the fast speed, c_f in the magnetosphere.

Sen (1964) and Rudermann and Wright (1998). The contour plot also shows that the maximum in growth rate for any flow speed occurs when $\alpha \approx \pi/4$. Walker (1981) showed that the maximum growth rate of modes propagating in a system where the field and flow are at an arbitrary angle to one another occurs when the propagation of the modes is close to perpendicular to the direction of the magnetic field - therefore minimising the stabilising effect of magnetic tension. Here, there is no component of the flow perpendicular to the magnetic field and the modes are stable there. Thus the maximum in the growth rate here will occur at an intermediate angle at which the destabilising effect of the flow dominates over the stabilising effects of magnetic tension.

In Figure 6.17 we show the dispersion of the fast body modes when they are stable. We have taken $\alpha = \pi/6$ and $v_o = 3$ so that

$$\frac{c_f - c_{s2}}{\cos\alpha} < v_o < \frac{c_f + c_{s2}}{\cos\alpha} \tag{6.9}$$

is satisfied. In (a) we can see that the phase speed of each mode decreases and tends towards c_f as $k \to \infty$. In (b) we have plotted the x-component of the magnetospheric wavenumbers, m_1, for each mode. When the phase speed of a mode is $v_o \cos\alpha + c_{s2}$ the real part of m_1 is an integer multiple of π. As k increases the phase speed decreases and m_1 increases reaching $m_1 = (2n+1)\,\pi/2$ when $v_{ph} = v_o \cos\alpha$ (shown by a dotted line in (a)), at which point m_1 has a maximum and then decreases slightly before increasing and tending back towards $m_1 = (2n+1)\,\pi/2$ as $v_{ph} \to c_f$ and $k \to \infty$. This maximum may be explained by

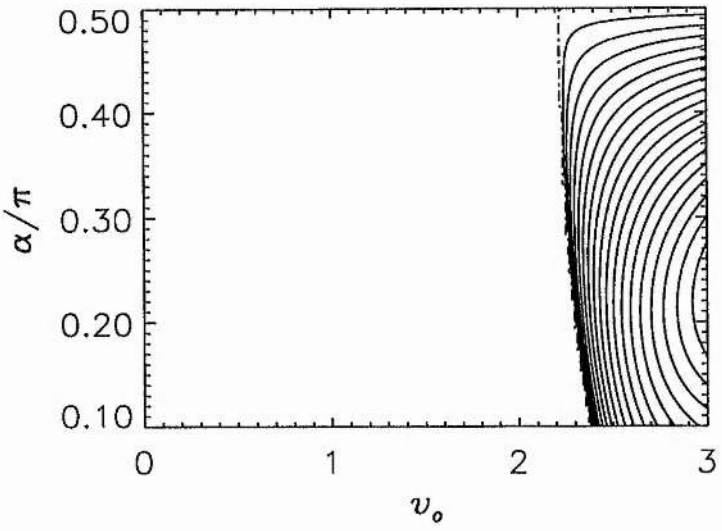

Figure 6.16: A contour plot of the growth rate, ω_i, of the fast surface mode against v_o and α. The dot-dashed line shows the onset of instability, and the solid contours represent regions of instability where $\omega_i < 0$.

noting that, in the dispersion relation for stable body modes,

$$\tan(m_1) \sim \frac{1}{(v_{ph} - v_o \cos\alpha)^2}, \tag{6.10}$$

so that $\tan(m_1) \to \infty$ as the phase speed approaches $v_o \cos\alpha$ from both above and below. Therefore, the value of the tan term increases to infinity as the phase speed decreases towards $v_o \cos\alpha$, and then decreases again (remaining positive) as the phase speed continues to decrease. Thus m_1 increases to $m_1 = (2n+1)\,\pi/2$ and then decreases as the phase speed continues to decrease.

Figure 6.18 shows the phase speed and growth rate of the first two harmonics when $v_o = 5$ and $\alpha = \pi/6$ (so that $v_o \cos\alpha > c_f + c_{s2}$) in which case the modes can become unstable. As for the case studied in Chapter 3, we find that there are two stable fast body modes for each harmonic, a positive and a negative energy wave, and that the onset of the instability occurs when these two modes coalesce. The diamonds in Figure 6.18(a) shows the point where the coalescence of the modes is predicted to occur by the method detailed in Section 3.5. The growth rates of these modes once they are unstable are bounded in this case. However, as with the flanks case (Chapter 3) there will always be one fast mode which has unbounded growth rate and has a dominantly surface mode character.

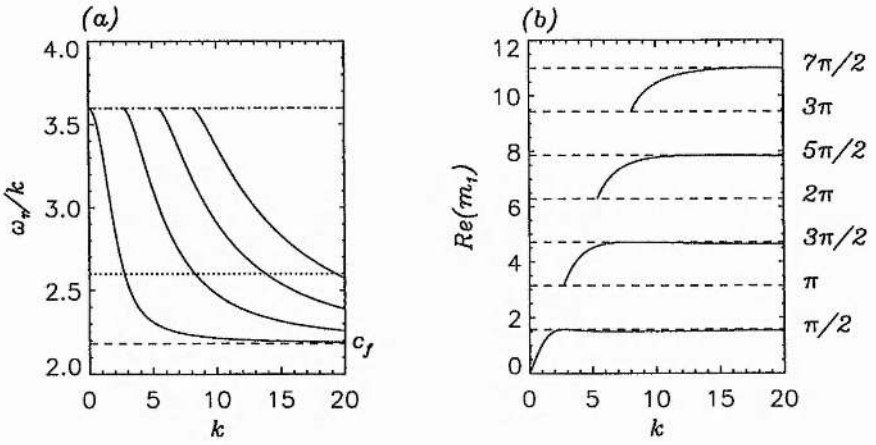

Figure 6.17: The dependence of the phase speed (a) and x-component of the wavenumber in the magnetosphere (b) of the fast body modes on k when $\alpha = \pi/6$ and $v_o = 3$. The dashed line in (a) indicates the position of the fast speed, c_f in the magnetosphere, while the dot-dashed line shows the upper limit for the existence of stable modes, $v_{ph} = v_o \cos\alpha + c_{s2}$. The dotted line shows $v_{ph} = v_o \cos\alpha$. The dashed lines in (b) indicate integer multiples of $\pi/2$.

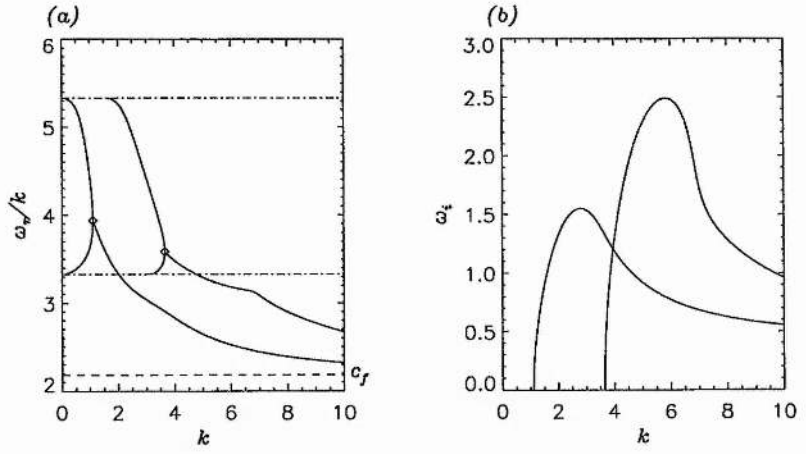

Figure 6.18: The dependence of the phase speed (a) and growth rate (b) of the fast body mode harmonics on k when $\alpha = \pi/6$ and $v_o = 5$. The dashed line in (a) indicates the position of the fast speed, c_f in the magnetosphere, while the dot-dashed lines shows the upper and lower limits for the existence of stable modes, $v_{ph} = v_o \cos\alpha \pm c_{s2}$.

6.4.2 $\alpha = 0$

We now consider the dispersion of the fast surface and body modes when the propagation of the modes is parallel to both the magnetospheric magnetic field and the flow in the magnetosheath.

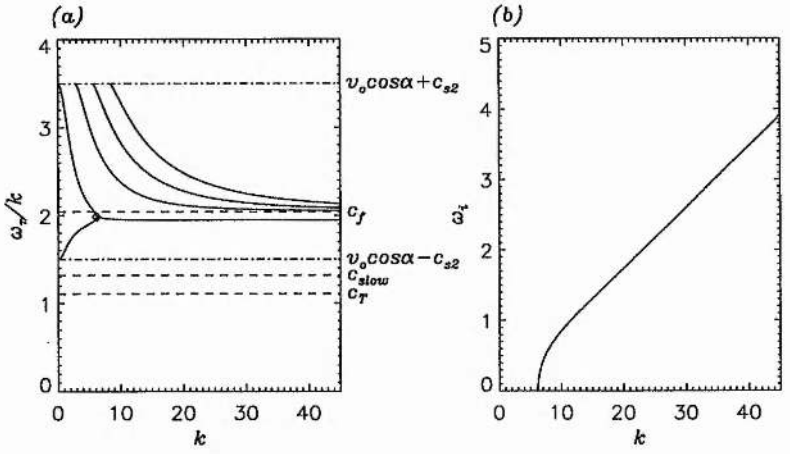

Figure 6.19: The dependence of the phase speed (a) and growth rate (b) of the fast body mode harmonics and the fast surface mode on k when $\alpha = 0$ and $v_o = 2.5$. The dashed lines in (a) indicates the position of the fast speed, c_f, the slow speed, c_{slow}, and the tube speed, c_T, in the magnetosphere, while the dot-dashed lines shows the upper and lower limits for the existence of stable modes, $v_{ph} = v_o \cos\alpha \pm c_{s2}$.

Figure 6.19 shows the dispersion of the fast modes when $v_o = 2.5$ and $\alpha = 0$, i.e.,

$$v_o \cos\alpha - c_{s2} < c_f < v_o \cos\alpha + c_{s2}, \tag{6.11}$$

and we would expect the fast body modes to be stable for all k. The second, third and fourth body mode harmonics are indeed stable for all k and have $v_{ph} \to c_f$ as $k \to \infty$. However, the phase speed of the fundamental body mode decreases through c_f (the mode remains stable through this transition) and coalesces with the fast surface mode, becoming unstable. This fast surface mode is the one with negative energy formed when the slow surface mode restabilises. This behaviour is totally different to that found for these modes when $\alpha \neq 0$ (shown in Figure 6.17). Once the two modes have coalesced, the growth rate is unbounded as k increases, but the phase speed remains constant below the fast speed. The point where the two modes coalesce may be predicted using the same method as that detailed in Section 3.5.

Figure 6.20 shows the real (solid lines) and imaginary (dot-dashed lines) parts of the x-component of the wavenumber in the magnetosphere for the modes shown in Figure 6.19. The dashed lines indicate integer multiples of $\pi/2$. For the higher harmonics, the wavenumber is $n\pi$ when the phase speed is $v_o + c_{s2}$.

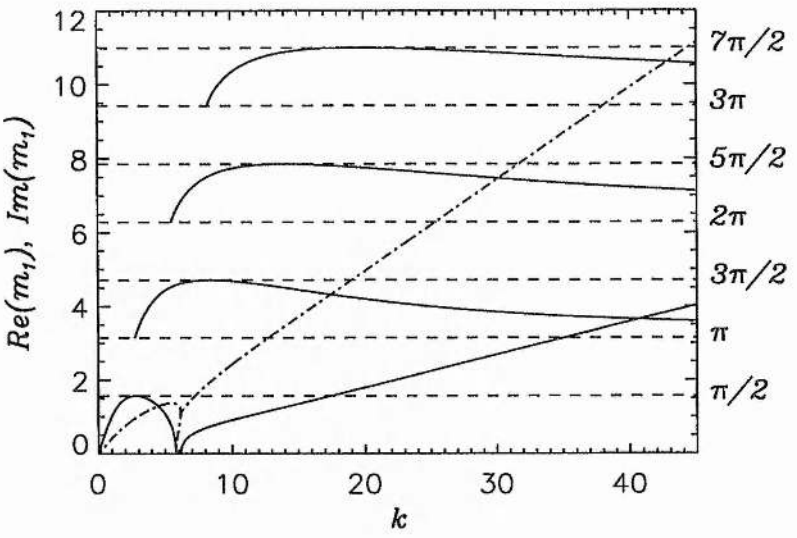

Figure 6.20: The dependence of the x-component of the wavenumber in the magnetosphere, m_1, on k when $v_o = 2.5$ and $\alpha = 0$. The solid lines show the real parts of the wavenumber and the dot-dashed lines show the imaginary parts. The dashed lines show integer multiples of $\pi/2$.

As k increases, the phase speed decreases and m_1 increases reaching a maximum when $v_{ph} = v_o$ with $m_1 = (2n-1)\,\pi/2$ (which may be explained in the same way as for the $\alpha \neq 0$ case). Then, increasing k further, the phase speed continues to decrease approaching c_f. Now the wavenumbers tend back towards $m_1 = n\pi$. Again, this is different to the $\alpha \neq 0$ case where $m_1 \to (2n-1)\,\pi/2$ for large k. The reasons for these discrepancies in behaviour will be explained in Section 6.4.3. The wavenumber of the fundamental mode is initially zero, and increases as k increases reaching a maximum when $v_{ph} = v_o$ and $m_1 = \pi/2$. As the phase speed of the mode decreases through c_f, the real part of the wavenumber decreases to zero, and the imaginary part of the wavenumber becomes non-zero when $v_{ph} < c_f$, i.e., the mode becomes a fast surface mode. As k increases further the two modes coalesce and become unstable, and at this point the wavenumber becomes complex.

In Figure 6.21 we see the variation of the behaviour of this fast mode with v_o for various values of k. For all values of k the mode is a leaky fast surface mode for low v_o, which becomes stable when $v_o = c_{slow} - c_{s2}$. The phase speed of the mode then increases as v_o increases and crosses the line $v_{ph} = c_f$. At this point the mode becomes a stable fundamental body mode. The phase speed increases to a maximum, with the maxima occurring at larger values of v_{ph} for smaller values of k (since the phase speed of a fast body mode decreases as k increases) and then decreases to the point at which the instability begins. For

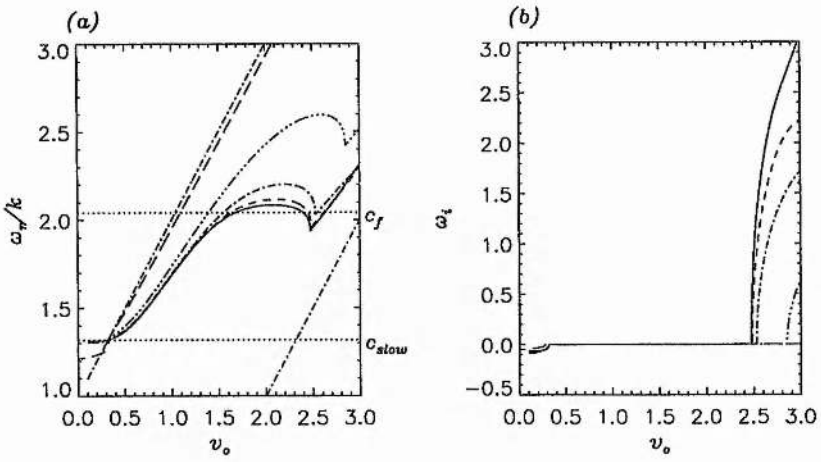

Figure 6.21: The dependence of the phase speed (a) and growth rate (b) of the fundamental fast body mode harmonics/the fast surface mode on v_o when $\alpha = 0$ and $k = 10$ (solid line), $k = 7.5$ (dashed line), $k = 5$ (dot-dashed line), $k = 2.5$ (triple dot-dashed line) and $k = 0.5$ (long dashed line). The dotted lines in (a) indicates the fast speed, c_f, and the slow speed, c_{slow}, in the magnetosphere, while the diagonal dot-dashed lines shows the upper and lower limits for the existence of stable modes, $v_{ph} = v_o \cos\alpha \pm c_{s2}$.

$k = 10$ (solid line) and $k = 7.5$ (dashed line) the onset of instability occurs when the phase speed is below the fast speed. Therefore, for these values of k, the mode becomes a stable fast surface mode again just before the onset of the instability. For lower values of k, the onset of instability occurs for phase speeds above the fast speed, so that the mode remains a stable fast body mode up to the point at which the instability begins. This mode is the upper (coalescing) mode shown in Figure 6.19a, the lower mode comes from the restabilisation of the unstable slow surface mode into a fast surface mode as discussed in Section 6.3 and is a negative energy wave. The transition of the fast surface mode into a fast body mode occurs for lower flow speeds as k decreases, and as $k \to 0$, the point of transition occurs when

$$v_o = c_f - c_{s2}, \tag{6.12}$$

which corresponds to the first flow speed for which stable fast body modes may propagate. Therefore, the fast surface mode and the fundamental fast body mode correspond to the same branch of solutions of the dispersion relation when $\alpha = 0$.

Figure 6.22 shows the phase speed (solid lines) and growth rate (dot-dashed lines) of this mode as functions of k for various values of v_o. In (a) we have taken $v_o = 2$ and here the mode is a stable fast body mode for all k, with $v_{ph} \to c_f^+$ as $k \to \infty$. The slow surface mode has not restabilised to become a fast

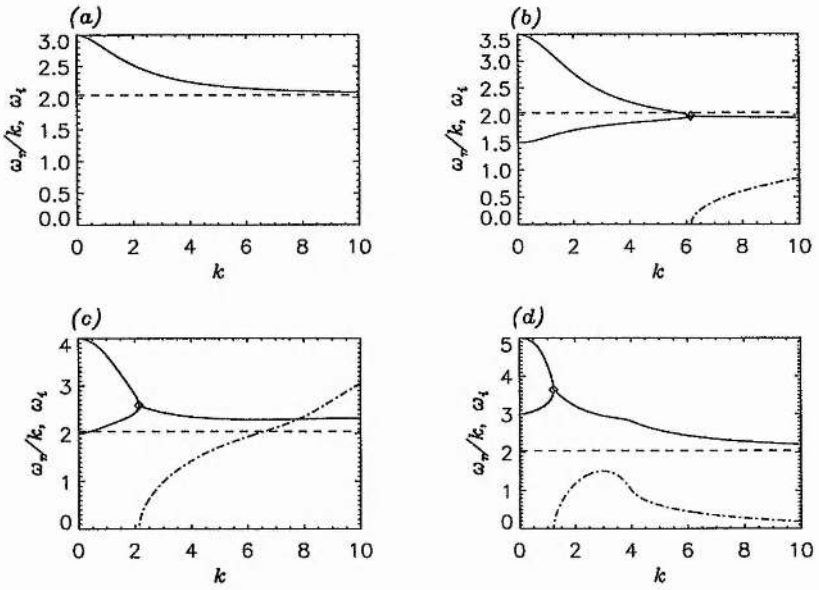

Figure 6.22: The phase speed (solid lines) and growth rate (dot-dashed lines) of the fundamental fast mode and the negative energy wave (where applicable) as functions of k when $\alpha = 0$ and (a) $v_o = 2$, (b) $v_o = 2.5$, (c) $v_o = 3$ and (d) $v_o = 4$. The dashed lines show the position of the fast speed, c_f.

surface mode yet for this flow speed and so this mode is not plotted here. In (b) we have increased the flow speed to $v_o = 2.5$ (which is the case shown in Figure 6.19) we see that the mode is a fast body mode for small k, becoming a fast surface mode just before becoming unstable as k increases. When $v_o = 3$ (in (c)), the negative energy mode has phase speed just below the fast speed when $k \to 0$ so that it is a fast surface mode here. As k increases, the mode becomes a fast body mode, coalescing with the upper mode to become unstable. When $v_o = 2.5$, the mode is dominantly a surface mode as $k \to \infty$, however when $v_o = 3$, the real part of m_1 grows faster than the imaginary part. Finally, in (d), the flow speed is increased to $v_o = 4$, and the modes are both fast body modes for small k. For large k, the growth rate is bounded.

Finally, we look at the behaviour of a fast body mode with negative phase speed (corresponding to a mode propagating earthwards in the magnetotail). Figure 6.23 shows the phase speed and growth rate of the second harmonic fast body mode as functions of the flow speed in the magnetosheath. Modes with negative phase speed are stable when the phase speed satisfies the same inequalities as for positive phase speed (Equation (6.1)). In this case we find the mode is unstable for large negative flow speeds, becomes stable while the flow speed is still negative, and as the flow speed increases, the mode becomes leaky. This is different to the modes with positive phase speed which are leaky for low (or negative flow speeds)

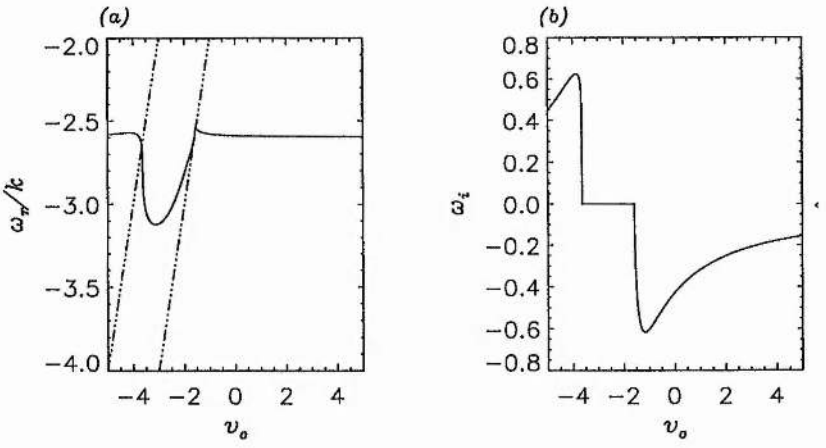

Figure 6.23: The dependence of the phase speed (a) and growth rate (b) of the second fast body mode harmonic on v_o when $\alpha = 0$ and $k = 5$. The diagonal dot-dashed lines shows the upper and lower limits for the existence of stable modes, $v_{ph} = v_o \cos\alpha \pm c_{s2}$.

and unstable for high flow speeds. Thus we would expect modes propagating towards the Earth in the magnetotail to be leaky. However, we find that the decay rate, ω_i, approaches zero as the flow speed increases, so that the modes will not loose energy very quickly as they propagate towards the earth.

6.4.3 Explaining the Difference Between $\alpha \neq 0$ and $\alpha = 0$

The dispersion relation for stable fast body modes is

$$\tan(m_1) = \frac{\epsilon}{c_{s2}} \frac{\left(v_{ph}^2 - v_{a1}^2 \cos^2\alpha\right)}{\left(v_{ph} - v_o \cos\alpha\right)^2} \times \sqrt{\frac{\left(c_{s2}^2 - \left(v_{ph} - v_o\cos\alpha\right)^2\right)\left(c_f^2 + c_{slow}^2\right)\left(v_{ph}^2 - c_T^2\right)}{\left(v_{ph}^2 - c_f^2\right)\left(v_{ph}^2 - c_{slow}^2\right)}}, \tag{6.13}$$

while that for stable fast surface modes is

$$\tanh(n_1) = \frac{\epsilon}{c_{s2}} \frac{\left(v_{ph}^2 - v_{a1}^2 \cos^2\alpha\right)}{\left(v_{ph} - v_o \cos\alpha\right)^2} \times \sqrt{\frac{\left(c_{s2}^2 - \left(v_{ph} - v_o\cos\alpha\right)^2\right)\left(c_f^2 + c_{slow}^2\right)\left(v_{ph}^2 - c_T^2\right)}{\left(c_f^2 - v_{ph}^2\right)\left(v_{ph}^2 - c_{slow}^2\right)}}, \tag{6.14}$$

where m_1 is the wavenumber in the x-direction in the magnetosphere and $n_1 = im_1$. Examining this equation we find different behaviours in the two cases (i) $\alpha \neq 0$, and (ii) $\alpha = 0$. Taking the first case and

letting $v_{ph} \to c_f$ on the right hand side of Equations (6.13) and (6.14) we find that

$$|\tan(m_1)| \to \infty, \quad \text{and} \quad |\tanh(n_1)| \to \infty, \tag{6.15}$$

respectively. Therefore, when $v_{ph} \to c_f^+$ (body modes)

$$m_1 \to \frac{(2n+1)\,\pi}{2}. \tag{6.16}$$

However, when $v_{ph} \to c_f^-$ (surface modes) there are no real values of n_1 which satisfy the equation, and thus there may be no stable surface modes with phase speeds close to c_f.

Conversely, when $\alpha = 0$, $c_f = v_{a1}$ and the dispersion relation for stable body modes reduces to

$$\tan(m_1) = \epsilon \frac{\sqrt{\left(v_{ph}^2 - v_{a1}^2\right)\left(c_{s2}^2 - (v_{ph} - v_o\cos\alpha)^2\right)}}{c_{s2}\left(v_{ph} - v_o\cos\alpha\right)^2} \times \sqrt{\frac{\left(c_f^2 + c_{slow}^2\right)\left(v_{ph}^2 - c_T^2\right)}{\left(v_{ph}^2 - c_{slow}^2\right)}}, \tag{6.17}$$

and the equation for fast surface modes reduces to

$$\tanh(n_1) = \epsilon \frac{\sqrt{\left(v_{a1}^2 - v_{ph}^2\right)\left(c_{s2}^2 - (v_{ph} - v_o\cos\alpha)^2\right)}}{c_{s2}\left(v_{ph} - v_o\cos\alpha\right)^2} \times \sqrt{\frac{\left(c_f^2 + c_{slow}^2\right)\left(v_{ph}^2 - c_T^2\right)}{\left(v_{ph}^2 - c_{slow}^2\right)}}. \tag{6.18}$$

Thus when $v_{ph} \to c_f^+$, $\tan(m_1) \to 0$ so that

$$m_1 \to n\pi, \tag{6.19}$$

and when $v_{ph} \to c_f^-$, $\tanh(n_1) \to 0$ and therefore

$$m_1 \to 0. \tag{6.20}$$

In other words, both stable body and surface modes may have phase speeds close to the fast speed in this case. This explains how, in this case, the character of the fast modes may change smoothly between having an oscillatory and an evanescent character in the magnetosphere. We can see this transition in Figure 6.19a when the phase speed of the fundamental fast cavity mode decreases to below c_f while the mode is still stable (therefore changing from a body to a surface mode). In Figure 6.22(c) we see the phase speed of the fast surface mode increasing through c_f, so in this case the mode changes from a fast surface mode to a fast body mode.

6.5 Discussions and Conclusions

We have investigated the trapping and excitation of modes in the magnetotail. We have used a finite plasma beta in order to demonstrate the behaviour of both fast and slow magnetosonic modes. However, the plasma beta in the tail lobes is typically of the order of 10^{-4} (Saunders, 1991), so we would expect the propagation of fast modes to dominate in this region.

We have found that the speed at which fast surface modes first become unstable varies little with the direction in which the modes are propagating. This is in agreement with the results found by Pu and Kivelson (1983). However, we did not find the upper cutoff speed reported by Pu and Kivelson. This is because the bounded magnetotail does not allow the energy generated by the instability to be carried away from the boundary to infinity. The maximum growth rate of these modes is found to occur at an angle of about $\pi/4$. This is due to the stabilising force of the magnetic tension and the destabilising effect of the flow varying with angle. Walker (1981) found that the most unstable modes propagate at angles close to perpendicular to the magnetic field. In our model, the flow has no effect perpendicular to the magnetic field, so the maximum growth rate will occur at some intermediate position.

Fast body modes may first become unstable when $v_o \cos\alpha = c_f + c_{s2}$, so that modes propagating parallel to the flow and magnetic field will become unstable first. We found that the behaviour of both the fast surface mode and the fast body mode is different for modes propagating parallel to the magnetic field than for those propagating perpendicular to it. The stable fundamental fast body mode and the stable fast surface mode (having positive energy) correspond to the same branch of the solution of the dispersion relation when $\alpha = 0$ with the phase speed of the mode able to change across c_f, and the character of the mode changing at that point. When $\alpha \neq 0$, these modes are separate and the phase speed of the fast surface mode may not approach the fast speed.

The slow modes in this model have small bounded growth rates, and if we were to decrease the plasma beta we would find that these growth rates would be even smaller. The low value of the plasma beta in the magnetotail means that these modes would be unlikely to be observed in this region.

We take the width of the magnetotail to be 25 R_E and the sound speed in the magnetosheath as 100km/s. Although we have used a density ratio of 0.192 in our calculations, this was merely for convenience so we could calculate the qualitative behaviour of the modes without needing to have overly high flow speeds. A more realistic value of the density ratio would be 0.02, corresponding to an Alfvén speed of about 700km/s. With typical magnetosheath flow speeds of 500km/s, and the onset of instability for the fast surface modes being close to the Alfvén speed, we can see that the fast magnetopause surface mode is

unlikely to be KH unstable in this region. Rudermann and Wright (1998) discussed this behaviour and showed that below the critical speed for the KHI, negative energy surface waves may propagate on the magnetopause. These may drive Alfvén resonances within the magnetotail and when this occurs the surface mode becomes unstable and both the surface mode and the resonance grow. Therefore, any unstable modes observed on the magnetosphere are likely to be caused by this resonant interaction between negative energy waves and Alfvén waves rather than directly by the KHI.

In our calculations we have also found negative energy waves, although we do not drive any Alfvén resonances as our magnetotail is taken to be uniform and the velocity shear is a vortex sheet. We have shown that these unstable modes correspond to modes which have phase which propagate in the positive y-direction in the rest frame of the magnetosheath, but in the negative y-direction in the magnetospheric rest frame. The onset of instability occurs at the coalescence of positive and negative energy waves.

Observations of oscillations in the magnetotail show that fast modes may be excited down tail and propagate earthward (Elphinstone et al., 1995). Models of this have tended to treat the magnetopause as a perfectly reflecting boundary trapping these modes within the magnetotail (e.g., Allan and Wright, 1998; Wright, 1994). An important consequence of our model is that we may better understand the nature of the interaction of these modes with the magnetopause. We have shown that modes propagating towards the Earth in the magnetotail (i.e., those modes which have negative phase speeds) are leaky for positive flow speeds. However, the growth rate (or in this case, the decay rate) of each mode becomes very small as the flow speed increases. Therefore, we expect the modes to be essentially stable and for the majority of the wave energy to be reflected from the magnetopause. We conclude therefore that the assumption of a reflecting magnetopause in the waveguide models is a reasonable approximation, particularly with fast magnetosheath flow.

The dimensional frequency of the fast waveguide modes in our model is about 4 mHz which is of the same order of magnitude as those observed (e.g., by Herron, 1967).

Overall we have found that the magnetotail will be stable to the Kelvin-Helmholtz instability for most values of the flow speed in the magnetosheath. However, both earthward and tailward propagating fast body modes will be leaky with small decay rates, and will lose only a small amount of energy as they reflect from the magnetopause, so that treating the magnetosphere in this region as a perfect reflector is a reasonable approximation and waveguide models should be successful in predicting the behaviour of these modes.

If surface or waveguide modes are observed to be unstable in the magnetotail, this could point to the occurance of a resonant instability operating (e.g., see Rudermann and Wright, 1998), and is an important calculation for future research.

Chapter 7

Conclusions and Further Work

"There is no more common error than to assume that, because prolonged and accurate mathematical calculations have been made, the application of the result to some fact of nature is absolutely certain." A. N. Whitehead

7.1 Conclusions

In this thesis we have considered the trapping and excitation of modes in the magnetosphere, the coupling of these modes to FLRs and the space-time evolution of wave-packets composed of these modes.

In Chapter 2 we derived general conditions for the existence of stable modes in the magnetosphere (Equations (2.73) to (2.75)). We showed that these may be understood in terms of the phase speed of a mode, the speed of the flow in the magnetosheath and the direction in which the mode is propagating.

In Chapter 3 we showed that fast cavity modes on the magnetospheric flanks may be trapped for typical solar wind flow speeds and be driven unstable for solar wind speeds above $\sim$ 500km/s. This result is in agreement with the observations by Engebretson et al. (1998) that Pc5 wave power is significantly enhanced for flow speeds of $\sim$ 500km/s or more. Modes propagating quasi-parallel to the flow in the magnetosheath are most likely to become unstable. Fast surface modes may also be unstable, and those propagating parallel to the magnetosheath flow are unstable for any non-zero flow speed. For low flow speeds these modes have unbounded growth rates as k becomes large. However, for higher flow speeds, the fast surface mode becomes dominantly oscillatory in the magnetosphere and the growth rate becomes bounded. Above the flow speed at which this first occurs, there is always one of the fast body mode harmonics that becomes

dominantly evanescent in the magnetosphere and has an unbounded growth rate (i.e., has the characteristics of a surface mode). We also considered the propagation of slow magnetoacoustic modes. We found that the slow body modes are only stable for small ranges of flow speed that are highly dependent on the direction of propagation. When unstable (or leaky), the growth (or decay) rate of these modes are small and bounded. Slow surface modes are stable when there is no flow, and become unstable for a small range of flow speed, before restabilising as fast surface modes. The growth rate of these modes when unstable is also unbounded in k.

We have derived a method for predicting the exact point at which the onset of instability occurs and showed that this onset corresponds to the coalescence of a positive energy mode with a negative energy mode. We also showed that the phase speeds of the fast cavity mode harmonics at maximum growth rate are very similar. We used the theory of over-reflection (McKenzie, 1970a) and showed that the phase speed found at maximum growth rate in our model agreed with that at which spontaneous radiation of modes from the magnetopause should occur.

In Chapter 4 we considered the driving of FLRs by Kelvin-Helmholtz unstable fast cavity modes. We used a bounded non-uniform model of the magnetosphere and derived a dispersion relation. We used a numerical integration technique across the magnetospheric cavity to solve the dispersion relation and find the normal modes of the system. In this case we have assumed that the magnetic field lines are finite so that k_z is quantised and consider the dispersion of the modes as k_y changes. We found that the values of the azimuthal phase speeds of the normal modes at their maxima of growth rate are very similar. This agrees with observations by Ziesolleck and McDiarmid (1994) who found that simultaneously observed FLRs have a common phase speed. We compared these phase speeds to those predicted using the theory of over-reflection and found excellent agreement. The phases speeds are found to depend little on the amount of variation in the Alfvén speed across the magnetosphere. Thus we may predict the phase speeds of FLRs simply from the local properties at the magnetopause.

In Chapter 5 we considered the space-time evolution of a wave-packet on the magnetopause. We used the same model as in Chapter 3, but added a finite width boundary layer over which the flow speed changes continuously. The effect of this boundary layer is to limit those growth rates which are unbounded in Chapter 3. We used the theory of absolute and convective instabilities to predict the time asymptotic behaviour of these wave-packets and to assess their effect on the magnetosphere. We found that the fast surface mode wave-packets are absolutely unstable in the rest frame of the magnetosphere when the flow speed is very low, but become convectively unstable for higher flow speeds. The dominant length scale for these modes is δ (the half width of the boundary layer) and the e-folding length is $\sim \delta$. The spatial growth rate of the fast

surface mode wave-packets increases around the magnetosphere, but is of the order of 2 R_E close to the nose. These modes would then be expected to grow many orders of magnitude as they convect around the magnetosphere and non-linear effects will be important, leading to the broadening of the boundary layer.

Fast body mode wave-packets are also convectively unstable. However, the e-folding lengths of these are of the order of 20 R_E and they will not become unstable until they reach the flanks of the magnetosphere. Thus we would not expect these to grow to large amplitudes as they convect around the magnetospheric flanks. They will however drive FLRs in the magnetosphere which may be observed. The convective nature of these wave-packets means that the driver of a FLR will not grow to large amplitudes on the flanks and this explains the success and appropriateness of linear theory in modelling FLRs.

We also considered the behaviour of slow body and surface mode wave-packets. These were all found to be convectively unstable with very large e-folding lengths ($\sim 100 - 1000\ R_E$) and we would not expect these to grow to observable amplitudes on the flanks of the magnetosphere.

We compared our predictions to results from a computer simulation and found excellent agreement. The simulation results showed that when more than one type of unstable mode is present, the wave-packet may split into two sections, each corresponding to one of the mode types. Finally, we derived a quadratic approximation for the asymptotic growth rate as a function of reference frame using the information from the dispersion relation for real k. We showed that this approximation agreed well with the form of the growth rate found by solving the full dispersion relation.

In Chapter 6 we consider the nature of the magnetopause boundary in the magnetotail. We showed that the high value of the Alfvén speed in this region means that very large flow speeds are required for the trapping or excitation of modes in this region. We found that most modes (propagating in both the positive and negative y-direction) will be leaky, but that the decay rate of modes can be small so that the assumption of a perfectly reflecting magnetopause boundary in waveguide models is reasonable, especially for fast magnetosheath flows. We found that when fast modes propagate parallel to both the magnetic field in the magnetosphere and the magnetosheath flow their behaviour is different to that for modes propagating in other directions. In this case, only one of the stable, positive energy fast surface and first harmonic body modes may exist for any flow speed, and we explained this in terms of the form of the dispersion relation. Increasing the flow speed we find that the transition between these stable modes is smooth. The onset of instability was again found to occur at the coalescence of a positive energy mode with one with negative energy. We conclude that any unstable modes observed in the tail lobes are likely to be caused by the resonant interaction of negative energy waves with Alfvén waves described by Rudermann and Wright (1998).

7.2 Suggestions for Further Work

As with all mathematical modelling of a physical structure, the models presented in this thesis are only approximations to the extremely complex situations they are trying to emulate. In addition, where we have considered extensions or modifications to a model, we have studied only one at a time. In order to extend the work presented in this thesis we must combine the effects seen for some of the individual variations made, and relax some of the main assumptions.

7.2.1 The Driving of Alfvén Resonances by a Pulse

In Chapter 4 we considered the driving of Alfvén resonances in the magnetosphere by Kelvin-Helmholtz unstable fast cavity modes. We looked at the normal modes of the system and the azimuthal phase speeds associated with the fastest growing modes. Then, in Chapter 5 we looked at the space-time development of a finite pulse on the magnetopause. We suggested that the convective nature of the instability associated with fast body mode wave-packets explains the success of linear theory in explaining the observed FLRs, although the uniform magnetosphere used in this case did not allow the formation of any resonances. In order to examine further the driving of these resonances, calculations of the space-time development of a pulse on the magnetopause with a non-uniform magnetosphere could be made. This would combine the non-uniform magnetosphere feature of Chapter 4 with the boundary layer form of the flow profile used in Chapter 5. The properties or the wave-packets in this model could then be used to calculate the number of cycles for which a resonance would be driven. This, along with appropriate computer simulations, could be used to determine whether an isolated pulse or a continuous small perturbation of the magnetopause would be the most probable driving form for the observed FLRs. The azimuthal phase speeds of the resonances could also be measured to see if a common speed is found in the simulations. It is worth noting that it would be reasonable to undertake these calculations in a cold plasma limit as the calculation in Chapter 5 showed that the slow modes had very small spatial growth rates, and these modes may not couple to Alfvén resonances.

7.2.2 The Evolution of a Pulse in the Magnetotail

In Chapter 5 we considered the evolution of a pulse on the flanks of the magnetosphere. We estimated the length of flank around which the wave-packets could convect before the geometry of the magnetosphere changes and the wave-packets enter the magnetotail. An extension of this work would be to consider the further evolution of these wave-packets. Initially, a calculation of whether Kelvin-Helmholtz driven

instabilities in the tail would be expected to be absolute or convective should be undertaken. Although the tail is expected to be stable to the KHI in general, other instabilities also exist at the boundary between the magnetotail and the magnetosheath, e.g., the resonant interaction of negative energy waves with Alfvén resonances that has already been mentioned, and the absolute or convective nature of these instabilities could also be studied.

7.2.3 More Realistic Geometries

Throughout this thesis, we have assumed that the magnetosphere extends infinitely in the azimuthal direction and is straight. While this assumption is reasonably valid in the magnetotail, the flanks of the magnetosphere are curved and the depth of the magnetosphere varies around the flanks. An interesting extension to our work would be to examine the effects of a curved geometry on the propagation of modes on the magnetospheric flanks.

Also, as mentioned in Chapter 5, the thickness of the boundary layer and the speed of the flow in the magnetosheath both increase around the flanks. In order to study the effects of these features, a computer simulation containing profiles in the azimuthal (as well as the radial) direction could be considered. Seed perturbations could then be fed in from the nose end of the simulation and their development along a more realistic magnetopause considered. This would give greater insight into the spatial development of small perturbations and would confirm the results found from the analysis in Chapter 5.

7.2.4 Comparisons to Observations

In considering the spatial and temporal evolution of disturbances to the magnetopause it is difficult to compare the results from the model to observations. This is due to the fact that single satellite data cannot easily separate spatial and temporal effects. Multi-satellite missions such as Cluster II should allow more detailed analysis of the development of disturbances in the magnetosphere and could separate the spatial and temporal effects. This, in conjunction with ground based observations that can already separate spatial and temporal effects would allow the study of the space-time evolution of the driving of FLRs and comparison with our results from Chapter 5.

Appendix A

Derivation of the Governing Ordinary Differential Equations

Here we derive the first order ordinary differential equations (ODEs) for the perturbed displacement and total pressure used in Chapters 2, 4 and 5. Here we assume that all the equilibrium quantities vary continuously in the x-direction, so that the equilibrium magnetic field is

$$\mathbf{B_o} = B_{oy}(x)\,\hat{\mathbf{y}} + B_{oz}(x)\,\hat{\mathbf{z}}, \tag{A.1}$$

and the equilibrium flow is given by

$$\mathbf{v_o} = v_o(x)\,\hat{\mathbf{y}}, \tag{A.2}$$

with the equilibrium pressure and density defined as

$$\rho_o = \rho_o(x) \quad \text{and} \quad P = P(x)\,. \tag{A.3}$$

We are using quantities normalised by the equilibrium sound speed (c_{s2}) and density (ρ_{o2}) in the magnetosheath. Lengths are normalised by the depth of the magnetosphere (d), times by d/c_{s2}, pressures by the quantity ΓP_2 and magnetic fields by the quantity $\sqrt{\Gamma P_2 \mu_o}$, where Γ is the ratio of specific heats. We then add small perturbations to each of these quantities, so that $\mathbf{B} = \mathbf{B_o} + \mathbf{b}$, $\mathbf{v} = \mathbf{v_o} + \mathbf{u}$, $\rho = \rho_o + \rho_1$ and $p = P + p_1$. When we linearise the ideal MHD equations (see Section 1.2.1), we obtain the linearised induction equation

$$\left(\frac{\partial}{\partial t} + \mathbf{v_o}.\nabla\right)\mathbf{b} + (\mathbf{u}.\nabla)\,\mathbf{B_o} = (\mathbf{B_o}.\nabla)\,\mathbf{u} + (\mathbf{b}.\nabla)\,\mathbf{v_o} - \mathbf{B_o}\,(\nabla.\mathbf{u})\,; \tag{A.4}$$

the linearised equation of motion

$$\rho_o \left(\frac{\partial}{\partial t} + \mathbf{v_o}.\nabla \right) \mathbf{u} + \rho_o \left(\mathbf{u}.\nabla \right) \mathbf{v_o} = -\nabla p_T + \left(\mathbf{B_o}.\nabla \right) \mathbf{b} + \left(\mathbf{b}.\nabla \right) \mathbf{B_o}; \tag{A.5}$$

the linearised continuity equation

$$\left(\frac{\partial}{\partial t} + \mathbf{v_o}.\nabla \right) \rho_1 + \left(\mathbf{u}.\nabla \right) \rho_o = -\rho_o \nabla.\mathbf{u}; \tag{A.6}$$

and the linearised adiabatic energy equation

$$\left(\frac{\partial}{\partial t} + \mathbf{v_o}.\nabla \right) p_1 + \left(\mathbf{u}.\nabla \right) P = c_s^2 \left(\frac{\partial}{\partial t} + \mathbf{v_o}.\nabla \right) \rho_1 + c_s^2 \left(\mathbf{u}.\nabla \right) \rho_o, \tag{A.7}$$

where $c_s^2 = \Gamma P/\rho_o$ is the square of the equilibrium sound speed. The equilibrium is invariant in the y- and z-directions and time. So we may consider each decoupled Fourier mode of the form $\mathrm{e}^{i(k_y y + k_z z - \omega t)}$ independently, where k_y and k_z are the wavenumbers in the y- and z-directions respectively and ω is the frequency. The directions of the equilibrium magnetic field, flow and the tangential wave vector $\mathbf{k} = (0, k_y, k_z)$ are shown in Figure 2.2. We define $k = \sqrt{k_y^2 + k_z^2}$, with α as the angle between $\mathbf{k}$ and $\mathbf{B_o}$ and χ as the angle between $\mathbf{B_o}$ and $\mathbf{v_o}$. For the purposes of this analysis, it is helpful to define new co-ordinates in the $y - z$ plane. We take unit vectors parallel and perpendicular to the equilibrium magnetic field (denoted $\mathbf{e}_{\|}$ and $\mathbf{e}_{\perp}$, respectively). Then the component of the flow speed along the magnetic field is given by

$$\mathbf{v_o}.\mathbf{e}_{\|} = v_o \cos\chi, \tag{A.8}$$

the component of the wave-vector along the magnetic field is

$$\mathbf{k}.\mathbf{e}_{\|} = k \cos\alpha, \tag{A.9}$$

and the operator $\mathbf{v_o}.\nabla$ is given by

$$i\mathbf{v_o}.\mathbf{k} = ikv_o \cos\left(\chi - \alpha\right), \tag{A.10}$$

and

$$\mathbf{B_o}.\nabla = ikB_o \cos\alpha. \tag{A.11}$$

The x-component of Equation (A.5) is

$$i\omega' \rho_o u_x = \frac{dp_T}{dx} - ikB_o \cos\alpha b_x, \tag{A.12}$$

(where $\omega' = \omega - kv_o \cos\left(\chi - \alpha\right)$ is the Doppler shifted frequency) and the x-component of Equation (A.4) gives

$$b_x = -\frac{kB_o \cos\alpha}{\omega'} u_x. \tag{A.13}$$

Combining these two expressions, we obtain our first ODE which is

$$\frac{dp_T}{dx} = i\rho_o \left(\omega'^2 - k^2 v_a^2 \cos^2\alpha\right) \frac{u_x}{\omega'}. \tag{A.14}$$

In order to find the second ODE we rearrange Equation (A.6) to give

$$\rho_o \frac{du_x}{dx} = i\omega' \rho_1 - u_x \frac{d\rho_o}{dx} - i\rho_o k \cos\alpha u_{\|} - i\rho_o k \sin\alpha u_{\perp}, \tag{A.15}$$

where $u_{\|}$ and $u_{\perp}$ are the components of the perturbed velocity in the directions parallel and perpendicular to the magnetic field respectively. The component of Equation (A.5) perpendicular to the magnetic field may be written as

$$\omega' \rho_o u_{\perp} = k \sin\alpha p_T - kB_o \cos\alpha b_{\perp} - i\rho_o \sin\chi u_x \frac{dv_o}{dx}, \tag{A.16}$$

and that of Equation (A.4) gives an expression for $b_{\perp}$,

$$b_{\perp} = -\frac{kB_o \cos\alpha}{\omega'} u_{\perp} + i\frac{sin\chi}{\omega'} b_x \frac{dv_o}{dx}. \tag{A.17}$$

Substituting Equations (A.17) and (A.13) into (A.16) we obtain

$$u_{\perp} = \frac{\omega' k \sin\alpha}{\rho_o \left(\omega'^2 - k^2 v_a^2 \cos^2\alpha\right)} p_T - i\frac{\sin\chi}{\omega'} u_x \frac{dv_o}{dx}. \tag{A.18}$$

Now we take the component of Equation (A.5) parallel to the magnetic field, which may be written as

$$\omega' \rho_o u_{\|} = k \cos\alpha p_T - kB_o \cos\alpha b_{\|} + ib_x \frac{dB_o}{dx} - i\rho_o \cos\chi u_x \frac{dv_o}{dx}, \tag{A.19}$$

and the component of the induction equation (A.4) in this direction gives $b_{\|}$ as

$$b_{\|} = -\frac{i}{\omega'} u_x \frac{dB_o}{dx} + \frac{B_o k^2 \sin^2\alpha}{\rho_o \left(\omega'^2 - k^2 v_a^2 \cos^2\alpha\right)} p_T - iB_o \frac{d}{dx}\left(\frac{u_x}{\omega'}\right), \tag{A.20}$$

where we have used

$$\frac{d}{dx}\left(\frac{u_x}{\omega'}\right) = \frac{1}{\omega'}\frac{du_x}{dx} + \frac{u_x}{\omega'^2} k \cos\left(\chi - \alpha\right) \frac{dv_o}{dx}. \tag{A.21}$$

Substituting Equations (A.20) and (A.13) into (A.19) enables us to express $u_{\|}$ as

$$u_{\|} = \frac{k\cos\alpha}{\rho_o \omega'} \left\{\frac{\omega'^2 - k^2 v_a^2}{\omega'^2 - k^2 v_a^2 \cos^2\alpha}\right\} p_T - \frac{i\cos\chi}{\omega'} u_x \frac{dv_o}{dx} + i\frac{k\cos\alpha v_a^2}{\omega'} \frac{d}{dx}\left(\frac{u_x}{\omega'}\right). \tag{A.22}$$

From Equation (A.7) we find

$$\begin{aligned} i\omega'\rho_1 - u_x \frac{d\rho_o}{dx} &= \frac{i\omega'}{c_s^2} p_1 - \frac{u_x}{c_s^2}\frac{dP}{dx} \\ &= \frac{i\omega'}{c_s^2}\left(p_T - B_o b_{\|}\right) + \frac{u_x}{c_s^2}\frac{d}{dx}\left(\frac{B_o^2}{2}\right), \end{aligned} \tag{A.23}$$

where we have used the equilibrium condition that

$$\frac{dp_{To}}{dx} = \frac{d}{dx}\left(P + \frac{B_o^2}{2}\right) = 0. \tag{A.24}$$

Substituting Equation (A.20) into (A.23) we obtain

$$i\omega'\rho_1 - u_x\frac{d\rho_o}{dx} - \frac{i\omega'}{c_s^2}\left(\frac{\omega'^2 - k^2v_a^2}{\omega'^2 - k^2v_a^2\cos^2\alpha}\right)p_T - \frac{\rho_o v_a^2\omega'}{c_s^2}\frac{d}{dx}\left(\frac{u_x}{\omega'}\right). \tag{A.25}$$

Finally, we substitute Equations (A.18), (A.22) and (A.25) into Equation (A.15) and (with some manipulation) we obtain our second ODE,

$$\frac{d}{dx}\left(\frac{u_x}{\omega'}\right) = \frac{im^2}{\rho_o\left(\omega'^2 - k^2v_a^2\cos^2\alpha\right)}p_T, \tag{A.26}$$

where

$$\begin{aligned} m^2 &= \frac{\omega'^4 - k^2\left(v_a^2 + c_s^2\right)\omega'^2 + k^4v_a^2c_s^2\cos^2\alpha}{\left(v_a^2 + c_s^2\right)\omega'^2 - k^2v_a^2c_s^2\cos^2\alpha} \\ &= \frac{\left(\omega'^2 - k^2c_f^2\right)\left(\omega'^2 - k^2c_{slow}^2\right)}{\left(c_f^2 + c_{slow}^2\right)\left(\omega'^2 - k^2c_T^2\right)}. \end{aligned} \tag{A.27}$$

Equations (A.14) and (A.26) apply to the general case in which the magnetosphere is taken to have a finite plasma beta and for magnetic fields at an arbitrary angle to the magnetosheath flow - this is the case considered in Chapter 2. In Chapter 4 we use these equations to integrate across the magnetosphere, assume the magnetospheric plasma to be cold (so that $c_s = c_{slow} = c_T = 0$, and $c_f = v_a$) and place the magnetic field perpendicular to the flow in the magnetosheath (so that $\chi = \pi/2$). In Chapter 5 we integrate only across the boundary layer, which we have taken to be field free (so that $v_a = c_{slow} = c_T = 0$ and $c_f = c_s$) and we again take $\chi = \pi/2$.

Appendix B

Derivation of the 'Pinching' Double Root Condition

In this appendix we outline the derivation of Briggs (1964) in order to derive the 'pinching' double root condition described in Chapter 5 we again consider the Fourier-Laplace integral for the plasma response (Equation (5.2)),

$$\psi(y,t) = \int_L \int_F \frac{w(\omega, k_y)}{D(\omega, k_y)} \mathrm{e}^{i(k_y y - \omega t)} dk_y d\omega, \tag{B.1}$$

and remember that $w(\omega, k_y)$, which represents the driving function, is assumed to be regular everywhere (see also Bers, 1983). We may rewrite Equation (B.1) as

$$\psi(y,t) = \int_L J(\omega, y)\, w(\omega, k_y)\, \mathrm{e}^{-i\omega t} d\omega, \tag{B.2}$$

where

$$J(\omega, y) = \int_F \frac{\mathrm{e}^{ik_y y}}{D(\omega, k_y)} dk_y. \tag{B.3}$$

Now we may perform this integration by closing the integration contour, assuming that D has only isolated singularities and that $\lim_{k_y \to \infty} D^{-1} \to 0$ at least as fast as k^{-1}. We close the contour in the upper half plane to find the solution for $y > 0$ and in the lower half plane when $y < 0$. We take a value of ω which is in the domain of absolute convergence, i.e., above the Bromwich contour, and find the zeros of D (which will be the poles of the integrand). Recall that we have denoted those solutions of the dispersion relation for which $k_i > 0$ (for values of ω within the domain of absolute convergence) as k_{yu}, and those with $k_i < 0$ as

k_{yl}. Now we expand the dispersion relation as a Laurent series in k_y close to one of its zeros, k_a say, which is a function of ω. The dispersion relation then becomes

$$\begin{aligned} D(\omega, k_y) &= D(\omega, k_a(\omega)) + (k_y - k_a)\frac{\partial D}{\partial k_y}(\omega, k_a(\omega)) + O\left((k_y - k_a)^2\right) \\ &= (k_y - k_a)\frac{\partial D}{\partial k_y}(\omega, k_a(\omega)) + O\left((k_y - k_a)^2\right). \end{aligned} \tag{B.4}$$

Using this, we may calculate the integral in Equation (B.3) using the residue theorem. We obtain

$$J(\omega, y) = 2\pi i \sum_{k_{yu}} \frac{e^{ik_{yu}(\omega)y}}{\partial D/\partial k(\omega, k_{yu}(\omega))}, \tag{B.5}$$

when $y > 0$, and when $y < 0$ the integral becomes

$$J(\omega, y) = -2\pi i \sum_{k_{yl}} \frac{e^{ik_{yl}(\omega)y}}{\partial D/\partial k(\omega, k_{yl}(\omega))} \tag{B.6}$$

(the minus sign arises because the integration is performed clockwise around the contour in this case). We may combine (B.5) and (B.6) to obtain a solution for any value of y,

$$\begin{aligned} J(\omega, y) &= H(y)\, 2\pi i \sum_{k_{yu}} \frac{e^{ik_{yu}(\omega)y}}{\partial D/\partial k_y(\omega, k_{yu}(\omega))} \\ &\quad -H(-y)\, 2\pi i \sum_{k_{yl}} \frac{e^{ik_{yl}(\omega)y}}{\partial D/\partial k_y(\omega, k_{yl}(\omega))}, \end{aligned} \tag{B.7}$$

where H is the heavyside function defined as

$$\begin{aligned} H(y) &= 1 \quad y \geq 0 \\ &= 0 \quad y < 0. \end{aligned} \tag{B.8}$$

Now we assume that there is double root of the dispersion relation at ω_o, k_o, such that

$$D(\omega_o, k_o) = \frac{\partial D}{\partial k_y}(\omega_o, k_o) = 0. \tag{B.9}$$

Then expanding D as a Laurent series in both ω and k about the point ω_o, k_o, and taking the leading order terms, we obtain

$$(k - k_o)^2 = C^2(\omega - \omega_o), \tag{B.10}$$

where

$$C^2 = -2\left(\frac{\partial D/\partial \omega}{\partial^2 D/\partial k^2}\right)_o. \tag{B.11}$$

Thus we may define two roots of the dispersion relation close to k_o. These are

$$k_1 = k_o + C(\omega - \omega_o)^{\frac{1}{2}}, \tag{B.12}$$

and

$$k_2 = k_o - C\left(\omega - \omega_o\right)^{\frac{1}{2}}. \tag{B.13}$$

We may now express the dispersion relation close to this double root as

$$D\left(\omega, k_y\right) = \left[k - k_1\left(\omega\right)\right]\left[k - k_2\left(\omega\right)\right] R\left(\omega, k_y\right), \tag{B.14}$$

where $R\left(\omega, k_y\right)$ is regular in the region of this double root. First we assume that the double root is formed by the merging of two of the k_{yu} roots. Substituting the above relationships into Equation (B.7) we obtain

$$J\left(\omega, y\right) = \frac{2\pi i H\left(y\right) \mathrm{e}^{ik_1 y}}{2CR\left(\omega - \omega_o\right)^{\frac{1}{2}}} - \frac{2\pi i H\left(y\right) \mathrm{e}^{ik_2 y}}{2CR\left(\omega - \omega_o\right)^{\frac{1}{2}}} + J_R\left(\omega, y\right), \tag{B.15}$$

where J_R contains the summation over the other poles which are not in the region of ω_o, k_o and which is assumed to be regular. Expanding the term $\mathrm{e}^{ik_1 y}/R$ in k_y, we find

$$\frac{\mathrm{e}^{ik_1 y}}{R} = \frac{\mathrm{e}^{ik_o y}}{R\left(\omega_o, k_o\right)} + \left(k_1 - k_o\right)\left(\frac{\partial}{\partial k_y}\left\{\frac{\mathrm{e}^{ik_y y}}{R}\right\}\right)_o + O\left(\left(k_1 - k_o\right)^2\right), \tag{B.16}$$

which, using Equation (B.12), becomes

$$\frac{\mathrm{e}^{ik_1 y}}{R} = \frac{\mathrm{e}^{ik_o y}}{R\left(\omega_o, k_o\right)} + C\left(\omega - \omega_o\right)^{\frac{1}{2}}\left(\frac{\partial}{\partial k_y}\left\{\frac{\mathrm{e}^{ik_y y}}{R}\right\}\right)_o + O\left(\left(k_1 - k_o\right)^2\right). \tag{B.17}$$

Similarly,

$$\frac{\mathrm{e}^{ik_2 y}}{R} = \frac{\mathrm{e}^{ik_o y}}{R\left(\omega_o, k_o\right)} - C\left(\omega - \omega_o\right)^{\frac{1}{2}}\left(\frac{\partial}{\partial k_y}\left\{\frac{\mathrm{e}^{ik_y y}}{R}\right\}\right)_o + O\left(\left(k_1 - k_o\right)^2\right), \tag{B.18}$$

and substituting these into Equation (B.15) and letting $\omega \to \omega_o$ (and $k_1 \to k_o$ and $k_2 \to k_o$) J becomes

$$J\left(\omega, y\right) = 2\pi i H\left(y\right)\left(\frac{\partial}{\partial k_y}\left\{\frac{\mathrm{e}^{ik_y y}}{R}\right\}\right)_o + J_R\left(\omega_o, y\right). \tag{B.19}$$

Therefore in this case (where the double root is composed of two k_{yu} roots), the behaviour of J is regular close to the double root and there is no singularity. If the double root were composed of two k_{yl} roots we would find the same result.

However, if we now suppose that the double root is composed of one k_{yu} and one k_{yl} root, Equation (B.15) is modified to become

$$J\left(\omega, y\right) = \frac{2\pi i H\left(y\right) \mathrm{e}^{ik_1 y}}{2CR\left(\omega - \omega_o\right)^{\frac{1}{2}}} + \frac{2\pi i H\left(-y\right) \mathrm{e}^{ik_2 y}}{2CR\left(\omega - \omega_o\right)^{\frac{1}{2}}} + J_R\left(\omega, y\right). \tag{B.20}$$

Remembering that $H\left(-y\right) = -H\left(y\right)$ we now find that in the limit $\omega \to \omega_o$, J becomes

$$J\left(\omega, y\right) = \frac{2\pi i \mathrm{e}^{ik_o y}}{2CR_o\left(\omega - \omega_o\right)^{\frac{1}{2}}} + 2\pi i H\left(y\right)\left(\frac{\partial}{\partial k_y}\left\{\frac{\mathrm{e}^{ik_y y}}{R}\right\}\right)_o + J_R\left(\omega_o, y\right). \tag{B.21}$$

In this case J is singular at the double root and so this double root will contribute to the integrand (B.1). Thus, we can see that it is double roots that satisfy the 'pinching' condition (i.e., formed from one k_{yu} and one k_{yl}) that will contribute to the space time evolution of a wave-packet.

Bibliography

Allan, W., and A. N. Wright, Hydrodynamic wave propagation and coupling in a magnetotail waveguide, *J. Geophys. Res., 103,* 2359, 1998.

Anderson, B. J., M. J. Engebretson, S. P. Rounds, L. J. Zanetti, and T. A. Potemra, A statistical study of Pc 3-5 pulsations observed by the AMPTE/CCE magnetic fields experiment 1. Occurrence distributions, *J. Geophys. Res., 95,* 10495, 1990.

Anderson, B. J., An overview of spacecraft observations of 10 s to 600 s period magnetic pulsations in the Earth's magnetosphere, in *Solar Wind Sources of Magnetospheric Ultra-Low-Frequency Waves, Geophys. Monogr. Ser.,* vol. 81, eds. M. J. Engebretson, K. Takahashi, and M. Scholer, p.25, AGU, Washington, D.C., 1994.

Bers, A., Space-time evolution of plasma instabilities - absolute and convective, in *Handbook of Plasma Physics I,* eds. M. N. Rosenbluth and R. Z. Sagdeev, Volume 1: Basic Plasma Physics I, eds. A. A. Galeev and R. N. Sudan, North-Holland Publishing Company, 1983.

Boyd, T. J. M., and J. J. Sanderson, Plasma dynamics, Nelson, London, 1969.

Brevdo, L., Absolute and convective instabilities and the e^N method for the prediction of the laminar-turbulent transition, *Z. angew. Math. Mech., 74,* T340, 1994.

Briggs, R. J., Electron-stream interaction with plasmas, Research Monogr. No. 29, The M.I.T Press, Cambridge, Mass., 1964.

Cairns, R. A., The role of negative energy waves in some instabilities of parallel flows, *J. Fluid Mech., 8,* 1, 1979.

Chandrasekhar, S., Hydrodynamic and Hydromagnetic Stability, Oxford University Press, New York, p.482, 1961.

Chen, L., and A. Hasegawa, A theory of long-period magnetic pulsations 1. Steady state excitation of field line resonance, *J. Geophys. Res., 79,* 1024, 1974a.

Chen, L., and A. Hasegawa, A theory of long-period magnetic pulsations 2. Impulsive excitation of surface eigenmode, *J. Geophys. Res., 79,* 1033, 1974b.

Dungey, J. W., Electrodynamics of the outer atmosphere, *Sci. Rep. 69,* Pa. State Univ., University Park, 1954.

Dungey, J. W., Electrodynamics of the outer atmosphere, in *Proceedings of the Ionosphere,* p.255, Physical Society of London, 1955.

Dungey, J. W., Interplanetary magnetic field and the auroral zones, *Phys. Rev. Lett., 6,* 47, 1961.

Dungey, J. W., The length of the magnetotail, *J. Geophys. Res., 70,* 1753, 1965.

Eastman, T. E., B. Popielawska, and L. A. Frank, Three-dimensional plasma observations near the outer magnetospheric boundary, *J. Geophys. Res., 90,* 9519, 1985.

Edwin, P. M., B. Roberts, and W. J. Hughes, Dispersive ducting of MHD waves in the plasma sheet: A source of Pi2 wave bursts, *Geophys. Res. Lett., 13,* 4, 373, 1986.

Elphinstone, R. D., D. J. Hearn, L. L. Cogger, J. S. Murphree, A. Wright, I. Sandahl, S. Ohtani, P. T. Newell, D. M. Klumpar, M. Shapshak, T. A. Potemra, K. Mursula, and J. A. Sauvaud, The double oval UV auroral distribution 2. The most poleward arc system and the dynamics of the magnetotail, *J. Geophys. Res. 100,* 12093, 1995.

Engebretson, M., K.-H. Glassmeier, M. Stellmacher, W. J. Hughes, and H. Luhr The dependence of high latitude Pc5 wave power on solar wind velocity and on the phase of high speed solar wind streams, *J. Geophys. Res., 103,* 26271, 1998.

Fejer, J. A., Hydromagnetic stability at a fluid discontinuity between compressible fluids, *J. Fluid Mech., 7,* 499, 1964.

Fenrich, F. R., J. C. Samson, G. Sofko, and R. A. Greenwald, ULF high- and low-m field line resonances observed with the Super Dual Auroral Radar Network, *J. Geophys. Res., 100,* 21535, 1995.

Fujita, S., K.-H. Glassmeier, and K. Kamide, MHD waves generated by the Kelvin-Helmholtz instability in a nonuniform magnetosphere, *J. Geophys. Res., 101,* 27, 317, 1996.

Herron, T. J., An average geomagnetic power spectrum for the period range 4.5 to 12900 seconds, *J. Geophys. Res., 72,* 759, 1967.

Hughes, W. J., Magnetospheric ULF waves: A tutorial with a historical perspective, in *Solar Wind Sources of Magnetospheric Ultra-Low-Frequency Waves, Geophys. Monogr. Ser.,* vol 81, Edited by M. J. Engebretson, K. Takahashi, and M. Scholer, p.1, AGU, Washington, D.C., 1994.

Jacobs, J. A., Y. Kato, S. Matsushita, and V. A. Troitskaya, Classification of geomagnetic pulsations, *J. Geophys. Res., 69,* 180, 1964.

Joarder, P. S., V. M. Nakariakov, and B. Roberts, A manifestation of negative energy waves in the solar atmosphere, *Solar Physics, 176,* 285, 1997.

Kivelson, M. G., J. Etcheto, and J. G. Trotignon, Global compressional oscillations of the terrestrial magnetosphere: The evidence and a model, *J. Geophys. Res., 89,* 9851, 1984.

Kivelson, M. G., and D. J. Southwood, Resonant ULF waves: A new interpretation, *Geophys. Res. Lett., 12,* 49, 1985.

Kivelson, M. G., and D. J. Southwood, Coupling of global magnetospheric MHD eigenmodes to field line resonances, *J. Geophys. Res., 91,* 4345, 1986.

Kokubun, S., Statistical character of Pc5 waves at geostationary orbit, *J. Geomag. Geoelectr., 37,* 759, 1985

Landau, L. D., and E. M. Lifshitz, Electrodynamics of continuous media, G.I.T.T.L., p.141 (in Russian), Moscow, 1953.

Liu, W. W., B. -L. Xu, J. C. Samson, and G. Rostoker, Theory and observation of auroral substorms: A magnetohydrodynamic approach, *J. Geophys. Res., 100,* 79, 1995.

Mann, I. R., A. N. Wright, and P. S. Cally, Coupling of magnetospheric cavity modes to field line resonances: A study of resonance widths, *J. Geophys. Res., 100,* 19441, 1995.

Mann, I. R., A. N. Wright, K. J. Mills, and V. M. Nakariakov, Excitation of magnetospheric waveguide modes by the magnetosheath flow, *J. Geophys. Res., 104,* 333, 1999.

Manuel, J. R., and J. C. Samson, The spatial development of the low latitude boundary layer, *J. Geophys. Res., 98,* 17367, 1993.

Miles, J. W., On the reflection of sound at an interface of relative motion, *J. Acoust. Soc. Am., 29,* 226, 1957.

Mills, K. J., and A. N. Wright, Azimuthal phase speeds of FLRs driven by Kelvin-Helmholtz unstable waveguide modes, *J. Geophys. Res.,* In Press, 1999a.

Mills, K. J., and A. N. Wright, Trapping and Excitation of Modes in the Magnetotail, *Phys. of Plasmas,* submitted, 1999b.

Mills, K. J., A. N. Wright, and I. R. Mann, Kelvin-Helmholtz driven modes of the magnetosphere, *Phys. of Plasmas,* In Press, 1999a.

Mills, K. J., A. Longbottom, A. N. Wright, and M. Rudermann, The absolute and convective instability on the magnetospheric flanks - an absolute and convective instability approach, *J. Geophys. Res.,* submitted, 1999b.

Miura, A., and P. L. Pritchett, Nonlocal stability analysis of the MHD Kelvin-Helmholtz instability in a compressible plasma, *J. Geophys. Res., 87,* 7431, 1982.

Miura, A., Anomalous transport by magnetohydrodynamic Kelvin-Helmholtz instabilities in the solar wind-magnetosphere interaction, *J. Geophys. Res., 89,* 801, 1984.

Miura, A., Simulation of Kelvin-Helmholtz instability at the magnetosphere boundary, *J. Geophys. Res., 92,* 3195, 1987.

Miura, A., Kelvin-Helmholtz instability at the magnetopause boundary: Dependence on the magnetosheath sonic Mach number, *J. Geophys. Res., 97,* 10655, 1992.

Miura, A., Dependence of the magnetopause Kelvin-Helmholtz instability on the orientation of the magnetosheath magnetic field, *Geophys. Res. Lett., 22,* 2993, 1995.

McClay, J. F., and H. R. Radoski, Hydromagnetic propagation in a theta-model geomagnetic tail, *J. Geophys. Res., 72,* 4525, 1967.

McKenzie, J. F., Hydromagnetic wave interaction with the magnetopause and the bow shock, *Planet. Space Sci., 18,* 1, 1970a.

McKenzie, J. F., Hydromagnetic oscillations of the geomagnetic tail and plasma sheet, *J. Geophys. Res., 75,* 5331, 1970b.

Nakariakov, V. M., and B. Roberts, Magnetosonic waves in structured atmospheres with steady flows, 1. Magnetic slabs, *Solar Physics, 159,* 213, 1995.

Paschmann, G., Plasma structure of the magnetopause and boundary layer, in *Magnetospheric Boundary Layers,* (ESA SP-148, Paris), p25, 1979.

Press, W. H., S. A. Teukolsky, W. T. Vetterling and B. P. Flannery, Numerical Recipes in Fortran (2nd edition), Cambridge University Press, Cambridge, 1992.

Pu, Z. Y., and M. G. Kivelson, Kelvin-Helmholtz instability at the magnetopause: Solution for compressible plasmas, *J. Geophys. Res., 88,* 841, 1983.

Ribner, H. S., Reflection, transmission, and amplification of sound by a moving medium, *J. Acoust. Soc. Am., 29,* 435, 1957.

Rickard, G. J., and A. N. Wright, Alfvén resonance excitation and fast wave propagation in magnetospheric waveguides, *J. Geophys. Res., 99,* 13455, 1994.

Rickard, G. J., and A. N. Wright, ULF pulsations in a magnetospheric waveguide: Comparison of real and simulated satellite data, *J. Geophys. Res., 100,* 3531, 1995.

Roberts, B., Wave propagation in a magnetically structured atmosphere, I: Surface waves at a magnetic interface, *Solar Physics, 69,* 27, 1981a.

Roberts, B., Wave propagation in a magnetically structured atmosphere, II: Waves in a magnetic slab, *Solar Physics, 69,* 39, 1981b.

Roberts, B., Magnetohydrodynamic waves, in *Solar System Magnetic Fields, Geophys. and Astrophys. Monographs*, Edited by E. R. Priest, Chapter 3, Dordrecht, Holland, 1986.

Rudermann, M. S., and A. N. Wright, Excitation of resonant Alfvén waves in the magnetosphere by negative energy surface waves on the magnetopause, *J. Geophys. Res., 103*, 26573, 1998.

Ruohoniemi, J. M., R. A. Greenwald, K. B. Baker, and J. C. Samson, HF radar observations of Pc5 field line resonances in the midnight/early morning MLT sector, *J. Geophys. Res., 96,* 15697, 1991

Samson, J. C., R. A. Greenwald, J. M. Ruohoniemi, T. J. Hughes, and D. D. Wallis, Magnetometer data and radar observations of magnetohydrodynamic cavity modes in the Earth's magnetosphere, *Can. J. Phys., 69,* 939, 1991.

Samson, J. C., B. G. Harrold, J. M. Ruohoniemi, and A. D. M. Walker, Field line resonances associated with MHD waveguides in the magnetosphere, *Geophys. Res., Lett., 19,* 441, 1992.

Samson, J. C., and R. Rankin, The coupling of solar wind energy to MHD cavity modes, waveguide modes, and field line resonances in the Earth's magnetosphere, in *Solar Wind Sources of Magnetospheric Ultra-Low-Frequency Waves, Geophys. Monogr. Ser.*, vol 81, Edited by M. J. Engebretson, K. Takahashi, and M. Scholer, p.253, AGU, Washington, D.C., 1994.

Saunders, M., The Earth's magnetosphere, in *Advances in Solar System Magnetohydrodynamics*, Edited by E. R. Priest and A. W. Hood, Chapter 16, Cambridge University Press, Cambridge, 1991.

Seboldt, W., Nonlocal analysis of low-frequency waves in the plasma sheet, *J. Geophys. Res., 95,* 10471, 1990.

Sen, A. K., Effect of compressibility on Kelvin-Helmholtz instability in a plasma, *Phys. Fluids, 7,* 1293, 1964.

Siscoe, G. L., Resonant compressional waves in the geomagnetic tail, *J. Geophys. Res., 74,* 6482, 1969.

Siscoe, G. L., Solar system magnetohydrodynamics, in *proceedings of the 1982 Boston College Theory Institute in Solar-Terrestrial physics*, eds. R. L. Carovillano and J. M. Forbes, *Reidel,* Mass., 1982.

Smith, J. M., B. Roberts, and R. Oliver, Magnetoacoustic wave propagation in current sheets, *Astron. Astrophys., 327,* 377, 1997.

Southwood, D. J., The hydromagnetic stability of the magnetospheric boundary, *Planet. Space Sci., 16,* 587, 1968.

Southwood, D. J., Some features of field-line resonances in the magnetosphere, *Planet. Space Sci., 22,* 483, 1974.

Spreiter, J. R., and S. S. Stahara, A new predictive model for determining solar wind-terrestrial planet interactions, *J. Geophys. Res., 85,* 6769, 1980.

Stewart, B., On the great magnetic disturbance which extended from August 2 to September 7, 1859 as recorded by photography at the Kew Observatory, *Phil. Trans. Roy. Soc. Lond., 11,* 407, 1861.

Thomas, V. A., and D. Winske, Kinetic simulations of the Kelvin-Helmholtz instability at the magnetopause, *J. Geophys. Res., 98,* 11425, 1993.

Triantafyllou, G. S., Note on the Kelvin-Helmholtz instability of stratified fluids, *Phys. Fluids, 6,* 164, 1994.

Twiss, R. Q., On oscillations in electron streams, *Proc. Roy. Soc., (London), B64,* 654, 1951.

Twiss, R. Q., Propagation in electron-ion streams, *Phys. Rev., 88,* 1392, 1952.

Walker, A. D. M., The Kelvin-Helmholtz instability in the low-latitude boundary layer, *Planet. Space Sci., 29,* 293, 1981.

Walker, A. D. M., J. M. Ruohoneimi, K. B. Baker, and R. A. Greenwald, Spatial and temporal behaviour of ULF pulsations observed by the Goose Bay HF radar, *J. Geophys. Res., 97,* 12,187, 1992.

Walker, A. D. M., Excitation of magnetohydrodynamic cavities in the magnetosphere, *J. Atmos. and Solar Terrestrial Phys., 60,* 1279, 1998.

Wright, A. N., Dispersion and wave coupling in inhomogeneous MHD waveguides, *J. Geophys. Res., 99,* 159, 1994.

Wright, A. N., and G. J. Rickard, ULF pulsations driven by magnetopause motions: Azimuthal phase characteristics, *J. Geophys. Res., 100,* 23703, 1995.

Wright, A. N., K. J. Mills, M. S. Rudermann, L. Brevdo, The absolute and convective instability of the magnetospheric flanks, *J. Geophys. Res.,* In Press, 1999.

Wu, C. C., Kelvin-Helmholtz instability at the magnetopause boundary, *J. Geophys. Res., 91,* 3042, 1986.

Zhu, X. M., and M. G. Kivelson, Analytic formulation and quantitative solutions of the coupled ULF wave problem, *J. Geophys. Res., 93,* 8602, 1988.

Ziesolleck, C. W. S., and D. R. McDiarmid, Auroral latitude Pc5 field line resonances: Quantized frequencies, spatial characteristics, and diurnal variations, *J. Geophys. Res., 99,* 5817, 1994.